

UNCLASSIFIED

AD NUMBER

AD372384

CLASSIFICATION CHANGES

TO: **unclassified**

FROM: **confidential**

LIMITATION CHANGES

TO:

**Approved for public release, distribution
unlimited**

FROM:

**Distribution authorized to U.S. Gov't.
agencies and their contractors;
Administrative/Operational Use; MAY 1966.
Other requests shall be referred to Air
Force Rocket Propulsion Lab., AFSC,
Edwards AFB, CA.**

AUTHORITY

**AFRPL ltr, 7 May 1973; AFRPL ltr, 7 May
1973**

THIS PAGE IS UNCLASSIFIED

SECURITY

MARKING

**The classified or limited status of this report applies
to each page, unless otherwise marked.
Separate page printouts MUST be marked accordingly.**

**THIS DOCUMENT CONTAINS INFORMATION AFFECTING THE NATIONAL DEFENSE OF
THE UNITED STATES WITHIN THE MEANING OF THE ESPIONAGE LAWS. TITLE 18,
U.S.C., SECTIONS 793 AND 794. THE TRANSMISSION OR THE REVELATION OF
ITS CONTENTS IN ANY MANNER TO AN UNAUTHORIZED PERSON IS PROHIBITED BY
LAW.**

**NOTICE: When government or other drawings, specifications or other
data are used for any purpose other than in connection with a defi-
nitely related government procurement operation, the U. S. Government
thereby incurs no responsibility, nor any obligation whatsoever; and
the fact that the Government may have formulated, furnished, or in any
way supplied the said drawings, specifications, or other data is not
to be regarded by implication or otherwise as in any manner licensing
the holder or any other person or corporation, or conveying any rights
or permission to manufacture, use or sell any patented invention that
may in any way be related thereto.**

CONFIDENTIAL

AFRPL-TR-66-71

(UNCLASSIFIED TITLE)

**BERYLLIUM EROSION CORROSION INVESTIGATION
FOR SOLID ROCKET NOZZLES**

Second Technical Progress Report

4
8
3
2
7
6

**W. L. Smallwood, et al.
Aeronutronic Division of Philco Corporation**

TECHNICAL REPORT AFRPL-TR-66-71

May 1966

In addition to security requirements which must be met, this document is subject to special export controls and each transmittal to foreign governments or foreign nationals may be made only with prior approval of AFRPL (RPPR-STINFO), Edwards, California 93523.

D D C
REF ID: A6521
JUN 3 1966

**Air Force Rocket Propulsion Laboratory
Research and Technology Division
Air Force Systems Command
Edwards Air Force Base, California**

NOTICE: This material contains neither recommendations nor conclusions of the National Defense Science and Engineering Graduate School. It is the property of the United States within the meaning of the espionage laws, Title 18 U.S.C., Sections 770 and 771, the transmission or revelation of which in any manner to an unauthorized person is prohibited by law.

DECLASSIFIED AFTER 12 YEARS

CONFIDENTIAL

Qualified requestors may obtain copies of this report from DDC.

"When U.S. Government drawings, specifications, or other data are used for any purpose other than a definitely related Government procurement operation, the Government thereby incurs no responsibility nor any obligation whatsoever, and the fact that the Government may have formulated, furnished, or in any way supplied the said drawings, specifications, or other data, is not to be regarded by implication or otherwise, or in any manner licensing the holder or any other person or corporation, or conveying any rights or permission to manufacture, use, or sell any patented invention that may in any way be related thereto."

CONFIDENTIAL

REF ID: A64989 5119-
[Handwritten mark]

(UNCLASSIFIED TITLE)

**BERYLLIUM EROSION CORROSION INVESTIGATION
FOR SOLID ROCKET NOZZLES**

Second Technical Progress Report

**W. L. Smallwood, et al.
Aeronutronic Division of Philco Corporation**

In addition to security requirements which must be met, this document is subject to special export controls and each transmittal to foreign governments or foreign nationals may be made only with prior approval of AFRPL (RPPR-STINFO), Edwards, California 93523

NOTICE: This material contains information affecting the National Defense of the United States within the meaning of the Espionage Laws, Title 18 U.S.C., Sections 793 and 794, the transmission or communication of which in any manner to an unauthorized person is prohibited by law.

DOWNGRADED AT 3 YEAR INTERVALS; DECLASSIFIED AFTER 12 YEARS

CONFIDENTIAL

FOREWORD

This report is submitted in accordance with the requirements of Contract AF 04(611)-10753, sponsored by the Air Force Rocket Propulsion Laboratory, Edwards Air Force Base, Edwards, California. The Air Force Technical Monitor is J. H. Shock, Captain, USAF/RPMC. The contract is under the administrative control of Defense Contract Administration Services, Anaheim Region Office, 1548 State College Blvd, Anaheim, California. The contract is being performed by Aeronutronic Division of Philco Corporation, Ford Road, Newport Beach, California. A major propellant manufacturing subcontract is being performed by Atlantic Research Corporation, Shirley Highway at Edsall Road, Alexandria, Virginia. This report describes the program technical progress from 1 October 1965 through 15 March 1966. The report covers a specific segment of work rather than work accomplished during a calendar quarter.

This report has been assigned a secondary report number for internal recording and control purposes. The secondary designation is Aeronutronic Technical Report C-3498, abbreviated as ADP-TR-C-3498.

In addition to the principal author, the authors listed in alphabetical order below have made major contributions to the report sections as indicated:

Section II: H. L. Moody
 A. M. Saul

Section III: R. M. Hale
 J. K. Hall
 F. C. Price

Section IV: R. D. Hackett

Section V: J. G. Baetz

Section VI: R. K. Murray

This report contains classified information extracted from: (1) confidential attachments to the basic Contract AF 04(611)-10753 dated 14 May 1965 (2) Aeronutronic Proposal, Beryllium Erosion Corrosion Investigation for Solid Propellant Rocket Nozzles (U), Volume I, Applied Research Laboratories Publication No. P-14355 (C), dated 20 November 1964 and (3) references marked with an asterisk.

Publication of this report does not constitute Air Force approval of the reports findings or conclusions. It is published only for the exchange and stimulation of ideas.

Approving Authority: AFRPL/RPMC

UNCLASSIFIED ABSTRACT

This is the second technical progress report for Contract AF 04(611)-10753, covering the period 1 October 1965 to 15 March 1966. The program is directed toward understanding the mechanisms of corrosion and erosion of graphite, tungsten, and ablative plastic materials in beryllium propellants. Propellants, grain designs, motor-nozzle configurations, and materials have been selected for 22 small motor tests using 100-pound grains. Four aluminum analog tests are included to provide direct comparisons of the two propellant systems. The grain design and double base propellants were selected for five 500-pound development motor tests. Graphite and tungsten inserts will be used with two submerged nozzle configurations. Results of the first seven small motor tests are presented. Four beryllium and three aluminum analog propellants were tested as remotely located end burners. The edge grain pyrolytic graphite throat heat sink is common to all tests together with asbestos phenolic insulation and ATJ graphite nozzle inlet and exit cones. Detailed laboratory post-test analyses were performed on the hardware, deposit, and exhaust particle samples. Ballistic data were reduced to provide throat deposition histories and propellant performance. These data and the thermocouple measurements were used to characterize nozzle thermal history and exhaust convection and radiation heat transfer coefficients. Measured corrosion, heat transfer, and deposition are discussed in terms of physical and analytical models. The test results tend to confirm predicted similarities in beryllium and aluminum propellant behavior. Deposition and combustion problems may be primarily responsible for materials problems with beryllium propellants.

CONTENTS

SECTION		PAGE
I	INTRODUCTION	1
II	ANALYTICAL STUDIES	
	2.1 Objectives, Scope, and Summary	4
	2.2 Propellant Chemistry and Performance	6
	2.3 Nonideal Propellant Chemistry and Performance . .	10
	2.4 Fluid Mechanics	22
	2.5 Heat Transfer	23
	2.6 Conclusions, Recommendations and Future Work . .	82
III	LABORATORY STUDIES	
	3.1 Objectives, Scope and Summary	85
	3.2 Condensed Phase Reaction Studies	86
	3.3 Condensed Phase Impaction and Deposition	89
	3.4 Post Test Analysis	108
	3.5 Conclusions, Recommendations, and Future Work . .	176
IV	CORRELATION STUDIES	
	4.1 Objectives, Scope and Summary	180
	4.2 Correlation	184
	4.3 Motor Test Instrumentation	194
	4.4 Conclusions, Recommendations, and Future Work . .	213
V	MOTOR DESIGN, FABRICATION AND TEST	
	5.1 Objectives, Scope and Summary	216
	5.2 Small Motor Tests	221
	5.3 Development Motor Tests	278
	5.4 Conclusions, Recommendations, and Future Work . .	279

CONTENTS (Continued)

SECTION	PAGE
VI INDUSTRIAL HYGIENE AND SAFETY	283
VII PROGRAM INTEGRATION AND DEMONSTRATION	
7.1 Program Integration	285
7.2 Program Demonstration	292
REFERENCES	293
DISTRIBUTION	295

ILLUSTRATIONS

FIGURE	PAGE
1 Average Boundary Layer Specific Heat for Beryllium Propellants - 800 Psia	11
2 Average Boundary Layer Specific Heat for Beryllium Propellants - 400 Psia	12
3 Average Boundary Layer Specific Heat for Aluminum Propellants	13
4 Influence of Propellant Exhaust - Pyrolysis Gas Mixture Ratio on Mixture Temperature	20
5 Influence of Propellant Exhaust - Pyrolysis Gas Mixture Ratio on Excess Oxidizing Species Concentration.	21
6 Comparison Between Analytical and Measured Heat Transfer Coefficients as a Function of Nozzle Area Ratio	25
7 Total Heat Absorbed by Throat Heat Sink Versus Effective Heat Transfer Coefficient.	38
8A Temperature Response of Heat Sink Backwall for Firing T-1. 49	
8B Temperature Response of Heat Sink Backwall for Firing T-1	50
8C Temperature Response of Heat Sink Backwall for Firing T-1	51
8D Temperature Response of Heat Sink Backwall for Firing T-1	52

ILLUSTRATIONS (Continued)

FIGURE		PAGE
9A	Temperature Response of Heat Sink Backwall for Firing T-2	53
9B	Temperature Response of Heat Sink Backwall for Firing T-2	54
10A	Temperature Response of Heat Sink Backwall for Firing T-3	55
10B	Temperature Response of Heat Sink Backwall for Firing T-3	56
11A	Temperature Response of Heat Sink Backwall for Firing T-4	57
11B	Temperature Response of Heat Sink Backwall for Firing T-4	58
12A	Temperature Response of Heat Sink Backwall for Firing T-5	59
12B	Temperature Response of Heat Sink Backwall for Firing T-5	60
13A	Temperature Response of Heat Sink Backwall for Firing T-6	61
13B	Temperature Response of Heat Sink Backwall for Firing T-6	62
14A	Temperature Response of Heat Sink Backwall for Firing T-7	63
14B	Temperature Response of Heat Sink Backwall for Firing T-7	64
15	Throat Temperature Response With Deposition for Firing T-1	69
16	Throat Temperature Response With Deposition for Firing T-7	70
17	Throat Temperature Response for Firing T-4	71

ILLUSTRATIONS (Continued)

FIGURE		PAGE
18	Throat Temperature Response for Firing T-5	72
19	Throat Radial Temperature Profile at 12 Seconds for Firing T-5	73
20	Throat Temperature Response With Deposition for Firing T-3	74
21	Throat Temperature Response With Deposition for Firing T-6 (#1)	75
22	Throat Temperature Response With Deposition for Firing T-6 (#2)	76
23	Throat Temperature Response With Deposition for Firing T-2	77
24	Time Lapse Sequence of Oxide Impingement on ATJ Graphite - Surface 45 Degrees to Stream.	91
25	Time Lapse Sequence of Alumina Impingement on Asbestos Phenolic - 1.0 Second Between Frames - Surface 45 Degrees to Stream	92
26	Time Lapse Sequence of Beryllia Impingement on Asbestos Phenolic - 1.0 Second Between Frames - Surface 45 Degrees to Stream	93
27	"Motor-Nozzle Contour for Remote End Burner Tests" . . .	95
28	Effect of Particle Size on Wall Impingement for Conventional Nozzle Contour.	97
29	Dependence of Total Deposit Thickness on Free Stream BeO Particle Size Range.	98
30	NASA Modeling Study Hardware	101
31	NASA Study - Grain Port Shape and Grease Shear Patterns - Zero Burn Time.	102
32	NASA Study - Grain Port Shape and Grease Shear Patterns - 20 Second Burn Time	103

ILLUSTRATIONS (Continued)

FIGURE	PAGE
33 NASA Study - Grease Shear and Stagnation Pattern - Zero Burn Time	104
34 NASA Study - Grease Shear and Stagnation Pattern - 20 Second Burn Time.	105
35 Nozzle from Test T-1 - Entrance Cone View.	109
36 Nozzle from Test T-1 - Exit Cone View.	110
37 Nozzle from Test T-1 - Cross Section	111
38 Section of Asbestos-Phenolic Aft Closure From Test T-1	112
39 Cross Section of Asbestos-Phenolic Entrance Cone Insulator From Test T-1.	113
40 Nozzle Insert from Test T-2 - Entrance Section View. .	116
41 Nozzle from Test T-2 - Exit Section View	117
42 Nozzle from Test T-2 - Graphite Entrance Cone.	118
43 Nozzle from Test T-2 - Cross Section	119
44 Cross Section of Asbestos-Phenolic Aft Closure from Test T-2.	120
45 Cross Section of Asbestos-Phenolic Entrance Cone Insulator from Test T-2.	121
46 Nozzle from Test T-3 - Entrance Section View	123
47 Nozzle from Test T-3 - Exit Section View	124
48 Nozzle from Test T-3 - Graphite Entrance Cone.	125
49 Nozzle from Test T-3 - Cross Section	126
50 Motor Test T-3 - Aft Closure Insulator	127
51 Nozzle from Test T-4 - Entrance Section View	129

ILLUSTRATIONS (Continued)

FIGURE		PAGE
52	Nozzle from Test T-4 - Exit Section View	130
53	Nozzle from Test T-4 - Cross Section	131
54	Nozzle from Test T-4 - Exit Section View	132
55	Motor Test T-4 - Aft Closure Insulator	133
56	Nozzle from Test T-5 - Entrance Section View	136
57	Nozzle from Test T-5 - Exit Section View	137
58	Nozzle from Test T-5 - Graphite Entrance Cone.	138
59	Nozzle from Test T-5 - Cross Section	139
60	Motor Test T-5 - Aft Closure Insulator	140
61	Nozzle from Test T-6 - Entrance Section View	143
62	Nozzle from Test T-6 - Exit Section View	144
63	Nozzle from Test T-6 - Graphite Entrance Cone.	145
64	Nozzle from Test T-6 - Cross Section	146
65	Motor Test T-6 - Aft Closure Insulator	147
66	Nozzle from Test T-7 - Entrance Section View	149
67	Nozzle from Test T-7 - Exit Cone View.	150
68	Nozzle from Test T-7 - Graphite Entrance Cone.	151
69	Nozzle from Test T-7 - Cross Section	152
70	Motor Test T-7 - Aft Closure Insulator	153
71	Minuteman II Nozzle Tested with Aluminum Propellant - Entrance Section	155
72	Minuteman II Nozzle Tested with Aluminum Propellant - Throat Insert Section.	155

ILLUSTRATIONS (Continued)

FIGURE	PAGE
73 Minuteman II Nozzle Tested with Beryllium Propellant - Entrance Section	157
74 Minuteman II Nozzle Tested with Beryllium Propellant - Nozzle Cross Section	157
75 Electron Photomicrograph of Particles on Glass Slide Particle Collector-Motor Test T-4	160
76 Electron Photomicrograph of Particles in Glass Tube-Motor Test T-3.	160
77 Electron Microphotograph of Particles on Glass Slide-Motor Test T-1.	161
78 Electron Microphotograph of Particles on Brass Plate Particle Collector-Motor Test T-3	161
79 Electron Microphotograph of Particles on Brass Plate Particle Collector-Motor Test T-4	162
80 Electron Microphotograph of Particles on Copper Slide Particle Collector-Motor Test T-2	162
81 Electron Microphotograph of Particles in Glass Tube-Motor Test T-2.	163
82 Electron Microphotograph of Particles in Glass Tube-Motor Test T-4.	163
83 Electron Microphotograph of Particles on Glass Slide-Motor Test T-2.	164
84 Electron Microphotograph of Particles on Glass Slide-Motor Test T-2.	164
85 Photomicrograph of Alumina Particles Collected in Vial No. 1 from Motor Test T-5.	166
86 Photomicrograph of Alumina Particles Collected in Vial No. 3 from Motor Test T-5.	167
87 Photomicrograph of Alumina Particles Collected in Vial No. 5 from Motor Test T-5.	168

ILLUSTRATIONS (Continued)

FIGURE		PAGE
88	Photomicrograph of Alumina Particles Collected in Vial No. 3 from Motor Test T-6	169
89	Photomicrograph of Alumina Particles Collected in Vial No. 3 from Motor Test T-7	170
90	Electron Microphotograph of β Beryllia	172
91	Electron Microphotograph of β Beryllia	172
92	Electron Microphotograph of β Beryllia	173
93	Nozzle Erosion Rate as a Function of Chamber Pressure for Selected Double Base Propellants	188
94	Nozzle Throat Erosion Rate as a Function of Chamber Pressure for Selected Composite Propellants.	190
95	Thermocouple Locations on Nozzle T-1 through T-7 (A-G) .	195
96	Thermocouple Locations for Nozzle T-20	201
97	Thermocouple Locations for Nozzle T-12	202
98	Thermocouple Locations for Nozzle T-13	203
99	Thermocouple Locations for Nozzles T-21 and T-22 . . .	204
100	Thermocouple Locations for Nozzles T-16 and T-17 . . .	205
101	Thermocouple Locations for Nozzles T-18 and T-19 . . .	206
102	Hy-Cal Engineering Special Submerged Thermocouple. . .	207
103	Aeronutronic Special Submerged Thermocouple Design (Typical Installation)	208
104	Radiometer Performance	210
105	Exhaust Plume Particle Sampler No. 1	212
106	Exhaust Plume Particle Sampler No. 2	214

ILLUSTRATIONS (Continued)

FIGURE		PAGE
107	Modified Motor Case Design - End Burning Grains	223
108	Motor Case Design - Internal Burning Grains Type I.	224
109	Motor Case Design - Internal Burning Grains Type II	225
110	Motor Case Design - Internal Burning Grains Type III.	226
111	Nozzle Design for Test T-16	228
112	Nozzle Design for Test T-17	229
113	Nozzle Design for Tests T-18 and T-19	230
114	Nozzle Design for Test T-20	232
115	Nozzle Design for Tests T-21 and T-22	233
116	Action Time Definition - TSI Method	235
117	Action Time Definition - ADP Method	235
118	Chamber Pressure and Thrust Versus Firing Time Test T-1. .	238
119	Chamber Pressure and Thrust Versus Firing Time Test T-2. .	239
120	Chamber Pressure and Thrust Versus Firing Time Test T-3. .	240
121	Chamber Pressure and Thrust Versus Firing Time Test T-4. .	241
122	Chamber Pressure and Thrust Versus Firing Time Test T-5. .	242
123	Chamber Pressure and Thrust Versus Firing Time Test T-6. .	243
124	Chamber Pressure and Thrust Versus Firing Time Test T-7. .	244

ILLUSTRATIONS (Continued)

FIGURE	PAGE
125 R_b and K_n Versus Chamber Pressure for Arcocel 191F . . .	250
126 R_b and K_n Versus Chamber Pressure for Arcane 24F	251
127 R_b and K_n Versus Chamber Pressure for Arcocel 319BRF . .	252
128 R_b and K_n Versus Chamber Pressure for Arcane 54F	253
129 R_b and K_n Versus Chamber Pressure for Arcane 60.	254
130 R_b and K_n Versus Chamber Pressure for Arcocel 390. . . .	255
131 R_b and K_n Versus Chamber Pressure for Arcocel 389. . . .	256
132 Change in Nozzle Throat Radius Versus Firing Time Test T-1. .	259
133 Change in Nozzle Throat Radius Versus Firing Time Test T-2 .	260
134 Change in Nozzle Throat Radius Versus Firing Time Test T-3 .	261
135 Change in Nozzle Throat Radius Versus Firing Time Test T-4 .	262
136 Change in Nozzle Throat Radius Versus Firing Time Test T-5 .	263
137 Change in Nozzle Throat Radius Versus Firing Time Test T-6 .	264
138 Change in Nozzle Throat Radius Versus Firing Time Test T-7 .	265
139 Estimated Change in Nozzle Throat Radius Versus Firing Time Using a Composite of the K_n and F/P Methods Test T-1 .	268
140 Estimated Change in Nozzle Throat Radius Versus Firing Time Using a Composite of the K_n and I'P Methods Test T-2 .	269

ILLUSTRATIONS (Continued)

FIGURE	PAGE
141 Estimated Change in Nozzle Throat Radius Versus Firing Time Using a Composite of the K_n and F/P Methods Test T-3	270
142 Estimated Change in Nozzle Throat Radius Versus Firing Time Using a Composite of the K_n and F/P Methods Test T-4	271
143 Estimated Change in Nozzle Throat Radius Versus Firing Time Using a Composite of the K_n and F/P Methods Test T-5	272
144 Estimated Change in Nozzle Throat Radius Versus Firing Time Using a Composite of the K_n and F/P Methods Test T-6	273
145 Estimated Change in Nozzle Throat Radius Versus Firing Time Using a Composite of the K_n and F/P Methods Test T-7	274

TABLES

TABLE	PAGE
I Parameters Used to Evaluate the Radiation Heat Transfer Coefficient of Firing T-1	33
II Comparison of Radiative and Convective Heat Transfer Coefficients for Firing T-1	33
III Material Thermal Properties Employed in Throat Conduction-Drop Analysis	42
IV Propellant and Rocket Motor Parameters Used in Thermal Analysis of Motors T-1 through T-7.	65
V Q_T/A and h_{eff} Versus Area Ratio for Motors T-1 through T-7	66
VI Throat Heat Transfer Coefficients for Tests T-1 through T-7	67
VII Throat Insert Interface Contact Conductance	68
VIII Results of Low Melting Compound Survey.	88
IX Cold Flow Modeling and Rocket Motor Impingement Parameters for the End Burner-Conventional Nozzle Contour.	96
X Particle Impingement Comparison of Be and NASA Nozzles with Star Grain Port.	106
XI Motor Test T-1 Deposit Analysis	114
XII Motor Test T-2 Deposit Analysis	115
XIII Motor Test T-3 Deposit Analysis	128

TABLES (Continued)

TABLE		PAGE
XIV	Motor Test T-4 Deposit Analysis	134
XV	Motor Test T-5 Deposit Analysis	141
XVI	Motor Test T-6 Deposit Analysis	142
XVII	Motor Test T-7 Deposit Analysis	148
XVIII	AFRPL Minuteman (Al) Nozzle Deposit Analysis	154
XIX	AFRPL Minutemen (Be) Nozzle Deposit Analysis	158
XX	Motor Test Data for Throat Erosion Correlations	186
XXI	Nozzle Deposition and Erosion Data	192
XXII	Thermal Instrumentation List (for Small Scale Motor Tests)	196
XXIII	Quality of Thermocouple Data.	197
XXIV	Post Test Thermocouple Examination Comments.	199
XXV	Small Motor Design Summary.	218
XXVI	Ballistic Data, Tests T-1 through T-7	236
XXVII	General Nozzle Throat Performance	246
XXVIII	Cumulative Beryllium Sampling Results	284

CONFIDENTIAL

SECTION I (C)

INTRODUCTION

This report describes the technical progress made under Contract AF 04(611)-10753, "Beryllium Erosion Corrosion Investigation for Solid Rocket Nozzles," during the period 1 October 1965 to 15 March 1966. Serious delays in the motor test portion of the program have occurred during this period. The minimum objective of this report is to present the results of the first series of motor tests. The second objective is to summarize the progress in the analytical, laboratory, correlation, and design study areas of the program through the end of the reporting period.

The technical effort on the contract began on 1 June 1965. The current scheduled completion date for the technical effort is 16 August 1966. However, the current estimate of the actual completion date is 17 October 1966 with the distribution of the final report expected on 30 December 1966. The third technical progress report will have the minimum objective of including the results of all the small motor tests not covered in this report. It is estimated that this report will be distributed by 15 August 1966.

The overall objectives and scope of the program were described in Section I of the First Quarterly Progress Report, Reference 1. Briefly, the program objectives are to:

- (1) Provide an understanding of the mechanisms of erosion and corrosion with beryllium propellants.
- (2) Determine what nozzle materials and designs can be used with beryllium propellants.
- (3) Successfully demonstrate the performance of a test weight nozzle system with a beryllium propellant.

CONFIDENTIAL

CONFIDENTIAL

Generally speaking, analytical studies, laboratory studies, correlation studies, and rocket motor test firings are being used to achieve the program goals. Major design parameters under consideration include: (1) propellant formulation, (2) grain design, (3) nozzle contour, (4) thrust level, (5) motor configuration, and (6) materials. The primary materials of interest are graphite, dense tungsten, and re-enforced ablative insulation. Cooled nozzle concepts are excluded from consideration in the program. Both composite and composite modified double base beryllium propellants, with theoretical impulse in the 280 to 285 second range, are being used. Aluminum analogs are also being tested.

The program technical approach is based on two major assumptions. In the first place, it is expected that the important differences between comparable beryllium and aluminum propellants are confined to: (1) metal phase combustion mechanics and (2) condensed phase impaction, deposition, and flow. The second major assumption is that presently used design and analysis techniques fail to accurately characterize some or all of the following phenomena: (1) convective heat transfer, (2) corrosive species and reaction products mass transport, (3) ablative materials pyrolysis products mass addition to the nozzle boundary layer, and (4) the character and behavior of condensed phases in the exhaust. The second assumption is not restricted to beryllium propellants. It is expected that an advanced understanding of the beryllium erosion and corrosion mechanisms can not be achieved unless the important heat and mass transfer processes are well characterized.

During the period covered by Reference 1, emphasis was placed on the analysis, laboratory study, and motor design areas. Four beryllium and three aluminum analog propellant formulations were selected for use in the testing phases of the program. The theoretical and nonequilibrium performance and corrosivity characteristics of the propellants were calculated. Progress was made toward improving convective heat transfer theory and procedures were established for nozzle post-test thermal analysis. Cold flow modeling and condensed phase reaction studies were completed in the laboratory. Arc plasma impingement experiments and a low melting beryllium compound survey were initiated as part of the laboratory studies. Propellant grain, motor configuration, and nozzle designs were completed for the early 100-pound motor tests. Four propellant grains and several sets of motor hardware were delivered to AFRPL for test. However, no motor tests were completed during the first reporting period.

The technical effort of the program is divided into four major areas. The report is patterned after this division. The analytical, laboratory, data correlation, and motor test efforts are covered in Sections II through V, respectively. Section VI contains a summary of the industrial hygiene program results. Section VII presents a brief discussion of the integration of the results in the individual tasks toward the achievement of the primary

CONFIDENTIAL

CONFIDENTIAL

objectives of the program. The format of each of the sections is essentially identical to that used in Reference 1. It is hoped that this will facilitate the comparison and integration of results presented in different reports. To maximize continuity, the same format will be followed in succeeding reports.

CONFIDENTIAL

CONFIDENTIAL

SECTION II (C)

ANALYTICAL STUDIES

2.1 (U) OBJECTIVES, SCOPE, AND SUMMARY

a. Objectives

The primary objectives of the analytical studies were given in Paragraph 2.1 of Reference 1 and have not changed. During the second reporting period, the following subtasks were to be completed:

- (1) Calculate the flame side heat transfer and surface temperature history for each of the cases in Motor Tests T-1 through T-7 using the corded thermocouple data.
- (2) Estimate the chamber stay times for the grain designs and motor configurations to be used in the small motor tests.
- (3) Evaluate the corrosivity of mixtures of fine propellant combustion products with insulation pyrolysis products with respect to graphite.
- (4) Estimate heats of reaction between equilibrium propellant exhausts and the nozzle throat materials of interest.
- (5) Predict the end burning grain deposition rates using the cold flow modeling results (Paragraph 3.3b, Reference 1).
- (6) Compare surface regression measurements from Motor Tests T-1 through T-7 with the qualitative and quantitative corrosion models.

CONFIDENTIAL

CONFIDENTIAL

b. Scope

The scope of work planned in the analytical studies was presented in Paragraph 2.1.b of Reference 1. While there has been no significant change in the planned scope, the slow rate of motor testing has necessitated the deferment of some of the effort. The major emphasis during the period has been placed on the thermal analysis of the motor tests. In turn, this has required rather extensive consideration of the condensed phase deposit effects.

c. Summary of Progress

The specific elements of work completed during the second reporting period are summarized below:

- (1) Propellant formulations have been selected for all of the remaining motor tests.
- (2) Consideration of metal particle ignition and combustion models has continued.
- (3) Measured motor ballistic performance has been compared with the ideal performance for the seven propellant formulations.
- (4) The corrosivity of exhaust gas-pyrolysis gas mixtures with graphite has been examined.
- (5) Limited progress has been made in the fluid mechanics studies.
- (6) The thermocouple data from Motor Tests T-1 through T-7 have been reduced and preliminary comparisons of the heat transfer coefficients with theory have been made.
- (7) Two measurements of the condensed phase cloud radiation in the chamber were made and the results interpreted.
- (8) The thermal insulation, resulting from condensed phase deposition on the nozzle throat surface, has been evaluated using the deposit thickness histories obtained from the motor test ballistic data.

CONFIDENTIAL

CONFIDENTIAL

2.2 (C) PROPELLANT CHEMISTRY AND PERFORMANCE

a. (C) Propellant Selection

In advance of the initiation of this program, it was generally noted that the response of case insulation and nozzle materials to state-of-the-art beryllium propellant exhausts was both erratic and extreme relative to that experience with aluminum propellants. At the present time, it is apparent that such an observation is too general to be useful. Thus, as discussed in Paragraph 5.2.b, beryllium propellants will exhibit highly individualistic characteristics with respect to their influence on motor hardware. This is believed to be a direct result of the beryllia deposition phenomena and/or of serious differences in metal combustion kinetics.

The original propellant selection criteria, described in Paragraph 2.2 of Reference 1, were established to provide reasonable assurance that the general class of state-of-the-art beryllium propellants would be well represented in the program. This selection of propellants has been reviewed in terms of the hypothetical combustion model. The results are discussed in Paragraph 2.3. For the present, that discussion and the discussion of the test results given in Paragraph 5.2 will be anticipated. Thus, it is presumed that nozzle erosion will be a function of deposition and metal combustion kinetics.

Having taken this position, a number of modifications in the choice of propellant formulation for the individual small motor tests have been made. In general, greater use will be made of the Arcocel 319BRF and Arcane 54F propellants, at the expense of the Arcocel 191F propellant. This shift of emphasis to the propellant variable necessarily limits the extent to which geometric design and materials parameters will be investigated. The end result is expected to be that more information will be obtained regarding the deposition and metal combustion effects as a function of propellant formulation. To this end, a new series of tests (T-21 and T-22) has been created in an attempt to precipitate nonequilibrium metal combustion with a simple (to analyze) motor-nozzle design.

It is expected that the small motor test results will be most useful in supporting or refuting the hypothetical and analytical models being examined. The overall program objective, of course, is to identify and understand the primary mechanisms of corrosion-erosion. The detailed analytical examination of the phenomena that are basic to all propellants, hardware, and tests is essential to achieving the required understanding of the exhaust materials interaction problem. Ultimately, effective analytical and configuration design techniques and controls will be established.

In the interim, two points should be considered. First, a new set of propellant selection criteria must be established for research and materials evaluation programs. In cases when propellants are selected without

CONFIDENTIAL

CONFIDENTIAL

regard to materials problems, a net set of hardware design criteria, semi-empirically tailored to the given propellant, will be required. Generalized criteria, such as oxidation ratio, XSO, flame temperature, metal loading and (possibly) ideal performance parameters, may be of very little value. However, when it is predicted or demonstrated that deposition and metal combustion effects are essentially absent (or irrelevant), then beryllium propellant selection criteria should reduce to those which are successful with aluminized propellants. The second point involves the interpretation of the motor test data reported here. The deposition and corrosion data are characteristic of these particular tests and must not be quantitatively extrapolated to other tests or designs. The one major exception is the gas side heat transfer. This particular data, except for the inherent accuracy problem, should be representative of the propellants tested. The effective heat transfer coefficients are dependent on radiation and deposition and cannot be applied generally.

A good illustration of the systematic selection of propellants for a missile system may be found in Reference 2, Section II.A. Here, the most important selection criteria were: availability (and state of development), ideal theoretical performance, and measured performance. Propellants were classified in accordance with their ingredients in much the same manner as was done in this contract. It should be noted that the types of beryllium propellants presently being used are well represented in Table III, page 9 of Reference 2. From this table it may be observed that the impulse efficiencies for the beryllium propellants are typically lower than the aluminum propellants. Conceivably, this could be the result of either deposition or combustion effects.

Reference 2, Section II.C.1, also considers nozzle materials selection. Apparently, based on Aerojet's experience, beryllium propellants are regarded as being much more corrosive to graphite materials than aluminum propellants. The results of the present program suggest that while this may be true in some motors and for some propellants, it is not necessarily true in general. It is suggested that the blame for the apparent corrosiveness of beryllium propellants lies jointly with the design and the propellant formulation. Of course, it should not be assumed that the design criteria for beryllium propellants, which may ultimately be developed as a cure, will be more acceptable than the excessive corrosion-erosion. In any event, the recommendations of Reference 2 include a requirement for a nozzle development study effort to demonstrate nozzle design feasibility. It is possible that, in the long run, it may be more attractive to revise the propellant selection in such a way as to minimize both the nozzle materials problem and the nozzle development requirement. It is expected that the results of the present program will constitute a practical step in that direction.

CONFIDENTIAL

CONFIDENTIAL

b. (C) Propellant Characterization

(1) (U) Ballistic Performance

The ideal ballistic performance parameters calculated for the seven propellants, selected for use in this program are given in Table VI of Reference 1. Such data are used for comparison purposes in the discussions of nonideal performance in Paragraph 2.3.

(2) (U) Ideal Exhaust Composition

No data have been generated during the reporting period to supplement the ideal exhaust compositions which were given in Table .II of Reference 1.

(3) (C) Ideal Corrosion Theory

A highly idealized corrosion prediction technique was described in Paragraph 2.2.b(3) of Reference 1. It is the objective of such a theory to relate the boundary layer conductances for heat and mass transfer. It cannot, of course, be applied when protective deposits are present on the nozzle throat surfaces. It is restricted to the case of reactions which produce gaseous products by gaseous reactions with solids. It is also required that the boundary layer be well developed both thermally and chemically. Strictly speaking, the wall must be isothermal, there should be no free stream pressure gradients, and the Lewis number should be unity. In using the theory, an absolute requirement is that the chemical composition of the free stream (exhaust and/or boundary layer) must be known. The addition of ablation product, from dissimilar materials upstream of the point of interest, violates the requirements of the simple theory. Significant axial temperature gradients along the nozzle contour also violate the theory. Nevertheless, comparison of the theory with the motor test results should be informative. It is ultimately expected that empirical correlations of the simple theory can be developed and used for design purposes.

The ideal corrosion theory predicts a low temperature threshold for corrosion by the propellants of interest. For graphite, the ideal threshold temperature is approximately 1900°F. Below that temperature, the exhaust gases are essentially saturated with carbon and, consequently, are inert to graphite. Furthermore, the simple theory suggests that the corrosion rate should be about constant (independent of surface temperature) for double base propellants over the range of 2000 to 4000°F (beryllium) or to 3500°F (aluminum). The data from Motor Test T-3 (Arcocel 319BRF) and its analog, T-6 (Arcocel 390), indicate that corrosion started when the wall temperature reached approximately 2500°F. In each of these tests, oxide deposits began to coat the throat within a few seconds after the corrosion began. The deposit remained on the throat until the end of

CONFIDENTIAL

CONFIDENTIAL

firing. The measured erosion rate, over the short period when the corrosion apparently occurred, was slightly less than 0.001 inch per second. In comparison, Equation 17, Reference 1, predicts a rate which is only about 15 percent higher.

In Motor Test T-5 (Arcane 60), the alumina deposit was removed from the throat (or some fraction of it) when the surface temperature passed the alumina melting point (about 3700°F). The maximum throat surface temperature was about 3800°F. The pressure and thrust data strongly suggest that some deposit was still passing through the throat near the end of the test. The temperature measurements tend to average out any circumferential variations in heat transfer or deposition. Consequently, it is speculated that the bottom half of the nozzle may have been coated while the top half was not. If this is true, then the maximum erosion rate was also about 0.001 inch per second (the average being half of that value). In this case, the predicted rate is 4 to 5 times the measured value. Postfiring measurements of the nozzle throat (with deposits removed) showed it to be slightly elliptical. The beryllium analog firing T-4 (Arcane 54F) did not produce any surface regression since the deposit did not come off the throat until the motor pressure fell.

In each of the tests, other than T-3 and its analog T-6, the deposit first reached the throat when the surface temperatures were in the range of 2500 to 2800°F. No predeposition corrosion was observed in these tests. Evidently then, a corrosion threshold exists for the Arcocel 319BRF and its aluminum analog in the vicinity of 2500°F, not very far above the predicted value. Deposition may easily have obscured the existence of similar thresholds for the other propellants.

The Arcocel 191F and its analog, Arcocel 389, (Tests T-1 and T-7) were the only propellants to produce throat surface temperatures above 4200°F. This temperature is regarded as the threshold for the high temperature corrosion regime. That is, above this level, the hydrogen-graphite reactions become important. In each of these tests, the nozzle throats were somewhat elliptical so that the maximum surface regression could be as much as twice the average rate of about 0.0025 inch per second. The maximum throat surface temperatures were 4800 and 5200°F for Tests T-1 and T-7, respectively. It should be noted that the calculated throat surface temperature rise rate is severely reduced when corrosion begins. This is thought to be a consequence of the hydrogen reactions (producing acetylene) being endothermic. The net increase in the reaction rate, over the low temperature value of 0.001 inch per second for the other propellants, is about 0.002 inch per second. Again, this is an average value which could be much lower than the maximum due to nonuniform throat deposit coverage. The theoretical corrosion rate predicted for the beryllium propellant (191F) at 4800°F is 5 times the measured value. For the aluminum analog at 5200°F, the predicted value is a factor of 10 higher. From this, it could be argued that there are powerful kinetic reaction rate limitations which pertain for the hydrogen reactions in the high temperature regime.

CONFIDENTIAL

CONFIDENTIAL

While further study of the relationship between the simple theory and motor test data is required, several conclusions can be drawn. Thus, it is apparent that the qualitative behavior of the propellant analog pairs is extensively similar in terms of corrosion. At the same time, there is very little superficial similarity among the various formulations. However, the differences can be interpreted with some success by exploiting the simple corrosion theory during the portion of the firing period when deposit effects do not prevail. Finally, the magnitudes of the measured corrosion rates are not of the order expected when the metal phase has not burned completely.

c. (U) Propellant Thermal Properties

The average boundary layer specific heat, as a function of wall temperature, has been calculated for each of the propellants used in the program. Data were calculated at the nominal chamber pressure (800 psia) and at 400 psia (which approximates the throat pressure). The average specific heat, \bar{C}_p , is the average slope of the exhaust enthalpy-temperature curve (at constant pressure), taken from the stagnation enthalpy (no correction for recovery effect) to the exhaust enthalpy at the wall temperature of interest. The \bar{C}_p data for the beryllium propellants are given in Figures 1 and 2 for the 800 and 400 psia pressures, respectively. The same data for the aluminum propellants are given in Figure 3.

The step in the \bar{C}_p curves is a consequence of metal oxide fusion. If condensed beryllia is present in the boundary layer, it may not freeze as it approaches the wall. However, any beryllia which comes in contact with the wall or deposit surface may stick and then freeze, contributing to the heat transfer. Theoretically, there are limiting particle stream lines which suggest that, from some point on the contour (upstream of the throat), there will be no condensed material in the boundary layer. A significant change in \bar{C}_p , boundary layer density, and convective heat transfer coefficient would occur at such a point and persist downstream. Basically, a reduction in heat transfer is expected, possibly explaining the rapid decay in convective coefficients downstream of the throat observed with metalized solid propellants. The very small particle size of the beryllia (see Section III) suggests that it may be present in the boundary layer as far as the throat. The small particle size should permit a higher degree of freezing in the boundary layer than would otherwise occur. Consequently, while \bar{C}_p data may be somewhat conservative, they are being used as presented.

2.3 (C) NONIDEAL PROPELLANT CHEMISTRY AND PERFORMANCE

a. (C) Solid Propellant Combustion

One of the most powerful idealizations in chemical propulsion systems design and analysis is that the propellant combusts to the theoretical equilibrium state. In general, it may be assumed that this state is never achieved in

CONFIDENTIAL

CONFIDENTIAL

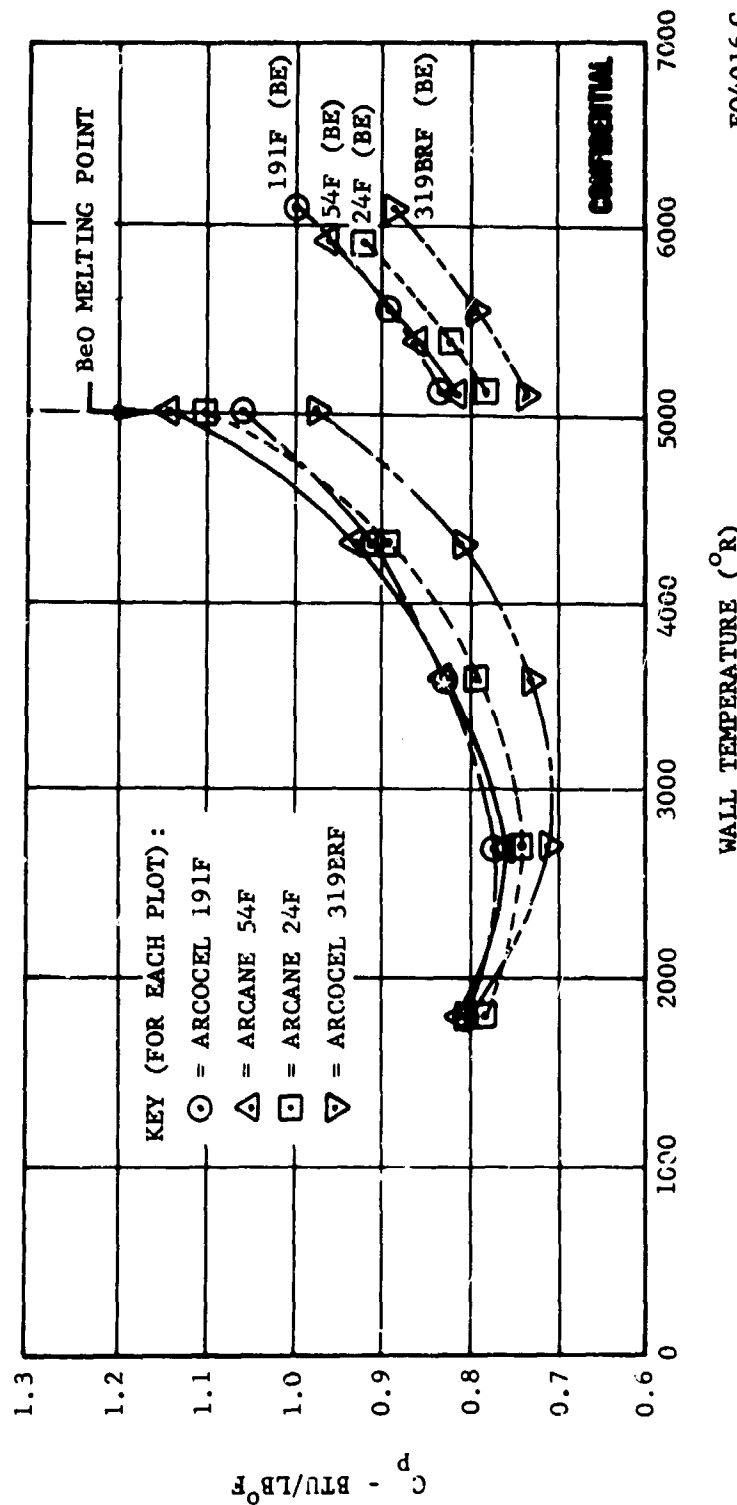


FIGURE 1. AVERAGE BOUNDARY LAYER SPECIFIC HEAT FOR BERYLLIUM
PROPELLANTS - 800 PSIA

CONFIDENTIAL

CONFIDENTIAL

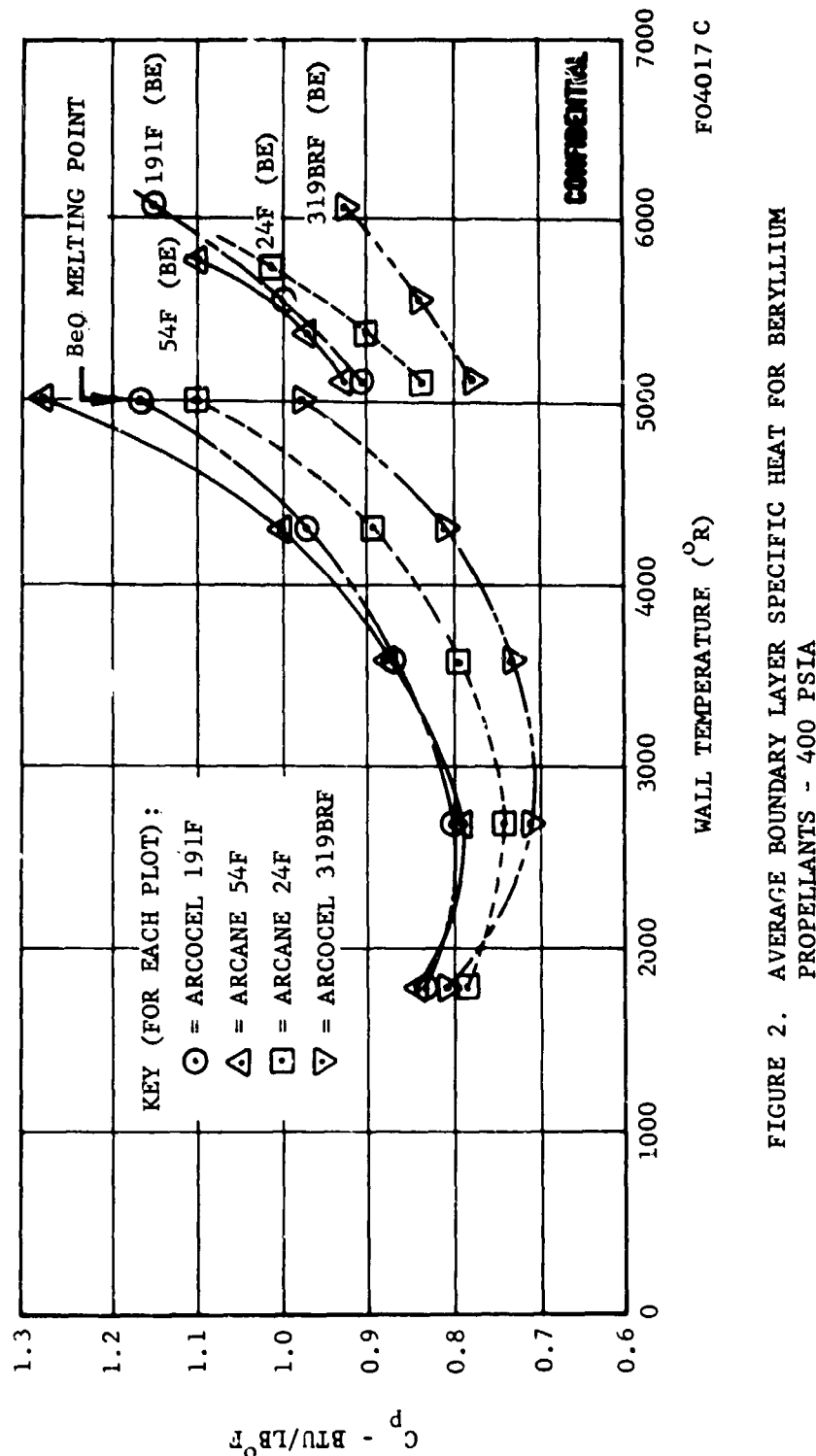


FIGURE 2. AVERAGE BOUNDARY LAYER SPECIFIC HEAT FOR BERYLLIUM
PROPELLANTS - 400 PSIA

CONFIDENTIAL

CONFIDENTIAL

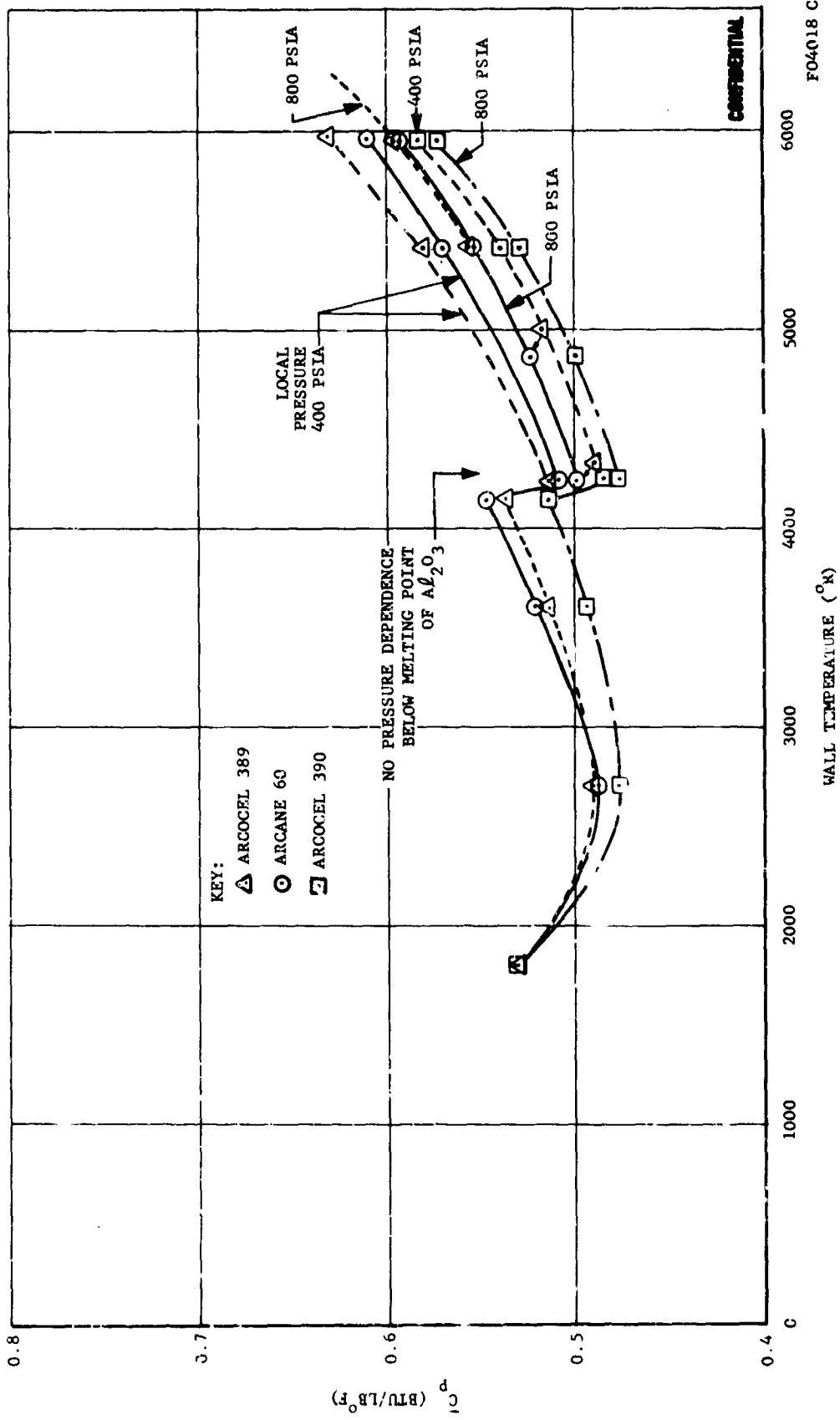


FIGURE 3. AVERAGE BOUNDARY LAYER SPECIFIC HEAT FOR ALUMINUM PROPELLANTS

CONFIDENTIAL

practice. Finite times are always required to complete chemical reactions even under the most ideal conditions. Fortunately, such times are very small. However, a solid propellant is far from ideal, at least in the sense that it is not microscopically homogeneous. A metalized solid propellant is even less homogeneous. The combustion process, then, becomes contingent on the mechanics of the mixing and heating processes. Since we are dealing with an open flow system, relatively large times and axial flow distances will potentially be required to achieve a degree of submicroscopic uniformity which approximates thermodynamic equilibrium.

This general situation is not uncommon in liquid propellant engines nor has it gone unrecognized in the solid propellant field. In the present program, the primary question has been reduced to determining whether beryllium propellant combustion mechanics or kinetics may be significantly different from what they are for aluminum. In either case, it is highly desirable, in the interpretation of nozzle heat transfer and corrosion, to have reasonably accurate knowledge of the characteristic times required to complete combustion in a practical sense. If such "stay-times" vary significantly among propellant systems or individual propellants, much of the nozzle corrosion-erosion confusion could probably be eliminated.

In examining a wide variety of beryllium propellant test data, some of which are discussed in Paragraph 4.2, the minimum in chamber stay-time appears to be in the range of one tenth to one millisecond. Maximum values depend primarily on motor scale and can be of the order of a second. In defining the stay-time, the shortest stream line distance from the propellant surface to the wall or to the nozzle throat is of interest. By neglecting the potential condensed phase velocity v_g and gas temperature variations along such stream lines, approximate stay-times are deduced directly. For comparison, the theoretical and experimental work of References 3 and 4 (for example) indicate that total metal particle burn times may fall in the range of one tenth to ten milliseconds.

The qualitative beryllium propellant combustion model described in Paragraph 2.3, Reference 1, hypothesizes that the beryllium metal particles actually leave the grain surface and are carried along by the gas phase. It is also supposed that the particle must ignite and burn in a gas phase which results from the "rapid" combustion of all other propellant ingredients. In contrast to aluminum, the beryllium particle may leave the grain surface without having melted. During and after particle ejection from the grain, surface oxidation should occur. The oxide coating would then act to slow the particle heating process and retard or eliminate further reactions with the encapsulated metal. If the oxide eventually melts, the beryllium vapor will become available for reaction. Consumption of the vapor will cause more vaporization and increased local temperatures, accelerating the combustion process until the supply of oxygen (as H_2O , etc.) becomes critical. In the event that the oxide coating is porous, beryllium vapor may leak out, permitting combustion at relatively lower rates and lower particle temperatures.

CONFIDENTIAL

CONFIDENTIAL

Originally, it was assumed that the ignition delay and combustion times were potentially the only important delays in the process of attaining the thermodynamic equilibrium. However, there may be one additional delay. Thus, the beryllium vapor flame should produce nonequilibrium concentrations of the metal chloride and hydroxide gases as well as beryllia, beryllium nitride, and beryllium carbide. Obviously, even a temporary compounding of beryllium with other than oxygen or water will increase the corrosivity of the exhaust with respect to carbon or tungsten. It is speculated that very long times may be required to complete the redistribution of the gaseous beryllium phases both because the free energy change is small and because gas reaction kinetics may be important. The production of nonequilibrium quantities of the hydroxides should not have a significant influence on either propellant performance or corrosion. That is, the hydroxide ($\text{BeO}\cdot\text{H}_2\text{O}$) is simply the association of two molecules which would have existed separately. On cooling in the nozzle boundary layer, the hydroxide should dissociate into beryllia gas and water or hydrogen. While the precipitated beryllia will be more reactive, it will exist at relatively low concentrations so that the diffusion transport rates will be low. In the free stream, the hydroxide may precipitate beryllia on existing particles causing them to grow.

The more dangerous situation would result from the formation of excess chlorides. Both propellant performance losses and increased corrosion should result. The credibility of this argument will be explored further by means of suitable data correlation and nonideal propellant performance analyses. The discussion in Paragraph b, following, compares the measured C-star data from the end burning grain tests. It is noted there that the highest efficiency was delivered by the Arcocel 319BRF propellant. This particular propellant, in addition to being the only beryllium formulation based on RDX, has the lowest weight percent of ammonium perchlorate. Unfortunately, the aluminum analog test was a hang fire and good performance data were not obtained. On the other hand, the Arcocel 389 and Arcane 60 aluminum propellants exhibited high efficiencies. Therefore, the beryllium propellant chloride content appears to be the most promising correlation parameter for the present.

The qualitative beryllium combustion model suggests a number of propellant and motor design parameters which should be useful in correlating corrosion data. Among these are (1) ideal flame temperature, (2) flame temperature without any metal burning, (3) oxide melting point, (4) oxidizing species concentrations at ideal combustion conditions, (5) oxidizing species concentrations without any metal combustion, (6) total chlorine concentration, (7) chlorine to hydrogen ratio without metal combustion, (8) percent of metal burning required to raise the flame temperature to the oxide melting point, (9) no lag chamber stay-time, (10) chamber velocity, (11) propellant burn rate and burn rate exponent, and (12) metal particle size distribution. All of these parameters may have an influence on the ignition delay, particle

CONFIDENTIAL

CONFIDENTIAL

burn time, and mixing time requirements for the metal particles. Several of the items are significantly different for the two metals of interest. The relationship of these parameters to experimental nozzle corrosion data will be examined in the correlation studies during the remainder of the program.

b. (C) Nonideal Ballistic Performance

Ballistic performance calculations have been performed for the seven propellant formulations as a function of the percent of the metal phase which is permitted to burn. The unburned metal's heat capacity is included but the metal is otherwise unaffected as it passes through the nozzle. Such a situation could physically occur when the total particle stay-times fall between the ignition delay and complete beryllium combustion times. Here, the complete combustion implies thermodynamic equilibrium. Intermediate nonequilibrium in the gas phases is not accounted for.

The results, C-star, and impulse for the Arcocel 191F and its analog, Arcocel 389, were presented in Figures 4 through 7 of Reference 1. The variation in C-star for all the beryllium and aluminum formulations is approximately linear between the following extremes:

<u>Propellant</u>	<u>0% Metal Burned (ft/sec)</u>	<u>100% Metal Burned (ft/sec)</u>
Arcocel 191F (Be)	4410	5450
Arcocel 389 (Al)	4160	5170
Arcocel 319BRF (Be)	4450	5510
Arcocel 390 (Al)	4230	5280
Arcane 54F (Be)	4200	5420
Arcane 60 (Al)	3900	5120
Arcane 24F (Be)	4230	5400

The variation in optimum specific impulse is also nearly a linear function of the percent metal burned. The variation in impulse for all the beryllium and aluminum propellants at the 25 and 100 percent metal combustion points is shown below:

<u>Propellant</u>	<u>25% Metal Burned (sec)</u>	<u>100% Metal Burned (sec)</u>
Arcocel 191F (Be)	233	278
Arcocel 389 (Al)	220	261
Arcocel 319BRF (Be)	235	282
Arcocel 390 (Al)	224	264
Arcane 54F (Be)	225	279
Arcane 60 (Al)	212	258
Arcane 24F (Be)	226	278

CONFIDENTIAL

CONFIDENTIAL

There is not a great deal of variation among the propellants in terms of the character of the dependence of performance on metal burning. Consequently, performance measurements should reflect incomplete combustion tendencies for any of these (and probably other) propellants. For this reason, the C-star and impulse efficiencies for the initial motor tests have been examined in detail. The C-star efficiencies have been calculated in two ways. First, the average value for each test was determined using the integrated average pressure, integrated average throat area, and the average mass flow (based on the original propellant weight and the action time). The second method used the instantaneous values of pressure, throat area and mass flow (compatible with the derived deposit and burn rate histories). The values selected represent levels maintained for a major portion of the action time. The impulse efficiencies have been calculated using the integral average delivered thrust and the average mass flow (based on the original propellant weight and the action time).

The impulses have been corrected for the divergence loss. However, it is clear from the motion pictures of Tests T-1 through T-7, that exit cone deposits caused some detachment and other side force producing effects. The results are given in the following table. It should be noted that the ideal C-star and impulse values correspond to the nominal 800 psia chamber condition. These values will eventually be corrected to the experimental average pressures.

<u>Propellant</u>	<u>\bar{P}_c (psia)</u>	<u>C*</u> <u>(average)</u>	<u>%</u>	<u>C*</u> <u>(instantaneous)</u>	<u>%</u>	<u>I_{SP} (average)</u>	<u>%</u>
Arcocel 191F (Be)	818	5170	95.0	4850	89.3	243	88.5
Arcocel 369 (Al)	935	4300	92.7	5100	98.5	230	88.1
Arcocel 319BRF (Be)	737	5525	100.2	5480	99.6	253	89.7
Arcocel 390 (Al)	536	4910	93.0	-	-	229	86.7
Arcane 54F (Be)	799	4890	90.3	4800	88.5	239	85.6
Arcane 60 (Al)	830	4910	95.9	4800	93.8	234	90.6
Arcane 24F (Be)	723	5055	93.7	4850	89.9	244	87.8

Evidently, the C-star and impulse efficiencies do not follow the same pattern, except possibly that the Arcane 54F gave the lowest performance in each category. The impulse efficiencies of the beryllium propellants are in the same order as the equilibrium HCl and H₂O concentration, but this does not hold for the aluminum propellants. The highest C-star efficiency was obtained from the Arcocel 319BRF which has only 8 percent ammonium perchlorate and by far the minimum equilibrium exhaust HCl and H₂O content. The beryllium performance does not correlate with the exhaust flame temperature without metal burning. In fact, it is doubtful that

CONFIDENTIAL

CONFIDENTIAL

there is a significant difference in the C-star efficiencies of the beryllium propellants other than the Arcocel 319BRF. The aluminum analogs may have significantly higher efficiencies.

Basically, the measured performance data do not provide an entirely clear reflection of the degree of combustion. However, it strongly suggests that complete combustion was not achieved. It is clear that neither type of C-star efficiency is entirely accurate. Further examination of the ballistic data and the evaluation of succeeding tests with these propellants are required before any final conclusions can be drawn. If it is ultimately confirmed that complete combustion was not achieved, some of the basic heat transfer results will have to be revised. The effect would be to increase the gas side convective coefficients. The interpretation of the corrosion data should not change a great deal.

c. (U) Nonideal Exhaust Compositions

At the close of the reporting period, several types of nonideal exhaust composition calculations were in progress. Primarily, an attempt is being made to examine the relationship among the H₂, HCl, H₂O and Be species in the vicinity of the burning metal particles. The relationship between NO, N₂, and Be is also being examined. These results will be presented in a later report.

d. (C) Nonideal Exhaust Corrosivity

Because beryllium has a low vapor pressure and BeO has a high melting point (2823°K), the model for nonequilibrium combustion of beryllium assumes that an oxide layer rapidly forms over the beryllium particle, inhibiting further vaporization and reaction. For the larger particles it is assumed that the metal must be heated to the temperature at which the oxide coating will melt before rapid burning of the beryllium will occur. In addition, it is assumed that the binder and oxidizer burn to equilibrium very close to the propellant grain surface.

A consequence of these two assumptions is that ignition of the metal particles must occur downstream of the propellant flame front. For small residence times, this means that the exhaust stream can mix with ablative insulation pyrolysis products before ignition of the beryllium particles can occur. Such mixing can have two major effects: (1) it can change the chemical composition of the gas mixture and hence, influence the subsequent combustion kinetics of the beryllium particles, and (2) it can change the temperature level of the gas mixture, also influencing the metal combustion kinetics. A limited study has been conducted to identify the chemical reactions and temperature changes associated with such mixing.

CONFIDENTIAL

CONFIDENTIAL

The identification of the pyrolysis gases requires an analysis of the decomposition of the virgin ablative material and the flow to the char surface. A simplified analytical technique has been developed at Aeronutronic under Contract AF 04(611)-9904, for carbon cloth and graphite cloth phenolics. For these materials, the analysis can be limited to defining the weight ratio of hydrogen to oxygen being generated. It is assumed that all the hydrogen and oxygen in the resin are removed during pyrolysis and that these gases are in equilibrium with the char at a fixed char temperature and local pressure. Thus, a carbon saturated gas system is generated consisting principally of gaseous CO, H₂, H₂O, CO₂, and, depending on temperature, CH₄ or C₂H₂ and C₂H. This carbon saturated gas stream is then allowed to mix and react with the combustion product free stream in fixed mixture ratios.

Initial pyrolysis gas temperatures of 3100°K, 2600°K, 2100°K, 1600°K and a pressure of 800 psia were selected for these calculations. The resultant data are shown in Figures 4 and 5. Figure 4 shows the equilibrium gas temperature as a function of the percent combustion product free stream from Arcocel 319BRF propellant. Zero beryllium combustion is assumed. The unburned metal is presumed to be at the temperature of the exhaust in order to include the heat capacity contribution of the metal.

The principal oxidizing specie in the combustion product free stream is H₂O. The subsequent oxidation by this H₂O of the hydrocarbons from the ablative insulation pyrolysis to CO and hydrogen not only is endothermic but also drastically reduces the concentration of those gaseous species which could supply oxygen to the metal. As indicated in Figure 5, the addition of more than about 25 percent pyrolysis gases (degas) to the combustion product gas stream would preclude complete oxidation of beryllium. There is not sufficient oxygen in the system to handle the additional carbon and the beryllium. Some of the beryllium combusting in such an environment will form condensed Be₂C or Be₃N₂, depending on the temperature conditions. Negative values shown in Figure 5 imply that the mixture is oxygen deficient with respect to complete beryllium metal combustion.

It is apparent that the pyrolysis products are capable of consuming thermal energy by both dilution and chemical reaction. Those reactions which occur on mixing will tend to reduce the oxygen available to beryllium. This will either prevent further burning or slow combustion considerably. It also becomes more likely that nonequilibrium quantities of gaseous and/or condensed beryllium species may appear in the boundary layer. While the contour may be locally shielded from the effects of the highly oxidizing exhaust, nonablating surfaces downstream could still be affected significantly since all of the available oxygen (with respect to graphite or tungsten) would not be consumed if beryllium particle burning is stopped during mixing of the exhaust and pyrolysis gases.

CONFIDENTIAL

CONFIDENTIAL

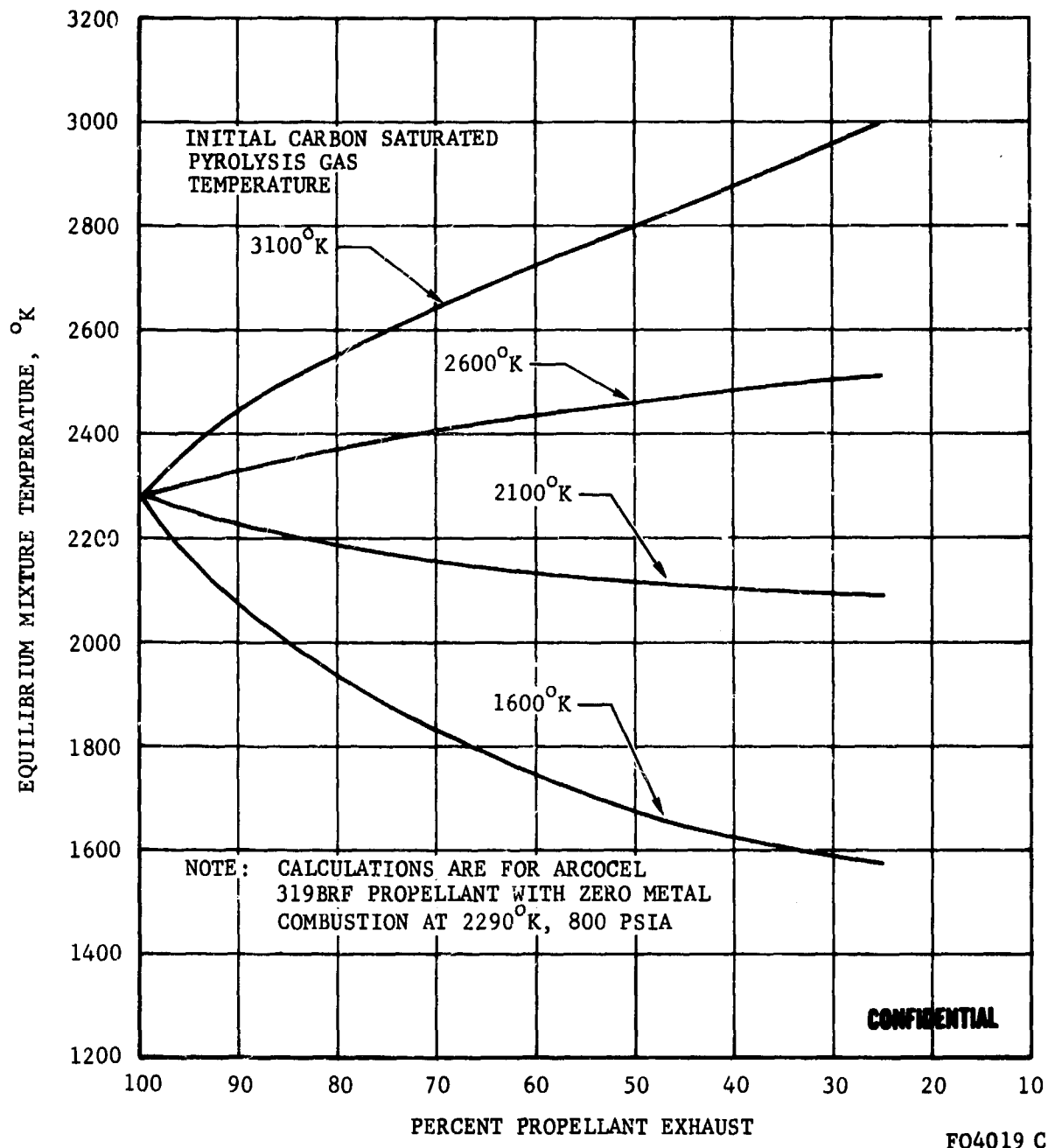


FIGURE 4. INFLUENCE OF PROPELLANT EXHAUST - PYROLYSIS GAS MIXTURE RATIO ON MIXTURE TEMPERATURE

CONFIDENTIAL

CONFIDENTIAL

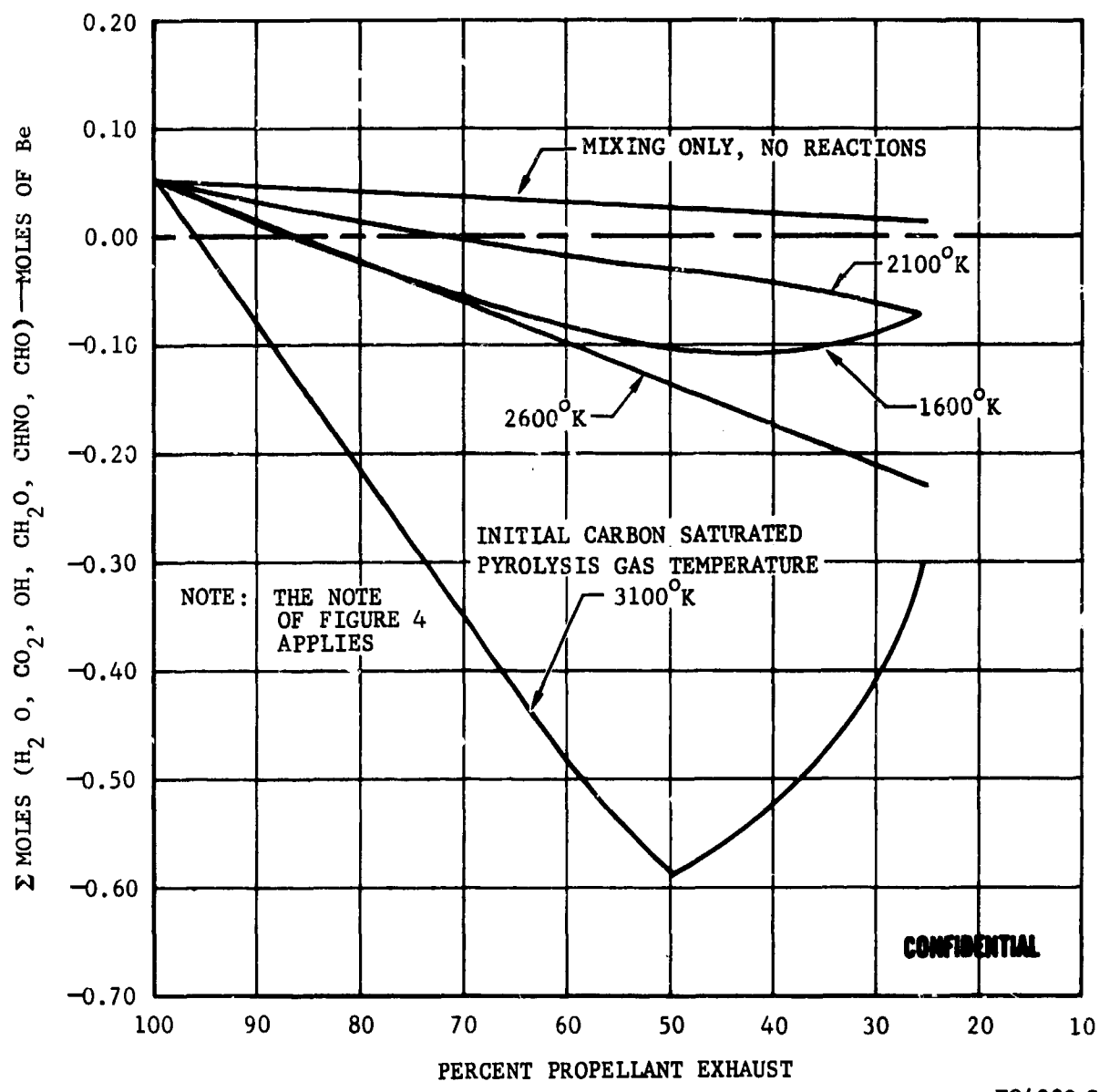


FIGURE 5. INFLUENCE OF PROPELLANT EXHAUST - PYROLYSIS GAS MIXTURE RATIO ON EXCESS OXIDIZING SPECIES CONCENTRATION

CONFIDENTIAL

CONFIDENTIAL

2.4 (U) FLUID MECHANICS

Several discussions regarding the two phase flow, grain design and boundary layer theory, have been included in Paragraphs 3.3, 5.3, and 2.5, respectively.

Two phase flow calculations have been postponed again due to the poor definition of the condensed phase particle size. For beryllium propellants, there may still be a possibility that the beryllia particle size distribution can be related to the original beryllium metal particle size distribution. Establishing such a relation requires a significant amount of effort in particle counting. The samples obtained in the initial motor firings may be somewhat biased.

It is presently felt that the open mouthed bottles on the second sampler (see Section IV) are the best. A cursory examination of several of the particle photographs (see Paragraph 3.4) suggests that there may be a continuous size variation but there are not very many of the largest particles. The largest beryllia particles are approximately 15 percent of the diameter of the largest beryllium metal particles in the propellant. If the particle sizes obtained from the internal burning grain tests are similar to those from the remote end burner tests, some particle counting would be in order. Current speculation is that alumina particles increase in size while they flow through the motor. If this is primarily a result of the condensation of alumina from the gaseous suboxides, hydroxides, and/or chlorides, then a comparable phenomenon may not exist for the beryllia.

In the correlation studies, some indication of the existence of poor metal particle combustion has been found. The no-lag chamber stay-times required for complete combustion of the Arcane 53 propellant (Paragraph 4.2) were estimated to be in the range of 3 to 4 milliseconds. During the next reporting period, the velocity and thermal lags for the metal particles will be estimated. The particle flight times and combustion temperatures will also be estimated. Motor Tests T-21 and T-22 (close end burner) are expected to provide data for comparison. Except for Test T-15, the other small motor tests should have chamber stay times in excess of those required to achieve particle ignition and combustion.

The grain design selected for use in the development motor tests is briefly described in Paragraph 5.3. Calculations of the heat transfer coefficient for the Arcocel 191F propellant, using the advanced boundary layer theory, are given in Paragraph 2.5.a. The results are generally quite encouraging in that the maximum convection coefficients are well above those predicted by the simpler techniques. Similar computations for the other propellant formulations will be performed for comparison purposes.

CONFIDENTIAL

CONFIDENTIAL

2.5 (C) HEAT TRANSFER

The major portion of the analytical studies effort during the reporting period has been devoted to the analysis of the heat transfer data from Motor Tests T-1 through T-7. The detailed design and instrumentation of the nozzles may be found in Paragraphs 5.2 and 4.3, respectively, of Reference 1. The subjects of convection, radiation, conduction/ablation, and deposition are discussed separately. The thermocouple measurements and calculated nozzle temperatures are given in Paragraph 3. These results are briefly discussed in Paragraph e(3). It should be kept in mind that these studies have two objectives: (1) to extend the limited thermocouple data to a complete characterization of the nozzle thermal history in support of the study of corrosion mechanisms, and (2) to provide a test of the analytical techniques used to predict the basic radiation and convection heat transfer capacities of beryllium propellants.

a. (C) Convection

The theoretical prediction of the rocket nozzle convective heat transfer coefficient can be undertaken at several levels of sophistication. The simpler techniques are typically derived from boundary layer theory by invoking a variety of relatively powerful assumptions. Often, as these techniques are adopted in practice, the assumptions are forgotten. Then, when nozzles hardware thermal design is predicated on criteria which underestimate the heat transfer, the corrosion resistance and structural capacity of the nozzle materials can be badly misjudged. Therefore, it is regarded as a fundamental requirement in this program that the heat transfer characteristics of beryllium propellants be examined as closely as possible. Three techniques are being studied to assess their abilities to predict the convective heat transfer data derived from the small motor tests. Unfortunately, the comparisons of theory with experimental results are dependent upon the techniques used to extend the thermocouple measurements to the flame side convective coefficients. The greatest error is thought to be introduced by using the throat deposit history derived from the ballistic data and by using unconfirmed oxide thermal property data.

The simplified Bartz equation (Equation 35, Reference 1) was not correlated with high energy propellant test data and should not be used. The primary objection to its use derives from the characterization of the exhaust specific heat. A significant portion of the chamber enthalpy (potential energy) does not appear as simple thermal energy (temperature). As flame temperatures increase, a greater fraction of the propellant energy is consumed "chemically" in dissociation, chemical reorganization, and vaporization. The use of frozen specific heats neglects this energy. The use of the thermochemical equilibrium specific heat in the combustion chamber represents a significant improvement. However, this value does not represent the specific energy of the propellant exhaust in the nozzle boundary layer. This is because the fraction of the energy which is

CONFIDENTIAL

CONFIDENTIAL

chemically stored varies with the static pressure and boundary layer temperatures. This can be seen by noting the changes in slope, with pressure, of the enthalpy-temperature curves, such as are shown in Figure 2 of Reference 1. Consequently, boundary layer average specific heats, calculated as a function of static pressure (Equation 36, Reference 1), should be employed with the Bartz equation. Because of the requirement to perform the additional thermochemical calculations, some of the simplicity of the original technique is lost.

The second analytical technique of interest is the JPL boundary layer computer program, Reference 5. This program is based on a number of perfect gas and shear laws which are of questionable validity. Nevertheless, it is convenient to use and the simplified Bartz equation was derived from the same theory.

The third analytical technique is an adaptation of the JPL theory. During the present and preceding contracts, the perfect gas and shear law assumptions have been replaced or revised. The one dimensional flow requirement can also be eliminated at the user's option. Wall blowing, surface reactions, and surface roughness effects can also be accounted for.

The first comparison of these techniques has been made during the reporting period. The results are shown in Figure 6. The lower curve is the perfect gas prediction obtained by using the original JPL program. The upper curve represents the real gas prediction for the Arcocel 191F propellant. This calculation was not extended beyond the throat and assumes one dimensional flow. Because of the deposit problem and the time averaging used in the motor test data reduction, this preliminary calculation also neglects blowing and ablation products film effects.

The experimental data points indicated in Figure 6 were obtained from Paragraph 2.5.e. Both the 191F and its aluminum analog, Arcocel 389, are represented. Only minor variations in the real gas heat transfer prediction are anticipated for these two propellants. Except for the two throat gas side data points, the experimentally derived points represent the effective heat transfer coefficients to the graphite surface. That is, the oxide deposits which persist over most of the firing period effectively reduce the heat transfer (consequently, the convective coefficient) at the graphite surface. Lacking the deposit thickness over the contour, the gas side convective coefficients cannot be deduced. They must, however, be significantly higher than the data points themselves.

Three factors should be considered in comparing the gas side coefficients at the throat with the real gas theory. First, the exact axial location of the throat thermocouples, relative to the location of the maximum heat transfer coefficient, is not known. In real gas, two dimensional flow, the peak heat transfer coefficient occurs upstream of the throat, possibly by as much as a quarter of an inch. The thermocouples were approximately

CONFIDENTIAL

CONFIDENTIAL

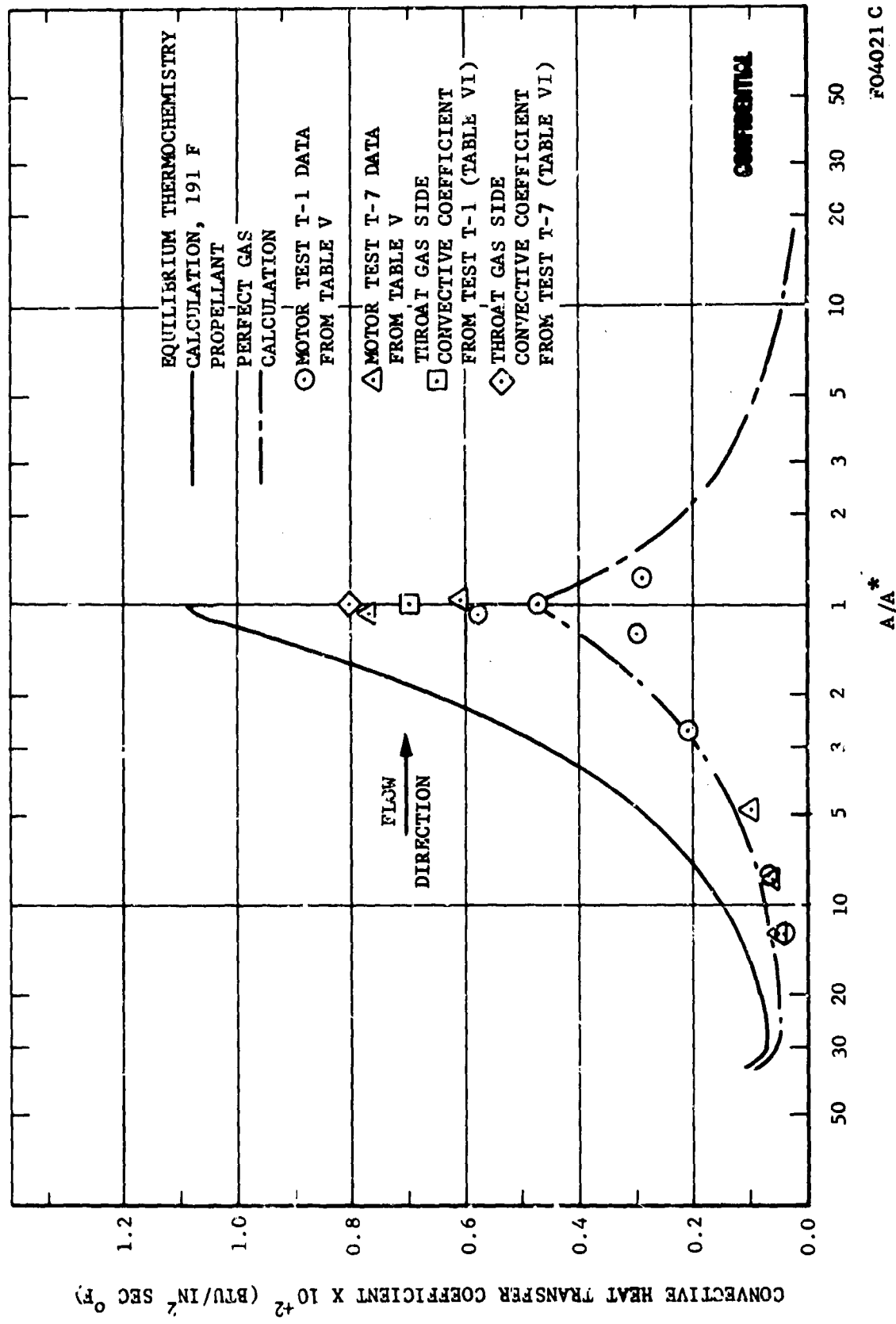


FIGURE 6. COMPARISON BETWEEN ANALYTICAL AND MEASURED HEAT TRANSFER COEFFICIENTS AS A FUNCTION OF NOZZLE AREA RATIO

CONFIDENTIAL

CONFIDENTIAL

centered on the pyrolytic graphite washers of 0.30 inch thickness. Even with the low C-direction thermal conductivity, some axial heat flux averaging must occur. Consequently, it is impossible to measure the peak heat transfer coefficient.

The second problem stems from the data reduction technique itself. An average chamber pressure is used in the iteration technique which eventually matches the total heat absorption and back wall temperature measurements. A wide variety of second order effects are necessarily introduced and their importance should be related to the character of the pressure excursion during the test. Thus, the gas side coefficient from Test T-7 may be a better value than that from T-1, while neither point is necessarily close to the actual maximum value. It should also be noted that the corrosion occurred in both tests, tending to lower the total heat transfer to the washer, and that the average pressures were not equal to 800 psia.

As discussed in Paragraph 2.3, there was a significant variation in the C-star values obtained in Tests T-1 and T-/. There appears to be real possibility that the 191F propellant exhaust has not achieved a thermochemical equilibrium composition. If this could be established, it would follow that the predicted heat transfer coefficients for the 191F propellant should be lowered while those for the 389 propellant would not change significantly. As noted in Paragraph 2.3, this situation apparently does not apply to Test T-3 (Arcocel 319BRF). The next step, then, will be to calculate the predicted convective coefficients for Test T-3 and compare the results with the measurements. The evaluation of the theoretical prediction techniques will continue through the remainder of the program.

b. (C) Radiation

The determination of the radiation boundary condition in a metalized solid propellant motor requires the specification of the energy emitted by the combustion products and the emissivity of the gas side surfaces. As reported in Reference 1, the determination of the radiant energy emitted by the combustion products requires knowledge of the scattering and absorption coefficients of the particle cloud. However, these coefficients are extremely dependent on particle size and temperature. Therefore, they must be determined at temperature levels and for particle size distributions which are nearly identical to the specific rocket motor in question. At the present time, the scattering and absorption coefficients for beryllium particle clouds are not available. This imposes a critical limitation on the prediction of radiative heat transfer. In addition to the specification of particle cloud scattering and absorption coefficients, the wall reflectivity is required to determine the portion of particle cloud radiation that is absorbed by the exposed hardware surfaces. For the motors studied in this program, the time and position dependency of the BeO or Al₂O₃ wall deposit complicates the estimation of wall emissivity.

CONFIDENTIAL

CONFIDENTIAL

With the objective of minimizing the influence of the above limitations in predicting radiative heat transfer, a portion of the thermal analysis's effort has been concentrated on particle cloud radiation in the rocket motors of this program. It has been found from this work that:

- (1) The radiative boundary condition is negligible compared with the convective in the nozzle entrance (area ratio less than 7), throat, and exit sections of the rocket motor (regardless of the existence of a deposition coating).
- (2) The particle cloud emissivity for beryllium propellants in the aft closure region (area ratio greater than 30) is nearly equal to the reported maximum particle cloud emissivity of aluminum propellants.
- (3) The gas side surface emissivity in the aft closure region may be assumed to be equal to that of the condensed oxide for the entire firing.

The first two observations were obtained from particle cloud radiation measurements in a beryllium motor firing. The third was based upon the deposition model of Paragraph 2.5.d. A discussion of the above is presented below.

(1) (U) Beryllia and Alumina Particle Cloud Radiation

For beryllia or alumina particle clouds, the reflectivities of the individual oxide particles are such that the radiant energy emitted by the particles and the gas side nozzle surfaces will experience a high level of scattering. The amount of scattering in the particle cloud will determine, in part, the emission characteristics of the cloud. For example, the total particle cloud emissivity for particle diameters greater than the wavelength of light being examined is given by the following expression (Reference 6):

$$\epsilon = \frac{\gamma^{\alpha} + \gamma^{51}}{\gamma^{\alpha} + \gamma^{52}} \left[1 - \exp(-\gamma^{\alpha} - \gamma^{52}) \bar{l} \right] \quad (1)$$

CONFIDENTIAL

CONFIDENTIAL

where:

γ^a is the absorption coefficient of the particle cloud

γ^{s1} is the scattering coefficient representing the energy scattered by a control volume in a specified direction

γ^{s2} is the scattering coefficient representing the energy scattered in the path length $\bar{\lambda}$

$\bar{\lambda}$ is the mean path length

From the above expression it can be seen that the maximum particle cloud emissivity (ϵ_m) is given by the following equation when the mean path length is very large:

$$\epsilon = \frac{\gamma^a + \gamma^{s1}}{\gamma^a + \gamma^{s2}}$$

For alumina particle clouds typical of aluminized propellant motors, the maximum cloud emissivity is between 0.25 and 0.4 and occurs at approximately a pressure of 500 psia and a path length of one foot (see References 6, 7, and 8).

To facilitate the comparison of beryllia cloud radiation with that of alumina, a radiometer was inserted in the aft closure of a beryllium propellant rocket motor (test T-3). With the radiometer in the chosen position, the chamber pressure and path length should insure the measurement of the maximum particle cloud emissivity. A discussion of the apparatus employed in the cloud emissivity measurement is presented in Section 4.3.a. To obtain the particle cloud hemispherical emissivity from the radiometer configuration used in test T-3, the following analysis was employed.

Total hemispherical emissivity is defined as:

$$\epsilon = \frac{E}{E_b}$$

where:

$$E = \int i d\omega$$

and

E = emissive power

i = intensity

ω = solid angle

The emissive power of the particle cloud is obtained from the temperature response of the radiometer using the following equation:

$$E = \frac{Cm}{A} \left(\frac{dT}{dt} \right) (1+r)$$

CONFIDENTIAL

CONFIDENTIAL

where:

C = specific heat of the radiometer's calorimeter

m = thermal mass of the calorimeter

dT/dt = rate of temperature rise of the calorimeter

r = reflectivity of the calorimeter surface

A = the surface area of the calorimeter which receives radiation

From Reference 6, the black body emissive power of the portion of the cloud that is seen by the calorimeter is,

$$E_B = 2\pi i_{bn} \int_0^{\beta} \cos \beta \sin \beta d\beta$$

where:

i_{bn} = the normal, black body intensity

β = the half angle of the opening

The normal black body intensity is given in Reference 6 as

$$i_{bn} = \frac{12\pi C_1}{90(C_2)^2} T^4$$

where:

$$C_1 = 0.18892 \times 10^8 \frac{\text{Btu}\mu^4}{\text{hr ft}^2}$$

$$C_2 = 25896 \mu R$$

From the above, the hemispherical emissivity of the cloud reduces to:

$$\epsilon = 3.03 \times 10^4 \left(\frac{Cm}{A} \right) \left(\frac{dT}{dt} \right) (1+r) \left(\frac{1}{\sin^2 \beta} \right) \left(\frac{1}{T^4} \right) \quad (2)$$

where the appropriate units are:

C, Btu/lb⁰F

m, lbm

CONFIDENTIAL

CONFIDENTIAL

dT/dt , $^{\circ}\text{F/sec}$

A, square inches

T, $^{\circ}\text{R}$

The constants of the radiometer and propellant used in test T-3 were

C = 0.06 Btu/lb $^{\circ}\text{F}$

m = 1.49×10^{-4} lbm

A = 0.00353 in. 2

r \sim 0.2

$\sin^2\theta \sim 0.8$

T = 6340 $^{\circ}\text{R}$

From Figure 105 of Paragraph 4.3.a, the temperature response of the calorimeter was 400°F/sec . Therefore, from Equation 2 the hemispherical emissivity of the particle cloud is approximately 0.28.

The measured hemispherical emissivity of the beryllium propellant combustion products, representing a maximum value, agrees with the reported maximum alumina cloud emissivity of References 7 and 8 (0.25 to 0.4). It is suggested that for propellants similar to those employed in this contract the values 0.28 and 0.30 be used as the maximum hemispherical particle cloud emissivities for beryllium and aluminum propellants, respectively. For engineering estimates, the maximum emissivity may be applied at locations in the rocket motor where the product of static pressure and mean path length ($P \times l$) is greater than 500 psia-ft. At locations in the motor where the pressure-path length product is less than 500 psia-ft, Equation 1 should be employed. However, to use Equation 1 for aluminum and beryllium propellants, the absorption coefficient (γ^a) and the path length scattering coefficient (γ^{sc}) must be determined. Reference 7 presents the required coefficients for alumina particle clouds. However, the appropriate beryllia coefficients have not as yet been found in the literature.

CONFIDENTIAL

CONFIDENTIAL

(2) (U) Gas Side Surface Reflectivity or Emissivity

The presence of an oxide deposit on the gas side surface of a rocket motor will alter both the wall emissivity and the wall temperature to be used in evaluating the radiation boundary condition. That is, the emissivity of condensed BeO or Al₂O₃ is considerably lower than that of the gas side surface materials (~ 0.2 compared to ~ 0.8). This causes a significant reduction in the amount of incident radiation that is absorbed by the wall. Also, the presence of a BeO or Al₂O₃ deposit provides a thermally insulative coating between the heat sink surface and the combustion products; this causes a reduction in radiative heat flux by raising the gas side surface temperature.

In order to obviate the need for specification of the deposit thickness history for the aft closure insulation surface, the measured effective heat transfer coefficients in the nozzle entrance section can be extrapolated to the aft closure region (see Paragraph 2.5). In this extrapolation, it is necessary to assume that the radiative component of the effective heat transfer coefficient is constant in the area ratio range of 12 to infinity and the convective component is dependent only on area ratio. This implies that: (1) the cloud emissivity is independent of location in this region, and (2) the deposit thickness and surface coverage is independent of location in this region. The second assumption is a practical requirement since the time dependent deposit thickness is extremely difficult, if not impossible, to determine in the aft closure and entrance section. The validity of assuming that deposit coverage is independent of location in this region is derived from the deposition model described in Paragraph 2.5d. However, the assumption of invariant aft closure deposit thickness is questionable for dissimilar gas side materials. When oxide deposits are present on the aft closure and nozzle entrance surfaces, it is suggested that an emissivity value of 0.2 be used.

(3) (C) Radiation Boundary Condition for Tests T-1 through T-7

The determination of the radiation boundary condition at nozzle locations where the product $P \times \bar{I}$ is less than approximately 500 psia-ft is limited by the lack of absorption and scattering coefficient data for beryllia particle clouds. For the rocket motors studied in this program, the region at which $P \times \bar{I}$ is equal to 500 psia-ft is at an upstream area ratio of approximately 30. The fraction of the total heat flux due to radiation decreases at nozzle locations downstream of this point. The nozzle location at which the radiation boundary condition may be neglected can be obtained by comparing the predicted radiative and convective heat transfer coefficients. Also, the effect of deposition on the entrance section total heat flux can be determined by comparing the measured effective heat transfer coefficient (defined in Paragraph 2.5.c) with the predicted radiative and convective heat transfer coefficient. From Paragraph 2.5.c the measured effective heat transfer coefficients, for firing T-1 at an

CONFIDENTIAL

CONFIDENTIAL

entrance area ratio of 12.4 and 8.0, are 0.00037 and 0.00064 Btu/in.² sec^{0.5}, respectively. From References 9 and 10, the radiation heat transfer coefficient may be approximated by the following expression:

$$h_r \sim \frac{8r}{T_g - T_w} \sim \frac{\epsilon_p \epsilon_w \sigma (T_g^2 + T_w^2)(T_g + T_w)}{1 - (1 - \epsilon_p)(1 - \epsilon_w)} \quad (3)$$

where

T_g = local static temperature

T_w = local gas side surface temperature

ϵ_p = particle cloud emissivity

ϵ_w = gas side surface emissivity

To evaluate the radiation boundary condition, the parameters presented in Table I were employed in Equation 3.

The comparison between predicted radiative and convective heat transfer coefficients are presented in Table II. Also presented in Table II is the approximate area of the deposit versus time curve and mean deposit thickness as obtained from the measured effective heat transfer coefficient.

CONFIDENTIAL

CONFIDENTIAL

TABLE I. PARAMETERS USED TO EVALUATE
THE RADIATION HEAT TRANSFER COEFFICIENT OF FIRING T-1

Parameter	<u>Entrance Area Ratio</u>		Remarks
	<u>12.4</u>	<u>8.1</u>	
T _g	6770°R	6770°R	Theoretical combustion temperature.
T _w	5000°R	5200°R	Approximated mean surface temperature for total firing time.
ε _p	0.2	0.13	BeO cloud emissivity assuming dependence of BeO absorption and scattering coefficients on area ratio is identical to Al ₂ O ₃ (see Reference 11 for variation of Al ₂ O ₃ cloud emissivity with area ratio).
ε _w	0.2	0.2	Surface emissivity with deposition.
	0.8	0.8	Surface emissivity without deposition.

TABLE II. COMPARISON OF RADIATIVE AND CONVECTIVE HEAT TRANSFER COEFFICIENTS FOR FIRING T-1

Parameter	<u>Entrance Area Ratio</u>		Remarks
	<u>12.4</u>	<u>8.6</u>	
Predicted Radiative Heat Transfer Coefficient (Btu/in. ² sec °F) - hr	0.00031 0.00052	0.00024 0.00036	With Deposit Without Deposit
Predicted Gas Side Convective Heat Transfer Coefficient - h _c	0.000525 0.00095	0.00072 0.0013	Perfect Gas (Paragraph 2.5a) Real Gas (Paragraph 2.5a)
Measured Effective Heat Transfer Coefficient (Btu/in. ² sec °F) - h _{eff}	0.00037	0.00064	
h _r /(h _r + h _c) (real gas h _c)	0.24 0.35	0.15 0.22	With Deposit Without Deposit
h _r /(h _r + h _c) (perfect gas h _c)	0.37 0.49	0.25 0.33	With Deposit Without Deposit
Area Under Deposit Versus Time Curve (in.-sec)	5.95 4.7	2.85 1.62	Real Gas h _c Perfect Gas h _c
Mean Deposit Thickness for Firing (inches)	0.34 0.27	0.16 0.093	Real Gas h _c Perfect Gas h _c

CONFIDENTIAL

CONFIDENTIAL

From Table II it can be postulated that the radiation boundary condition must be included in the thermal analysis at locations where the entrance area ratio is greater than 8.6. However, in the construction of Table II it was assumed that the dependence of the scattering and absorption coefficients on area ratio is identical for BeO and Al_2O_3 . Therefore, radiation fractions shown in Table II must be considered as approximate and preliminary. In the thermal analyses of the rocket motors studied in this program, the radiative boundary condition will be neglected at nozzle locations downstream of an entrance area ratio of about 7. Determination of the radiation boundary condition, between entrance area ratios of approximately 30 and 7 for beryllium motors, is limited by the unavailability of beryllia absorption and scattering coefficients. At entrance area ratios greater than 30, a constant beryllia cloud emissivity of 0.28 may be employed.

c. (C) Conduction/Ablation

The determination of the thermal behavior and corrosion-erosion characteristics of the rocket motor and propellant combinations of Motor Tests T-1 through T-7 have been accomplished by employing the thermal analyses and techniques reported in Reference 1. However, the capacity of the thermal analyses to accurately predict the nozzle temperature response is somewhat limited by the inability of the analyses to predict the extent of deposition. From post-test observation of the aft closure, entrance, and throat sections of rocket motors T-1 through T-7, together with an analysis of the corresponding pressure traces, it is found that an alumina or beryllia deposit was present on the gas side surfaces of these motor sections during the major portion of the firing period. Since the oxide deposit acts as both a thermal and a chemical insulator, the deposit must be characterized in the analysis if the true convective heat transfer and corrosion mechanics are to be understood. At the present time, the deposit history can be most accurately determined at the throat location. Therefore, during this reporting period, efforts have been concentrated on the thermal analysis of the pyrolytic graphite throat washer. In the entrance, throat, and exit sections, the semiempirical techniques developed in the first quarter were applied to characterize the gas side boundary condition in these sections. The characterization of the gas side

CONFIDENTIAL

boundary condition includes the combined effects of radiation, convection, and deposition. Thus, it is possible to obtain an indication of gas side heat transfer variation with nozzle location. The procedures employed in obtaining the predicted nozzle heat transfer are discussed below.

(1) (U) Chamber - Aft Closure Section

From post-test analysis of motors T-1 through T-7, the chamber and aft closure sections were found to be covered with an oxide deposit (alumina or beryllia) approximately 0.05 to 0.10 inch thick. From the deposition physical model presented in Paragraph 2.5d, it can be assumed that a deposit, the thickness of which is dependent on time and position, was present in this region for most of the firing period. The analysis of the thermal response of the gas side surface material in this region requires determination of the convective, radiative, and transient deposit thickness boundary conditions. From Paragraphs 2.5.a and 2.5.b, the convective and radiative boundary conditions can be determined with reasonable accuracy. However, with reference to Paragraph 2.5.d, specification of the transient deposit thickness in the chamber and aft closure region is, at the present time, impossible. Therefore, determination of the chamber and aft closure gas side material thermal response was not attempted in this quarter. An alternate approach in specifying the chamber-aft closure transient deposit thickness is presented in Paragraph 2.5.b-2; however, the resulting thermal predictions would be very approximate.

(2) (C) Entrance Section

That portion of the rocket motor entrance section consisting of a polycrystalline graphite material was analyzed using the semiempirical technique developed in the first quarter. This technique provides a characterization of the gas side boundary condition so that the net effect of radiation, convection, and deposition on surface heating is determined. A discussion of the technique employed in the determination of the entrance section gas side boundary condition for rocket motors T-1 through T-7 is presented below.

In motors T-1 through T-7, the back side of the polycrystalline entrance section was instrumented with three thermocouples, placed at three different axial positions. The entrance section is divided into three axial nodes, the centers of which correspond to the thermocouple locations. By applying an energy balance and conduction analysis to each, the total heat absorbed by the nodes during firing can be determined from the thermocouple response. That is,

$$Q_T = \rho C V T_e + \int_0^t q_1 dt + \int_0^{T_e} \frac{KA}{L} (\bar{T}_A - \bar{T}_B) dt \quad (4)$$

where:

ρ = node density

C = node specific heat

V = node volume

T_e = node temperature at time of equilibration

q_1 = heat dissipated from the node by backup material ablation

t_e = time of equilibration (time at which a radial isothermal condition is approached in the heat sink material)

The last term represents the axial conduction interchange between adjacent nodes and is determined by applying a conduction analysis to the entrance section. The temperature at equilibration is obtained from the thermocouple response using the equilibration time specified by the conduction analysis (approximately 30 seconds after shut down). The heat lost from the nodes during the firing and equilibration periods is approximated by assuming that, during firing, the heat loss is due solely to ablation of the backup insulator. As shown in Reference 11, the heat dissipated by ablation is negligible during firing. Therefore, the third term in Equation (4) becomes:

$$\int_{t_a}^{t_e} \dot{q}_1 dt$$

where:

t_a = the end of the thermal action time.

For times exceeding the equilibration time, a plot of \dot{q}_T versus time is obtained from the thermocouple trace using the equation below.

$$\dot{q}_T = \rho C V dT/dt$$

Here, dT/dt is the temperature-time slope of the thermocouple response at t and \dot{q}_T is defined as:

$$\dot{q}_T = \dot{q}_1 \pm \frac{KA}{L} (\bar{T}_A - \bar{T}_B)$$

CONFIDENTIAL

From the conduction analysis that is applied to the entrance section, the axial conduction term is determined and, therefore, \dot{q}_1 at times after equilibration can be calculated. To find \dot{q}_1 during the equilibration period, extrapolation of the \dot{q}_1 for times greater than t_e is employed using the heat dissipated by ablation versus time profiles of Reference 11. The error introduced in Q_T of Equation (4) by evaluating \dot{q}_1 in the above manner is small because in motors T-1 through T-7, the first term $CQV T_e$ is between 260 and 380 Btu and the second term is between 15 and 50 Btu.

To characterize the gas side boundary condition at the entrance thermocouple locations, an effective heat transfer coefficient is defined to include the radiation, convection, and deposition modes of heat transfer. The effective heat transfer coefficient is defined as

$$h_{\text{eff}} = \frac{Q_T}{A \int_0^{t_a} (T_r - T_w) dt} \quad (5)$$

where

Q_T = total local heat absorbed, found from Equation (4)

A = entrance section node surface area

T_r = local free stream recovery temperature

T_w = gas side surface temperature

t_a = thermal action time

As can be seen from Equation (5), the effective heat transfer coefficient represents the constant heat transfer coefficient (independent of time and pressure) that, when applied as a boundary condition to a conduction analysis, will predict the total heat actually absorbed (Q_T). To determine h_{eff} , it is necessary to determine a locus of Q_T/A versus h_{eff} values by repeated runs of a conduction program, using proper solid material thermal properties and free stream recovery temperatures. A sample of the Q_T/A versus h_{eff} curves is presented in Figure 7 for the throat location of motors T-1 through T-7.

The above analysis and techniques were applied to rocket motors T-1 through T-7, with the results presented in Paragraph 2.5.e. The thermal response of the entrance sections for these motors was not determined due to the large amount of deposition that was experienced during firing.

CONFIDENTIAL

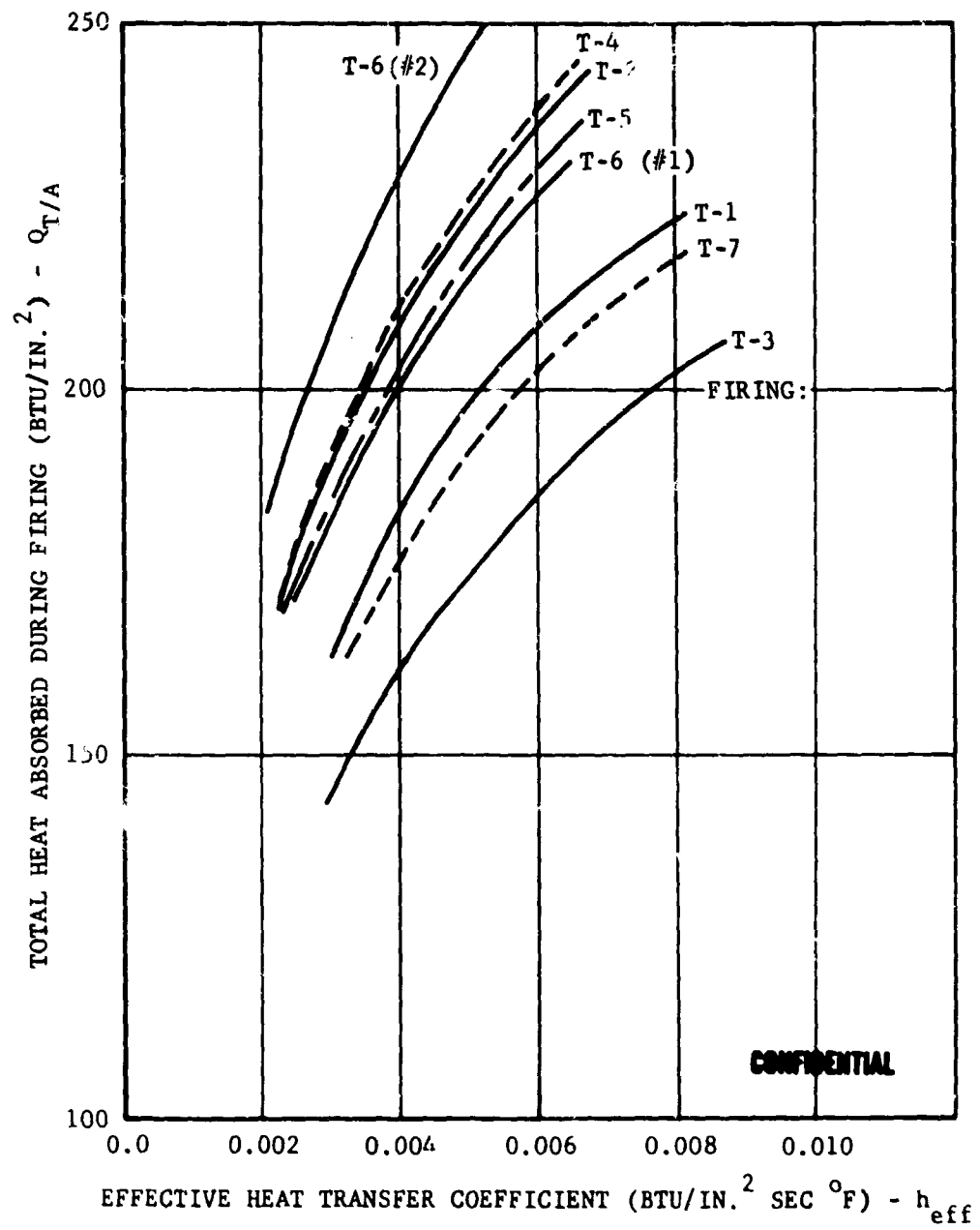


FIGURE 7. TOTAL HEAT ABSORBED BY THROAT HEAT SINK
VERSUS EFFECTIVE HEAT TRANSFER COEFFICIENT

F04022C

CONFIDENTIAL

(3) (U) Throat Insert and Exit Cone

The throat insert and exit sections of rocket motors T-1 through T-7 were extensively instrumented with thermocouples (see Paragraph 2.5.e). The resulting thermocouple data were employed in a semiempirical thermal analysis to characterize the gas side boundary conditions in much the same manner as was done in the entrance section. That is, an energy balance was applied to the heat sink material at each axial thermocouple location to determine the total heat absorbed during firing. The energy balance at the throat insert thermocouple locations may be written as:

$$Q_T = \left[\rho C V T_e \right]_{PG} + \left[\rho C V T_e \right]_{ATJ} + \int_0^{t_e} \dot{q}_l dt \quad (6)$$

Where the first and second terms on the right represent the total heat stored in the pyrolytic graphite and polycrystalline graphite heat sink, respectively, at the equilibration time. The third term represents the total heat lost by the heat sink materials during the firing and equilibration periods. The above energy balance does not include the axial conduction term of Equation 4 since the thermal conductivity of pyrolytic graphite in the "C" direction is low. The effective heat transfer coefficient is determined using Equation 5. The total heat absorbed by the throat insert and the corresponding effective heat transfer coefficients are presented in Paragraph 2.5.e for Motor Tests T-1 through T-7.

The determination of the thermal response and corrosion characteristics of the heat sink and insulative components of a rocket motor requires the inclusion of condensed wall deposits in the thermal analysis. At the present time, the thermal analysis is limited by the lack of an analytical deposition model with which to determine the local deposit behavior. However, a semiempirical technique can be used to predict the transient deposit thickness at the throat location (Paragraph 5.2.b). Therefore, to define and correlate the thermal response and corrosion characteristics of the propellant and rocket motor combinations studied in this program, a semiempirical conduction-deposition analysis was developed. This analysis essentially incorporates the deposit thickness history given in Paragraph 5.2.b and the measured effective heat transfer coefficient from Equation 5 in the conduction analysis of the throat heat sink material. The end result of this analysis is a prediction of both thermal response and gas side convective heat transfer at the throat location. The throat conduction-deposition analysis and the technique involved in determining throat thermal response are presented below.

A transient one-dimensional conduction program is applied to the throat washer and ATJ backing by dividing the material into radial nodes. The deposit is also divided into nodes. The thermal conductivity, density, and specific heat of the liquid and solid phase of deposit are assumed to be equal.

The contact resistance between the pyrolytic graphite and ATJ graphite heat sink is approximated in the following manner:

$$\frac{1}{R} (T_1 - T_3) = \frac{(\rho V)_{ATJ}}{\Delta t} \left[C'' T_2'' - C' T_2' \right]$$

where:

T_1 = P.G. backwall temperature (measured with thermocouple)

T_3 = ATJ surface temperature at P.G.-ATJ interface

T_2'' = ATJ backwall temperature at time $t + \Delta t$ (measured with thermo-couple)

T_2' = ATJ backwall temperature at time t (measured)

$(\rho V)_{ATJ}$ = product of density and volume of ATJ heat sink

C'' = specific heat of ATJ at T_2''

C' = specific heat of ATJ at T_2'

The temperature T_3 is determined from a conduction analysis applied to the ATJ heat sink, using the measured temperature response of the P.G. backwall (T_1) and a number of R values for contact resistance.

The free stream recovery temperature is assumed equal to the theoretical, equilibrium, chemical recovery temperature. From Paragraph 2.5.b, the radiative heat transfer was found to be negligible in the throat region. Therefore, the transient gas side convective heat transfer coefficient (h_c) is determined using the measured h_{eff} and a trial and error procedure. Initially, the average gas side convective heat transfer coefficient (\bar{h}_c) is determined from

$$\frac{1}{\bar{h}_c} = \frac{1}{h_{eff}} - \frac{1}{t_a K} \left[\int_0^{t_a} \delta dt \right] \quad (7)$$

h_{eff} = value determined from Equation 5

t_a = end of thermal action time

K = thermal conductivity of the wall deposit (independent of time and temperature)

δ = throat deposit thickness.

In Equation 7, the first term is the resistance between the free stream and the gas side surface (deposit surface with deposition, P.G. surface without deposition); the second term is the resistance between the free stream and the P.G. surface; the third is the resistance to heat flow through the deposit. To determine h_c from \bar{h}_c use is made (for practical reasons) of the simplified Bartz equation and the average chamber pressure of the motor firing, i.e.,

$$\bar{h}_c = \phi \left(\frac{\bar{P}_c}{100} \right)^{0.8} \quad (8)$$

and

$$h_c = \phi \left(\frac{P_c}{100} \right)^{0.8}$$

In Equation 8, \bar{P}_c is the average chamber pressure during the firing period and P_c is the chamber pressure at any time t .

The time and pressure dependent h_c is applied as the gas side boundary condition in the conduction analysis and the total heat absorbed by the heat sink material (Q_T , see Equation 6) is determined. That value can then be compared with measured Q_T . Since h_{eff} is determined from a conduction analysis that neglects the deposit effect in the calculation of T_w of Equation 5, the predicted and measured Q_T will not necessarily agree. Therefore, ϕ of Equation 8 is varied until agreement occurs. The thermal response of the heat sink material with deposit, together with the gas side convective heat transfer coefficient, is then determined.

The assumptions required in the above analysis are:

- (1) Energy transported to throat by deposit flow is negligible.
- (2) Energy involved in phase change of deposit is negligible.
- (3) Radiation is negligible.
- (4) Axial conduction is negligible compared to radial conduction.
- (5) Back side of ATJ is perfectly insulated.

- (6) Thermal properties of the solid and liquid phase of the deposit are equal and independent of temperature.
- (7) Ablation of beryllia and alumina is not important.

The material thermal properties employed in the conduction-deposition analysis of rocket motors T-1 through T-7 are presented in Table III.

TABLE III
MATERIAL THERMAL PROPERTIES EMPLOYED
IN THROAT CONDUCTION-DEPOSIT ANALYSIS

<u>Material</u>	<u>Temperature (°F)</u>	<u>Density (1b/in.³)</u>	<u>Local Specific Heat (Btu/1b °F)</u>	<u>Thermal Conductivity⁺⁴ (Btu/in. sec °F) x 10⁻⁴</u>
BeO	-	0.080	0.60	1.85
Al ₂ O ₃	-	0.133	0.35	0.60
Pyrolytic Graphite	350	0.0792	0.274	54
	500		0.30	40
	750		0.34	30
(a-b Direction)	1000		0.38	25
	1500		0.44	19
	2000		0.48	16
	3000		0.52	13
	4000		0.541	11.4
	5000		0.552	11.3
ATJ Graphite	350	0.0625	same as	13.2 9.3
(average of with and against grain)	1000		P.G.	5.9
	2000			4.6
	3000			3.8
	4000			3.2
	5000			

d. (U) Deposition Model

From the motor firing and laboratory test results of this program, together with the physical deposition model of Reference 11, the behavior of the alumina or beryllia wall deposit on rocket motors T-1 through T-7 has been defined. The similarities and differences between the alumina and beryllia deposition phenomena are also ascertained in terms of the effect on the nozzle thermal response and corrosive characteristics. The objectives of this paragraph are to present the physical deposition model for the propellant and rocket motor combinations studied in the second reporting period and to discuss the limitations involved in the formulation of an analytical model with which the nozzle thermal response is predicted.

(1) Physical Deposition Model

The physical model of Reference 11 considers that deposition initially occurs at specific locations on the rocket motor gas side surface as a direct result of particle impingement. The initial impingement profiles for the contours of rocket motors T-1 through T-7 are presented in Paragraph 3.3.b as a function of particle size. Of the total initial particles that impinge on the surface, part will re-enter the gas stream and part will remain on the surface. The quantity that remains on the surface will depend on: (a) the porosity, surface roughness, temperature, internal pyrolysis rate, and phase change of the surface material (mechanical attachment); (b) the particle velocity, size, and impingement angle with respect to the surface (momentum effects); and (c) the type of chemical reactions occurring between the deposit and the surface material (chemical attachment). The primary modes of mechanical attachment consist of: (a) the solidification of liquid alumina or beryllia on "cold" surfaces, and (b) the entrainment of liquid alumina or beryllia in a viscous liquid. The latter usually occurs early in the firing when silica or asbestos phenolic is employed as the gas side surface material, and is due to the phase change of the silica or asbestos reinforcement and when the oxide deposit surface is molten. The bond formed by the solidification of the oxide particles on the surface is usually weak and may be easily released by thermal stresses, free steam gas shear loading and gas flow, and/or pressure forces resulting from subsurface pyrolysis. Therefore, for asbestos phenolic gas side materials, it may be expected that deposition will be delayed due to the high pyrolysis mass flow associated with start-up. However, deposition will proceed at increased rates when the reinforcement material undergoes a chemical and/or physical phase change.

Chemical attachment of the oxide deposit to the gas side surface material will occur by the formation of a metal carbide. That is, the initial oxide reactions with graphite form a stable interlayer which inhibits further reactions. However, the thermochemical stability of the interlayer is strongly dependent on temperature and total pressure. From Reference 1, Be_2C becomes unstable with respect to $\text{Be}(\text{g})$ and $\text{CO}(\text{g})$ at a temperature

near 4000°F and total pressure of one atmosphere. At rocket pressures, the stability temperature exceed the BeO melting point. Also, from Reference 11, Al_4C_3 becomes unstable at temperatures of about 3600 and 5500°F at pressures of and a total 14.7 and 1000 psi, respectively. Consequently, the chemical stability of oxide deposits will vary along the nozzle contour in accordance with the wall temperature and static pressure variations.

From the above it can be seen that the differences between alumina and beryllia attachment can be related to the differences in oxide melting points (3704 and 4635°F for Al_2O_3 and BeO, respectively) and decomposition temperature of the metal carbide. It should also be noted that the deposition or impingement rate will increase with increasing particle size.

Once deposition has been initiated, the deposit will cause irregularities along the motor contour. Depending, of course, on the magnitude in contour irregularities, the particle impingement rate will increase, producing increased deposition. Since the free surface of the deposit is convectively and radiantly heated and conductively cooled, a time will be reached when the surface of the deposit will melt. At this time, the gas wall shear will cause the liquid portion of the deposit to flow downstream. If the deposit wets the surface (which occurs when Al_4C_3 or Be_2C is present) and the surface material is not ablating or pyrolyzing, the velocity profile in the liquid will be nearly linear and the deposit flow will resemble Couette flow. However, if the surface material undergoes internal pyrolysis, as does the chamber and aft closure materials of this program, the pyrolysis gas will cause bubbling of the liquid deposit and the flow will be nonuniform. The liquid oxide velocity profile will, of course, react to variations in the liquid-gas interfacial shear and, strictly speaking, to variations in the solid-liquid interface roughness. Consequently, a linear velocity gradient should not be assumed in the vicinity of the nozzle throat.

As the deposit flows downstream, the portion of the deposit coming in contact with an exposed portion of the surface will generally solidify (depending upon the surface temperature). As the deposit builds up at this location, a thickness is reached at which the surface heating exceeds the heat conducted to the heat sink material, so that surface deposit gas side surface melting will occur and flow will start again. For the rocket motor configurations studied in this program, a surface material discontinuity occurs in the entrance section at area ratios of approximately 19 and 4 (asbestos phenolic - ATJ graphite and ATJ graphite - pyrolytic graphite, respectively). Since the change in material thermal conductivities at these locations is considerable, it may be expected that a significant change in deposit thickness early in the firing will occur. That is, as the deposit flows from the asbestos phenolic to the ATJ, and from the ATJ to the pyrolytic graphite, the deposit will undergo a high degree of

solidification. Since the heat conducted from the deposit to the heat sink material is initially proportional to the heat sink thermal conductivity, the deposit thickness will be larger for the high conductivity materials. The change in deposit thickness at these locations may be sufficient to cause a significant irregularity in contour so as to promote local particle impingement, thereby increasing the local deposition rate.

As the firing proceeds, the heat sink surface temperatures will increase, causing a decrease in deposition thickness. The decrease in deposit thickness will, in turn, cause the deposition or particle impingement rate to decrease if the deposit irregularities in the contour caused increased impingement. When, at a given location, the heat sink material's surface temperature is above the melting point of the deposit and particle impingement is not present, the deposit mass entering and leaving this location are equal. That is, no further accumulation of the oxide can occur and the deposit thickness will begin to decrease. At this heat sink surface temperature, the mechanisms causing the attachment of impinging particles will change. Mechanical attachment will undergo a severe change since the deposit is no longer in the solid phase at the wall. Also, the importance of chemical attachment via the formation of Al_4C_3 or Be_2C is decreased due to the potential decrease in stability of these compounds at temperatures above the oxide melting points. If the heat sink surface temperature exceeds the pressure dependent decomposition temperatures of Al_4C_3 or Be_2C , the chemical attachment mechanism is lost. Then, the deposit flow may be expected to degenerate into a bead or droplet type. However, when asbestos or silica phenolic is employed as the gas side surface, the maximum char surface temperature that can be expected is between 3400 and 3600°F, depending on the free stream shear imposed on the carbonaceous char. This maximum expected temperature is below the melting point of both alumina and beryllia. Therefore, apparent strengthening of the char should result while the deposit is retained in either solid or liquid form. In this program, deposits were retained during the entire firing and no char regression was observed.

When the polycrystalline graphite entrance and pyrolytic graphite throat insert surfaces of motors T-1 through T-7 are above the melting of BeO or Al_2O_3 , the deposit mass flow rate may be nearly constant and approximately equal to the deposit mass flow leaving the asbestos phenolic aft closure. Since the contour area decreases and the wall shear increases in these regions, the mean deposit velocity increases. This does not necessarily imply that the deposit thickness will decrease as the throat is approached. However, for small enough mass flow rates or high enough deposit velocities, the deposit surface tension and viscous shear forces will precipitate beading or droplet flow. When the graphite surface temperatures exceed the interlayer stability temperature, a nonwetting condition exists between the oxides and the carbon. This could cause a transition to droplet type flow for significantly thicker deposits. Non-uniform deposit thickness in the circumferential direction will occur for

droplet flow and nonuniform corrosion will occur. A nonuniform circumferential thickness will also result from gravitational effects.

From the above it can be seen that the differences between alumina and beryllia deposit physical behavior can be related to the differences in melting points, thermal conductivity, oxide particle size in free stream, and propellant combustion temperatures.

The behavior of the deposit in the exit cone is not necessarily similar to that in the aft closure, entrance section, and throat insert section. That is, in the exit cone, the free stream is supersonic and the convective heat transfer coefficient and static pressures are considerably less than in the throat insert. Since the decomposition temperature of Al_4C_3 and Be_2C decreases with decreasing pressure, the heat sink surface temperature may exceed the decomposition temperature, and the initial oxide deposit flowing downstream from the throat insert will not necessarily wet portions of exit cone. This will cause a bead or droplet type deposit flow. In the exit cone regions, where the metal carbide interlayer is stable, chemical attachment will occur. The time required to melt the exit cone deposit could be significantly longer than in the throat due to the difference in convective heat transfer. The formation of an exit cone deposit can significantly alter the free stream flow field (supersonic flow), complicating the deposit behavior and thrust data. The transient behavior of the plume observed (motion pictures) in both aluminum and beryllium propellant firings is indicative of the complicated deposition behavior in the exit cone (i.e., plume separation and plume flow field alteration).

(2) Analytical Deposition Model

As can be seen from the physical model, a useful analytical model for the deposition phenomena will require (1) the prediction of the transient deposit history and impingement rates experienced in the motor; (2) the specification of such property data as liquid alumina and beryllia thermal conductivity, density, specific heat and viscosity; (3) the investigation of the mechanisms affecting alumina and beryllia wetting and attachment to gas side surface materials; and (4) the determination of free stream particle size. Since an oxide deposit provides both a thermal and chemical protective barrier between the gas side surface material and the combustion products, the determination of the thermal and corrosion characteristics of a metalized propellant rocket motor requires specification of the transient deposit thickness. At the present time, only the throat deposit history can be determined by empirical means (Paragraph 5.2). Therefore the throat is the only location where the thermal response analyses have been applied (Paragraph 2.5.c).

CONFIDENTIAL

In Reference 1, an approximate analytical deposition model was presented. The application of that model to the nozzles of this program will, however, be deferred until (1) some of the required assumptions can be verified and/or revised, and (2) some of the important material property data are available. The assumptions that must be verified and/or revised and the required material property data are summarized and discussed below:

(a) Assumptions

- . Use of cold flow modeling and analytical considerations to determine transient impingement locations and rate. This assumption is questionable due to the alteration of the nozzle contour by the deposit. A significant axial change in gas side material thermal conductivity will alter the deposit thickness, causing additional sites where impingement may occur.
- . All particles that impinge on the wall will stick. This assumption seems reasonable when the gas side surface is in the liquid state (i.e., entrainment of impinging particles). However, it is questionable for solid surfaces as shown by the plasma studies (Paragraph 3.3.a).
- . The deposit wets the gas side surface materials (droplet or bead type flow does not exist). This assumption is invalid for wall temperatures above the effective decomposition temperature of the carbide interlayer.
- . Omission of internal pyrolysis mass flow effect on deposition.
- . Trial and error procedure used in determining the mass mean particle diameter (\bar{d}) from measured throat deposition thickness. Any errors in the property data would magnify the error in \bar{d} determination; therefore, it is desired that \bar{d} be specified from particle collection studies.

CONFIDENTIAL

CONFIDENTIAL

(b) Property Data

- . Al_2O_3 and BeO liquid thermal conductivity, viscosity and density. These data have not been found in the literature; therefore, use could be made of the analytical expressions presented in Reference 12 for conductivity and viscosity.
- . Asbestos phenolic char thermal conductivity at high temperature . The presence of the deposit can lead to both unusually high char temperatures and to dilution of asbestos and silica.

e. (C) Motor Test Data and Thermal Analysis

(1) (C) Nozzle Thermal Data

The backside surfaces of the polycrystalline graphite entrance section, pyrolytic graphite throat insert, polycrystalline graphite throat insert sleeve, and the graphite exit cone of nozzles T-1 through T-7 were instrumented with thermocouples. The thermocouples were located at various axial positions so that the variation in the gas side surface boundary condition with area ratio could be determined and characterized for each motor firing. The temperature data acquired from each motor firing are presented in Figures 8 to 14. The start time ($t=0$) in each figure is identical to that in Figures 118 to 124 of Paragraph 5.2.b. Thermocouple selection and installation are discussed in Paragraph 4.3.

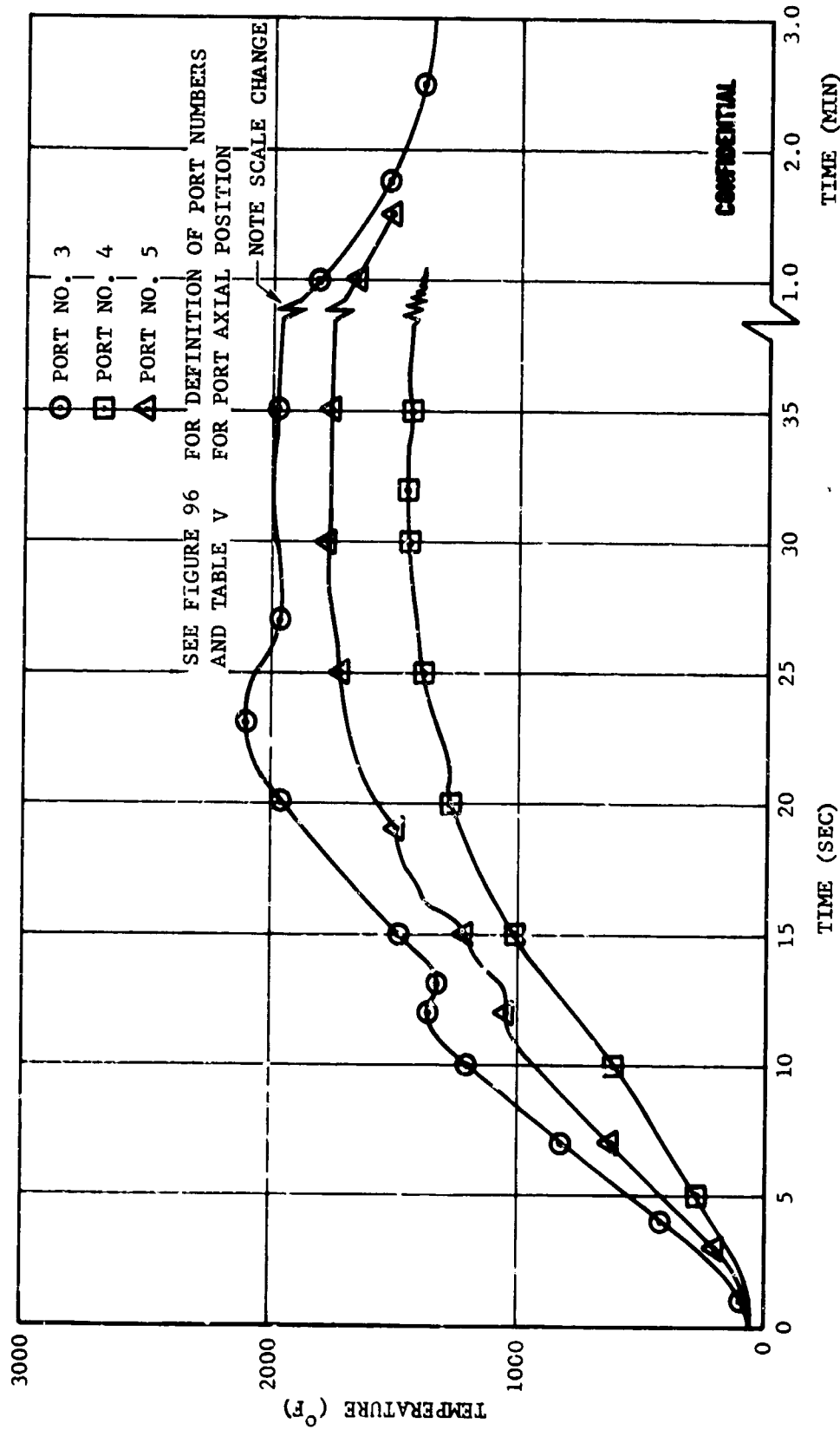
The photographs of the aft closure, entrance section and throat insert insulation char are presented in Paragraph 3.4.a. The surface regression measurements for the throat region of nozzles T-1 through T-7 are presented in Paragraph 5.2.b. No significant surface regression occurred in the aft closure, entrance cone and exit cone sections of these motors.

(2) (C) Nozzle Thermal Analysis

The results obtained by applying the thermal analyses described in Paragraph 2.5.c to nozzles T-1 through T-7 consist of (1) quantitative characterization of the gas side boundary condition in the entrance, throat, and exit sections; (2) determination of the gas side convective heat transfer coefficient at the throat; (3) prediction of heat sink thermal response at the throat, and (4) determination of the pyrolytic graphite washer-polycrystalline graphite sleeve interface conductances. The propellant and rocket motor parameters that were employed in the thermal analyses of Paragraph 2.5.c are presented in Table IV. The time $t=0$ corresponding to the firing time in Table IV are shown in Figures 118 through 124.

CONFIDENTIAL

CONFIDENTIAL



FO4023C

FIGURE 8A. TEMPERATURE RESPONSE OF HEAT SINK BACKWALL FOR FIRING T-1

CONFIDENTIAL

CONFIDENTIAL

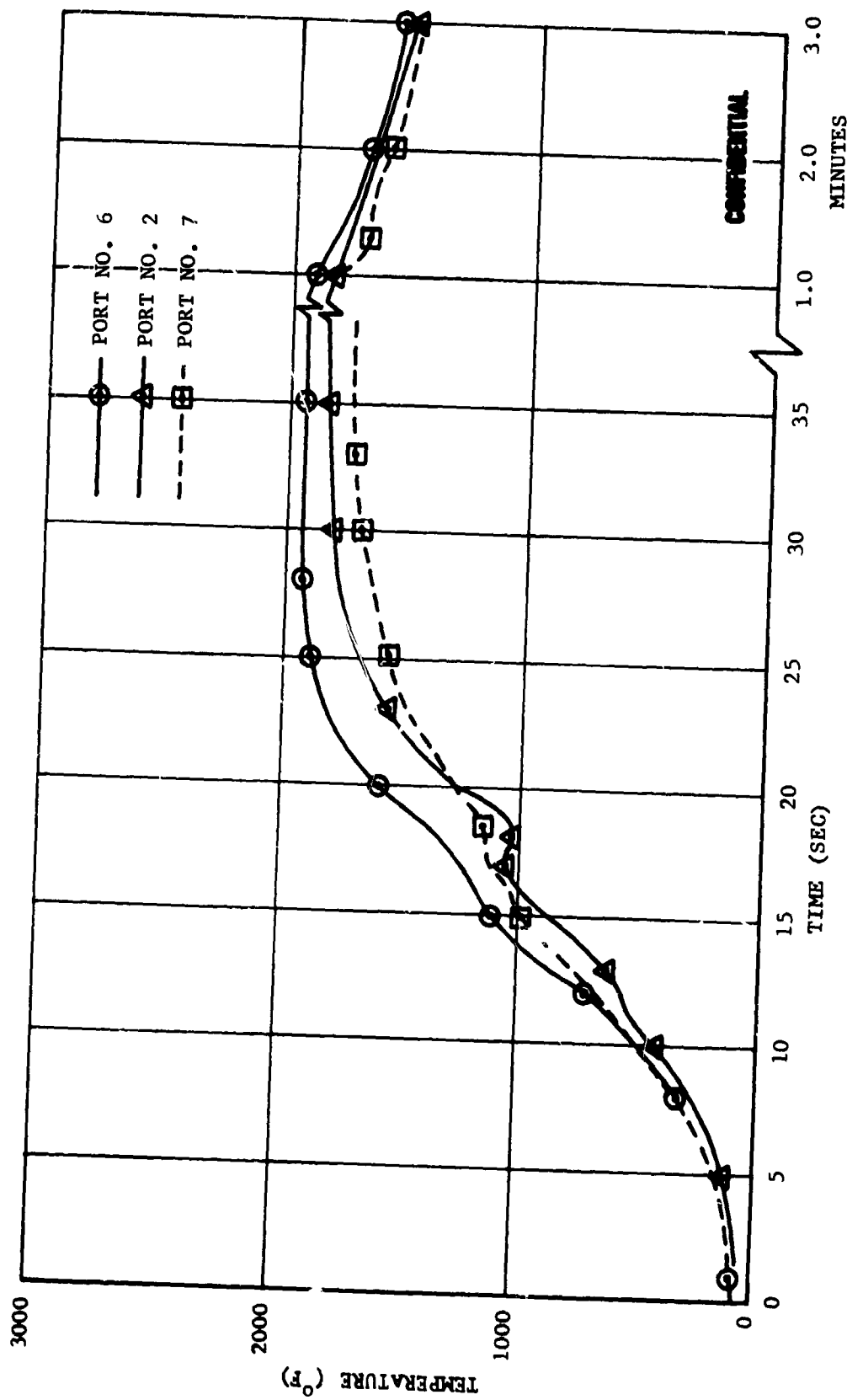
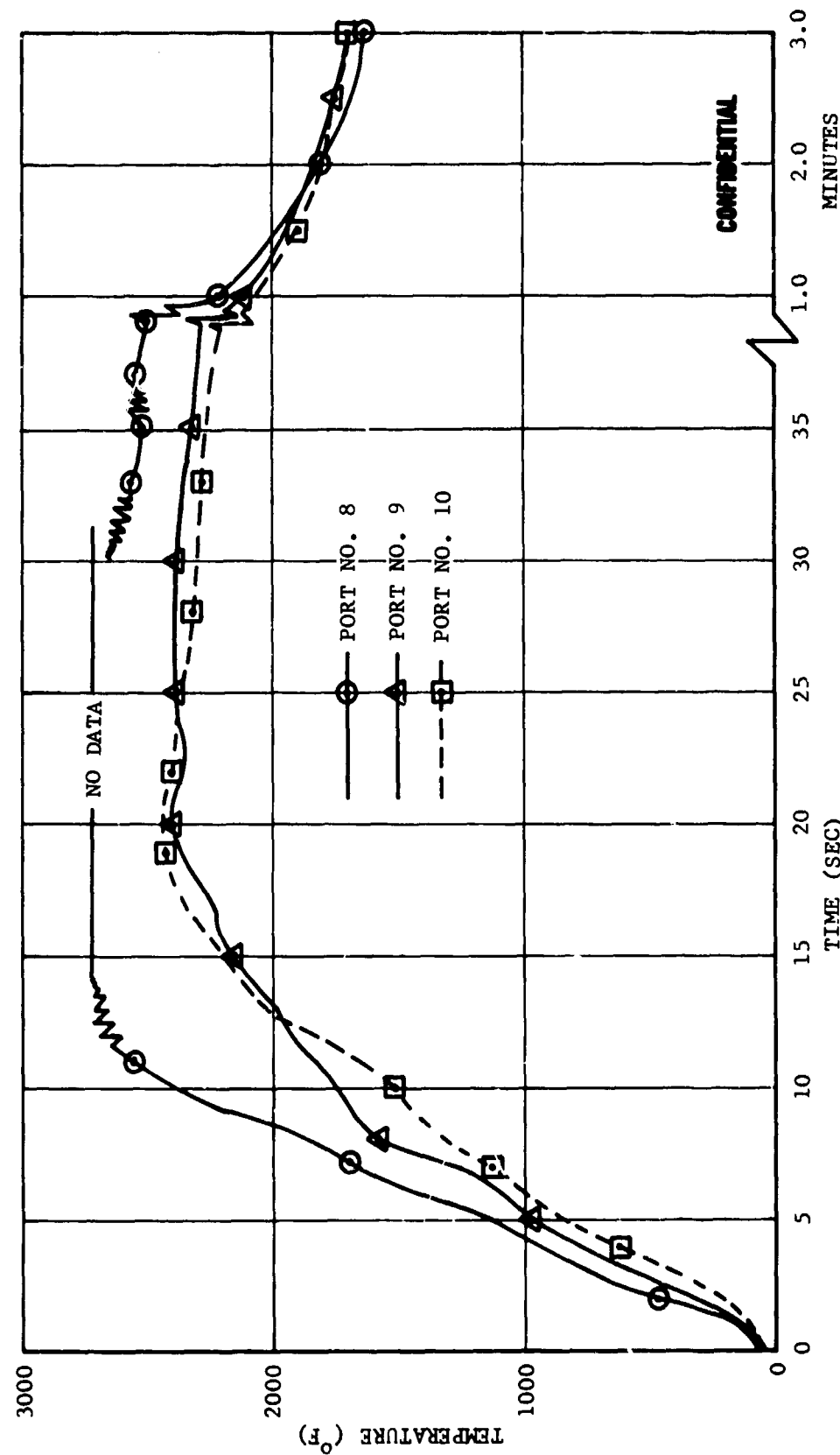


FIGURE 8B. TEMPERATURE RESPONSE OF HEAT SINK BACKWALL FOR FIRING T-1

FO4024 C

CONFIDENTIAL

CONFIDENTIAL



FO4025 C

FIGURE 8C . TEMPERATURE RESPONSE OF HEAT SINK BACKWALL FOR FIRING T-1

CONFIDENTIAL

CONFIDENTIAL

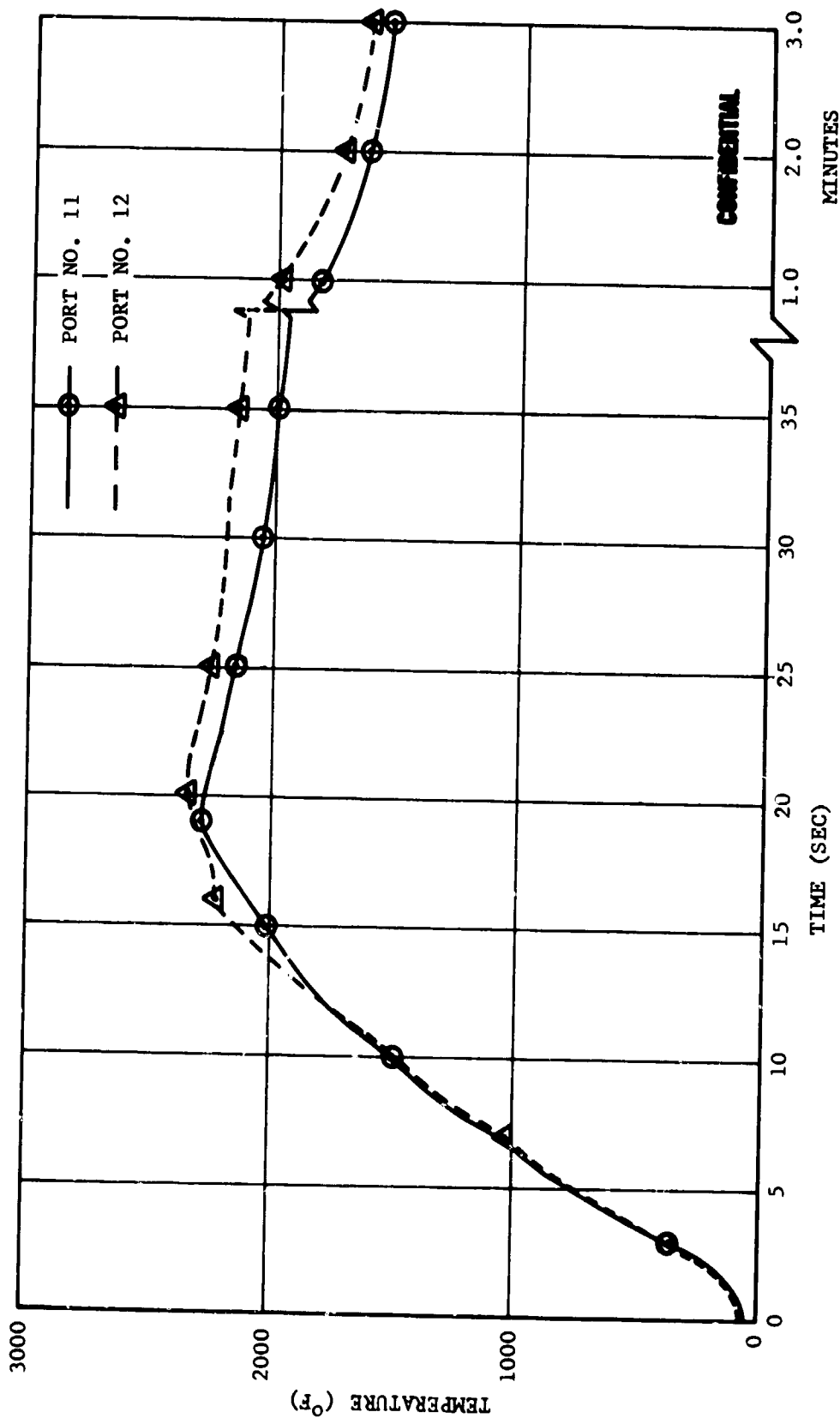


FIGURE 8L. TEMPERATURE RESPONSE OF HEAT SINK BACKWALL FOR FIRING T-1

FO4026 C

CONFIDENTIAL

CONFIDENTIAL

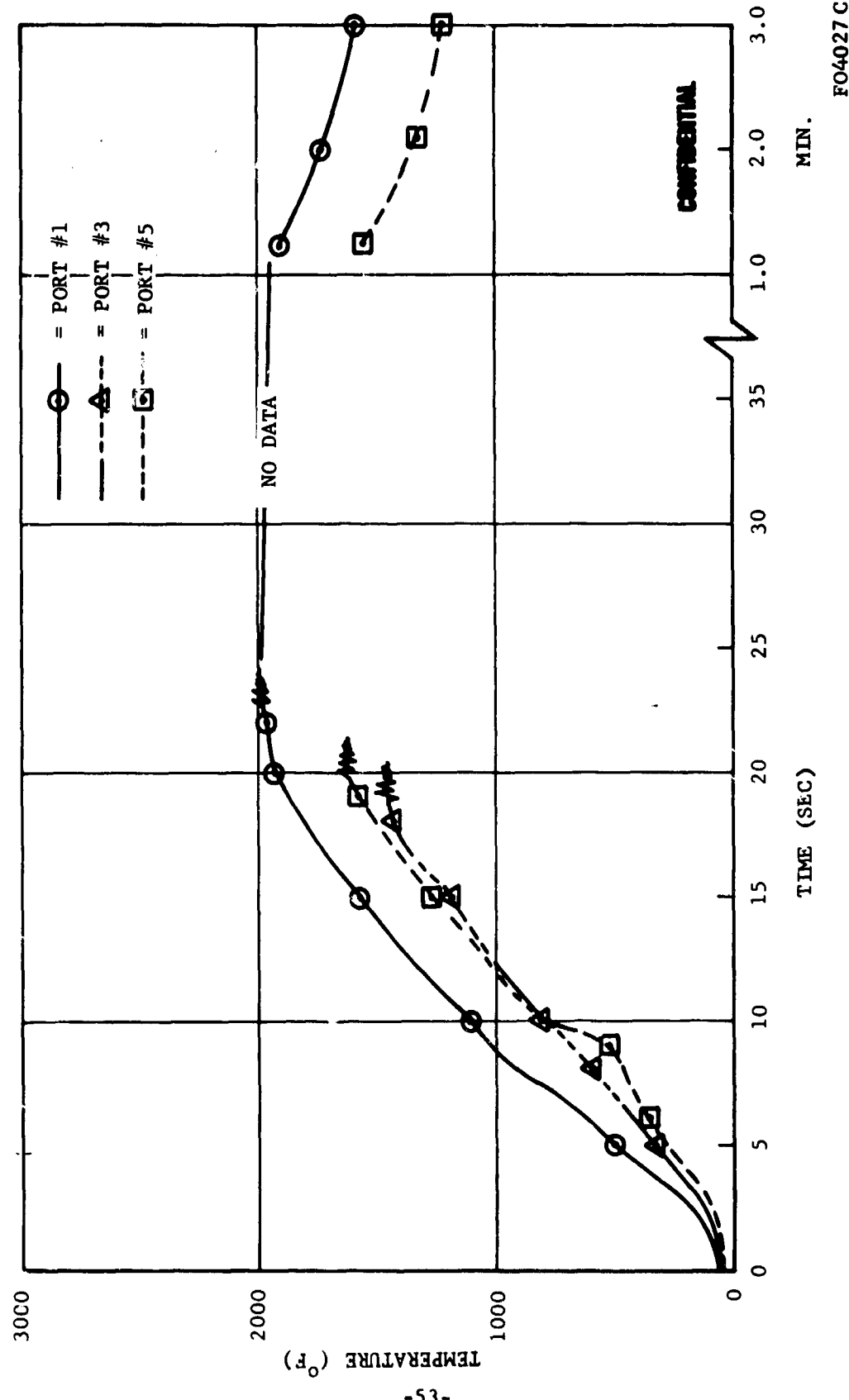


FIGURE 9A. TEMPERATURE RESPONSE OF HEAT SINK BACKWALL FOR FIRING T-2

CONFIDENTIAL

CONFIDENTIAL

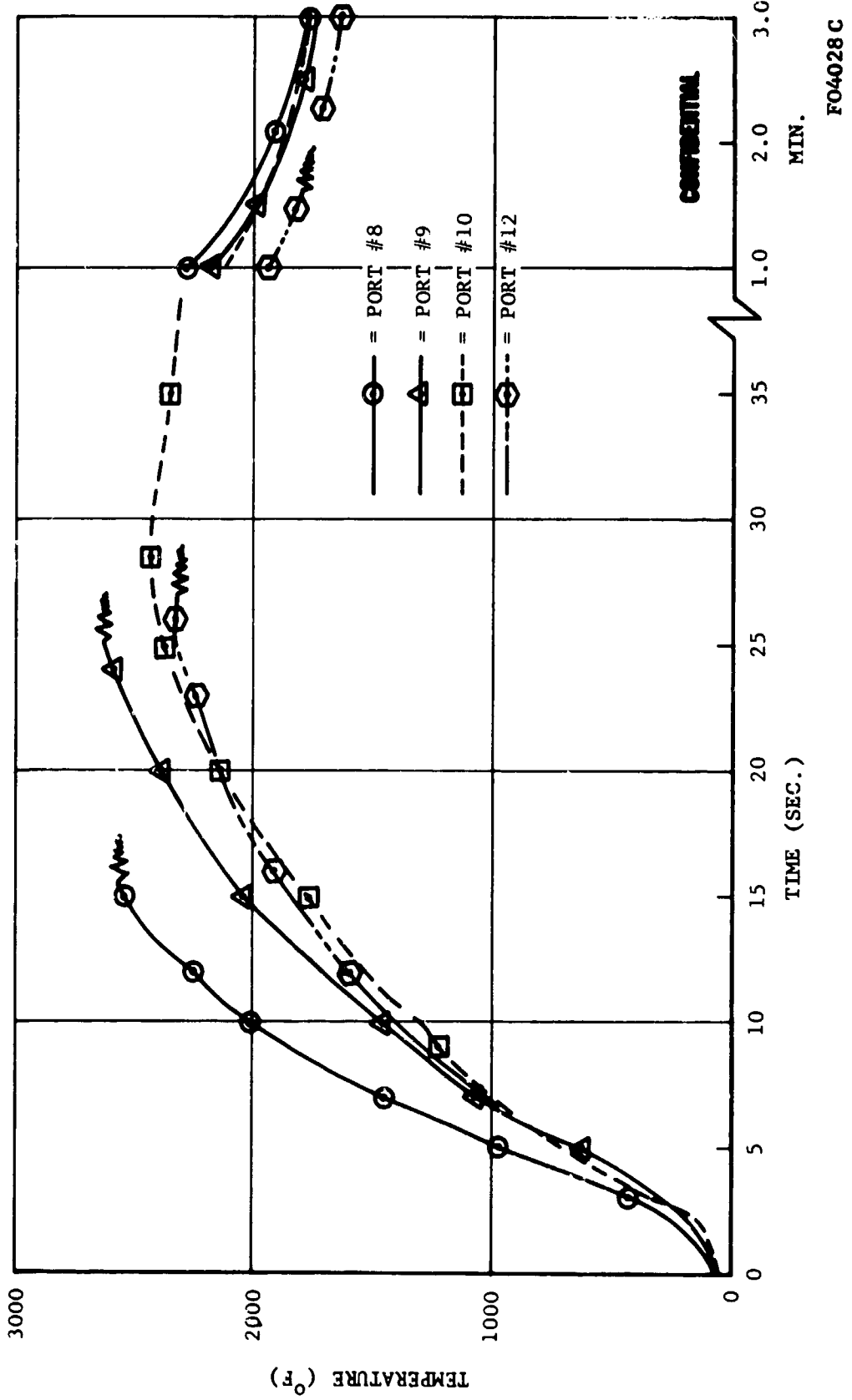


FIGURE 9B. TEMPERATURE RESPONSE OF HEAT SINK BACKWALL FOR FIRING T-2

CONFIDENTIAL

CONFIDENTIAL

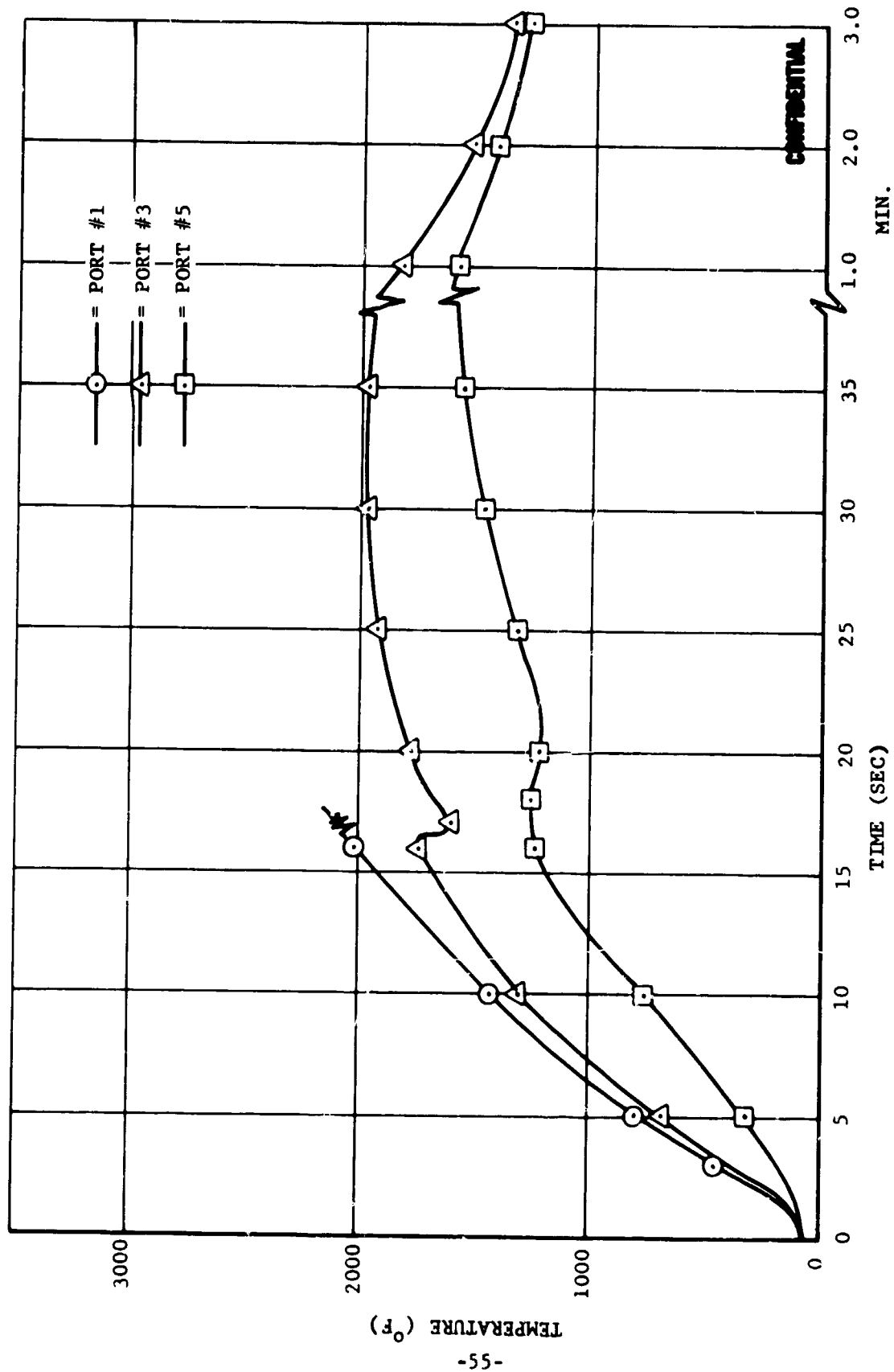


FIGURE 10A. TEMPERATURE RESPONSE OF HEAT SINK BACKWALL FOR FIRING T-3

CONFIDENTIAL

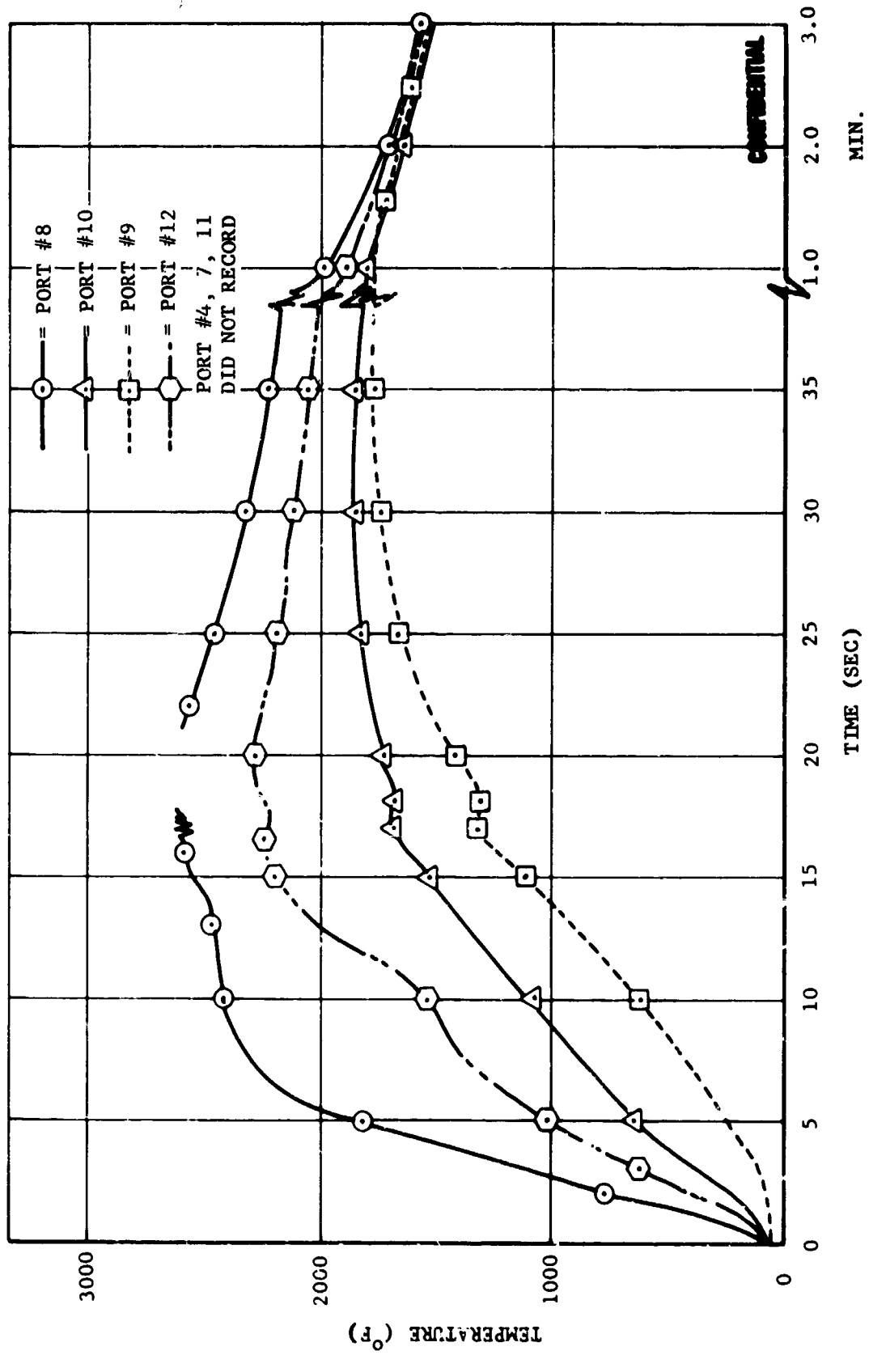


FIGURE 10B. TEMPERATURE RESPONSE OF HEAT SINK BACKWALL FOR FIRING T-3

CONFIDENTIAL

CONFIDENTIAL

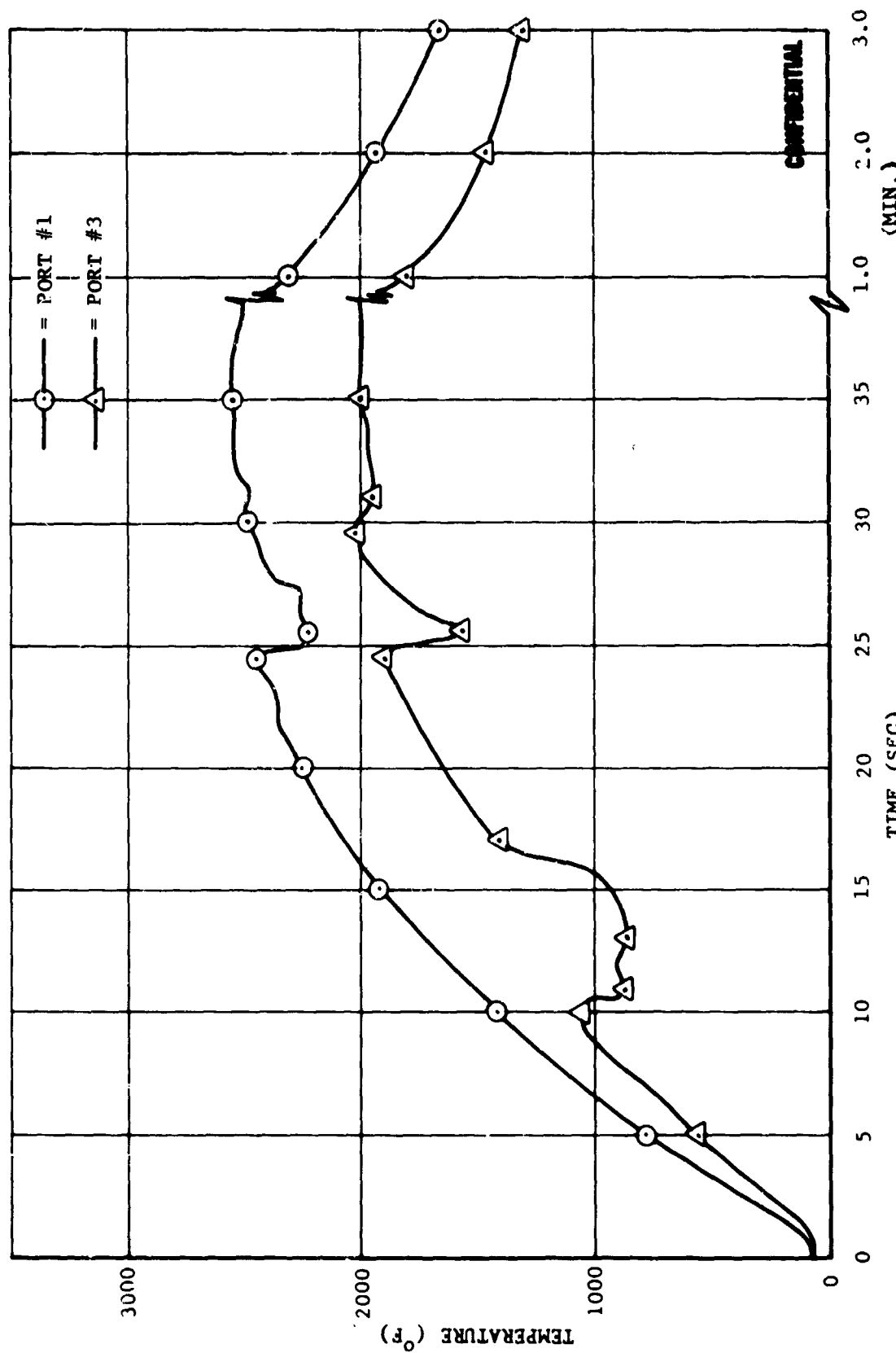


FIGURE 11A. TEMPERATURE RESPONSE OF HEAT SINK BACKWALL FOR FIRING T-4

FO4031C

CONFIDENTIAL

CONFIDENTIAL

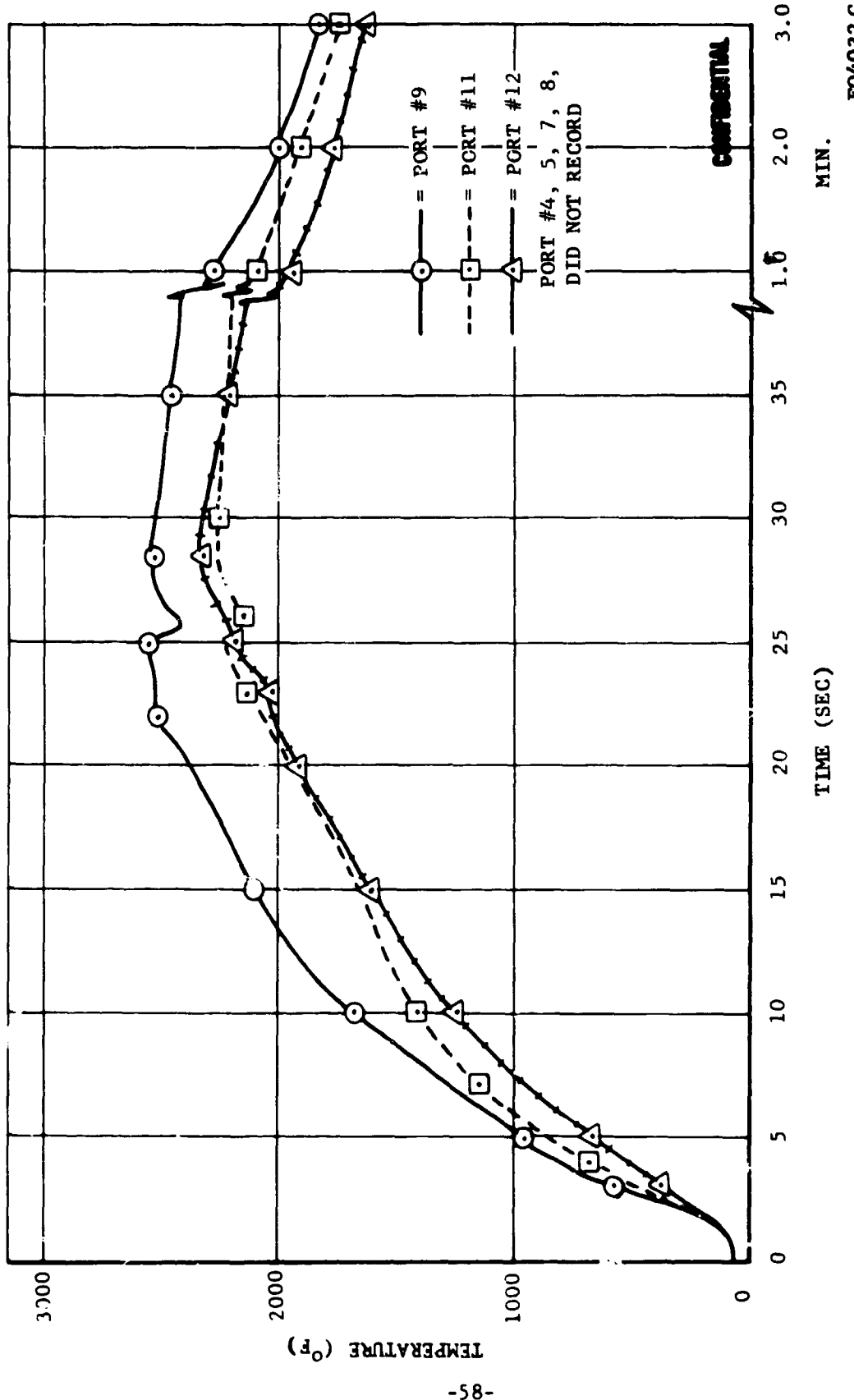


FIGURE 11B. TEMPERATURE RESPONSE OF HEAT SINK BACKWALL FOR FIRING T-4

CONFIDENTIAL

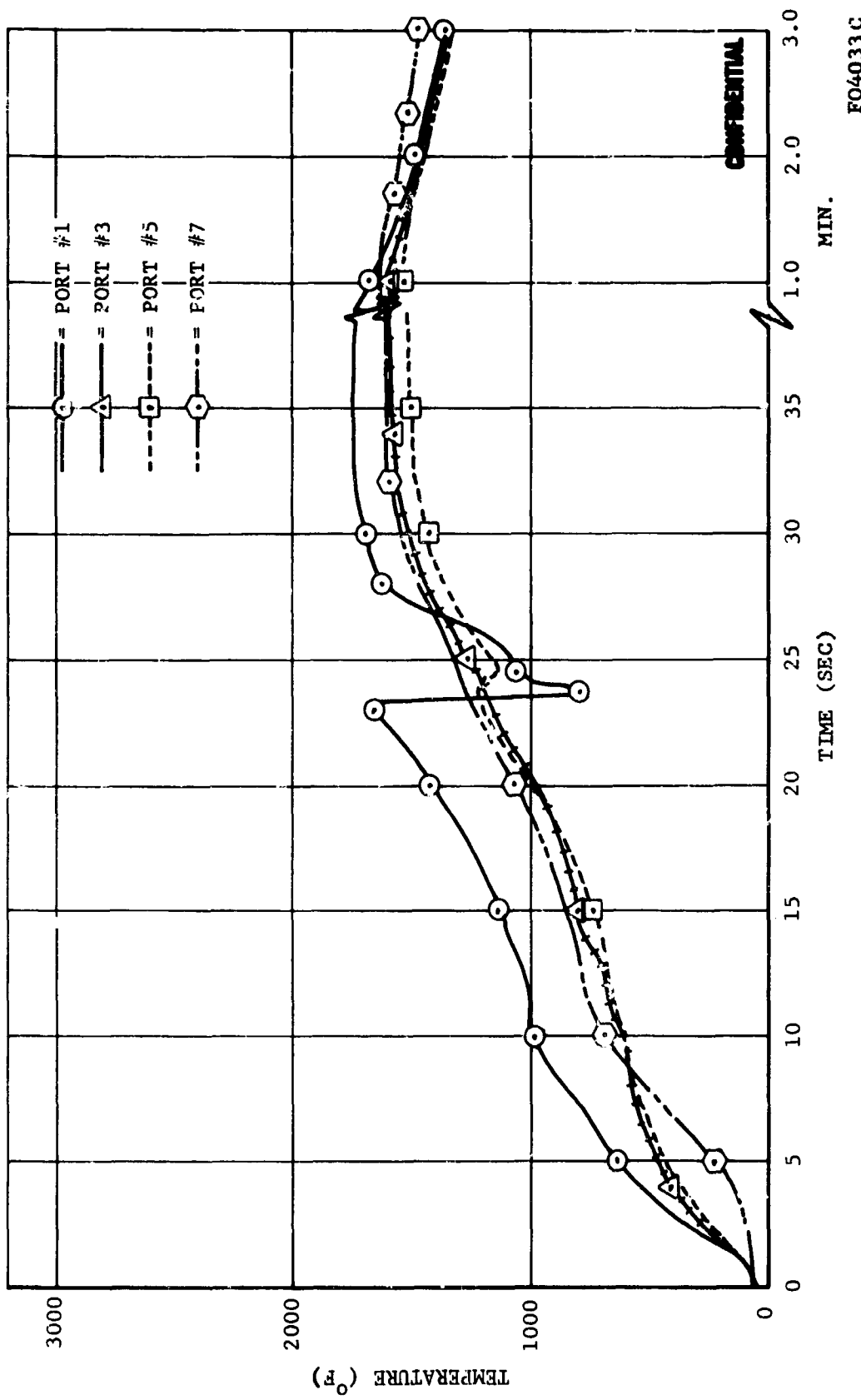


FIGURE 12A. TEMPERATURE RESPONSE OF HEAT SINK BACKWALL FOR FIRING T-5

CONFIDENTIAL

CONFIDENTIAL

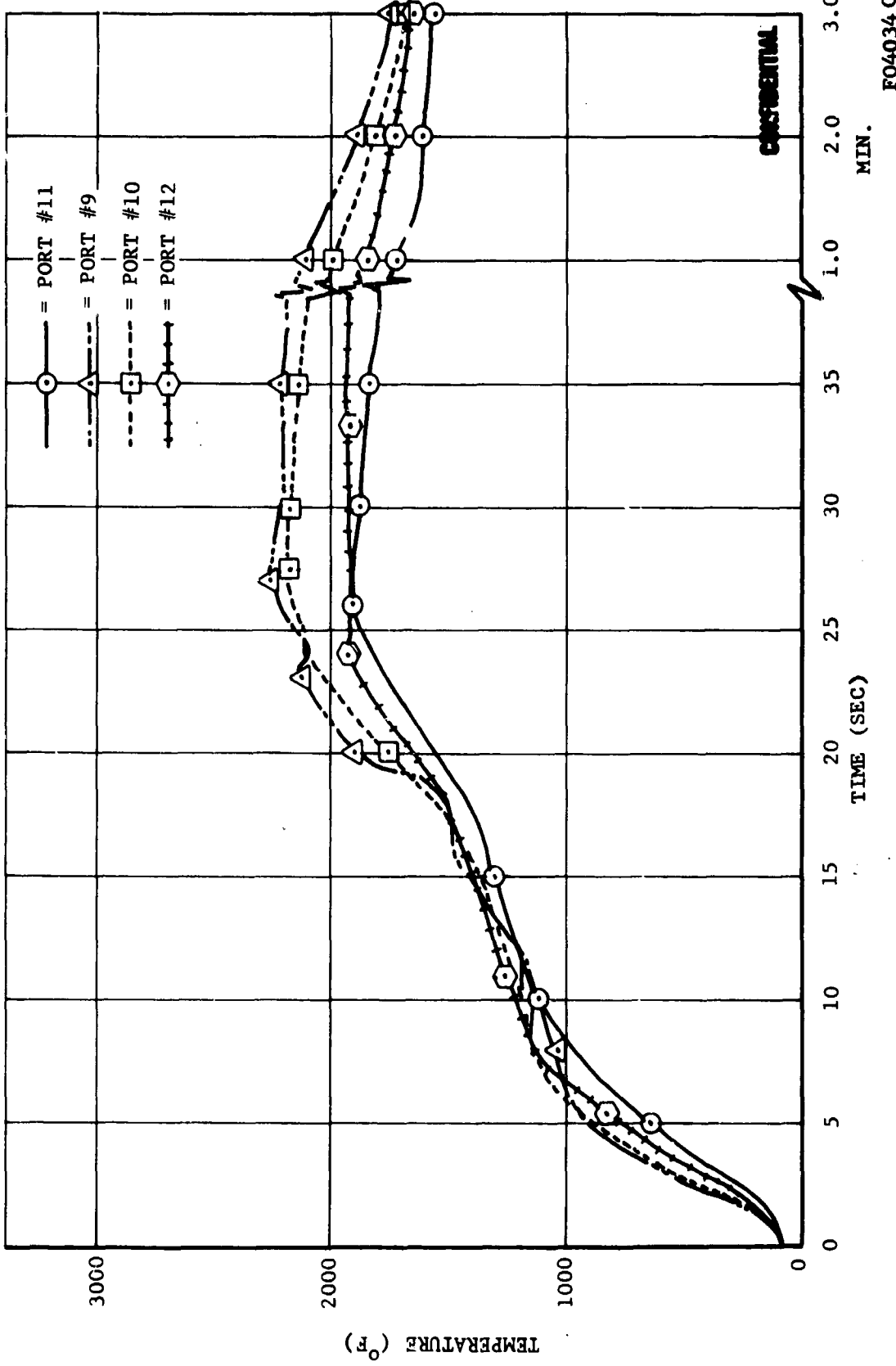


FIGURE 12B. TEMPERATURE RESPONSE OF HEAT SINK BACKWALL FOR FIRING T-5

CONFIDENTIAL

CONFIDENTIAL

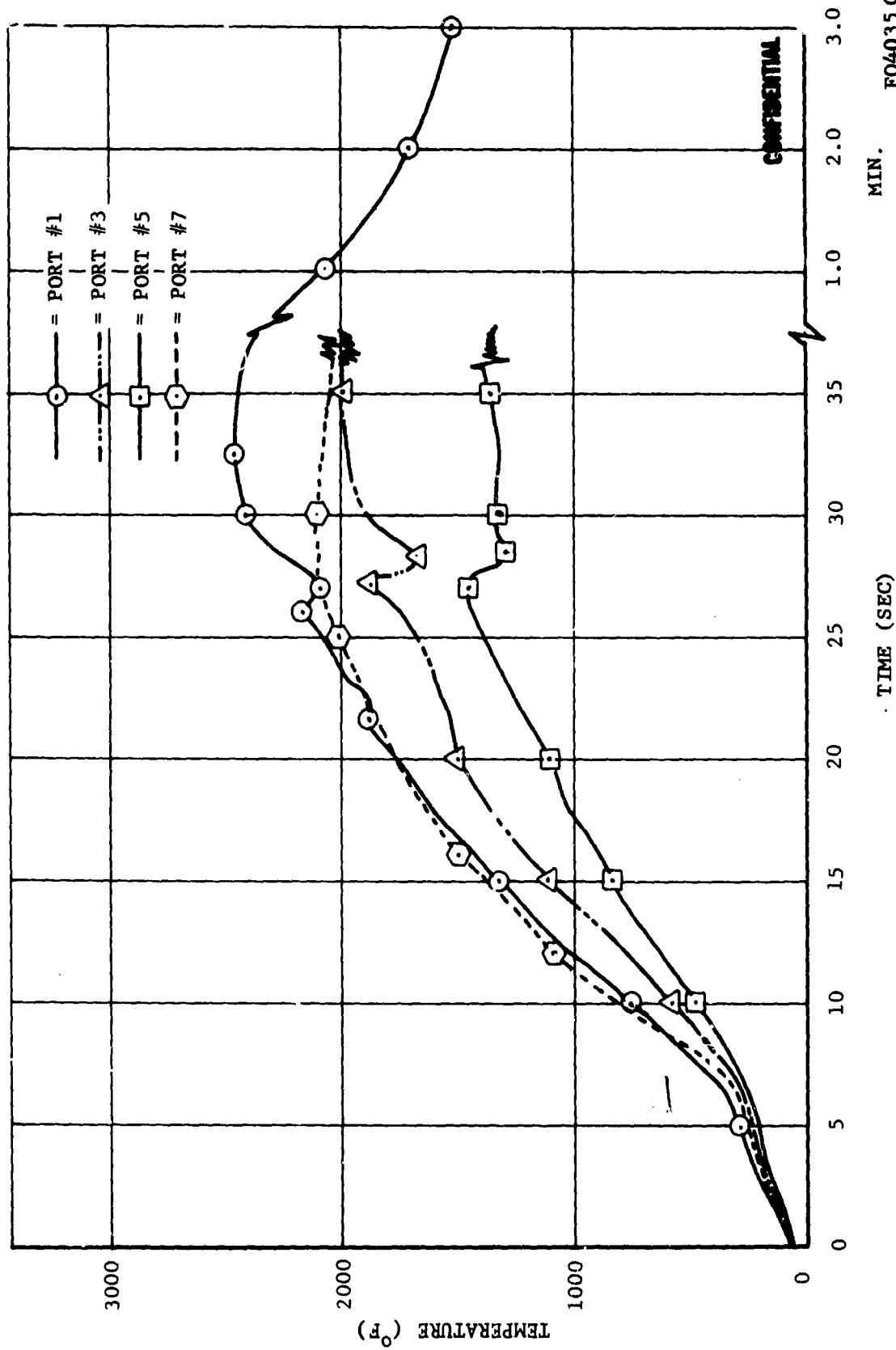


FIGURE 13A. TEMPERATURE RESPONSE OF HEAT SINK BACKWALL FOR FIRING T-6

CONFIDENTIAL

CONFIDENTIAL

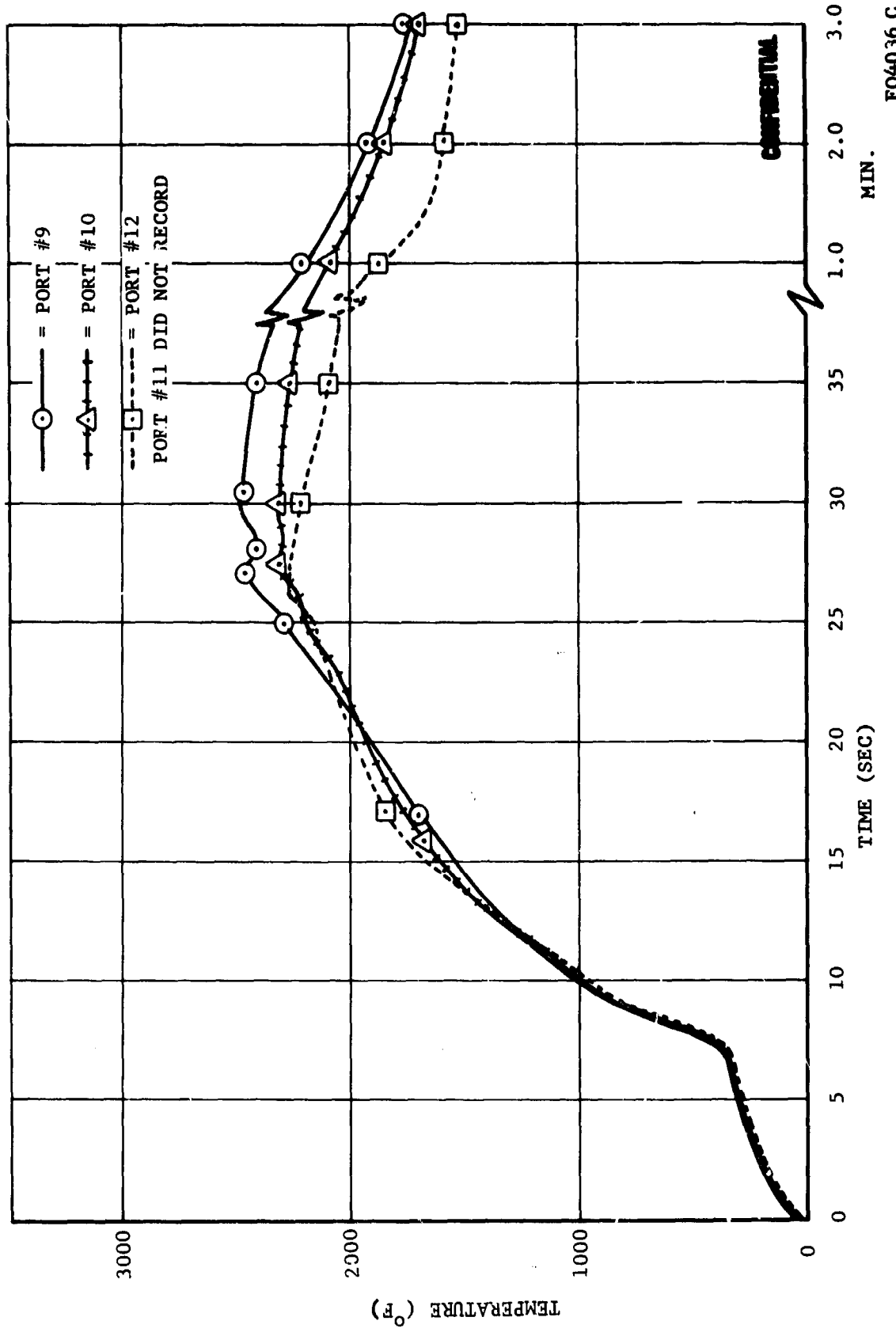


FIGURE 13B. TEMPERATURE RESPONSE OF HEAT SINK BACKWALL FOR FIRING T-6

CONFIDENTIAL

CONFIDENTIAL

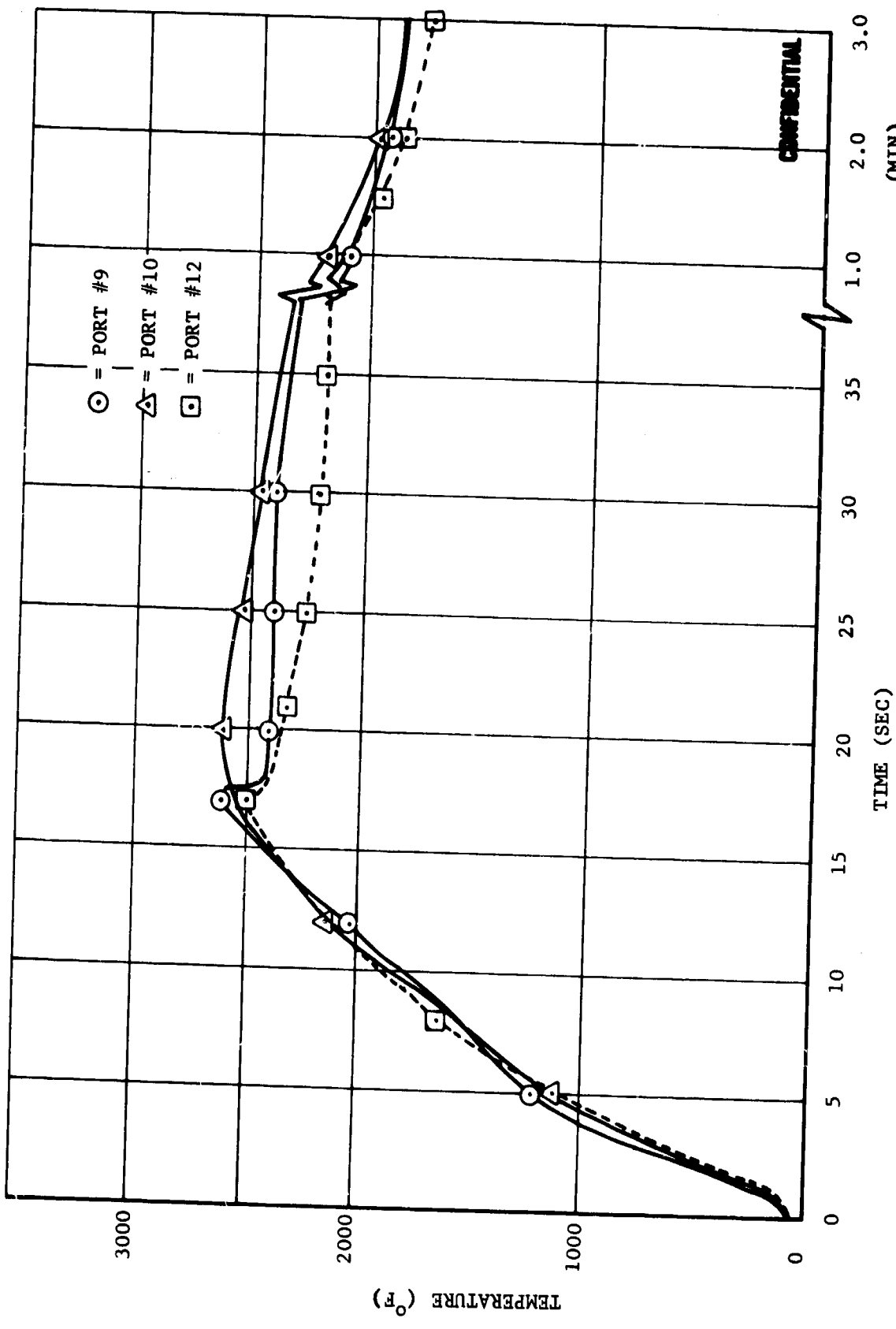


FIGURE 14A. TEMPERATURE RESPONSE OF HEAT SINK BACKWALL FOR FIRING T-7

F04037 C

CONFIDENTIAL

CONFIDENTIAL

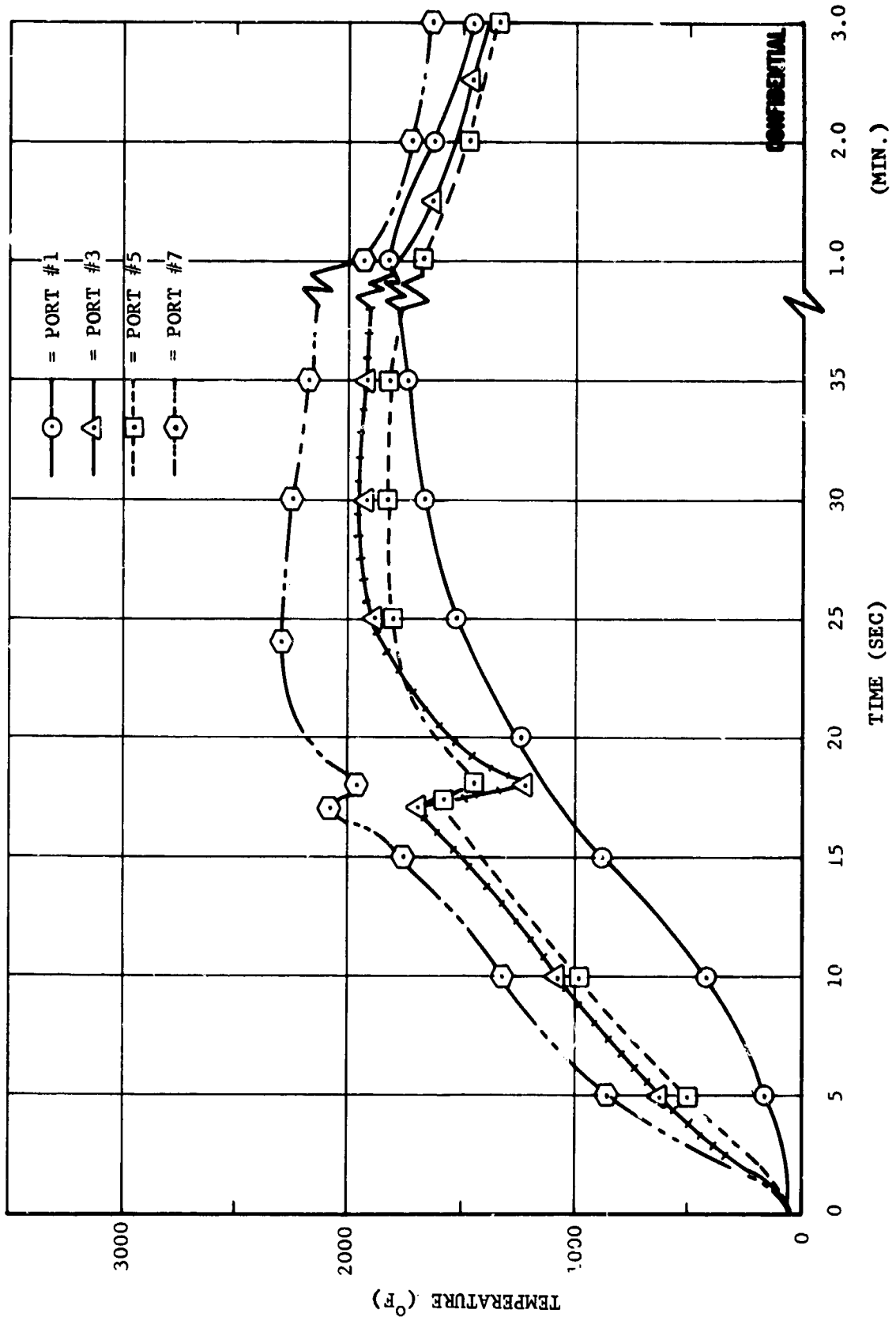


FIGURE 14.B. TEMPERATURE RESPONSE OF HEAT SINK BACKWALL FOR FIRING T-7

FO4038C

CONFIDENTIAL

CONFIDENTIAL

TABLE IV. PROPELLANT AND ROCKET MOTOR PARAMETERS USED IN THERMAL ANALYSIS OF MOTORS T-1 THROUGH T-7

Rocket Motor	Initial Throat Diameter (inches)	Theoretical Combustion Temperature ($^{\circ}$ R)	Ideal Throat Recovery Temperature ($^{\circ}$ R)	Firing Time** (sec)	Average Chamber Pressure** (psia)	Transient Chamber Pressure (psia)
T-1	1.166	6770	6610	17.4	870	Figure 118
T-2	1.030	6120	6020	24.5	840	Figure 119
T-3	1.1898	6340	6250	16.0	902	Figure 120
T-4	1.0295	6170	6050	24.0	834	Figure 121
T-5	1.044	6160	6090	23.0	853	Figure 122
T-6 (#1)*	1.200	6320	6260	21.6	636	Figure 123
T-6 (#2)*	1.200	6320	6260	26.6	534	Figure 123
T-7	1.146	6780	6660	16.5	952	Figure 124

*The firing of motor T-6 experienced a 5-second start delay during which time the chamber pressure was approximately 90 psia. Therefore two firing times were employed in the evaluation of the effective heat transfer coefficients.

**Firing times and average pressures have been selected specifically for use in the thermal analysis and do not necessarily agree with the action times and average pressures given in Paragraph 5.2.b.

The total heat absorbed per unit area of gas side surface (Equation 4 and 6) and the effective heat transfer coefficient (Equation 5) are presented in Table V as a function of area ratio for motors T-1 through T-7.

CONFIDENTIAL

CONFIDENTIAL

TABLE V. Q_T/A AND h_{eff} VERSUS AREA RATIO
FOR MOTORS T-1 THROUGH T-7

Rocket Motor	Parameter	Port Number (See Figure 96 in Section IV)						
		3	5	7	8	9	10	12
T-1	Area Ratio	-12.4	-8.0	-4.67	-2.66	-1.24	-1.01*	1.00
	Q_T/A -Btu/in ²	31.6	48.7	I.T.C.	110.	160.	202.	+1.21
	h_{eff} -Btu/in ² sec ^{0.7}	0.00037	0.00064	I.T.C.	0.0021	0.0030	0.0058	130.
T-2	Area Ratio	-15.8	-10.3	-6.00	-3.40	-1.59	-1.02*	0.0047
	Q_T/A	I.T.C.	I.T.C.	I.T.C.	108.	168.	206.	+1.54
	h_{eff}	I.T.C.	I.T.C.	I.T.C.	0.0016	0.0025	0.0042	I.T.C.
T-3	Area Ratio	-11.9	-7.68	-4.47	-2.55	-1.19	-1.01*	1.00
	Q_T/A	18.3	57.1	I.T.C.	88.4	121.	162.	+1.16
	h_{eff}	0.00024	0.0012	I.T.C.	0.0018	0.0022	0.0045	I.T.C.
T-4	Area Ratio	-15.8	-10.3	-6.00	-3.40	-1.59	-1.02*	1.00
	Q_T/A	I.T.C.	40.8	70.6	I.T.C.	172.	I.T.C.	+1.54
	h_{eff}	I.T.C.	0.00028	0.00090	I.T.C.	0.0027	I.T.C.	I.T.C.
T-5	Area Ratio	-15.4	-10.0	-5.81	-3.30	-1.55	-1.02*	1.00
	Q_T/A	31.3	30.8	49.8	I.T.C.	147.	178.	+1.50
	h_{eff}	0.00028	0.00034	0.00050	I.T.C.	0.00020	0.0031	I.T.C.
T-6 (#1)	Area Ratio	-11.6	-7.56	-4.41	-2.51	-1.17	-1.01*	1.00
	Q_T/A	I.T.C.	I.T.C.	61.9	I.T.C.	169.	205.	+1.13
	h_{eff}	I.T.C.	I.T.C.	0.00070	I.T.C.	0.0028	0.0046	I.T.C.
T-6 (#2)	h_{eff}						0.0024	
	Area Ratio	-12.8	-8.30	-4.83	-2.75	-1.29	-1.01*	1.00
	Q_T/A	33.1	39.9	58.7	I.T.C.	I.T.C.	209.	+1.25
T-7	h_{eff}	0.00045	0.00051	0.0010	I.T.C.	I.T.C.	0.0076	I.T.C.

*: Approximate Area Ratio.
 I.T.C.: Insufficient Thermocouple Data.
 Minus Area Ratio denotes Entrance Section.
 Plus Area Ratio denotes Exit Section.
 Q_T/A and h_{eff} based upon gas side surface area.

CONFIDENTIAL

CONFIDENTIAL

As discussed in Paragraph 2.5.c, the determination of h_{eff} from Q_T/A (Equation 5) requires a series of transient conduction computer computations applied to the rocket motor heat sink materials. These computations result in a plot of Q_T/A versus h_{eff} at different axial positions in the rocket motor. A sample plot of Q_T/A versus h_{eff} is shown in Figure 7 for the throat location.

The average and pressure dependent gas side convective heat transfer coefficients at the throat location, for nozzles T-1 through T-7, are presented in Table VI. The coefficients were obtained using the thermal analysis of Paragraph 2.5.c(1)(c) and the transient deposition data in Paragraph 5.2.b. Also, presented in Table VI for comparison is the throat convective heat transfer coefficients (average and variable pressure) obtained from theoretical calculations using the modified Bartz equation (Paragraph 2.5.a). An error analysis has not yet been performed for the technique involved in determining h_{eff} ; however, the error in h_{eff} is estimated to be +8.0 percent and -3.0 percent.

TABLE VI. THROAT HEAT TRANSFER COEFFICIENTS
FOR TESTS T-1 THROUGH T-7

Rocket Motor	Average Gas Side Convective Heat Coefficient (based on average \bar{P}_c presented in Table IV)		Pressure Dependent Gas Side Convective Heat Transfer Parameter ϕ [where: $h_c = \phi(P/100)^{.8}$]	
	Semi-empirically Determined (Section 2.5.c) (Btu/in. ² sec ⁰ F) \bar{h}_c	Modified Bartz ($T_w = 5400^{\circ}\text{R}$) (Btu/in. ² sec ⁰ F) \bar{h}_c	Semi-empirically Determined (Btu/in. ² sec ⁰ F)	Modified Bartz ($T_w = 5400^{\circ}\text{R}$) (Btu/in. ² sec ⁰ F)
T-1	0.00698	0.00653	0.00124	0.001161
T-2	0.00449	0.00573	0.000838	0.001073
T-3	0.00769	0.00576	0.00132	0.000994
T-4	0.00595	0.00627	0.00109	0.00115
T-5	0.00385	0.00495	0.000693	0.000891
T-6 (#1)	0.00607	0.00367	0.00138	0.000836
T-6 (#2)	0.00315	0.00320	0.000825	0.000836
T-7	0.00804	0.00565	0.00132	0.000935

CONFIDENTIAL

CONFIDENTIAL

The thermal response of the throat heat sink material for rocket motors T-1 through T-7 are shown in Figures 15 to 23. These figures were constructed using (1) the thermal analysis of Paragraph 2.5.c(1)(c), (2) the pressure dependent gas side convective heat transfer parameters of Table VI, and (3) the transient deposit thickness histories given in Paragraph 5.2.b.

The contact conductance ($C = 1/RA$, where R is the contact resistance) were calculated at the pyrolytic graphite insert-polycrystalline graphite (ATJ) sleeve interface. The results are tabulated in Table VII.

TABLE VII. THROAT INSERT INTERFACE
CONTACT CONDUCTANCE

<u>Motor Test</u>	<u>Axial Location in Motor (Area Ratio)</u>	Contact Conductance $C = \frac{Q}{A \Delta T} - \frac{\text{Btu}}{\text{in.}^2 \text{sec}^{\circ}\text{F}}$
T-1	-2.66	0.0006
	-1.24	0.0014
	1.00	0.0016
T-2		Insufficient Thermocouple Data
T-3	1.00	0.0011
T-4		Insufficient Thermocouple Data
T-5	1.00	0.00237
T-6	1.00	0.013
T-7	1.00	0.0011

CONFIDENTIAL

CONFIDENTIAL

PARAMETERS USED IN ANALYSIS:	
THROAT RECOVERY TEMPERATURE :	6610 °R
PRESSURE DEPENDENT GAS SIDE HEAT TRANSFER COEFFICIENT (MEASURED) :	$h = 0.00124 \left(\frac{P_c}{100}\right)^{0.8} \text{ Btu}/\text{IN.}^2 \text{ SEC } ^\circ\text{F}$
P.G. - ATJ CONTACT CONDUCTANCE :	0.0006 $\frac{\text{BTU}}{\text{IN}^2 \text{ SEC } ^\circ\text{F}}$

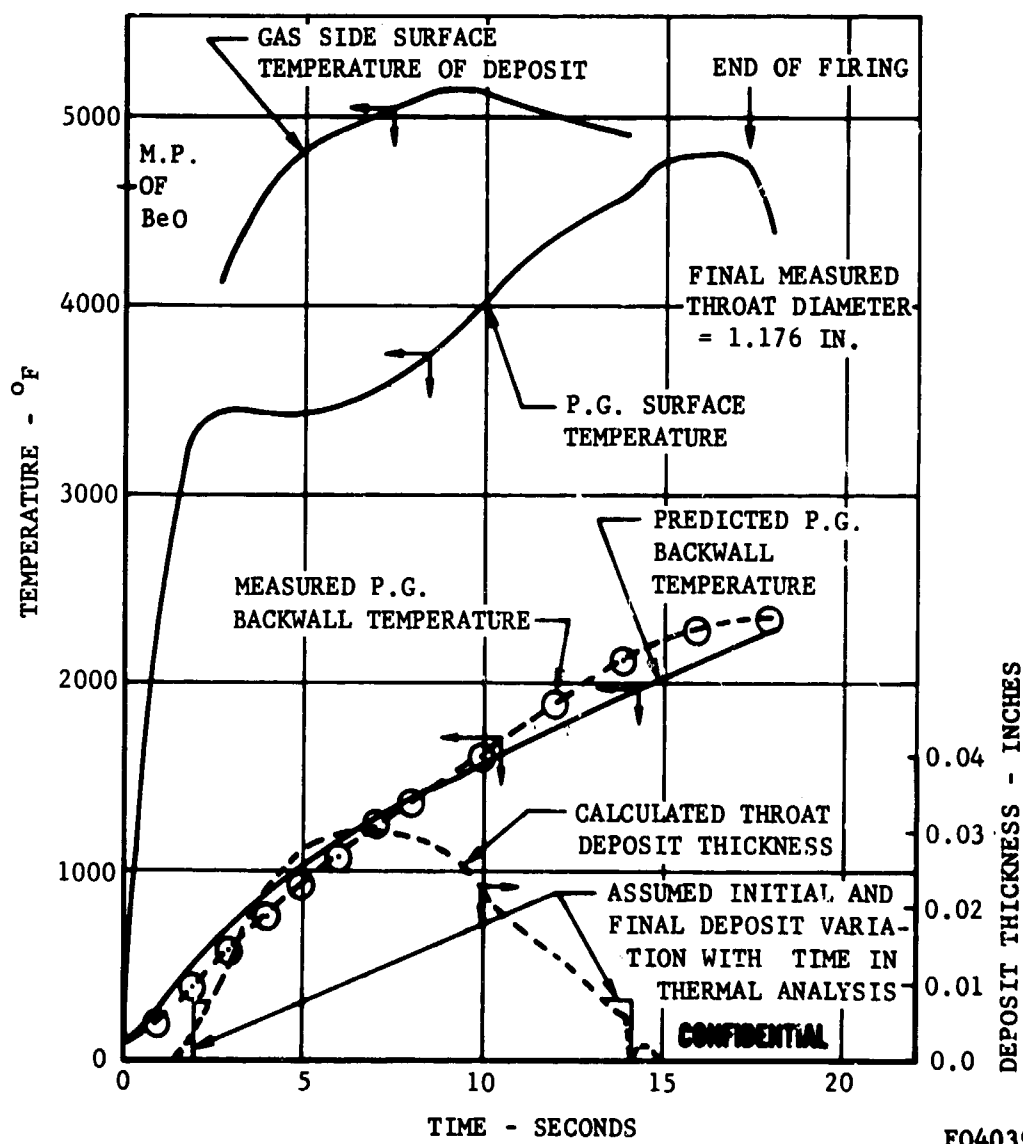
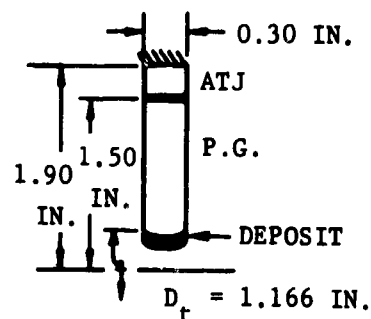


FIGURE 15. THROAT TEMPERATURE RESPONSE WITH DEPOSITION FOR FIRING T-1

CONFIDENTIAL

CONFIDENTIAL

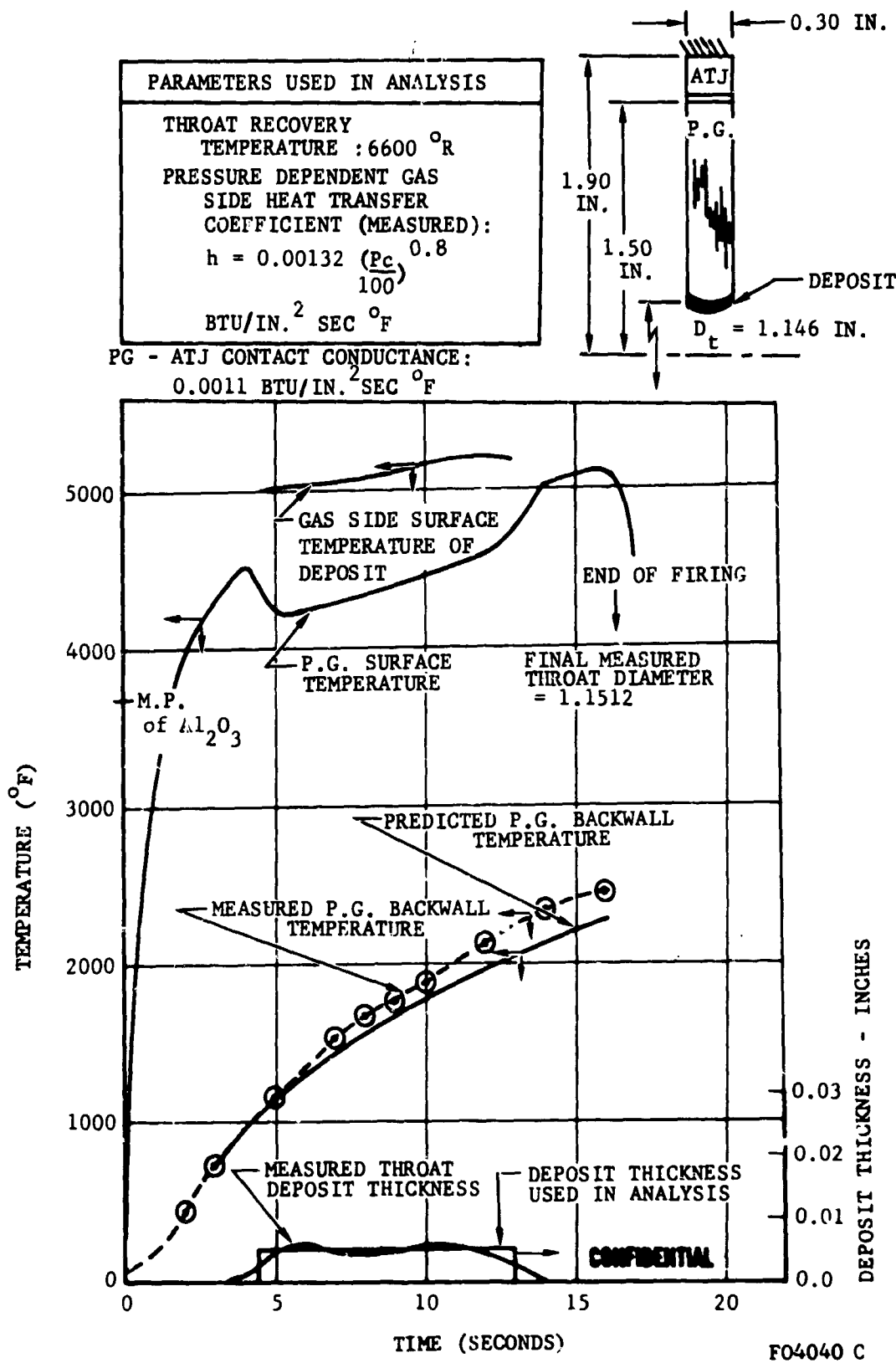


FIGURE 16. THROAT TEMPERATURE RESPONSE WITH DEPOSITION FOR FIRING T-7

CONFIDENTIAL

CONFIDENTIAL

PARAMETER USED IN ANALYSIS BOTH WITH AND WITHOUT DEPOSITION	
THROAT RECOVERY TEMPERATURE	: 6050 °R
PRESSURE DEPENDENT GAS SIDE HEAT TRANSFER COEFFICIENT (MEASURED):	
$h = 0.001092 \left(\frac{P.G.}{100} \right)^{0.8}$	BTU/IN. ² SEC °F
PG-ATJ CONTACT CONDUCTANCE:	
0.0006 BTU/IN. ² SEC °F	

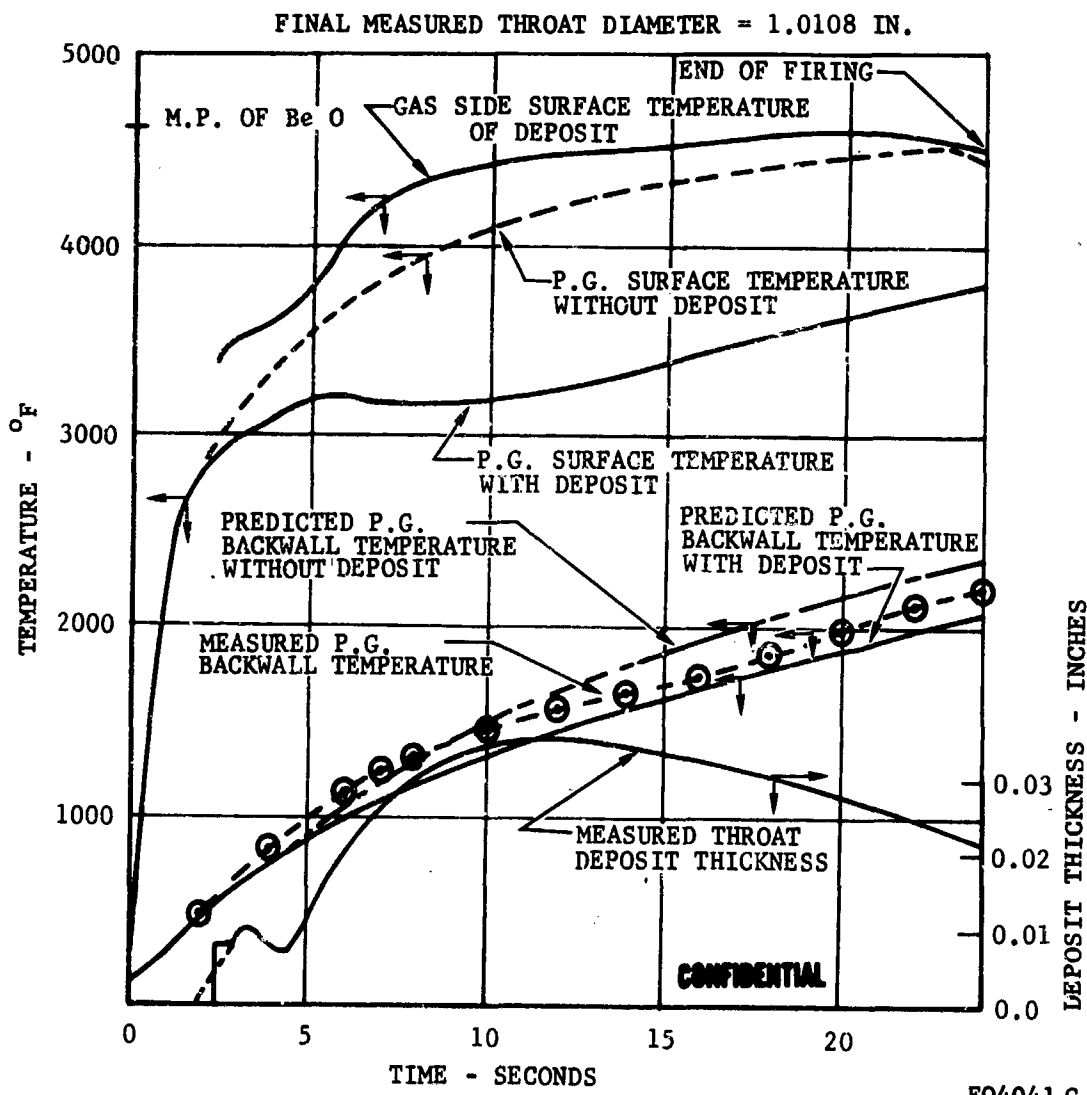
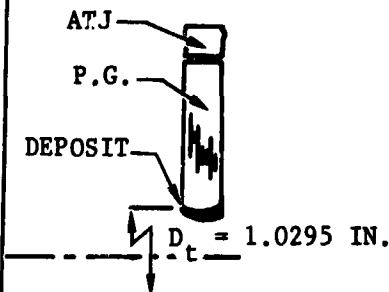
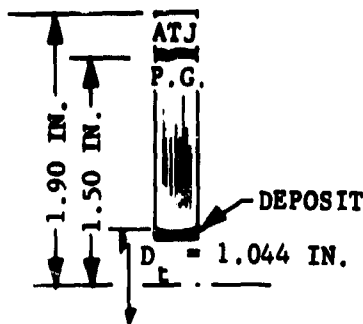


FIGURE 17. THROAT TEMPERATURE RESPONSE FOR FIRING T-4

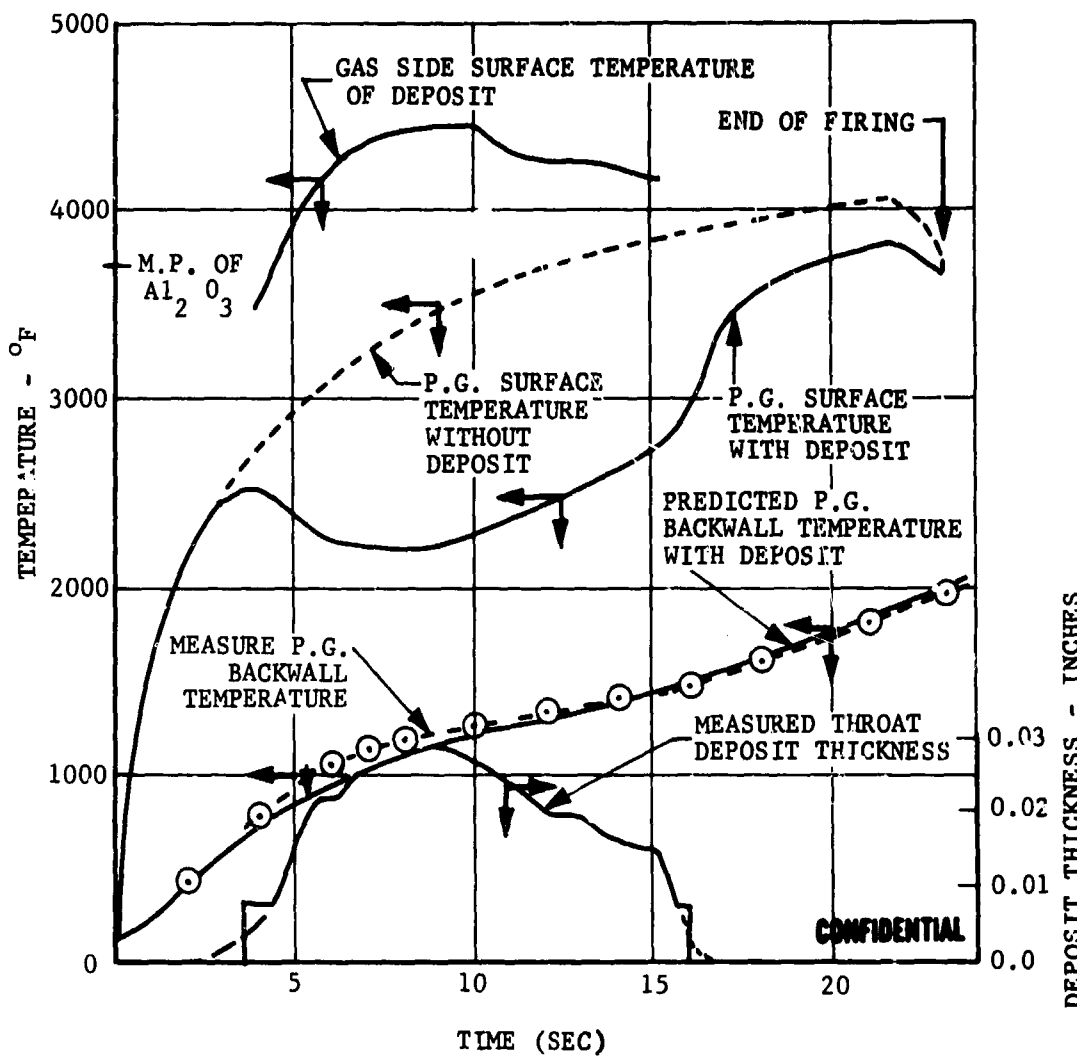
CONFIDENTIAL

CONFIDENTIAL

PARAMETERS USED IN ANALYSIS	
THROAT RECOVERY	TEMPERATURE : 6090 °R
PRESSURE DEPENDENT GAS SIDE	HEAT TRANSFER COEFFICIENT
(MEASURED)	$h = 0.000693 (P/100)^{0.8}$ BTU/IN. ² SEC °F
PG - ATJ CONTACT	CONDUCTANCE: 0.00237 BTU IN. ² SEC °F



FINAL MEASURED THROAT DIAMETER = 1.049 IN.

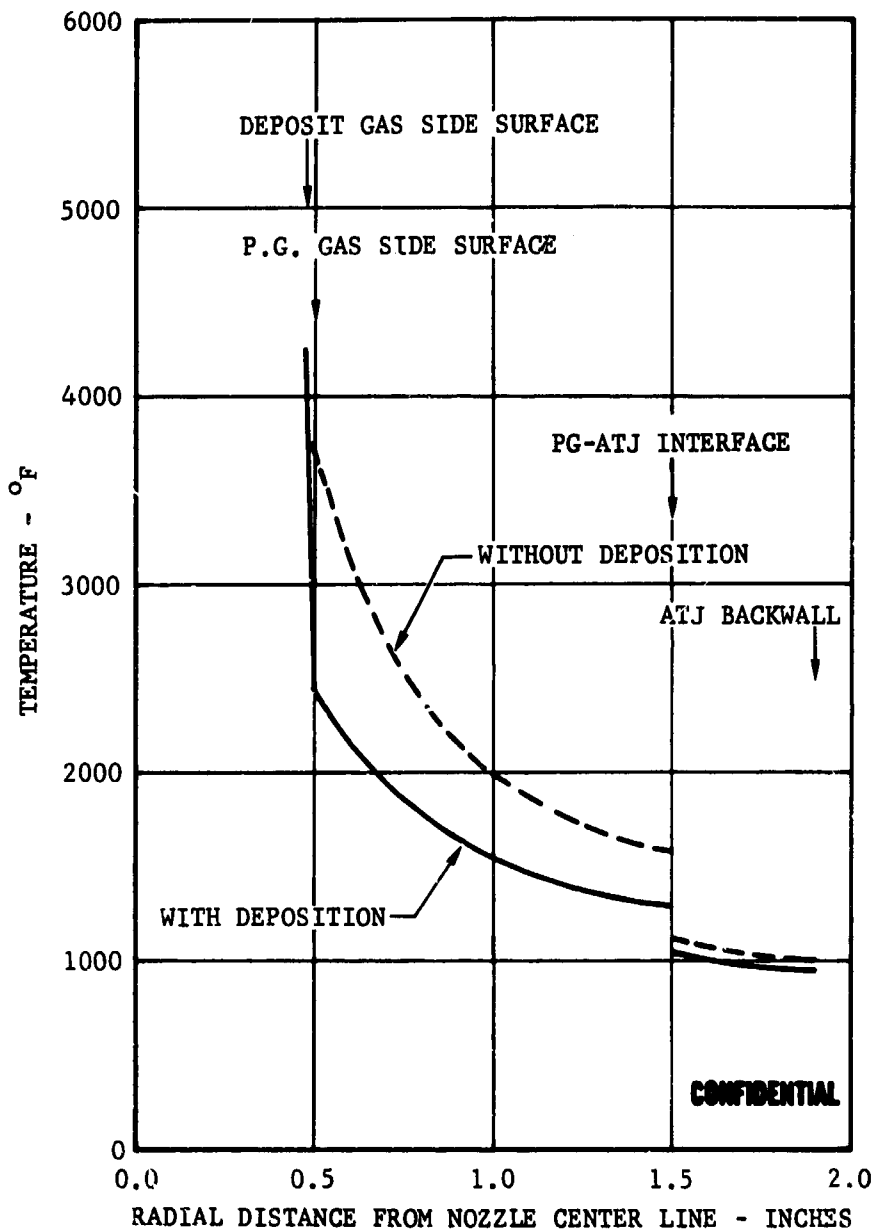


FO4042 C

FIGURE 18. THROAT TEMPERATURE RESPONSE FOR FIRING T-5

CONFIDENTIAL

CONFIDENTIAL



F04043 C

FIGURE 19. THROAT RADIAL TEMPERATURE PROFILE AT 12 SECONDS FOR FIRING T-5

CONFIDENTIAL

CONFIDENTIAL

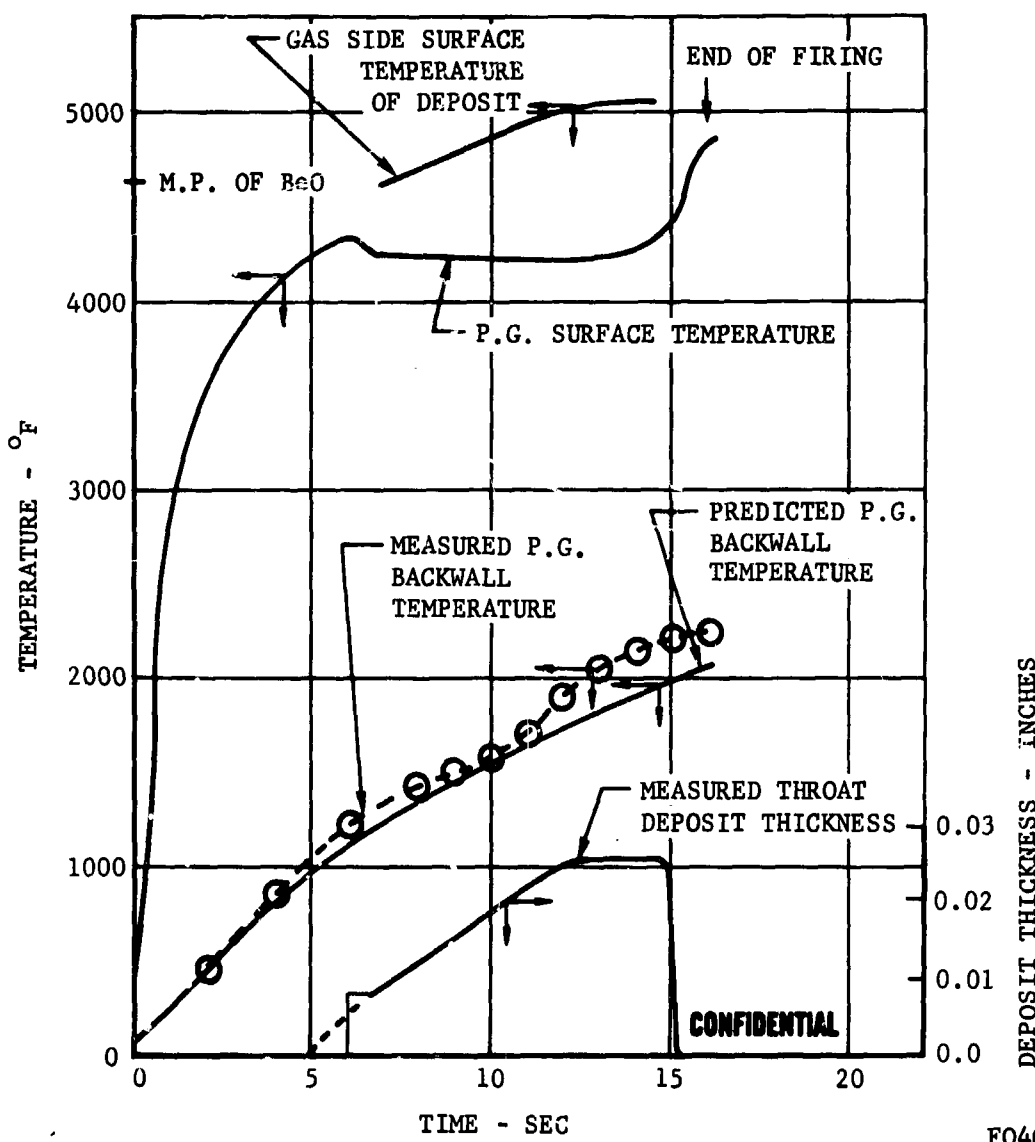
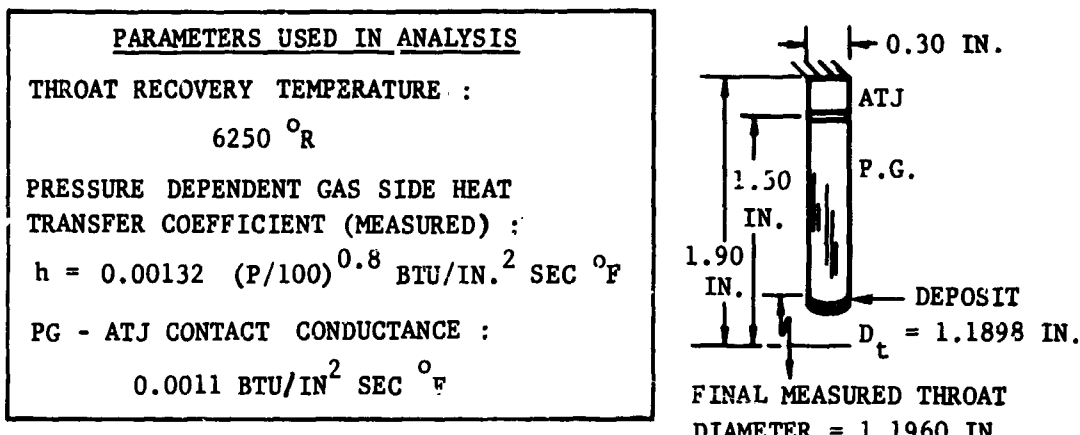
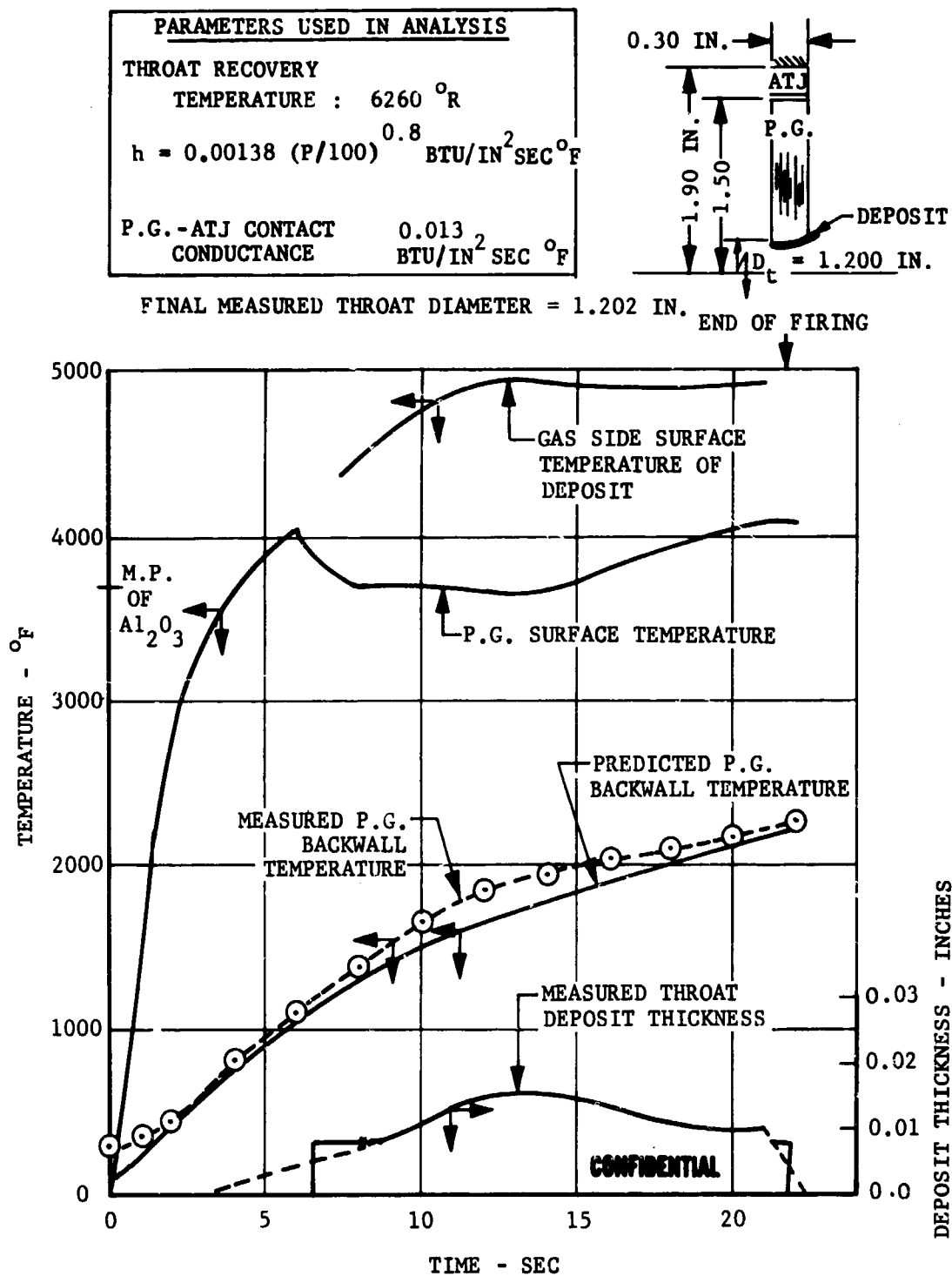


FIGURE 20. THROAT TEMPERATURE RESPONSE WITH DEPOSITION FOR FIRING T-3

CONFIDENTIAL

CONFIDENTIAL

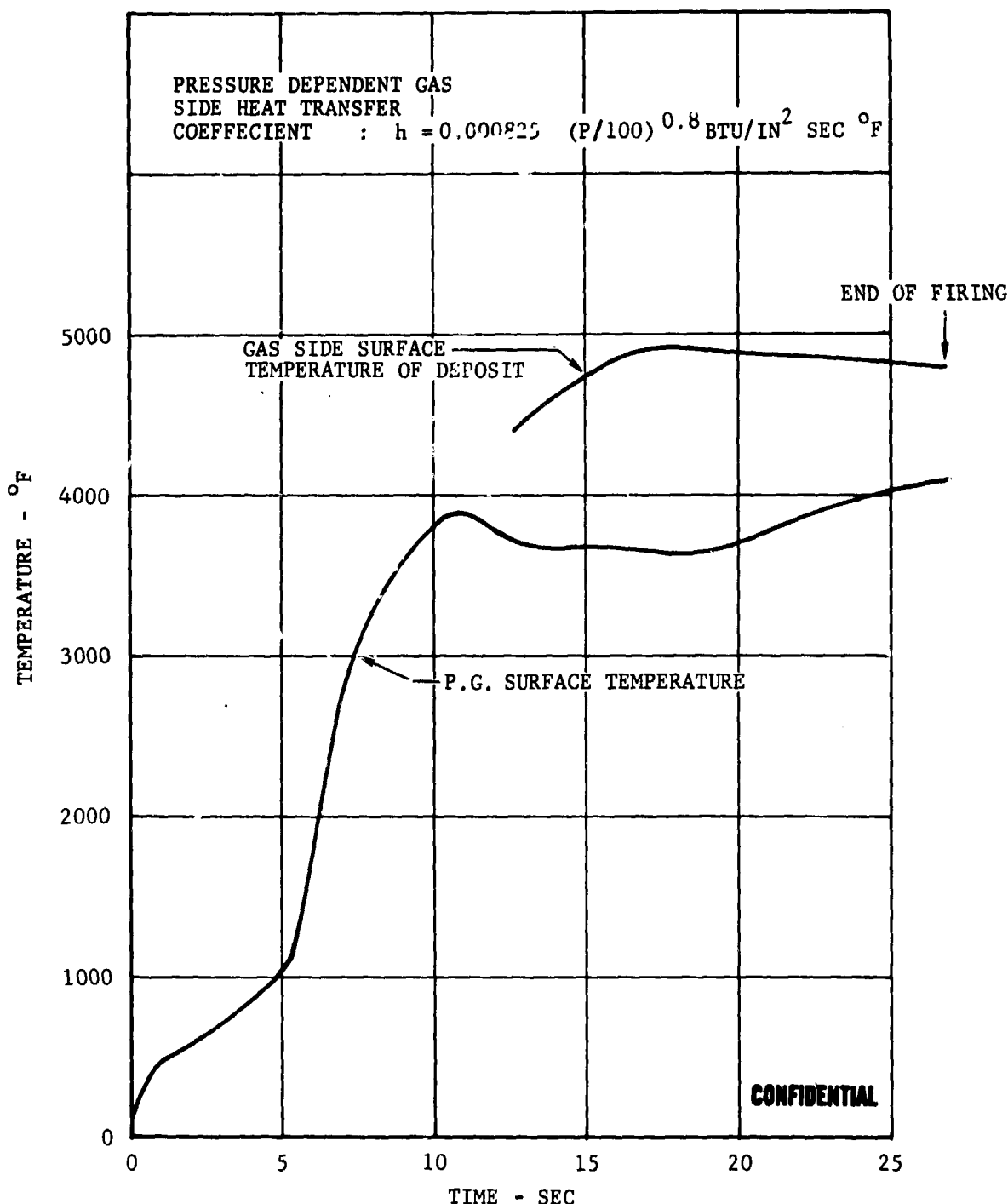


F04045 C

FIGURE 21. THROAT TEMPERATURE RESPONSE WITH DEPOSITION FOR FIRING T-6 (#1)

CONFIDENTIAL

CONFIDENTIAL



F04046 C

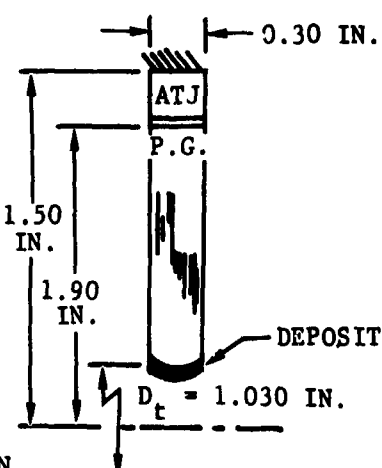
FIGURE 22. THROAT TEMPERATURE RESPONSE WITH DEPOSITION FOR FIRING
T-6 (#2)

CONFIDENTIAL

CONFIDENTIAL

PARAMETERS USED IN ANALYSIS

THROAT RECOVERY
TEMPERATURE - 6020°R
PRESSURE DEPENDENT
GAS SIDE HEAT TRANSFER
COEFFICIENT (MEASURED):
 $h = 0.000838 (\rho/100)^{0.8}$
 $\text{BTU}/\text{IN}^2 \text{ SEC } ^{\circ}\text{F}$
P.G. - ATJ CONTACT CONDUCTANCE
 $: 0.0024 \text{ BTU}/\text{IN}^2 \text{ SEC } ^{\circ}\text{F}$



FINAL MEASURED THROAT DIAMETER - = 1.029 IN

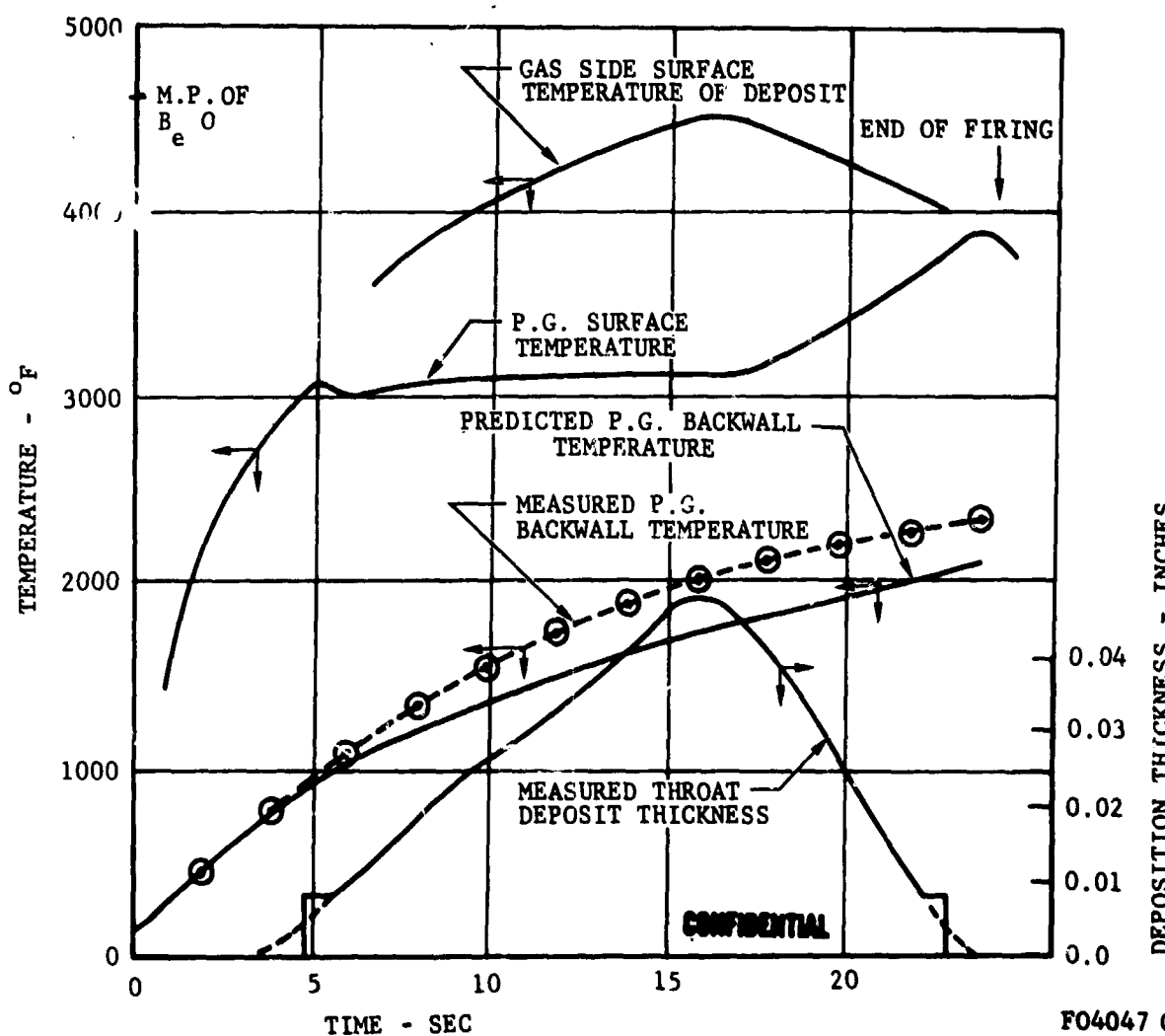


FIGURE 23. THROAT TEMPERATURE RESPONSE WITH DEPOSITION FOR FIRING T-2

CONFIDENTIAL

CONFIDENTIAL

(3) (C) Discussion of Results

The dependence of the effective heat transfer coefficient (h_{eff}) on nozzle area ratio is presented in Table V. As defined in Paragraph 2.5.c(2), this coefficient includes the combined effects of convection, radiation, and deposition on surface heat transfer. The determination of the local radiation and convection boundary conditions from h_{eff} requires independent specification of the local transient deposit thickness (see Paragraph 2.5.c(2)).

From Table V, the maximum effective heat transfer coefficient is shown to be upstream from the throat for all motor tests except T-3. The location of the maximum convective heat transfer coefficient is also predicted, from boundary layer theory, to be upstream from the throat. It may be reasonably assumed that the variation in transient deposit thickness between ports 10 and 12 of Table V is negligible, thus reflecting the predicted variation in convective heating in the h_{eff} values of Table V. However, a slight variation in the transient deposit thickness will greatly influence h_{eff} between ports 10 and 12. Referring to the throat transient deposit thickness, it can be seen that deposit removal during Test T-3 is considerably different from the other tests. Therefore, a plausible explanation for the anomalous behavior of h_{eff} in Test T-3 involves the detailed deposit behavior which cannot be deduced directly.

The variation in h_{eff} with area ratio also reflects the variation in local deposit thickness during the firing. From the physical deposition model of Paragraph 2.5.d, a significant variation in deposit thickness is expected when a change in surface material (and, consequently, the thermal conductivity) occurs along the wall contour. For the rocket motors of Table V, this occurs slightly upstream of port 5 and between ports 1 and 8. In comparing the variation in h_{eff} between ports 5 and 3, a significant increase in h_{eff} occurs for firings T-1 and T-3 indicating that a substantial axial change in deposit thickness existed during firing. This variation between ports 5 and 3 did not occur in motors T-5 and T-7. This may be explained by the fact that motors T-5 and T-7 were fired with aluminum propellants whereas beryllium propellants were employed in motors T-1 and T-3. That is, due to the large differences in Al_2O_3 and BeO melting points and thermal conductivities, more beryllia accumulates by freezing on the surface of the heat sink material than does alumina. The maximum gas side surface temperature of solid BeO exceeds solid Al_2O_3 ; therefore, the time required to liquify BeO deposit will be greater than that for the Al_2O_3 . From this it can be seen that the variation in BeO deposit thickness between thermally dissimilar materials will be greater than will be the case for alumina.

The influence of the deposit on the heat sink boundary condition can be seen by comparing the throat effective heat transfer coefficients of Table V with the semi-empirical average gas side convective heat transfer coefficients given in Table VI. From this comparison, it can be seen that the effect of

CONFIDENTIAL

CONFIDENTIAL

deposition on the heat sink material's thermal boundary condition is very important and must be included in the heat transfer analysis. This observation can also be deduced directly from Figures 15 through 23.

The correlation shown in Table VI between the semi-empirically determined convective heat transfer coefficient and the modified Bartz prediction is very good indicating the ability of the modified Bartz analysis to approximate throat convective heat transfer. Such agreement should be regarded as fortuitous because it ignores deposition. The thermal response of the throat washer for the rocket motors employing the highest flame temperature propellants (Arcocel 191F and 389 analogs) are shown in Figures 15 and 16. The effect of deposition on heat sink surface temperature is clearly evident. As predicted by the physical deposition model (Paragraph 2.5.d), the BeO throat deposit thickness for the beryllium propellant will be greater than the Al_2O_3 deposit for the aluminum analog (higher deposit thermal conductivity and melting temperature promotes greater deposit thickness).

Although the alumina thickness is considerably less than that of beryllia, the thermal insulation provided by the Al_2O_3 deposit in firing T-7 is significant due to its low thermal conductivity. The typical reversal of the surface temperature trend on arrival of the deposit derives from the fact that the heat transfer from the exhaust to the graphite washer surface is less than the radial heat conduction away from the surface. For firing T-7, the Al_2O_3 deposit at the throat was at all times in the liquid phase (i.e., P.G. surface temperature above Al_2O_3 melting point); therefore, the variation in throat deposit thickness can be attributed to variations in the upstream Al_2O_3 mass flow. In contrast, the initial BeO deposit was solid in test T-1. Therefore, the mass storage of BeO at the throat (increase in deposit thickness) may be attributed to both solidification of the on-coming deposit and to variation in upstream mass flow. As the firing proceeds, the deposit partially melts and the liquid flows downstream. At approximately 7 seconds during the firing, the deposit thickness starts to decrease due to increased liquification at the throat (increasing P.G. surface temperature) and/or reduced on-coming deposit mass flow. At 14 seconds, the P.G. surface temperature is equal to the melting point of BeO and no significant throat deposit is detectable during the remainder of the firing. However, as shown by both the physical deposition model and post test observations, deposition is present at all times in the aft closure region. From this, it is apparent that some deposit must pass through the throat. However, the oxide flow could easily be obscured by the corrosion occurring in the final few seconds. At relatively long firing times (greater than ~14 seconds for Tests T-1 and T-7), the polycrystalline graphite entrance and pyrolytic graphite throat insert surfaces are expected to be above the melting point of BeO or Al_2O_3 . Therefore, the deposit mass flow in this region may be nearly constant and approximately equal to the deposit mass flow leaving the asbestos phenolic aft closure. Both gravity and liquid acceleration effects should eventually promote circumferential nonuniformities in the deposit profile. The edge grain,

CONFIDENTIAL

CONFIDENTIAL

pyrolytic graphite washers, will be effective in damping out circumferential variations in h_{eff} . However, any portion of the graphite surface which is exposed to the gas stream will suffer chemical attack. Elliptical erosion of the throat will be the result.

From Figures 15 and 16, it is seen that throat deposition is initiated earlier for the beryllium propellant than for the aluminum. For equal flame temperature, chamber pressures, and rocket motor configurations (gas side surface materials), this observation could be explained if (1) beryllia particle sizes in the chamber for propellant 191F are greater than the alumina particles of propellant 389, (2) the viscosity of liquid BeO is greater than that of liquid Al_2O_3 , or (3) beryllia may degrade the contour smoothness to the greater degree, promoting effectively higher axial deposit propagation rates.

The deviation between the predicted and measured P.G. backwall temperature of Figures 15 and 16 may be caused by (1) an error in the assumed thermal conductivity of liquid Al_2O_3 or BeO, (2) errors inherent in the semi-empirically determined convective heat transfer coefficient, (3) inaccuracies in the derived deposit thickness history, and (4) thermocouple errors.

The thermal response of the P.G. throat washer, for the Tests T-4 and T-5 (composite analogs) are presented in Figures 17 and 18, respectively. The transient throat deposit thickness for the beryllium firing exceeds that for the aluminum, as was observed in firing T-1 and T-7. The difference in BeO deposition, between Tests T-1 and T-4, and Al_2O_3 deposition, between Tests T-7 and T-5, can be attributed to the difference in flame temperatures (6170 and 6770 °R, respectively). As shown by the physical deposition model of Paragraph 2.5.d, higher flame temperatures will cause an increase in surface temperature levels (for comparable heat transfer coefficients). Therefore, less time is required to reach the deposit melting point, causing a decrease in the amount of deposit that will solidify. Although the deposit thickness is greater for the beryllium propellant (T-4) than its aluminum analog (T-5), the effect of the Al_2O_3 deposit on P.G. surface temperature is greater (lower Al_2O_3 thermal conductivity).

In firing T-4, a decrease in deposit throat thickness occurs at approximately 12 seconds. At this time, the deposit surface temperature is predicted to be 100°F below the melting point of BeO. As hypothesized by the physical deposition model, a decrease in local deposit thickness will occur only if a portion of the deposit liquifies. This indicates that (1) the convective heat transfer coefficient employed in the thermal analysis is low, (2) the transient deposit thickness is low, (3) the thermal conductivity of BeO is in error, and/or (4) there are phenomena not accounted for in the physical deposition model. From recently obtained data, the thermal conductivity of BeO was found to be 1.6×10^{-4} Btu/in.sec°F. In the thermal analysis of Test T-4, a BeO conductivity of 1.85×10^{-4} Btu/in.sec°F was employed. Therefore, the predicted BeO gas side surface temperature should be slightly

CONFIDENTIAL

CONFIDENTIAL

lower than may be expected if the revised conductivity is employed. For the aluminum propellant (T-5), the decrease in throat deposit thickness occurs after the deposit surface has reached the Al_2O_3 melting point. However, the time at which deposit removal is complete, corresponds to a P.G. surface temperature of 3200°F. As noted from the deposit thickness history, a very rapid decrease occurs at this time suggesting that the liquid deposit became unsatiable. The molten products of asbestos pyrolysis could also be important. It is doubtful that all of the deposit was actually removed at the time indicated by the deposit history since corrosion was in progress.

For comparison, the P.G. surface temperature was calculated (Tests T-4 and T-5) assuming that the BeO and Al_2O_3 deposit was not present. The no-deposit and deposit calculations employed the same convective heat transfer coefficient. The resulting differences in P.G. surface temperature is significant, with the maximum differences being 980 and 1300°F for BeO and Al_2O_3 , respectively. The effect of the deposit on the throat radial temperature profile is shown in Figure 19. From Figure 19, it can be seen that the deposit effect must be included in any structural analyses applied to the P.G. washer.

The thermal response of the throat washer for Tests T-3 and T-6 (Arcocel 319BRF and its 390 analog) are presented in Figures 20 and 21, respectively. As can be seen in Table IV, the T-3 and T-6 propellant combustion temperatures are less than T-1 and T-7 and greater than T-4 and T-5. Therefore, it is expected that the BeO and Al_2O_3 deposit thickness for T-3 and T-6 will be greater than T-1 and T-7, respectively. However, the deposit thickness of T-3 was less than T-1. This is probably due to the higher throat surface temperature on arrival of the deposit in Test T-3. The Al_2O_3 deposit thickness variation with combustion temperature correlates as expected. In firing T-6, a delay of 5 seconds in uniform propellant burning was encountered (see pressure trace of Figure 123); therefore, it is impossible to compare the times at which throat deposition was initiated for firings T-3 and T-6. The effect of the ignition delay on P.G. surface temperature for T-6 is shown in Figures 21 and 22. Figure 22 employed the trial 2 throat heat transfer coefficient given in Table VI over a firing time of 26.6 seconds. In Figure 21, the throat heat transfer coefficient of trial 1 was employed over a firing time of 21.6 seconds. Trial 1 neglects the 90 psi chamber pressure that prevailed for the first 5 seconds of firing.

The time at which a decrease in deposit thickness is encountered in T-3 is at the end of the firing. This decrease is almost instantaneous, suggesting that the chamber pressure decay and P.G. surface temperature were such that the carbide interlayer decomposed, causing the deposit to be blown off. This observation is confirmed to some extent by the movies. From Figure 21, the P.G. surface temperature was above the Al_2O_3 melting point at times when the throat deposit was present. Therefore, the variation in throat deposit thickness was not due to phase transformation of the deposit but to variation in the upstream deposit mass flow.

CONFIDENTIAL

CONFIDENTIAL

The throat thermal response for firing T-2 is shown in Figure 23. This beryllium propellant (24F) has a combustion temperature nearly equal to that in Tests T-4 and T-5. Therefore, the deposit thickness could be comparable to T-4. However, the deposit thicknesses were somewhat dissimilar. The graphite surface temperature at deposit arrival was apparently about 200°F lower in Test T-2 and T-4. At the time when the deposit thickness decreases in Test T-2 (16 seconds), the deposit gas side surface temperature is 110°F below the melting point of BeO. Also, the predicted P.G. backwall temperature is considerably lower than the measured. These observations suggest that the gas side connective heat transfer used in the thermal analysis was lower than the actual value.

The contact conductances between the P.G. backwall surface and the ATJ sleeve are presented in Table VII. These contact conductances are very important in the analysis of the backup insulation pyrolysis process.

During firing, the heat dissipated by ablation is insignificant in the thermal response of the polycrystalline graphite entrance and pyrolytic graphite throat insert (Reference 11). Also, the aft closure insulation boundary condition is difficult to determine due to the deposition phenomena encountered during firing. Therefore, during the second quarter, the thermal response of the insulation materials was not determined. However, some interesting conclusions can be obtained from the aft closure, entrance, and throat insert photographs of Paragraph 3.4.a, and the thermocouple data of Paragraph 2.5.e. From the photographs of Paragraph 3.4.a, a significant variation in pyrolysis zone thickness exists between the aft closure gas side and entrance-throat insert backup reinforced plastic. The thin pyrolysis zone in the aft closure region indicates very little heat soak time in the low temperature region during the cooldown period. When the plastic is employed as a heat sink backup insulator, the heat stored in the heat sink is primarily dissipated by ablation. Therefore, the time that the pyrolysis zone is at low decomposition temperatures is significantly longer than that for the aft closure. The heat dissipated by ablation in aft closure consists primarily of heat stored in the char and remaining deposit.

From the thermocouple responses of Paragraph 2.5.e, it is noted that at the time of shutdown a significant decrease in thermocouple temperature is experienced. This phenomenon was also experienced during Contract AF 04(611)-9904. The explanation is that cooling of the thermocouple tip occurs as the stored pyrolysis gases depressurize during shutdown.

2.6 (C) CONCLUSIONS, RECOMMENDATIONS AND FUTURE WORK

a. (C) Conclusions

The results of the initial program motor tests were sufficiently complicated to preclude any final conclusions. Several of the most probable conclusions are given below.

CONFIDENTIAL

CONFIDENTIAL

- (1) The behavior of beryllium propellants does not generally compare with that of aluminum propellants because of significant differences in the deposition and metal combustion mechanics. Deposition tends to magnify material's thermal behavior differences while providing corrosion protection. Without deposition, poor beryllium propellant combustion tends to magnify the apparent corrosivity of the exhaust. The coupling of propellant burn rate properties with throat deposition tends to accentuate otherwise minor differences among beryllium propellants.
- (2) Propellant materials selection criteria, based on idealized propellant performance characteristics, may be valid only when deposition and combustion problems can be neglected. Low delivered performance and poor nozzle performance should be closely related.
- (3) The accurate prediction and interpretation of heat transfer and corrosion are contingent upon the characterization the exhaust composition and the deposit thickness history. In addition, the propellant burn rate dependence on pressure, propellant burn area, and oxide deposit thermal properties must be known.
- (4) The thermal measurements from Tests T-1 through T-7 provide qualitative support to the theoretical corrosion model and to the deposit thickness histories derived from the ballistic data. The gas side heat transfer coefficients appear to be related to C-star performance. These coefficients are in fairly good agreement with the results of the advanced boundary layer theory prediction.
- (5) The analysis of the motor performance for the remote end burning grain tests indicates that complete beryllium propellant combustion may not have been achieved as planned. According to the qualitative combustion model, this could have occurred if the small number of the largest particles (35 to 50 microns) failed to ignite in the low velocity chamber flow. Such unburned particles could have easily escaped detection in the post test analysis of the hardware and exhaust samples.

CONFIDENTIAL

CONFIDENTIAL

- (6) The thermal instrumentation appears to have provided very high quality data. However, the edge grain pyrolytic graphite washers tend to average out circumferential variations in heat flux due to nonuniform oxide deposition. Some axial averaging of the heat flux is also thought to occur. These factors reduce the degree to which the thermocouples can resolve thermal and chemical events occurring along the contour.

b. (U) Recommendations

The development of analytical heat transfer, corrosion and deposition techniques has not progressed enough to warrant unqualified recommendation of their use. The combination of deposition and propellant combustion phenomena continues to provide the best source of materials problems with beryllium propellants. It is recommended that these factors be carefully examined in other test programs. More consideration should be given to these factors in the selection of propellants and materials in the advanced hardware design stage.

c. (U) Future Work

During the remainder of the program, the major analytical effort will be devoted to the reduction of the motor test thermal data and comparison of the results with theory. Emphasis will be placed on the heat transfer, corrosion, deposition, and metal combustion prediction problems. The analytical studies will be coordinated more extensively with the data correlation studies.

CONFIDENTIAL

SECTION III (C)

LABORATORY STUDIES

3.1 (U) OBJECTIVES, SCOPE AND SUMMARY

a. Objectives

The objectives of the laboratory studies were described in detail in the First Quarterly Progress Report, Reference 1. These have not changed during the present reporting period. During this period, the objectives of the effort were limited to: (1) completion of the condensed phase reaction studies, (2) continued interpretation of the cold flow modeling results, (3) specification of the post-test analysis procedures, and (4) completion of the post-test analysis of the hardware, deposits, and exhaust particle samples from the first seven motor tests.

b. Scope

Reference 1 describes the initial, overall scope of the laboratory studies phase of the program. It has been necessary to reduce the scope of the arc plasma impaction and deposition studies. While the initial graphite surface temperatures could be varied as planned, it was not possible to control the subsequent thermal state of the samples during impaction. In general, extensive deposit buildup was experienced in these experiments. The rapid change in the apparent impingement surface angle led to the abandonment of the effort to evaluate deposition character as a function of impact angle. With respect to the post-test analysis of hardware from other programs, efforts will be made to obtain Aerojet (ADOBE), Thiokol, and Atlantic Research hardware in addition to the NOTS nozzles discussed in this report. It is expected that some emphasis will be given to studying nozzles which

featured the use of tungsten inserts. Finally, an effort is being made to augment the cold flow modeling study results from this program with those from another program currently in progress at Aeronutronic.

c. Summary of Progress

The objectives of the laboratory studies during the second reporting period have been attained. The following elements of work have been completed or are in progress as indicated.

- (1) The survey of the beryllium-carbon-tungsten-nitrogen system has been completed.
- (2) The arc plasma impaction and deposition studies have been completed.
- (3) The post-test analysis of the hardware and condensed phase deposits has been completed for the first seven motor tests.
- (4) The post-test analysis of the hardware from a NOTS program has been completed.
- (5) The post-test analysis of the hardware from the internal burning grain tests is in progress.
- (6) An effort to relate cold flow modeling test results from two programs is in progress.

3.2 (U) CONDENSED PHASE REACTION STUDIES

a. Interaction of Beryllium Compounds With Graphite and Tungsten

The results of this phase of the laboratory studies have been reported in Reference 1. This study was concerned with the condensed phase reactions of BeO and Be_3N_2 with graphite and tungsten.

b. Survey For Low Melting Compounds

An experimental survey of the Be-W, Be-N-W, and the Be-C-N systems has been completed. These experiments involved the heating of samples of the appropriate composition to a predetermined temperature for a given period of time. The samples were cooled and subsequently examined by x-ray diffraction to identify all phases present.

(1) Procedure

The raw materials used were in the form of -325 mesh powders except for the tungsten which was pressing powder with an average particle size in the range of 2 to 4 microns. There were no impurities in the tungsten powder which could be detected by X-ray diffraction. The main impurity in the beryllium compounds was beryllium oxide. All beryllium compounds had 4 to 10 percent beryllium oxide content. The powders were weighed to 50 atomic percent of each compound and mixed with a mortar and pestle in an argon atmosphere in a dry box. Each mixture was loaded into a one-inch diameter polyethelyne tube and isostatically pressed at 15,000 psi. This pressure was sufficient to produce a compact with sufficient strength to permit handling without the use of a binder. The compacted powders were then returned to the dry box where they were cut into cubes, approximately 1/2 inch on a side. This was the sample which was used for the reaction studies.

The samples were removed from the dry box and placed in a vacuum bell jar. The samples which contained tungsten were placed on a piece of sheet tungsten and the samples which contained carbon were supported by a piece of graphite. The samples were heated by an inductively-heated graphite susceptor. Temperatures were measured with a micro-optical pyrometer which was focused directly on the sample through a hole in the susceptor. The tests which were run in a vacuum were made at pressures lower than 10^{-4} torr. The tests which were run in an atmosphere were made at a pressure of approximately 1/2 atmosphere. These tests were run by evacuating the chamber and back-filling with regular bottled gas.

(2) Experimental Results

The experimental results are summarized in Table VIII. They do not disclose any previously unknown or unexpected results. Two beryllium-tungsten alloys (WBe_2 and WBe_{12}) were found. Although these alloys have previously been reported (References 13, 14), they have not been extensively examined and many properties are unknown. The results tend to confirm the existence of the WBe_{12} alloy with a melting point in the region of 1250 to 1300°C. This compound would precipitate surface melting of tungsten inserts when beryllium metal comes in contact with the insert. The WBe_2 alloy apparently has a much higher melting point. Unfortunately, no information is available on the melting point. The Be-W system is very similar to the Be-Mo system, in which phases of the same composition are formed. The $MoBe_2$ phase has a melting point some 400°C above the liquidus temperature of the $MoBe_{12}$ phase. It would be expected that the WBe_2 phase would be more refractory than the WBe_{12} phase, probably by approximately 400°C.

TABLE VIII
RESULTS OF LOW MELTING COMPOUND SURVEY

<u>Initial Mixture</u>	<u>Atmosphere</u>	<u>Temperature (°C)</u>	<u>Reaction Time (Minutes)</u>	<u>Final Composition</u>
Be and W	Vacuum	1200	30	Sample very soft, no sintering Be + W.
Be and W	Vacuum	1250	30	Sample very soft, no sintering Be + W.
Be and W	Vacuum	1300	30	Sample well sintered, some melting observed with microscope W, WBe ₂ , WBe ₁₂ .
Be and W	1/2 N ₂	1300	30	Some melting observed, sample sintered W, WBe ₂ , WBe ₁₂ .
Be ₃ N ₂ -W	Vacuum	1500	30	Sample very soft, no sintering W, Be ₃ N ₂ , low BeO.
Be ₃ N ₂ -W	1/2 A	1800	30	Sample fairly well sintered W, β-Be ₃ N ₂ , low BeO.
Be ₃ N ₂ -W	1/2 A	2100	30	Sample quite hard, well sintered W, no Be compounds.
Be ₃ N ₂ -Be ₂ C	1/2 A	1800	30	Sample well sintered, considerable loss of part of sample, sample is brown in color. Be ₂ C, low Be ₃ N ₂ , BeO, very low β-Be.
Be ₃ N ₂ -Be ₂ C	1/2 A	2100	30	Sample quite hard, well sintered, lost considerable weight, sample is brown in color. Be ₂ C, low BeO, very low β-Be ₃ N ₂ and β-Be.
Be ₂ C-W	Vacuum	1300	30	No change in sample, no sintering W 60-70, α-W ₂ C 10-15, Be ₂ C 5-10, W ₃ O 5-10.
Be ₂ C-W	Vacuum	1700	30	No visible change in sample, no sintering. α-W ₂ C 50-60, W 30-40, WC 5-10, Be ₂ C 2-5, W ₃ O 2-5, W ₃ O 2-5.
Be ₂ C-Be	Vacuum	1300	30	No visible change in sample Be ₂ C 70-80, 10-15 BeO, α-Be 10-15, β-Be 3-6.
Be ₂ C-Be	Vacuum	1700	30	Considerable change in sample, color changed from light brown to dark gray. Be ₂ C 75-85, BeO 20-25.
Be ₂ C-Be	Vacuum	2100	5	Run terminated because of large amount of out gassing. Be ₂ C 80-90, BeO 10-15.

There were no nitrides formed when Be and W were heated in nitrogen at 1300°C. There were no new compounds formed between Be_3N_2 and W, Be_3N_2 and Be, or Be_2C and Be.

All samples made showed considerable loss of beryllium at the higher temperatures tested. This is due to the increased vapor pressure of the beryllium and its direct loss through vaporization. The BeO detected was the result of some oxygen impurity in the argon test gas and the BeO impurity in the raw materials.

The Be_2C -W system produced two new compounds, W_2C and WC, which would probably not lead to any problems with tungsten inserts. Formation of these compounds would be very detrimental to a tungsten insert but there would be little likelihood that the carbides would be formed via reaction with Be_2C . That is, if Be_2C were present as an exhaust product, there would be enough carbon available in the exhaust stream to form the tungsten carbides directly.

3.3 (C) CONDENSED PHASE IMPACTION AND DEPOSITION

a. (U) Arc Plasma Studies

The arc plasma studies of condensed phase accumulation and removal have been completed. During this reporting period, the alumina impingement results (Reference 1) were extended to asbestos phenolic. The beryllia impingement on asbestos phenolic and graphite was also studied. For all tests, the effluent argon gas from the Plasmadyne SG-1 arc jet, with the entrained oxide, was directed to give 45 degree impingement on the test specimen. The stagnation pressure on the model was approximately one atmosphere to accommodate the arc jet design and the safety precautions required when operating with beryllia entrainment.

Secondary heating of the specimen, by other than arc jet impingement, was not employed in the testing. A consequence of this was a decrease in specimen temperature, from the preheat level, once oxide powder entrainment was initiated. This decrease varies markedly with the particular oxide. The lower thermal conductivity and more extensive deposition of the alumina resulted in the greater test specimen temperature decrease. A second marked difference was noted between beryllia and alumina impingement on both graphite and asbestos phenolic. Whereas the alumina would stick and continue to build up on either substrate, the beryllia would only partially stick (graphite) or build up only to a limited thickness (asbestos phenolic).

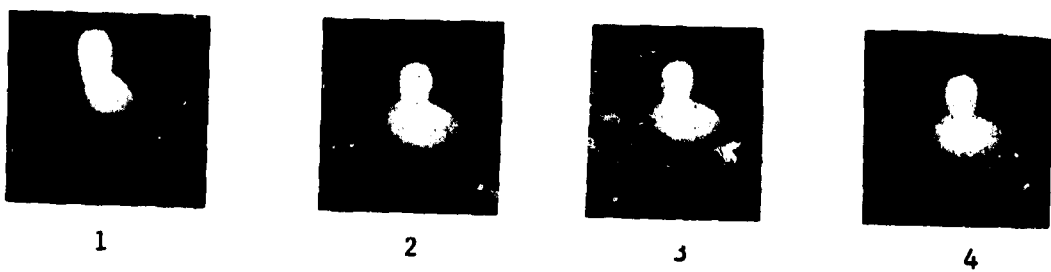
The alumina impingement on graphite resulted in sticking when the graphite surface temperature was below about 2000°C (3600°F). Above this initial surface temperature, the alumina reflected from the surface. As expected, the net heat transfer to the oxide coated graphite was not adequate to maintain a high temperature for more than about 15 seconds. Once the alumina started to stick, the graphite surface temperature was reduced due to the thermal imbalance between the graphite sample radiation losses (uncoated surfaces) and the conduction through the insulating oxide layer. The surface of the thick deposits melted, permitting considerable overflow of alumina.

The analysis of the adhering deposit revealed a combination of alumina carbide and α alumina for initial sample surface temperatures above about 1500°C (2700°F). Below this temperature, reduced amounts of Al_4C_3 were observed and the alumina shifted toward the γ phase as the temperature was further reduced. Figure 24A shows the typical time lapse appearance of the specimen. Frame 10 shows another view of a test to more clearly indicate the relative position of the arc jet gas and the specimen. It should be noted that as the alumina is building up, there is some run off of molten alumina with low Al_4C_3 content relative to the underlying material.

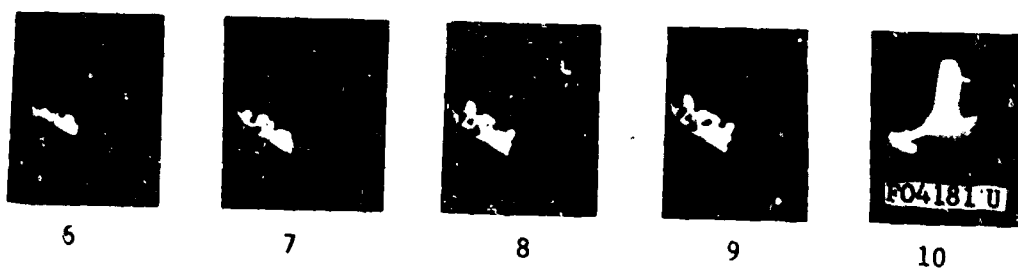
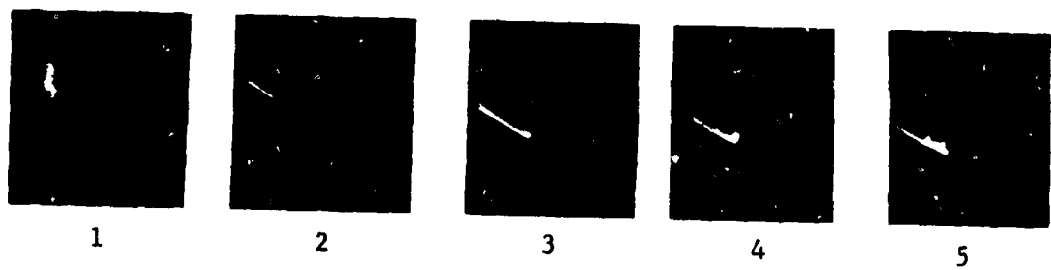
In contrast, the beryllia tended to stick on the graphite only very slightly (see Figure 24B). The analysis of the deposit revealed nothing other than beryllia, suggesting that the adherence in this experiment was primarily by mechanical means. No beryllium carbide was found as a counterpart to the aluminum carbide. The surface temperature of the graphite did not drop as far during the beryllia impingement and appeared to reach a near stable value of about 2200°C (4000°F) when the beryllia buildup stopped.

For impingement on asbestos phenolic, each oxide was rejected for a short time corresponding to approximately that required to develop a stable char layer. Once the char has formed, the oxides would stick. Typical sticking sequences are shown for alumina in Figure 25 and beryllia in Figure 26. In both cases, a similar pattern was noted; that is, the oxide appeared to stick predominately in the magnesium silicate liquid. Whereas the beryllium resulted in a mixture of beryllia and magnesium silicate, the alumina formed magnesium aluminate and magnesium silicate over the general range of compositions and mixtures. Once again, the alumina deposit could be built up to a considerable thickness in comparison with the beryllia deposit.

The overall results of the testing indicate that the alumina was sticking, at least in part, as a result of chemical bonding with new aluminum compounds formed. This chemical combination sticking was not observed



A-BERYLLIA



B-ALUMINA

FIGURE 24. TIME LAPSE SEQUENCE OF OXIDE IMPINGEMENT ON ATJ GRAPHITE - SURFACE 45 DEGREES TO STREAM

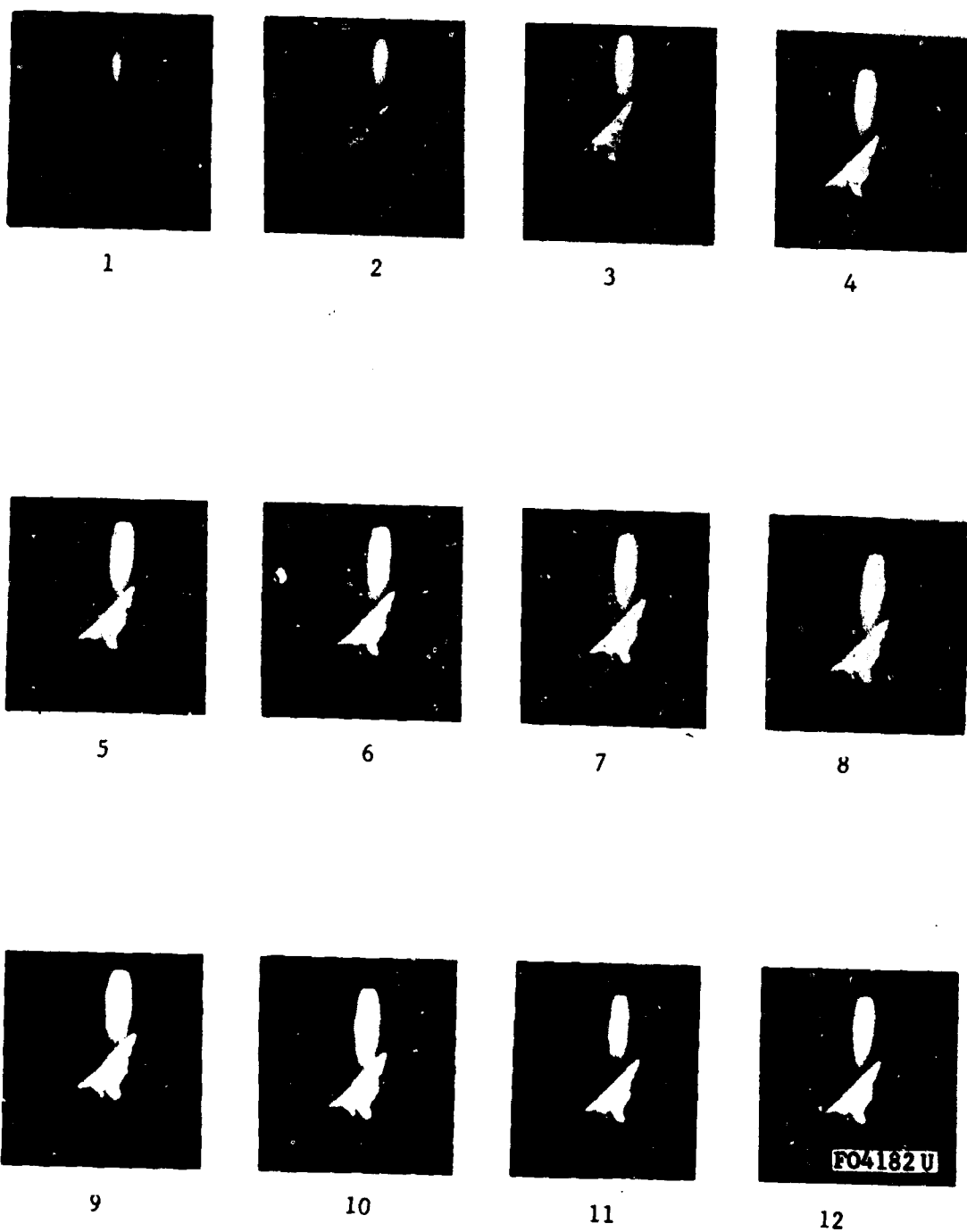


FIGURE 25. TIME LAPSE SEQUENCE OF ALUMINA IMPINGEMENT ON ASBESTOS PHENOLIC - 1.0 SECOND BETWEEN FRAMES - SURFACE 45 DEGREES TO STREAM

CONFIDENTIAL



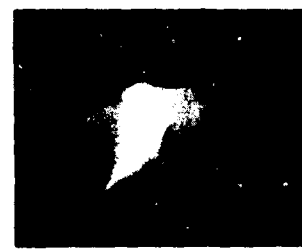
1



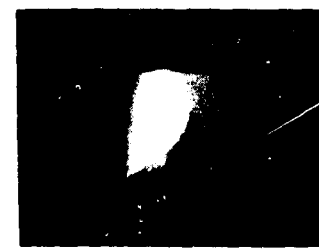
2



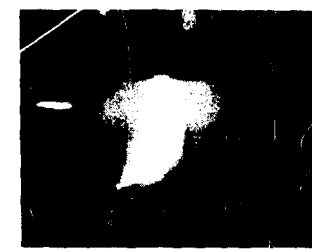
3



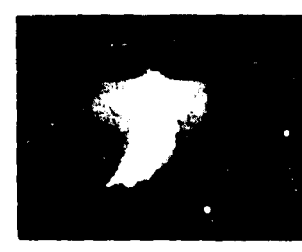
4



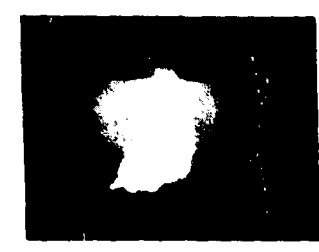
5



6



7



8



9

FIGURE 26. TIME LAFSE SEQUENCE OF BERYLLIA IMPINGEMENT ON ASBESTOS PHENOLIC - 1.0 SECOND BETWEEN FRAMES - SURFACE 45 DEGREES TO STREAM

-93-

CONFIDENTIAL

THIS PAGE IS UNCLASSIFIED

CONFIDENTIAL

with beryllium. The general behavior of the beryllia impaction on graphite appears to be reasonable in light of the experimental results presented in Paragraph 3.2a of Reference 1. That is, at the experimental pressure and at temperatures above about 2200°C, the carbides of beryllium are unstable. Thus, the carbon monoxide gas and beryllium vapor produced when the impinging liquid beryllia reacts with graphite will drive the particles off the surface. Some mechanical sticking undoubtedly occurs, leaving a fused deposit. This type of deposit could easily be removed due to its inability to resist the subsequent impact stresses. This behavior should not be characteristic of higher pressure conditions where the beryllium carbide may persist up to at least the melting point of BeO.

For the present, testing has been discontinued because the pressure regime for expected beryllium chemical sticking is above the range of the arc jet. Further arc jet tests will be performed only if the motor firing data result in an anomalous behavior which appears amenable to controlled experimentation using this particular type of testing.

b. (C) Cold Flow Modeling

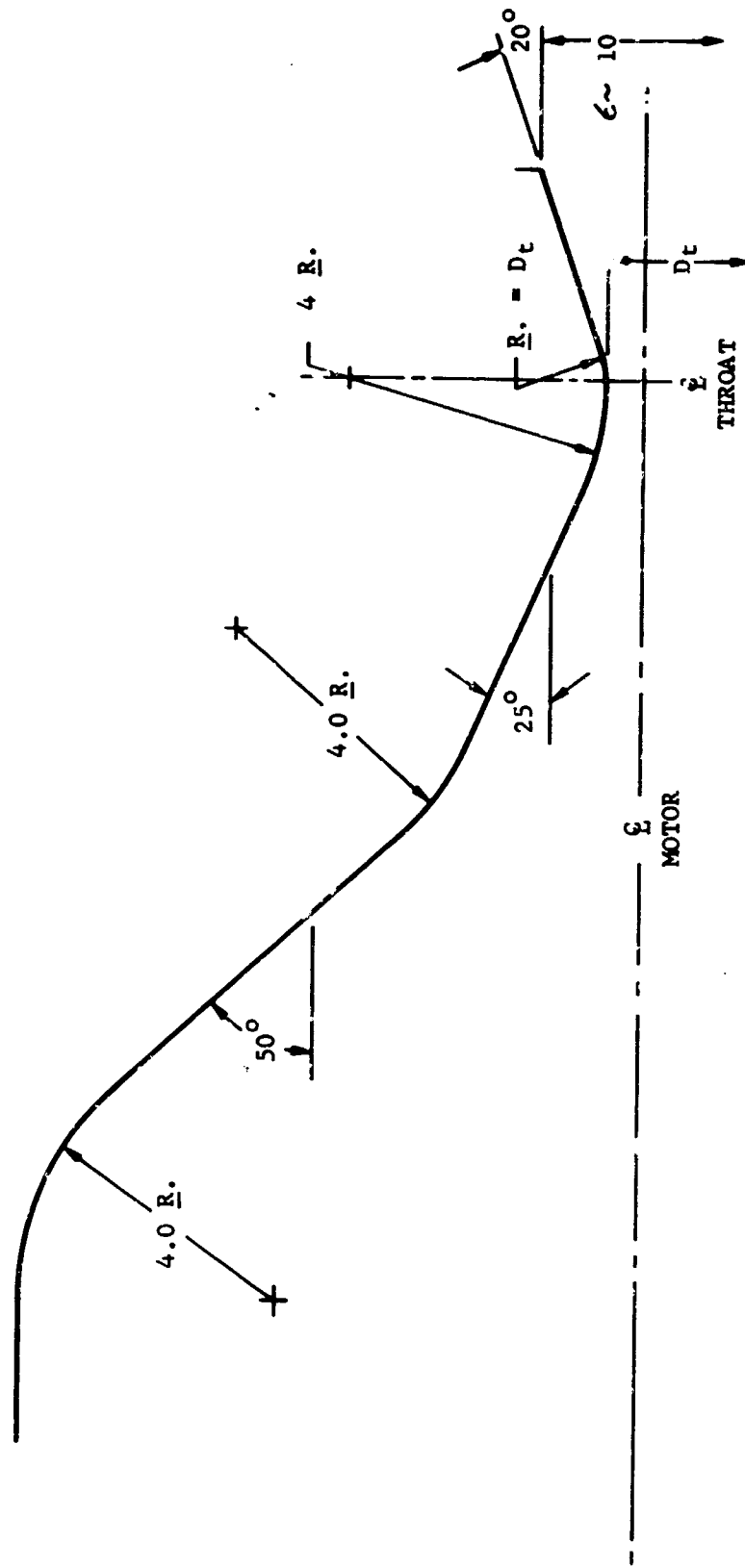
To aid in the understanding of particle impingement and in the development of a physical and analytical model for the deposition phenomena, the behavior of condensed phases in representative rocket motor flow fields has been examined by cold flow modeling. The results of the modeling study were presented in Paragraph 3.3b of Reference 1. Subsequently, several rocket motors have been fired and the deposition results have been compared with the modeling results. Also, during the second reporting period, the cold flow modeling techniques developed in this program have been applied in another contract (NASA Contract No. NAS 7-408). The results obtained from work on the NASA contract provide additional understanding of the mechanisms of condensed phase behavior. A discussion of the applicability of the cold flow test results to the rocket motor firings and selected results from the NASA contract is contained in the following paragraphs.

(1) (C) Application of Modeling Results to Motor Firings.

The motor configuration fired during the period consisted of remotely located end burning grain with a "conventional" nozzle contour (Figure 27). In the cold flow studies, this configuration was modeled to establish the magnitude and axial profile of particle impingement. The conditions and parameters, modeled in the cold flow, that affect impingement for the end burner-conventional nozzle configuration are presented in Table IX. Also presented in Table IX are the conditions and parameters that were representative of the motor firings.

CONFIDENTIAL

CONFIDENTIAL



FO4048 U

FIGURE 27. MOTOR-NOZZLE CONTOUR FOR REMOTE END BURNER TESTS

CONFIDENTIAL

THIS PAGE IS UNCLASSIFIED

CONFIDENTIAL

TABLE IX

COLD FLOW MODELING AND ROCKET MOTOR IMPINGEMENT PARAMETERS
FOR THE END BURNER-CONVENTIONAL NOZZLE CONTOUR

<u>Parameter</u>	<u>Cold Flow (Modeled Rocket Motor Parameter)</u>	<u>Rocket Motor (Beryllium Propellant)</u>
Particle Size (microns)	0-12	~ 1-6
Chamber Area Ratio	30.2	~ 360
Chamber Velocity (ft/sec)	72	~ 6
Aft Closure Angle (degrees)	47	50
Chamber Pressure (psia)	800	700 to 1200
Entrance and Aft Closure Gas Side Surface Condition	Smooth	Rough

The cold flow impingement results for the configuration of Table IX are presented in Figure 28. (Figure 28 is a reproduction of the 0 to 4.8μ and 4.8 to 12μ particle impingement data presented in Figure 30 of Reference 1). From Figure 28, it can be seen that impingement occurs only in the aft closure region (47 degree inlet section). For the beryllium propellants employed in this program, the propellant weight was 100 pounds with approximately 35 pounds of condensed BeO present in the combustion products. For present purposes, it is assumed that all the particles which impact remain at the corresponding impingement location (i.e., do not re-enter the boundary layer or melt and flow downstream). With this assumption, the deposition thickness at the end of firing is shown in Figure 29 as a function of the weight percent of particles in the 0 to 4.8μ and 4.8 to 12μ size range. Figure 29 was constructed using the impingement magnitude as given in Figure 29.

In applying the impingement profiles of Figure 28 and the deposition thickness of Figure 29, the following parameters must be considered:

- (1) Effect of chamber velocity on impingement.
- (2) Effect of aft-closure contour length on impingement location.
- (3) Effect of irregularities in contour due to deposit buildup on impingement magnitude and location.

CONFIDENTIAL

CONFIDENTIAL

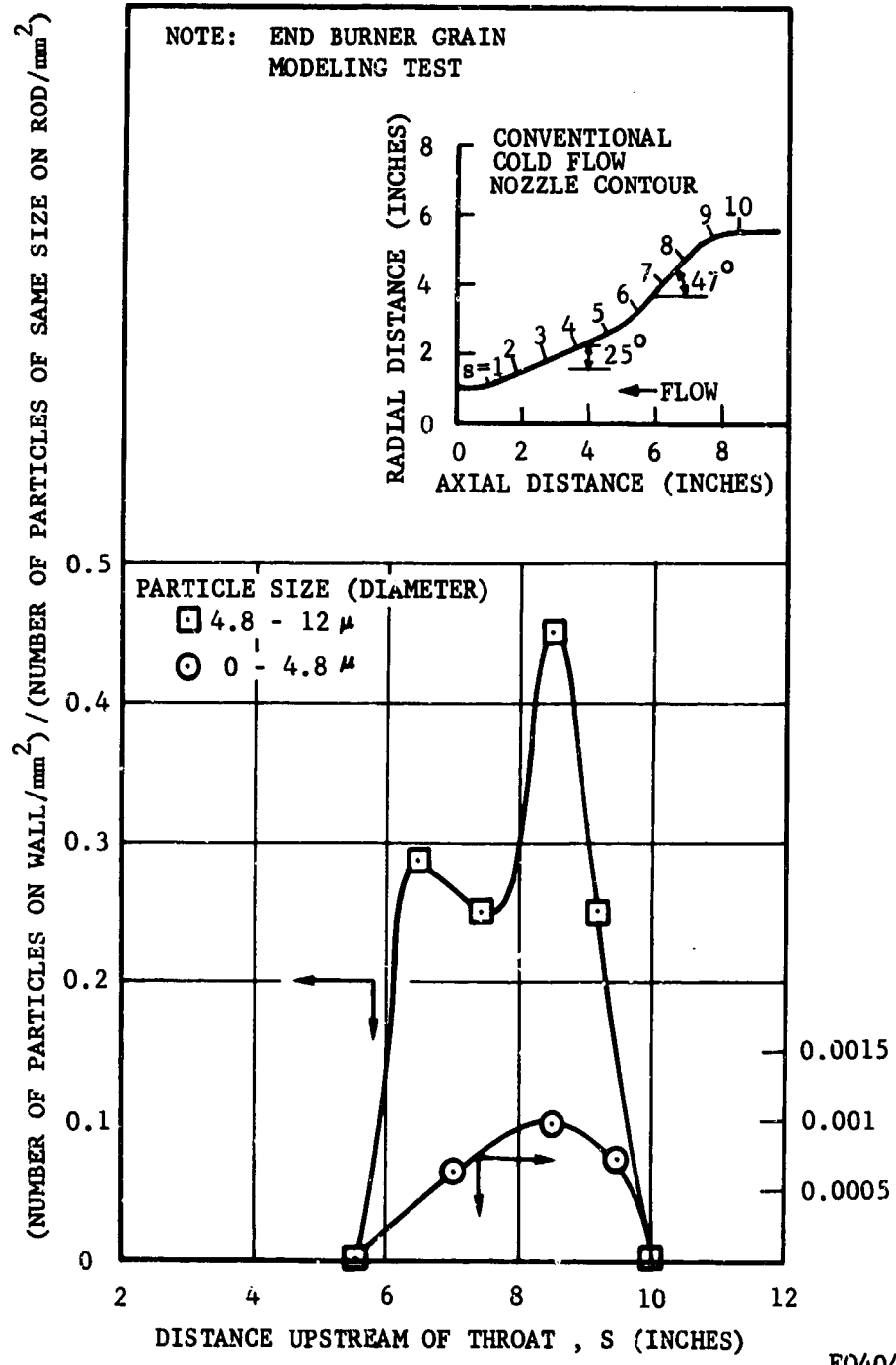


FIGURE 28. EFFECT OF PARTICLE SIZE ON WALL IMPINGEMENT FOR CONVENTIONAL NOZZLE CONTOUR

CONFIDENTIAL

CONFIDENTIAL

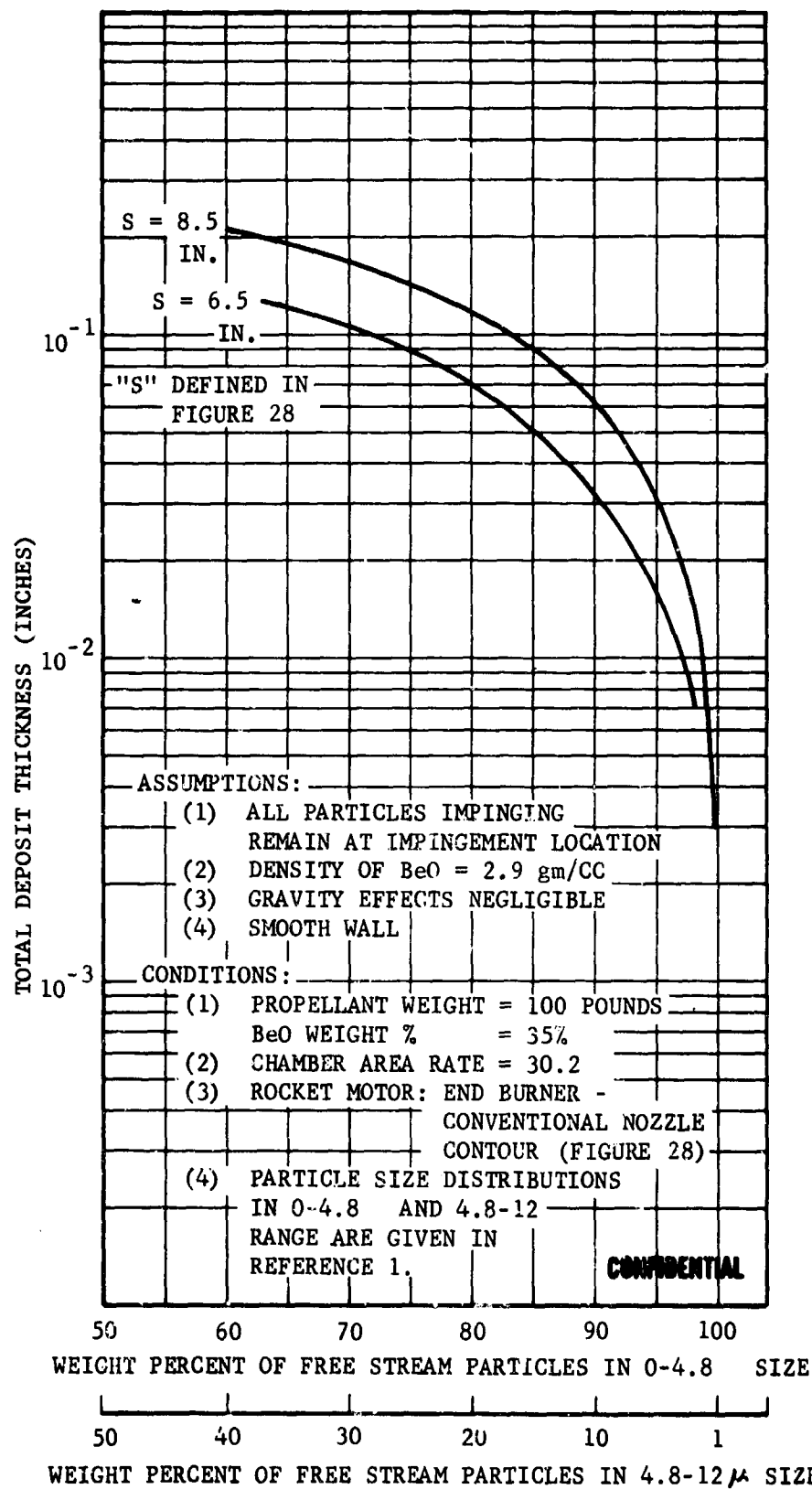


FIGURE 29. DEPENDENCE OF TOTAL DEPOSIT THICKNESS ON FREE STREAM BeO PARTICLE SIZE RANGE

CONFIDENTIAL

FO4050 C

CONFIDENTIAL

The effect of chamber velocity on impingement is two-fold. That is, as shown in Paragraph 3.3b of Reference 1, decreasing chamber velocity will decrease the impingement rate and increase the importance of the gravitational effect. In Figures 55 and 60, the relative importance of gravity on the deposition phenomena is evident (non-uniform deposit in circumferential direction). For the cold flow conventional nozzle contour, the axial surface length of the 47 degree aft closure is considerably less than that of the actual rocket motor. Therefore, the impingement location is not accurately determined from Figure 28. Also, as shown in Figures 55 and 60, the post test condition of the deposit is of the droplet or bead type. As reported in Reference 1 the effect of this type of deposit will increase impingement and, as a result, the deposition rates.

The post test deposit thickness in the aft closure section of the beryllium motors was measured to be 0.04 to 0.08 inch on the top and 0.05 to 0.10 inch on the bottom (horizontal firing). The thickness was nearly uniform in the axial direction of the aft closure. Using these measurements and entering Figure 29, it is found that the particles in the 0 to 4.8 size range represent 75 to 92 percent of the total condensed BeO weight. However, as stated above, the chamber velocity, gravitational force, discontinuity in contour, aft closure lengths, mass loss via flow to and through the nozzle, and total mass storage of impinged particles during firing and soak must be considered in using Figure 29. Nevertheless, the size distribution for BeO estimated in this manner appears to be reasonable with respect to the exhaust particle sampling results (Paragraph 3.4).

From Figure 28, it can be concluded that in the motor firings the impingement rate is small and will occur initially in the 47 degree aft closure section. From Figures 38 and 44, the aft closure char thickness is shown to be uniform in the axial direction. Also, from post-test analysis, no measurable surface regression was experienced during firing. These observations suggest that the initial impingement rate was at such a low value that no significant increase in heating or mechanical erosion due to impingement was encountered. However, the thermal and erosion protection provided to the char by the deposit may obscure any effects of higher initial impingement heating. Such effects were observed in the plasma studies (Paragraph 3.3a).

(2) (U) NASA Contract Modeling Study

Work has recently been completed in a cold flow study of the particle impingement and wall-gas shear gradients for the 156-2C rocket motor nozzle. This work was performed under Contract NAS 7-408, "Prediction of Three Million Pound Thrust Nozzle Insulation Performance." The motor

CONFIDENTIAL

CONFIDENTIAL

being studied is a 156 inch diameter solid booster with a six-pointed star grain and an unfilled aft closure. It is interesting to compare the results of this work with the beryllium propellant motor cold flow work. Also, a number of improvements in technique were made in the course of the NASA work which are relevant to the overall cold flow capabilities and methods evaluation.

In the NASA study, the model grains were designed with a gradually tapered upstream entrance to the grain port (Figure 30). This produced a more uniform particle distributed across the grain port. Ahead of that, a section of honeycomb was installed to reduce turbulence in the flow approaching the model. Gas-wall shear patterns were developed using grease coatings on the nozzle. The magnitude of local gas-wall shear would be inversely proportional to thickness of the remaining grease film after a test. In this work, only the polyethylene particles in the size range of 3.3 to 6.6 were counted and evaluated for particle impingement rate.

Table X compares the test conditions and impingement results of one test from each program. The particular tests have two features in common, namely, grain port shape and grain port velocity. Figures 31 and 32 show the grain shape for the zero and 20-second burn times modeled, looking upstream. In both cases, the peak impingement on the nozzle is directly in line with the grain star valley, indicating a zero angle of dividing streamline deflection. The grease on the grain models is a consequence of the recirculation flow which transported it from the nozzle inlet surfaces.

The grease smear patterns developed on the NASA nozzle are shown in Figures 33 and 34 for the zero and 20-second burn times, respectively. These data will be very useful in the convective heat transfer analysis since they show (1) precisely where the boundary layer growth begins, and (2) the areas of high and low shear which will inevitably be the areas of high and low heating rate and high and low ablation rate. The numbers on Figures 33 and 34 represent the peak value of impingement in lb/in.²/sec, along the lines. The length of the lines represents the contour length over which significant impingement occurred.

Analysis of the NASA cold flow modeling data produced a number of indications about the nature of the two-phase flow and the resulting wall impingement rates, for the nozzle studies, as follows:

- (1) Particle impingement occurs more in the gas recirculation regions and more so at lower grain port velocities.
- (2) The equivalent of a 1.6-inch layer of alumina hit the wall every second at the points of weak impingement. Another way

CONFIDENTIAL

THIS PAGE IS UNCLASSIFIED

FIGURE 30. NASA MODELING STUDY HARDWARE



FE4032 0

FIGURE 31. NASA STUDY - GRAIN FORT SHAPE AND GREASE SHEAR PATTERNS -
ZERO BURN TIME





FIGURE 32. NASA STUDY - GRAIN PORT SHAPE AND GREASE SHEAR PATTERNS -
20 SECOND BURN TIME



FIGURE 33. NASA STUDY - GREASE SHEAR AND STAGNATION PATTERN - ZERO
BURN TIME

FIGURE 34. NASA STUDY - GREASE SHEAR AND STAGNATION PATTERN -
20 SECOND BURN TIME



TABLE X
PARTICLE IMPINGEMENT COMPARISON OF Be AND NASA
NOZZLES WITH STAR GRAIN PORT

<u>Parameter</u>	<u>Be</u>	<u>NASA</u>
Grain/throat Area Ratio	1.71	1.70
Model Throat Diameter, inches	2.0	2.6
Distance along Nozzle Wall from Grain to Throat, inches	2.3	0.77
P_c , psia	65	54 and 69
Entrance Wall Angle to Axis	47 degrees	45 degrees
Grain Star Points	6	6
Mean Angle of Dividing Stream Line Deflection	0	0
Particles on Wall/Particles on Rod at Maximum Impingement Point		
0-10 μ	2.0	
3.3 - 6.6 μ		0.5
10 - 25 μ	0.55	

CONFIDENTIAL

of describing this would be that the equivalent of five complete layers of 13-micron particles hit the wall per millisecond.

- (3) Only a small fraction of the total wall exposed was subjected to impingement at any moment.
- (4) The potential heat flux from impinged particles is of the same order of magnitude as the convective heat flux. While this potential is not nearly reached (probably because particles bounce off the wall or off each other without coming to thermal equilibrium with the wall), it is a large enough factor that it should be accounted for in any complete heat flux and ablation analysis.

CONFIDENTIAL

THIS PAGE IS UNCLASSIFIED

CONFIDENTIAL

3.4 (C) POST TEST ANALYSIS

a. (C) Analysis of Motor Hardware

(1) (C) Current Program Hardware

The hardware from the first seven tests has been received and examined. The general procedure followed in the post test examination is given in Paragraph 3.4c. The results of the examination are given separately for each motor tested.

(a) (C) Motor Test T-1

Photographs of the nozzle entrance and nozzle exit sections in the "as received" condition are shown in Figures 35 and 36, respectively. A cross section of the nozzle is shown in Figure 37. There was no significant loss of material or excessive erosion experienced in this test. However, two pyrolytic graphite washers furthest upstream were delaminated. Figure 38 shows a cross section of the aft closure. This shows the uniform charring of the asbestos-phenolic insulator, and there were no areas where any grooving or excessive melting were observed. Figure 39 shows a section of the asbestos-phenolic entrance insulation where the expected axial variation in char thickness can be seen.

A series of deposit samples was taken from the hardware and examined. The results are given in Table XI. The deposits were not unusual as would be expected. The aft closure was thoroughly coated with BeO. There was some evidence of reaction of the BeO with the aft closure from the presence of Be₂C, but there were no beryllium/silicon compounds found. The MgO and Mg₂SiO₄ compounds are decomposition products of the asbestos. There was some aft closure material transported downstream onto the ATJ entrance cone in the form of MgO and Mg₂SiO₄. These compounds may have been transported either through melted material flow or vapor phase transport. There was essentially no BeO on the pyrolytic graphite throat washers. The deposits which were found in the throat area were fine fluffy powders which were identified as amorphous carbon. This was formed from the pyrolysis gases after the termination of the test. The ATJ exit cone was fairly well coated with BeO; however, there was not any Be₂C found.

The area upstream of the pyrolytic graphite throat washers was examined. This area was filled with RTV rubber for a spacer to allow for thermal expansion. The RTV rubber was completely charred and it appeared that the char was hard and approximately 0.06 inch thick. There was some BeO present in the spacer gap near the graphite flame front surface, indicating that some exhaust gases passed through the gap.

CONFIDENTIAL

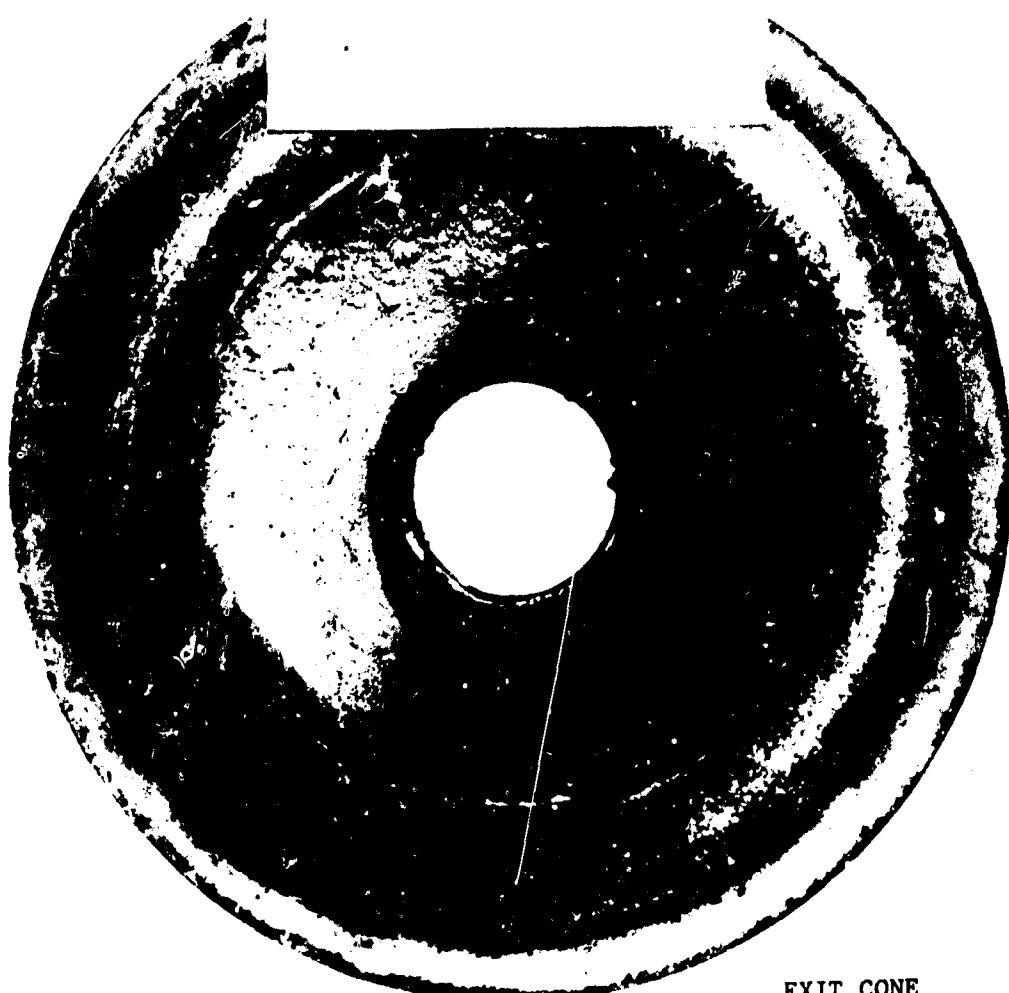
CONFIDENTIAL



FIGURE 35. NOZZLE FROM TEST T-1 - ENTRANCE CONE VIEW

CONFIDENTIAL

CONFIDENTIAL



EXIT CONE
TEST #C-1
PROPELLANT - 191P
CONFIDENTIAL FO4057C

FIGURE 36. NOZZLE FROM TEST T-1 - EXIT CONE VIEW

CONFIDENTIAL

CONFIDENTIAL

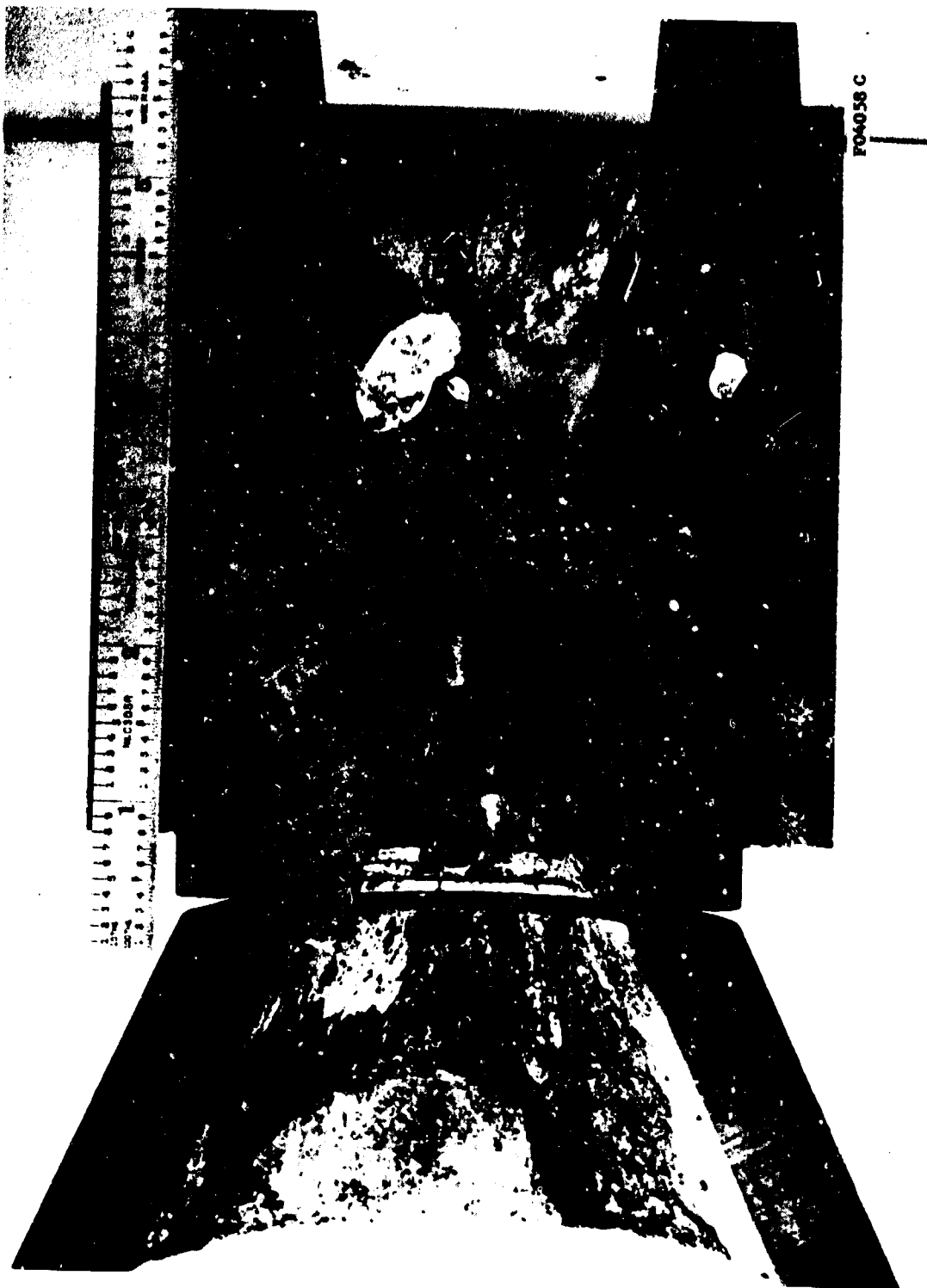
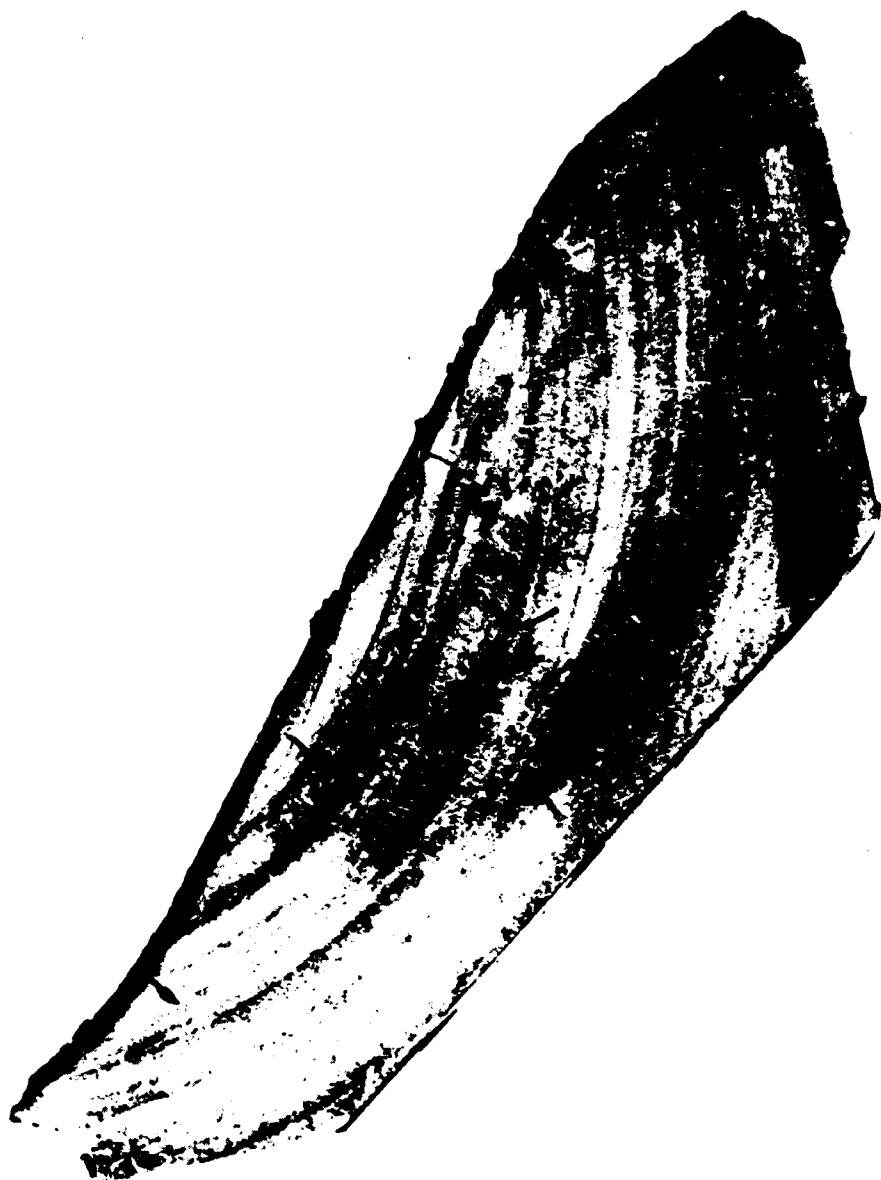


FIGURE 37. NOZZLE FROM TEST T-1 - CROSS SECTION

CONFIDENTIAL

CONFIDENTIAL



CONFIDENTIAL
FO4059 G

FIGURE 38. SECTION OF ASBESTOS-PHENOLIC AFT CLOSURE FROM TEST T-1

CONFIDENTIAL

CONFIDENTIAL



FIGURE 39. CROSS SECTION OF ASBESTOS-PHENOLIC ENTRANCE CONE INSULATOR
FROM TEST T-1

CONFIDENTIAL

CONFIDENTIAL

TABLE XI

MOTOR TEST T-1 DEPOSIT ANALYSIS (C)

<u>Sample No.</u>	<u>Location</u>	<u>Composition</u>	
T-1-1	Aft closure, near chamber insulation	BeO	- 70 to 80%
		Be ₂ C	- 5 to 10%
		MgO	- 5 to 10%
		Mg ₂ SiO ₄	- 5 to 10%
		Carbon	- 5 to 10%
T-1-2	Aft closure, approximately center area	BeO	- 60 to 70%
		Be ₂ C	- 5 to 10%
		MgO	- 10 to 20%
		Mg ₂ SiO ₄	- 10 to 20%
		Carbon	- 5 to 10%
T-1-3	ATJ entrance cone, approximately center area	BeO	- 80 to 90%
		Be ₂ C	- 2 to 5%
		MgO	- 2 to 5%
		Mg ₂ SiO ₄	- 5 to 10%
		Amorphous carbon	
T-1-4	Throat insert, black deposit of pyrolytic graphite	BeO	- 80 to 90%
		Graphite	- 10 to 20%
T-1-5	ATJ exit cone approximately center area	BeO	- 80 to 90%
T-1-6	Between ATJ entrance cone and first pyrolytic graphite washer, spacer area, front half near throat	Be ₂ C	
		Amorphous carbon	
		Amorphous carbon	
T-1-6	Spacer area, back half	α SiO ₂ (cristobalite)	

CONFIDENTIAL

CONFIDENTIAL

(b) (C) Motor Test T-2

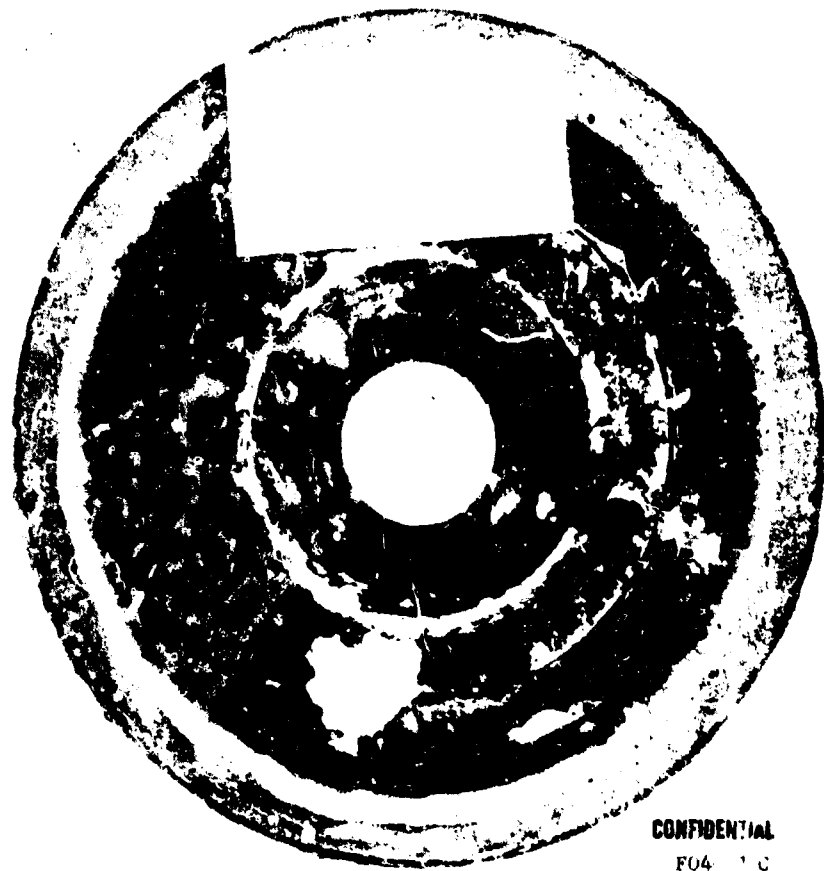
Photographs of the "as received" nozzle graphite inlet cone, pyrolytic graphite entrance and nozzle exit cone are shown in Figure 40, 41, and 42, respectively. A nozzle cross section is shown in Figure 43. There was no significant loss of material or excessive erosion experienced in this test. However, the three pyrolytic graphite washers furthest upstream were delaminated. Figure 44 shows a cross section of the asbestos-phenolic aft closure. This shows uniform charring of the insulator, and there were no areas where grooving or excessive melting were observed. Figure 45 shows a cross section of the asbestos-phenolic entrance cone. This shows the expected char and no excessive loss of material. A series of samples were analyzed from deposits on the hardware. The results are tabulated in Table XII.

TABLE XII. MOTOR TEST T-2 DEPOSIT ANALYSIS (C)

<u>Sample No.</u>	<u>Location</u>	<u>Composition</u>	
T-2-1	Aft closure, near chamber insulation	BeO	- 70 to 80%
		Be ₂ C	- 5 to 10%
		MgO	- 5 to 10%
		Mg ₂ SiO ₄	- 5 to 10%
T-2-2	Aft closure, at center area	BeO	- 70 to 80%
		MgO	- 5 to 10%
		Mg ₂ SiO ₄	- 10 to 20%
		Carbon	- 5 to 10%
		BeO, Be ₂ C	
T-2-3	Residual slag from chamber - typical black slag	BeO, Be ₂ C	
T-2-4	Residual slag from chamber, metallic-looking slag	BeO, Be ₂ C	
T-2-5	Black sooty deposit from convergent face of nozzle	Amorphous carbon	
T-2-6	ATJ exit cone, approximately center area	BeO	- 60 to 70%
		Mg ₂ SiO ₄	- 30 to 40%
		Plus carbon	

CONFIDENTIAL

CONFIDENTIAL



CONFIDENTIAL

F04 1 C

FIGURE 40. NOZZLE INSERT FROM TEST T-2 - ENTRANCE SECTION VIEW

-116-

CONFIDENTIAL

CONFIDENTIAL

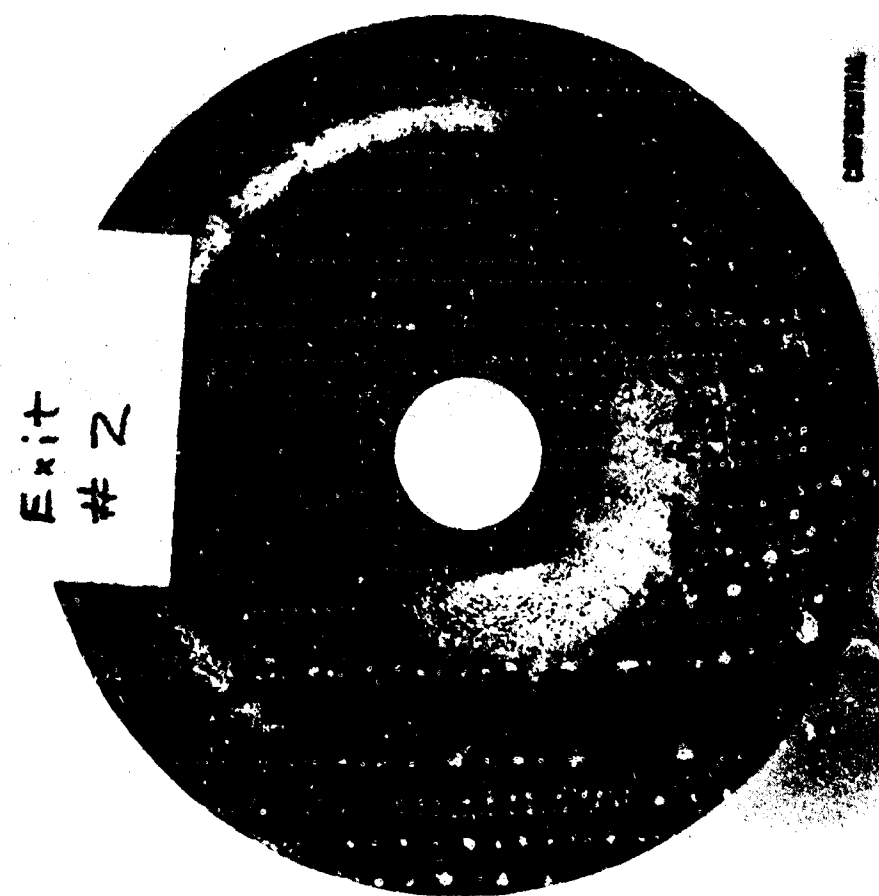


FIGURE 41. NOZZLE FROM TEST T-2 - EXIT SECTION VIEW

CONFIDENTIAL

CONFIDENTIAL



CONFIDENTIAL

F04063.C

FIGURE 42. NOZZLE FROM TEST T-2 - GRAPHITE ENTRANCE CONE

CONFIDENTIAL

CONFIDENTIAL



CONFIDENTIAL FO4064 C

FIGURE 43. NOZZLE FROM TEST T-2 - CROSS SECTION

CONFIDENTIAL

CONFIDENTIAL



FIGURE 44. CROSS SECTION OF ASBESTOS-PHENOLIC AFT CLOSURE FROM TEST T-2

CONFIDENTIAL

CONFIDENTIAL



CONFIDENTIAL
FC4066 C

FIGURE 45. CROSS SECTION OF ASBESTOS-PHENOLIC ENTRANCE CONE INSULATOR
FROM TEST T-2

CONFIDENTIAL

CONFIDENTIAL

The deposits were the same typical materials which would be expected. There was a relatively high percentage of material from the aft closure insulator found on the graphite exit cone. There were two fairly deep grooves in the graphite exit cones; one groove was approximately 0.1 inch wide and 0.2 inch deep and the other groove was 0.1 inch deep and 0.3 inch wide. There was nothing that could be found to indicate the mechanism which caused this grooving. The grooves were fairly well coated with BeO. The pyrolytic graphite throat washers were very clean with the only deposit being a fine, black, sooty material from the decomposition of the pyrolysis gases produced during soak back.

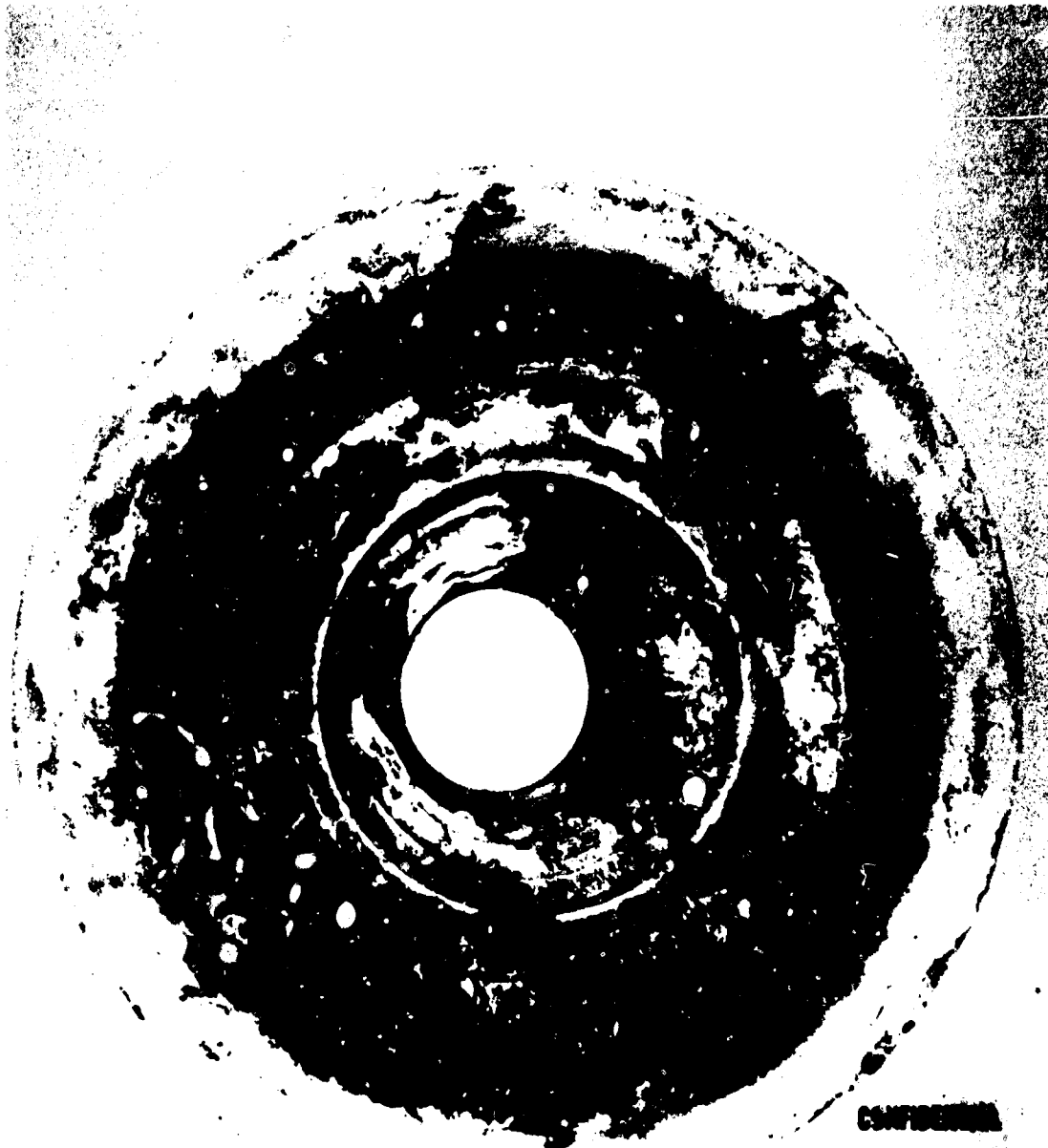
(c) (C) Motor Test T-3

Photographs of the nozzle entrance cone, pyrolytic graphite entrance, and exit cone in the "as received" condition are shown in Figures 46, 47, and 48, respectively. A nozzle cross section is shown in Figure 49. There was significant throat erosion or loss of material experienced in this test. A view of the aft closure insulation is shown in Figure 50. A series of samples from deposits on the hardware was analyzed. The results are given in Table XIII. There was some material on the pyrolytic graphite throat washers. This material was mostly from the asbestos, about 60 percent, and the remainder was BeO. The graphite exit cone had a thin (approximately 0.020 to 0.030 inch thick) even coating over the entire surface. This material was black and was mostly BeO. Most other exit cones had somewhat thicker, more irregular deposits which were usually white.

(d) (C) Motor Test T-4. Photographs of the nozzle entrance cone, pyrolytic graphite entrance, and exit cone are shown in the "as received" condition in Figures 51 and 52 respectively. A nozzle cross section is shown in Figure 53. There was considerable deposit found in the nozzle surfaces. For comparison, a view of the nozzle exit cone during motor disassembly is shown in Figure 54. Similarly, the asbestos-phenolic aft closure insulator is shown in Figure 55. A series of samples from the various deposits was analyzed. The results are given in Table XIV.

CONFIDENTIAL

CONFIDENTIAL



CONFIDENTIAL

FO4067 C

FIGURE 46. NOZZLE FROM TEST T-3 - ENTRANCE SECTION VIEW

CONFIDENTIAL

CONFIDENTIAL



FIGURE 47. NOZZLE PLATE, TEST T-3 - EXIT SECTION VIEW

-17-

CONFIDENTIAL

CONFIDENTIAL

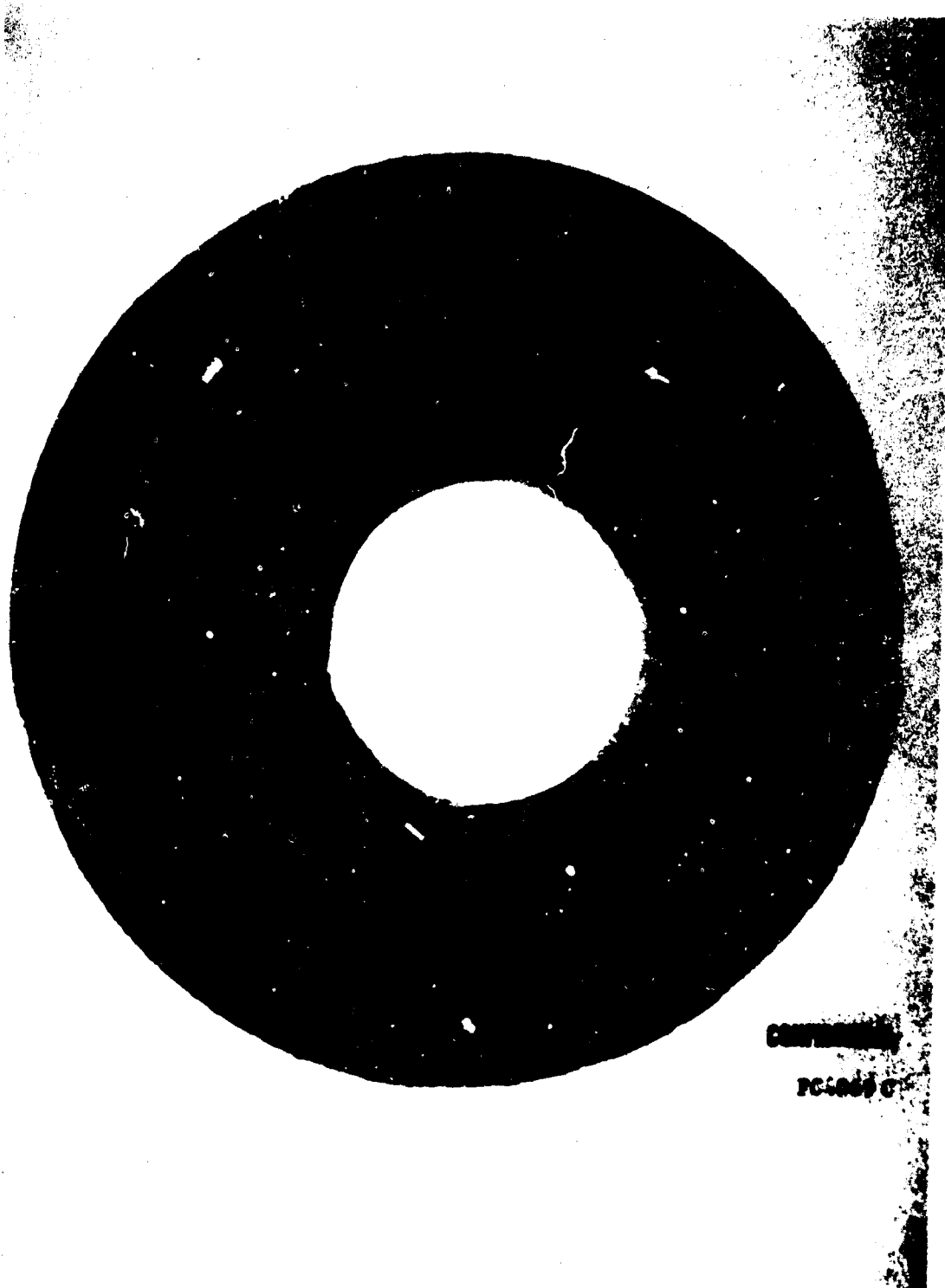


FIGURE 48. NOZZLE FROM TEST T-3 - GRAPHITE ENTRANCE CONE

CONFIDENTIAL

CONFIDENTIAL



FIGURE 49. NOZZLE FROM TEST T-3 - CROSS SECTION

CONFIDENTIAL

CONFIDENTIAL



CONFIDENTIAL

F04071 C

FIGURE 50. MOTOR TEST T-3 - AFT CLOSURE INSULATOR

CONFIDENTIAL

CONFIDENTIAL

TABLE XIII. MOTOR TEST T-3 DEPOSIT ANALYSIS (C)

Sample No.	<u>Location</u>	<u>Composition</u>	
T-3-1	Aft closure center area	BeO	- 70 to 80%
		Be ₂ C	- 5 to 10%
		MgO	- 5 to 10%
		Mg ₂ SiO ₄	- 5 to 10%
		Graphite	- 5 to 10%
T-3-2	Asbestos-phenolic entrance cone center area	BeO	- 80 to 90%
		MgO	- 5 to 10%
		Mg ₂ SiO ₄	- 5 to 10%
		Graphite	- 5 to 10%
T-3-3	Graphite entrance cone area near spacer	BeO	- 65 to 75%
		Mg ₂ SiO ₄	- 5 to 10%
		SiO ₂	- 2 to 5%
		Graphite	- 15 to 20%
T-3-4	Throat area	BeO	- 30 to 40%
		MgO	- 30 to 40%
		Mg ₂ SiO ₄	- 20 to 30%
T-3-5	Graphite exit cone	BeO	- 60 to 70%
		Mg ₂ SiO ₄	- 30 to 40%
T-3-6	Chamber residue	BeO, carbon	

CONFIDENTIAL

CONFIDENTIAL



CONFIDENTIAL

FO4072 C

FIGURE 51. NOZZLE FROM TEST T-4 - ENTRANCE SECTION VIEW

CONFIDENTIAL

CONFIDENTIAL



CONFIDENTIAL

F04073 C

FIGURE 52. NOZZLE FROM TEST T-4 - EXIT SECTION VIEW

CONFIDENTIAL

CONFIDENTIAL

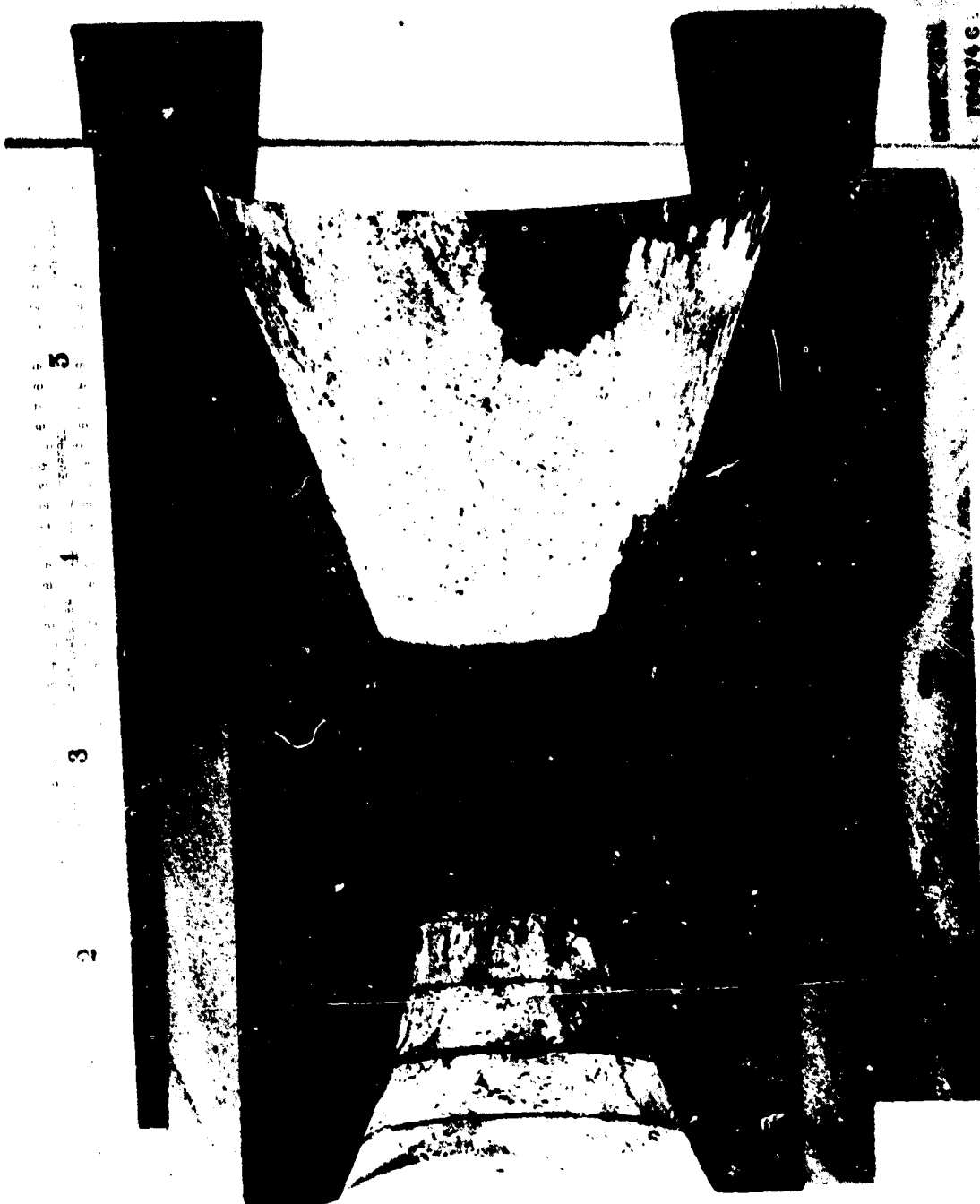


FIGURE 53. NOZZLE FROM TEST T-4 - CROSS SECTION

CONFIDENTIAL

CONFIDENTIAL



FIGURE 54. NOZZLE FROM TEST T-4 - EXIT SECTION VIEW

CONFIDENTIAL

CONFIDENTIAL



FIGURE 55. MOTOR TEST T-4 - AFT CLOSURE INSULATOR

CONFIDENTIAL

CONFIDENTIAL

TABLE XIV. MOTOR TEST T-4 DEPOSIT ANALYSIS (C)

<u>Sample No.</u>	<u>Location</u>	<u>Composition</u>	
T-4-1	Chamber - metallic deposit	BeO	- 70 to 80%
		Be ₂ C	- 5 to 10%
		Graphite	- 10 to 15%
		Unknown	- 5 to 10%
T-4-2	Aft closure, near chamber	Mg ₂ SiO ₄	
T-4-3	Aft closure, center area	BeO	- 75 to 85%
		Be ₂ C	- 5 to 10%
		MgO	- 5 to 10%
		Mg ₂ SiO ₄	- 5 to 10%
T-4-4	Throat area	Amorphous carbon	
T-4-5	Graphite entrance cone	BeO	- 80 to 90%
		MgO	- 5 to 10%
		Mg ₂ SiO ₄	- 5 to 10%
		BeO	- 15 to 20%
T-4-6	Throat area	MgO	- 60 to 70%
		Mg ₂ SiO ₄	- 10 to 15%
		BeO	- 95% +
		Graphite exit cone near pyrolytic graphite washers	
T-4-8	Graphite exit cone at trailing edge	BeO	- 60 to 70%
		MgO	- 25 to 30%
		Mg ₂ SiO ₄	- 10 to 15%

CONFIDENTIAL

CONFIDENTIAL

The deposit on the pyrolytic graphite throat area and the polycrystalline graphite was very thick (approximately 0.10 to 0.20 inch). The deposit was continuous and was removed in essentially one piece. The graphite underneath the deposit was not appreciably damaged in any way. The undamaged pyrolytic graphite washers were examined along with the one washer which was delaminated. The areas between the individual washers were examined and found to be fairly clean. There were only some small traces of amorphous carbon; no beryllium compounds were found.

(e) (C) Motor Test T-5

Test No. T-5 was the first test conducted with an aluminized propellant. Photographs of the nozzle entrance cone, pyrolytic graphite inlet and graphite exit cone was shown in Figures 56, 57, and 58, respectively. A cross section of the nozzle is shown in Figure 59. Figure 60 shows the asbestos-phenolic aft closure as received. It is evident that there was little damage to this section. The samples from the various areas were analyzed and the results are given in Table XV.

There was a large portion of the residue from the chamber found to be aluminum metal. There was also aluminum metal found on the asbestos-phenolic aft closure and the asbestos-phenolic entrance cone. The deposits on the aft closure were a mixture of the various forms of alumina. The various phases (α , γ , η) are formed during the cooling of the alumina at different rates. The exposed graphite surfaces were all coated with deposit which was mostly Al_2O_3 . There were no aluminum-carbon compounds found in the deposits. However, some of these compounds, Al_4C_3 for example, are unstable in air and would not be found unless examined immediately after the test. The unknown compound found on the aft closure appeared to be similar to a Mg-Al-O monoclinic modification of the spinel, $MgAl_2O_4$. The laboratory studies showed similar compounds formed in the plasma studies of Al_2O_3 on asbestos-phenolic substrates.

CONFIDENTIAL

CONFIDENTIAL



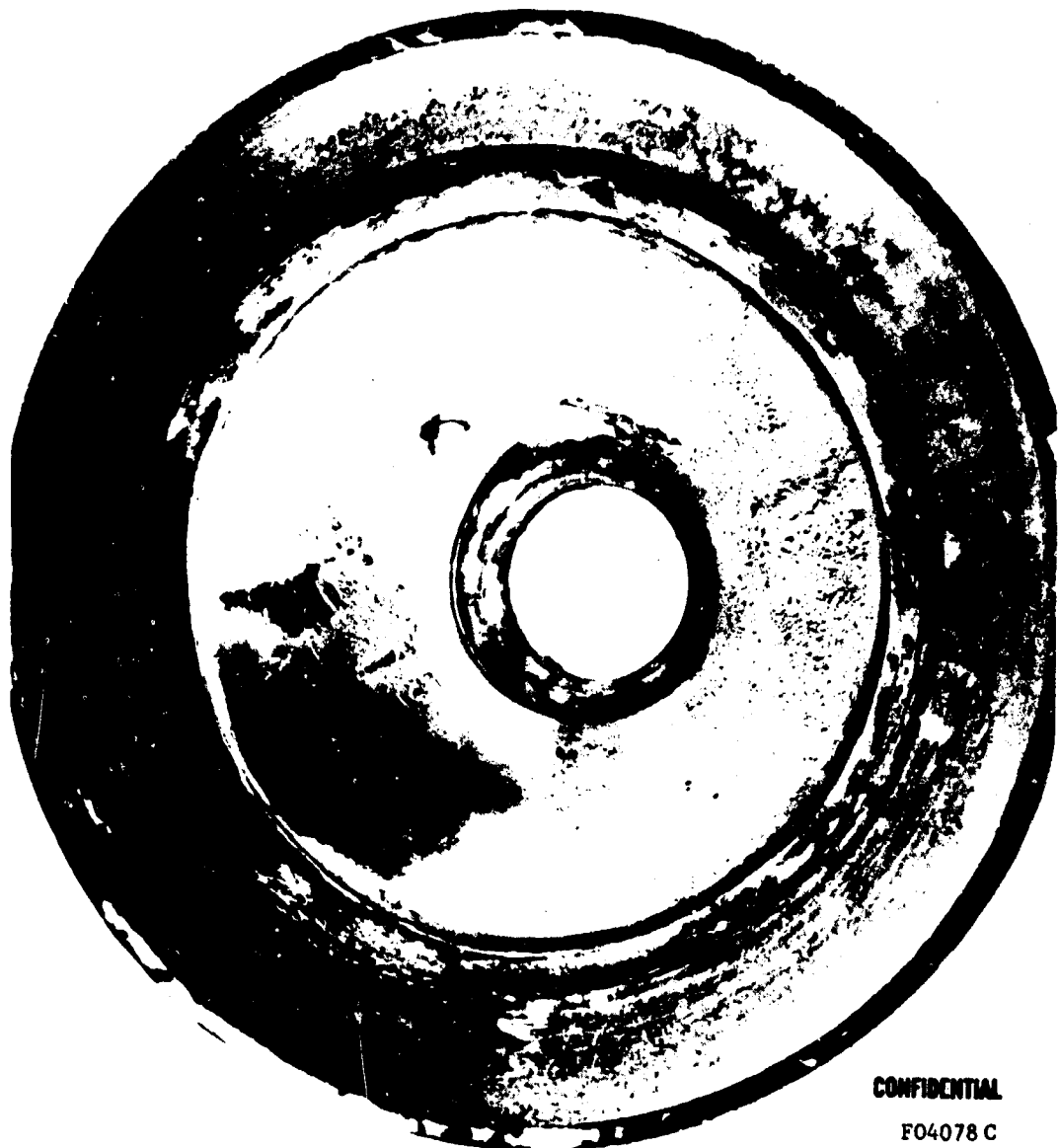
CONFIDENTIAL

F04077 C

FIGURE 56. NOZZLE FROM TEST T-5 - ENTRANCE SECTION VIEW

CONFIDENTIAL

CONFIDENTIAL



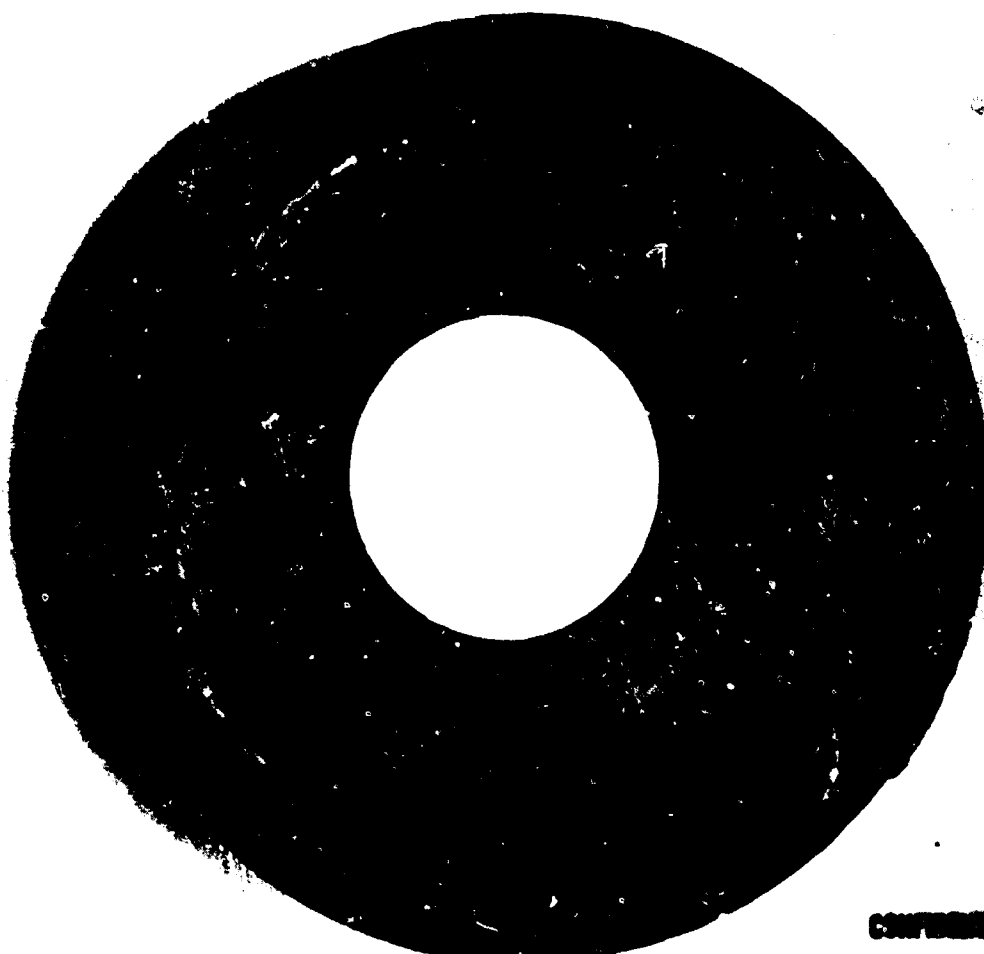
CONFIDENTIAL

F04078 C

FIGURE 57. NOZZLE FROM TEST T-5 - EXIT SECTION VIEW

CONFIDENTIAL

CONFIDENTIAL



~~CONFIDENTIAL~~

FO4879 C

FIGURE 58. NOZZLE FROM TEST T-5 - GRAPHITE ENTRANCE CONE

CONFIDENTIAL

CONFIDENTIAL

CONFIDENTIAL
FD-3500-C



FIGURE 59. NOZZLE FROM TEST T-5 - CROSS SECTION

CONFIDENTIAL

CONFIDENTIAL



CONFIDENTIAL

F04081 C

FIGURE 60. MOTOR TEST T-5 - AFT CLOSURE INSULATOR

-140-

CONFIDENTIAL

CONFIDENTIAL

TABLE XV . MOTOR TEST T-5 DEPOSIT ANALYSIS

<u>Sample No.</u>	<u>Location</u>	<u>Composition</u>
T-5-1	Chamber residue	Al - 75 to 85%
		Al_2O_3 - 10 to 20%
		$\alpha \text{Al}_2\text{O}_3$ - 5 to 10%
T-5-2	Aft closure center area	$\gamma \text{Al}_2\text{O}_3$ - 35 to 45%
		$\eta \text{Al}_2\text{O}_3$ - 25 to 35%
		$\alpha \text{Al}_2\text{O}_3$ - 5 to 10%
		Al - 2 to 5%
		Unknown - 10 to 20%
T-5-3	Aft closure, at asbestos-phenolic entrance cone	$\alpha \text{Al}_2\text{O}_3$ - 25 to 35%
		$\gamma \text{Al}_2\text{O}_3$ - 40 to 50%
		Al - 5 to 10%
		Mg_2C_3 - 15 to 20%
T-5-4	Asbestos-phenolic entrance cone	$\alpha \text{Al}_2\text{O}_3$ - 10 to 15%
		$\gamma \text{Al}_2\text{O}_3$ - 60 to 70%
		Al - 5 to 10%
		Mg_2SiO_4 - 10 to 15%
T-5-5	Graphite entrance cone	$\alpha \text{Al}_2\text{O}_3$ - 95% +
		$\gamma \text{Al}_2\text{O}_3$ - 5%
T-5-6	Graphite exit cone	$\alpha \text{Al}_2\text{O}_3$ - 100%
T-5-7	Throat area	$\alpha \text{Al}_2\text{O}_3$ - 100%

CONFIDENTIAL

CONFIDENTIAL

(f) (C) Motor Test T-6

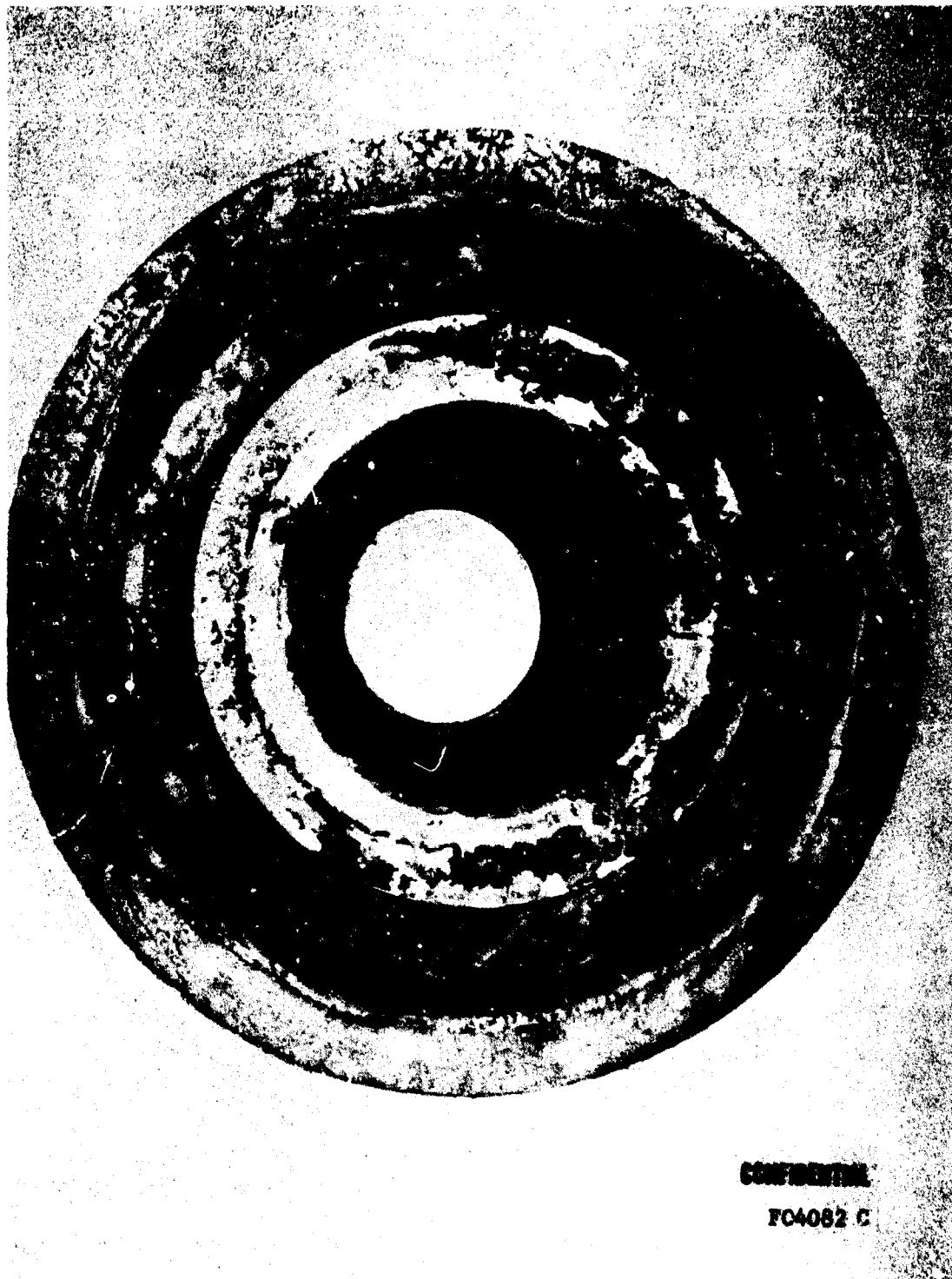
Photographs of the T-6 nozzle entrance cone, pyrolytic graphite inlet, and graphite exit cone are shown in Figures 61, 62 and 63, respectively. A nozzle cross section is shown in Figure 64, and a view of the aft closure is shown in Figure 65. The samples obtained from the various deposits were analyzed. The results are given in Table XVI. The deposits found on the exposed surfaces were typical of material normally found in these areas. The Mg_2C_3 found on the aft closure is a product of the decomposition of the asbestos. The αSiO_2 (cristobalite), found on the graphite entrance cone, is a decomposition product of the RTV rubber used for the spacer. The pyrolytic graphite throat washers were covered with a fairly even coat of deposit, αAl_2O_3 and γAl_2O_3 . There was no evidence of any aluminum compounds in between the individual pyrolytic graphite washers.

TABLE XVI. MOTOR TEST T-6 DEPOSIT ANALYSIS

<u>Sample No.</u>	<u>Location</u>	<u>Composition</u>	
T-6-1	Aft closure center area, surface deposit only	αAl_2O_3	- 5 to 10%
		γAl_2O_3	- 70 to 80%
		Mg_2C_3	- 5 to 10%
		Mg_2SiO_4	- 5 to 10%
T-6-2	Aft closure center area, material removed to bottom of char	Al	- 75 to 85%
		αAl_2O_3	- 5 to 10%
		γAl_2O_3	- 2 to 5%
		Mg_2SiO_4	- 5 to 10%
T-6-3	Graphite entrance cone near spacer area	Graphite	- 10 to 15%
		αSiO_2	- 10 to 15%
		αAl_2O_3	- 40 to 50%
		γAl_2O_3	- 35 to 45%
T-6-4	Throat area	αAl_2O_3	- 55 to 65%
		γAl_2O_3	- 35 to 45%
T-6-5	Graphite exit cone, center area	αAl_2O_3	- 20 to 30%
		γAl_2O_3	- 50 to 60%
		Mg_2C_3	- 20 to 30%

CONFIDENTIAL

CONFIDENTIAL



CONFIDENTIAL

FC4082 C

FIGURE 61. NOZZLE FROM TEST T-6 - ENTRANCE SECTION VIEW

-143-

CONFIDENTIAL

CONFIDENTIAL



CONFIDENTIAL

F04083 C

FIGURE 62. NOZZLE FROM TEST T-6 - EXIT SECTION VIEW

-144-

CONFIDENTIAL

CONFIDENTIAL

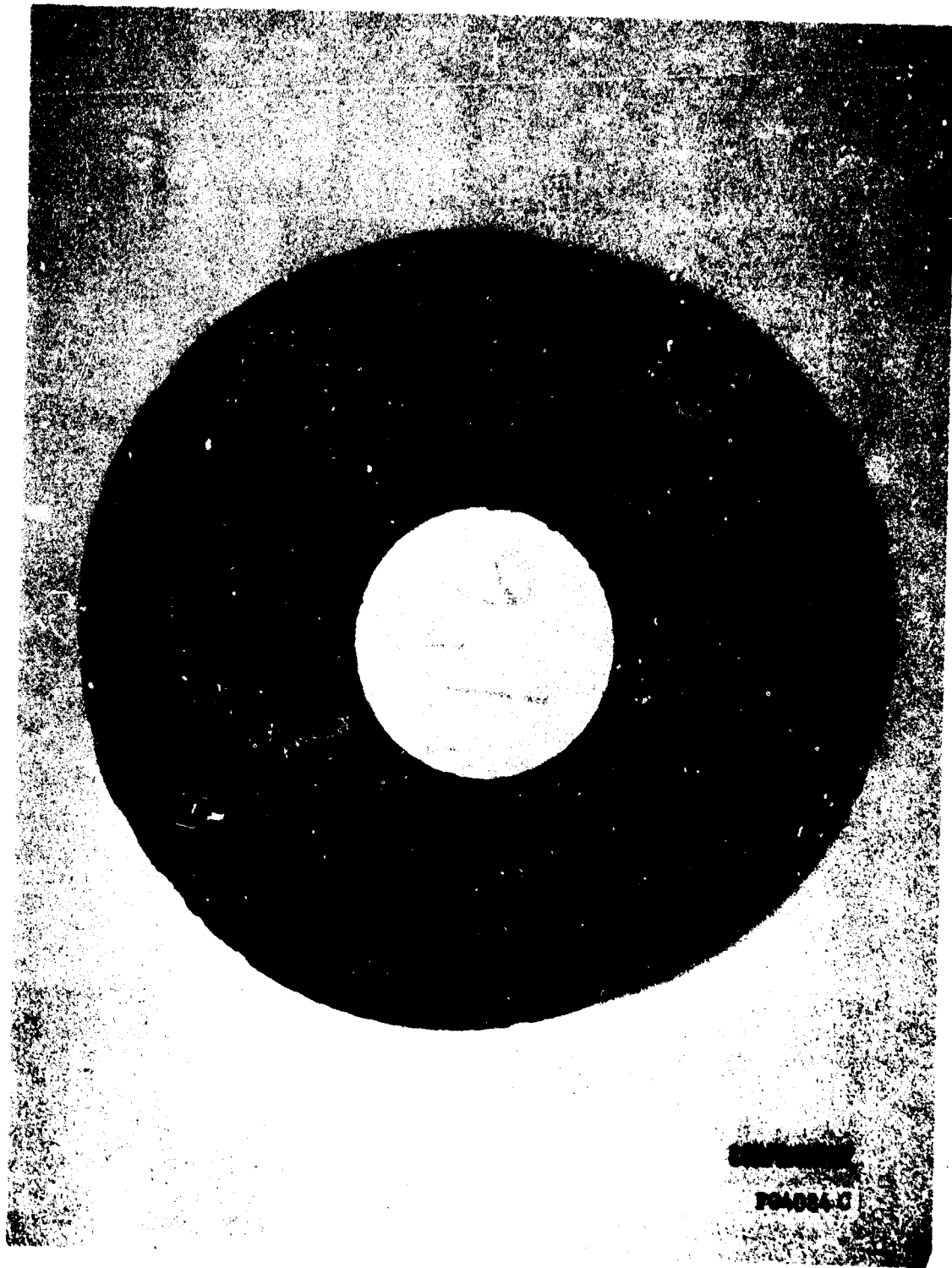


FIGURE 63. NOZZLE FROM TEST T-6 - GRAPHITE ENTRANCE CONE

CONFIDENTIAL

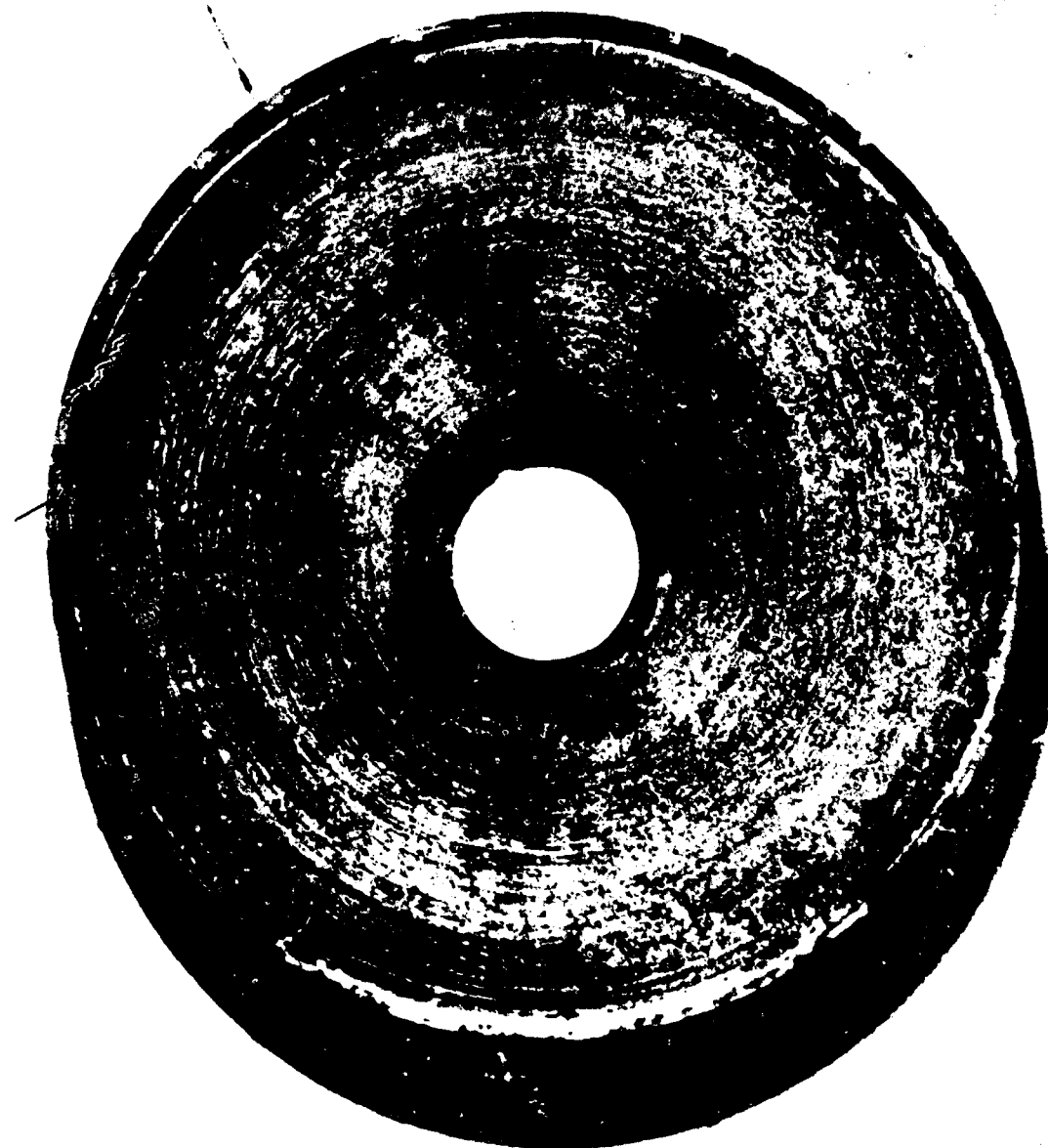
CONFIDENTIAL



FIGURE 64. NOZZLE FROM TEST T-6 - CROSS SECTION

CONFIDENTIAL

CONFIDENTIAL



CONFIDENTIAL

FO4086 C

FIGURE 65. MOTOR TEST T-6 - AFT CLOSURE INSULATOR

CONFIDENTIAL

CONFIDENTIAL

(g) (C) Motor Test T-7

Photographs of the T-7 nozzle entrance cone, pyrolytic graphite inlet and graphite exit cone are shown in Figures 66 , 67 and 68 , respectively. A cross section of the nozzle is shown in Figure 69 and a view of the aft closure insulator is shown in Figure 70. Samples from deposits taken from varicus areas on the hardware were analyzed. The results are given in Table XVII.

TABLE XVII. MOTOR TEST T-7 DEPOSIT ANALYSIS

Sample No.	Location	Composition	
T-7-1	Aft Closure, center area	αAl_2O_3	- 25 to 35%
		γAl_2O_3	- 40 to 50%
		Al	- 5 to 10%
		Mg_2SiO_4	- 15 to 20%
T-7-2	Graphite entrance cone	αAl_2O_3	- 40 to 50%
		γAl_2O_3	- 20 to 30%
		Mg_2SiO_4	- 20 to 30%
T-7-3	Throat area, light grey flakes	Amorphous carbon	95+ unknown 2 to 5%
T-7-4	Throat area, purple deposit	Amorphous carbon	
T-7-5	Graphite exit cone	αAl_2O_3	100%

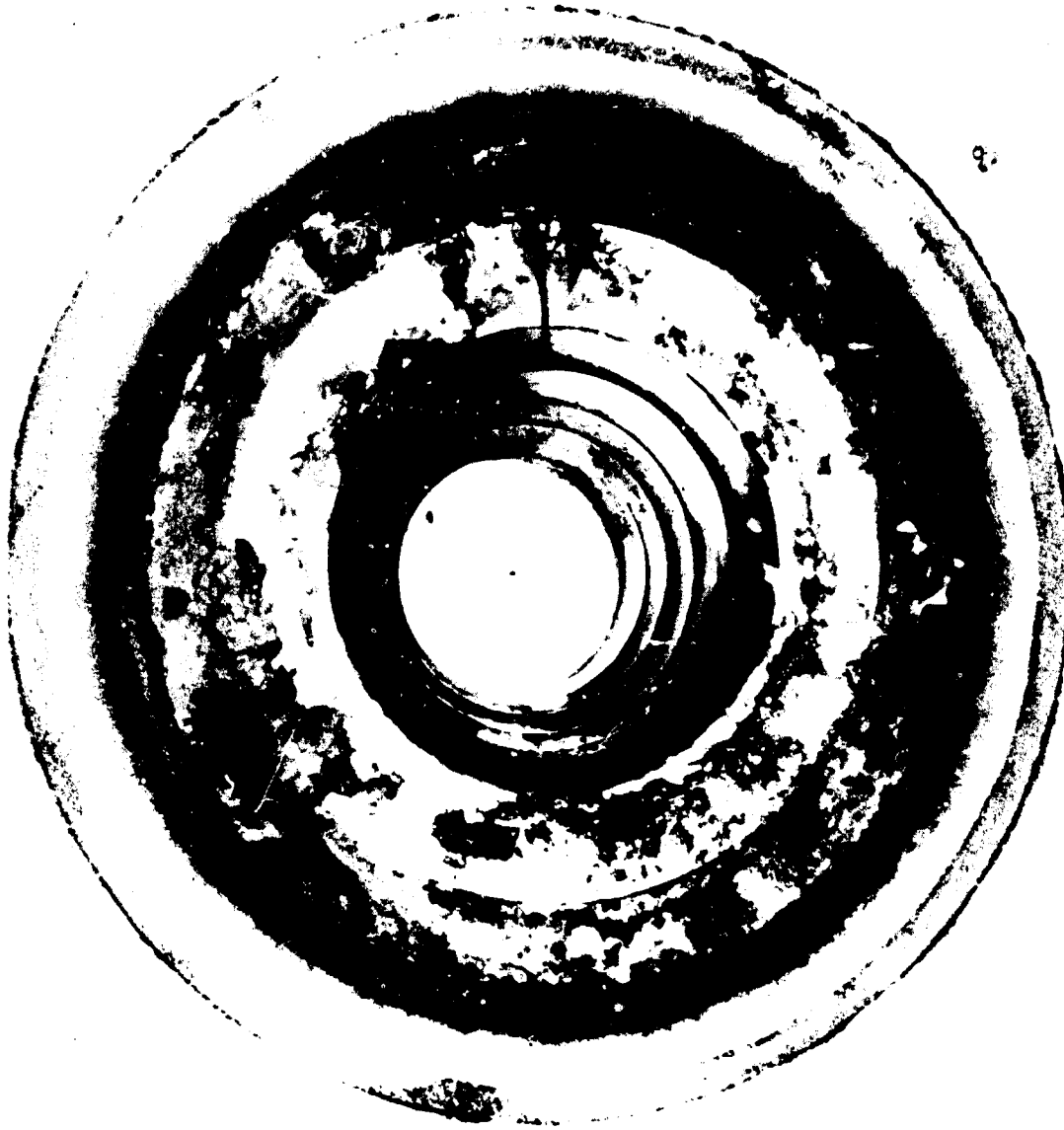
The flame front throat area was fairly clean and devoid of any deposits. However, there appeared to be a grey coating on the surface with some purple area. These coatings were found to be amorphous carbon, the product of pyrolyzing gases at the termination of the test. The graphite exit cone was coated with Al_2O_3 . The deposits on the aft closure were alumina and decomposition products of the asbestos-phenolic.

(2) (C) Hardware From Other Programs

Two nozzles were obtained from AFRPT for post-test analysis. These nozzles were designed and tested by AFRPL and utilized existing Minute Man II hardware. Both nozzles were of the same configuration and utilized pyrolytic graphite in the throat area. The nozzles were designed to be flight-weight hardware. One nozzle was tested with an existing Minute Man II aluminized propellant, and the other nozzle was tested with a beryllium analog of the aluminized propellant.

CONFIDENTIAL

CONFIDENTIAL



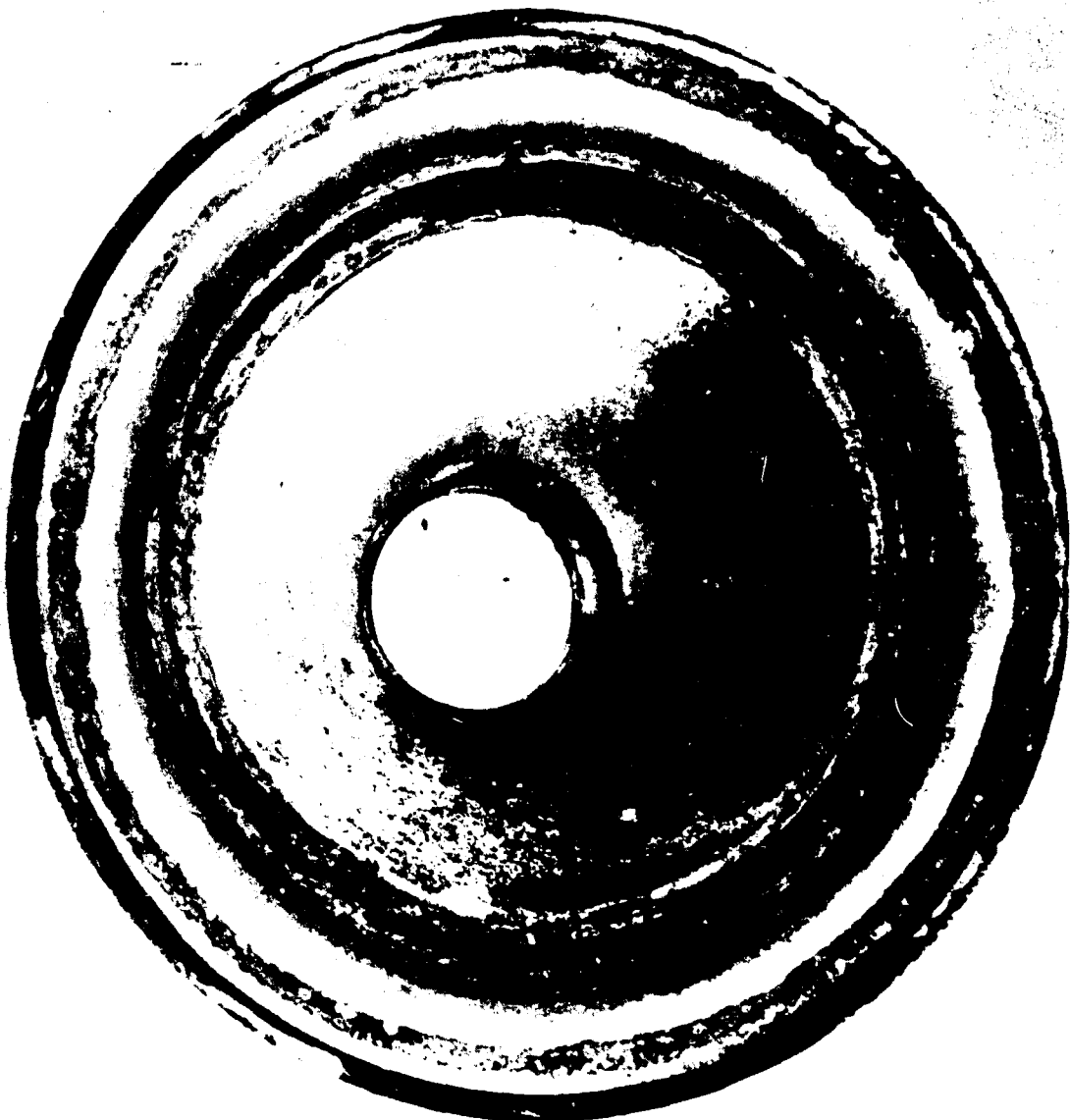
CONFIDENTIAL

FO4087 C

FIGURE 66. NOZZLE FROM TEST T-7 - ENTRANCE SECTION VIEW

CONFIDENTIAL

CONFIDENTIAL



CONFIDENTIAL

F04088 C

FIGURE 67. NOZZLE FROM TEST T-7 - EXIT CONE VIEW

-150-

CONFIDENTIAL

CONFIDENTIAL

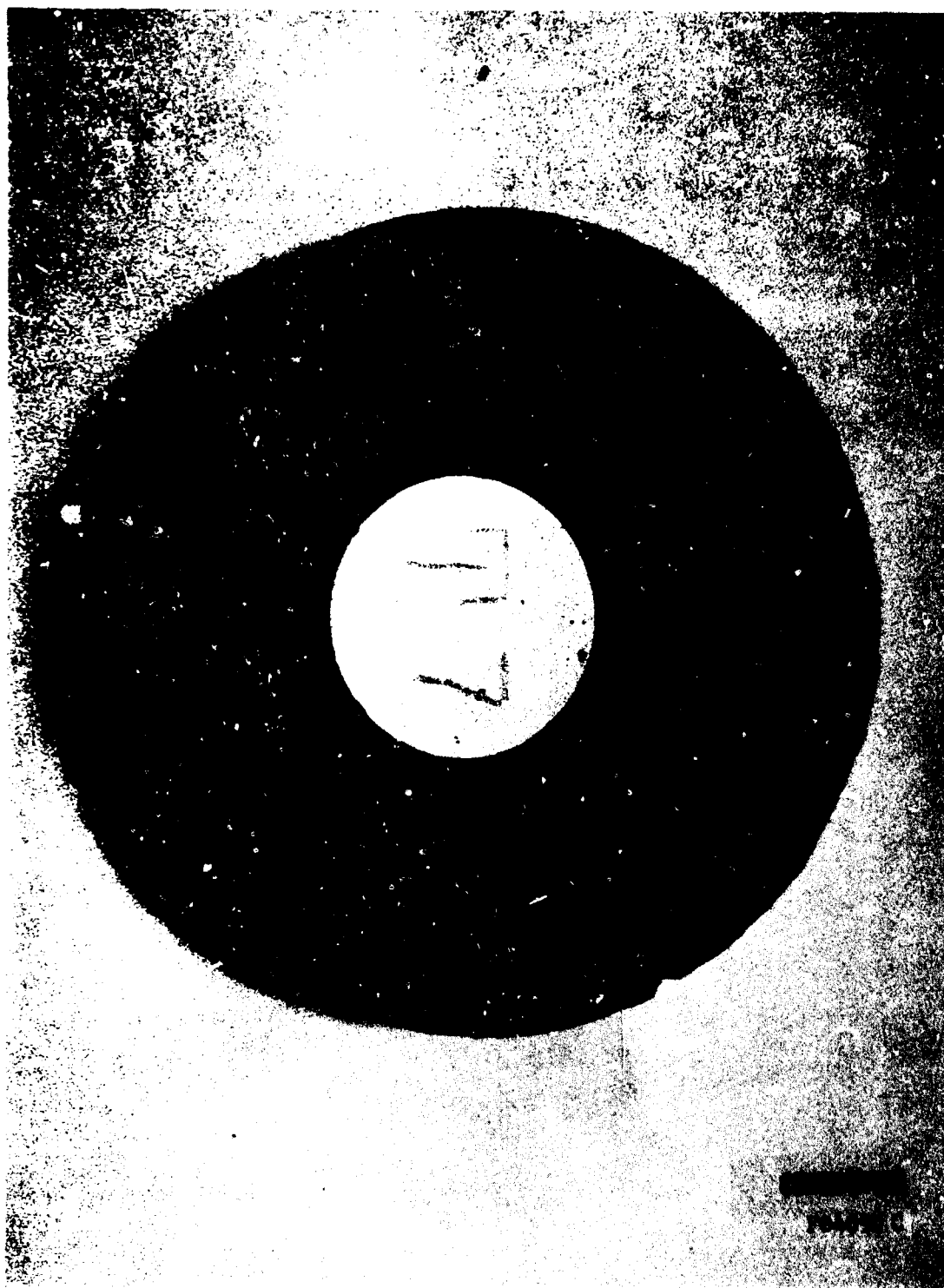


FIGURE 68. NOZZLE FROM TEST T-7 - GRAPHITE ENTRANCE CONE

CONFIDENTIAL

CONFIDENTIAL

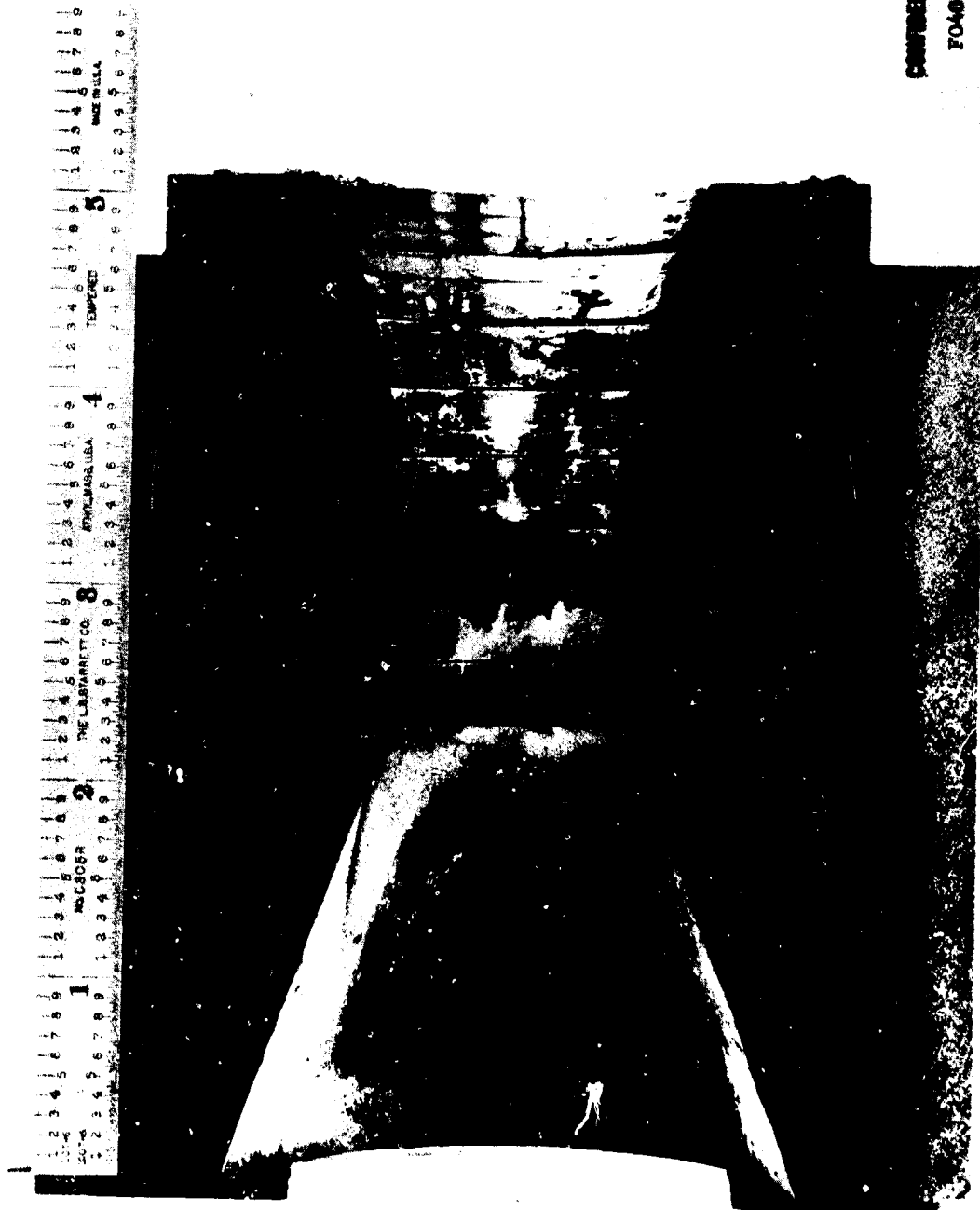
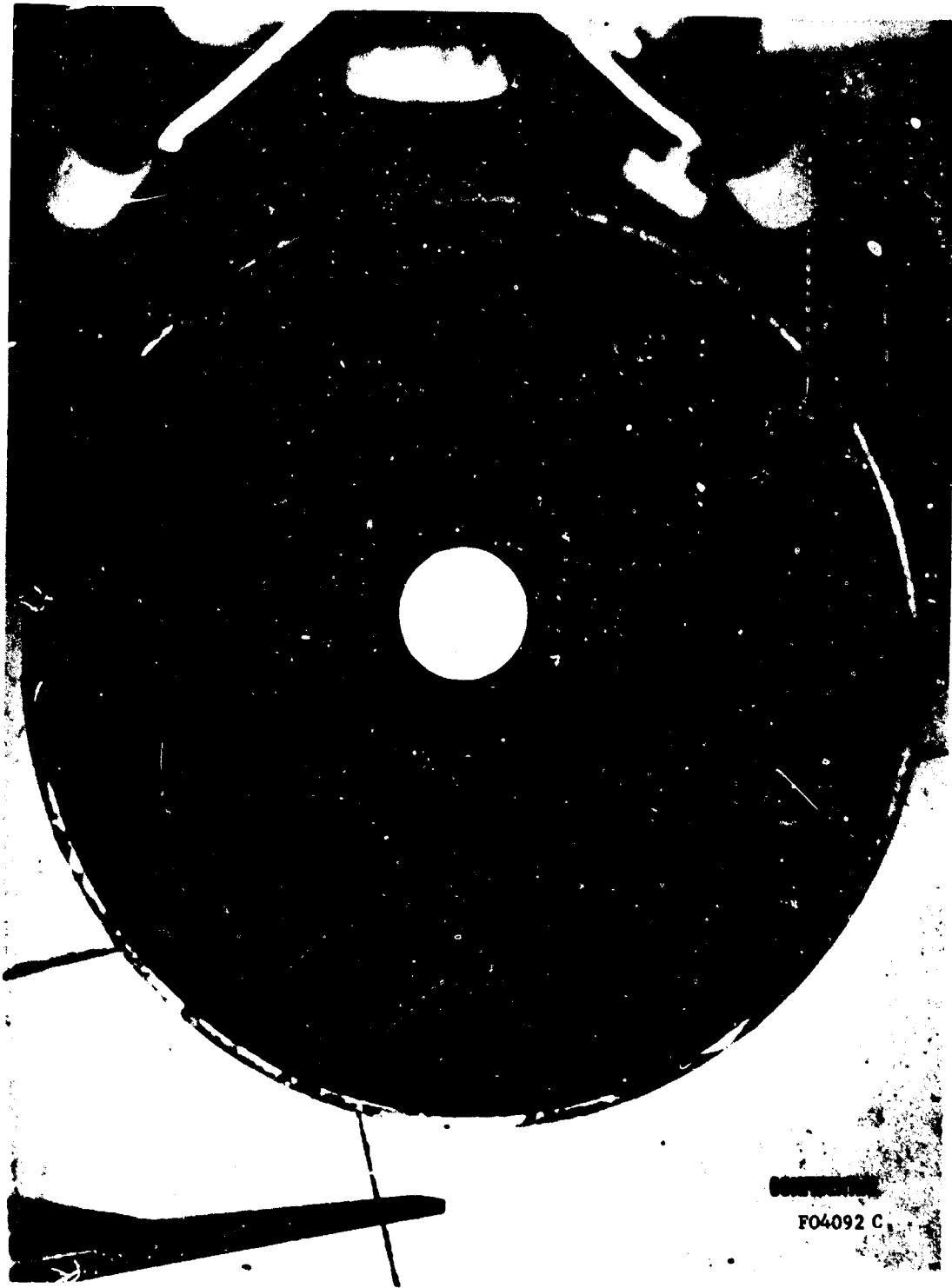


FIGURE 69. NOZZLE FROM TEST C-7 - CROSS SECTION

CONFIDENTIAL

CONFIDENTIAL



FO4092 C

FIGURE 70. MOTOR TEST T-7 - AFT CLOSURE INSULATOR

CONFIDENTIAL

CONFIDENTIAL

The nozzle from the aluminized propellant test is shown in the "as-received" condition in Figures 71 and 72. The nozzle was in very good condition. Throat erosion was minimal, approximately 0.001 to 0.003 on a 6.250 inch diameter. There was no evidence of gouging or excessive loss of material in the throat area. The graphite approach ring was completely gone, being lost during the test. This was a large graphite piece which apparently broke up and was not recovered. The graphite entrance cone was somewhat eroded but in fairly good shape. The graphite exit cone was in very good condition. A series of samples from deposits on the nozzle was analyzed. The results are given in Table XVIII.

TABLE XVIII. AFRPL MINUTEMAN (A) NOZZLE DEPOSIT ANALYSIS

Sample No.	Location.	Composition		
MMII - Al - 1	Graphite entrance cone near center area	Al_2O_3	-	30 to 40%
		Graphite	-	60 to 70%
MMII - Al - 2	Graphite entrance cone near pyrolytic graphite washers	Al_2O_3	-	60 to 70%
		Graphite	-	30 to 40%
MMII - Al - 3	Pyrolytic graphite washer throat surface	Al_2O_3		90+
MMII - Al - 4	Between pyrolytic graphite washers 2 & 3 near throat surface	Al_2O_3		20%
		Carbon		80%
MMII - Al - 5	Between pyrolytic graphite washers 2 & 3 near backside	Amorphous Carbon		
MMII - Al - 6	Graphite exit cone	Al_2O_3	-	70 to 80%
		Graphite	-	20 to 30%
MMII - Al - 7	Insulator behind pyrolytic graphite washers	Pyrolytic graphite		

There did not appear to be any gas flow between or behind the pyrolytic graphite washers. Figure 72 shows the extensive loss of graphite upstream of the pyrolytic graphite washers. The pyrolytic graphite tape which was used as an insulator behind the pyrolytic graphite washers was deformed so that it filled all available space. This might be expected since the pyrolytic graphite tape is a very soft, pliable material. By deforming in this manner, it would allow the entire back side of the washers to be uniformly insulated with little or no

CONFIDENTIAL

CONFIDENTIAL



CONFIDENTIAL
FO4093 C

FIGURE 71. MINUTEMAN II NOZZLE TESTED WITH ALUMINUM PROPELLANT -
ENTRANCE SECTION



CONFIDENTIAL
FO4093 C

FIGURE 72. MINUTEMAN II NOZZLE TESTED WITH ALUMINUM PROPELLANT -
THROAT INSERT SECTION

CONFIDENTIAL

CONFIDENTIAL

opportunity for hot spots to be established. The pyrolytic graphite tape also filled all possible channels for gas flow.

There were α alumina deposits found on all the flame front surfaces (graphite entrance cone, pyrolytic graphite washers, graphite exit cone). However, those deposits were all fairly thin (less than 0.020 inch) and somewhat irregular (coating was not continuous on any surface).

- The individual pyrolytic graphite washers were examined and found to be in very good condition with no laminations. C_0 spacing was measured near the flame front and found to be 6.842 Å. This value is in the same range as for normal as-deposited pyrolytic graphite. This indicates that the upper limit of temperature, to which the pyrolytic graphite was exposed (where the measurement was made, approximately 0.1 inch behind the flame front), was 4500° F.

The nozzle inlet, from the test using the beryllium propellant is shown in Figure 73 and a nozzle cross section is shown in Figure 74. The nozzle was of the same configuration as the nozzle used in the aluminized propellant test. The condition of the beryllium nozzle was equally good. There was essentially no change in the throat diameter (6.25 inches). The graphite approach ring was also lost during the test. However, the graphite throat entrance cone was not appreciably degraded during the test. A series of samples were analyzed from deposits on the nozzle. The results are summarized in Table XIX.

The deposits analyzed did not show any unexpected results. In general, most of the deposits were BeO and graphite. A deposit found between pyrolytic graphite washers 4 and 5 was found to be Be_2C . This must have been the reaction product of BeO, which ran between the washers, and the graphite. This nozzle also showed the pyrolytic graphite tape to be deformed so that it completely filled all of the cracks or depressions. Figure 74 shows how the pyrolytic graphite tape completely covers the back side of the pyrolytic graphite washers. There was no evidence of gas flow on the back side of the washers even though there was beryllium carbide found between the washers. The deposit taken from the spacer area was found to be silica and iron compounds. This would result from a filler of a silicone rubber filled with iron oxide which is commonly used. There were no beryllium compounds found in the spacer area.

The C_0 spacing was measured on the pyrolytic graphite throat washers at a point approximately 0.1 inch behind the flame front and found to be 6.840 Å. This value is very close to the C_0 spacing of normal as-deposited pyrolytic graphite.

CONFIDENTIAL

CONFIDENTIAL



CONFIDENTIAL
FO4094 C

FIGURE 73. MINUTEMAN II NOZZLE TESTED WITH BERYLLIUM PROPELLANT -
ENTRANCE SECTION



CONFIDENTIAL
FO4093 C

FIGURE 74. MINUTEMAN II NOZZLE TESTED WITH BERYLLIUM PROPELLANT -
NOZZLE CROSS SECTION

CONFIDENTIAL

CONFIDENTIAL

TABLE XIX. AFRPL MINUTEMAN (Be) NOZZLE DEPOSIT ANALYSIS

<u>Sample No.</u>	<u>Location</u>	<u>Composition</u>	
MMII Be-1	Graphite throat entrance cone at leading edge of flame front	BeO graphite	- 60 to 70% 30 to 40%
MMII Be-2	Graphite throat entrance cone at trailing edge of flame front.	BeO graphite	- 15 to 20% 75 to 80%
MMII Be-3	Pyrolytic graphite washers in throat	BeO pyrolytic graphite	- 85 to 90%
MMII Be-4	Graphite throat entrance cone, at most upstream edge	BeO graphite	- 10 to 15% 50%
MMII Be-5	Graphite throat exit cone, off flame front center area	BeO graphite	- 70 to 75% 25 to 30%
MMII Be-6	Graphite throat, exit cone, edge near pyrolytic graphite washers	BeO graphite	- 85 to 95% 10 to 15%
MMII Be-7	Pyrolytic graphite throat area near graphite throat exit cone	BeO	- 100%
MMII Be-8	Graphite throat exit cone at trailing edge	BeO graphite	- 85 to 95% 5 to 10%
MMII Be-9	Between pyrolytic graphite throat insert washer number 4 & 5	Pyrolytic graphite Be ₂ C	- 85 to 95% 5 to 10%
MMII Be-10	Deposit from spacer area	$\alpha F_{e_2} O_3$, $F_{e_3} O_4$ αF_e , $\alpha S_i O_2$	(cristobalite)

CONFIDENTIAL

CONFIDENTIAL

b. (C) Analysis of Condensed Phase Deposits

(1) (C) Current Program Samples

(a) (C) Beryllium Propellants

The exhaust plumes of Tests T-1 through T-7 were sampled for the condensed phases present. The sampling techniques are discussed in Section IV. The samples, which were collected in Motor Tests T-1, T-2, T-3 and T-4 have been examined, analyzed, and the results are reported herein. These tests featured the four beryllium metal containing propellant formulations and, presumably, complete combustion.

The results showed that the condensed phases in the exhaust plume were very similar to the particles which were collected on a similar test, the results of which were reported in Paragraph 3.4 of Reference 1. X-ray diffraction analysis showed all deposits to be α beryllia. This would be expected from examination of equilibrium burning calculations which show that all other phases which might be present would be in quantities too small to detect by x-ray diffraction analysis.

The particles were examined by electron microscopy. Typical examples of the particles are shown in Figures 75 through 84. The particles appeared to fall into two general size classifications: 1 to 3 microns and 0.01 to 0.2 micron. The larger particles were generally regular in shape, either the regular hexagonal crystal habit of α beryllia or spheres. However, some of the large particles definitely exhibit irregular shapes. Figure 75 shows some of the larger particles which have spherical and hexagonal shapes. Figure 77 shows an agglomeration of spherical particles. This agglomeration of particles was typical and was found most of the time.

The smaller particles were normally of the crystalline shapes with a smaller number being spherical. Figures 78, 79, and 80 show typical examples of the small particles. Figure 80 also shows a large sphere and a large hexagonal crystal.

Electron diffraction patterns were taken of many of the larger particles and all were found to be α beryllia. Clusters of fine particles were also examined and found to be α beryllia. However, these particles were generally melted by absorption of the beam energy and refused into different structures upon cooling. This may have masked any other crystal structure which was present (β beryllia, for example).

Samples taken off the various parts of the particle collector (described in Section IV) did not show any one method to be significantly more efficient than the others in terms of the quantity of material collected. No method appeared to give unique results in terms of the particle size

CONFIDENTIAL

CONFIDENTIAL

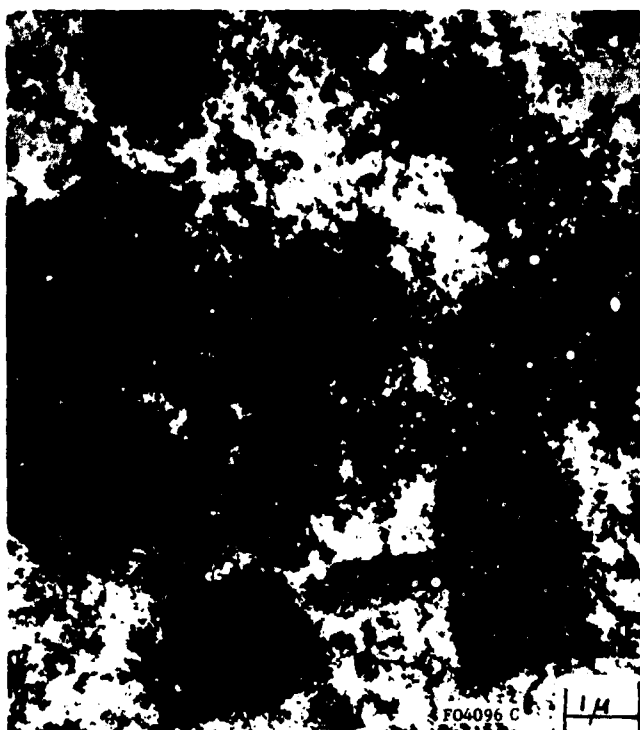


FIGURE 75. ELECTRON PHOTOMICROGRAPH OF PARTICLES ON GLASS SLIDE
PARTICLE COLLECTOR-MOTOR TEST T-4



FIGURE 76. ELECTRON PHOTOMICROGRAPH OF PARTICLES IN GLASS TUBE-
MOTOR TEST T-3

CONFIDENTIAL

CONFIDENTIAL



FIGURE 77. ELECTRON MICROPHOTOGRAPH OF PARTICLES ON GLASS SLIDE-MOTOR TEST T-1



FIGURE 78. ELECTRON MICROPHOTOGRAPH OF PARTICLES ON BRASS PLATE
PARTICLE COLLECTOR-MOTOR TEST T-3

CONFIDENTIAL

CONFIDENTIAL



**FIGURE 79. ELECTRON MICROPHOTOGRAPH OF PARTICLES ON BRASS PLATE
PARTICLE COLLECTOR-MOTOR TEST T-4**

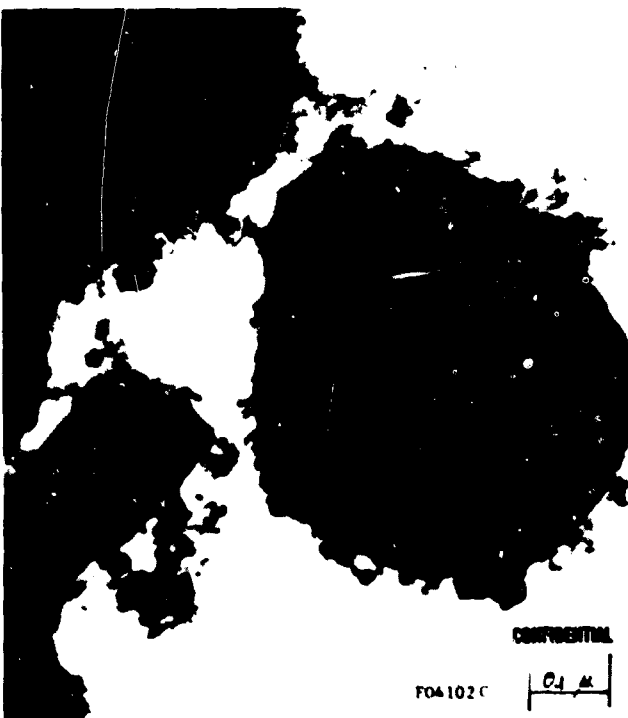


**FIGURE 80. ELECTRON MICROPHOTOGRAPH OF PARTICLES ON COPPER SLIDE
PARTICLE COLLECTOR-MOTOR TEST T-2**

CONFIDENTIAL

CONFIDENTIAL



FIGURE 81. ELECTRON MICROPHOTOGRAPH OF PARTICLES IN GLASS TUBE-MOTOR TEST T-2



FIGURE 82. ELECTRON MICROPHOTOGRAPH OF PARTICLES IN GLASS TUBE-MOTOR TEST T-4

CONFIDENTIAL

CONFIDENTIAL

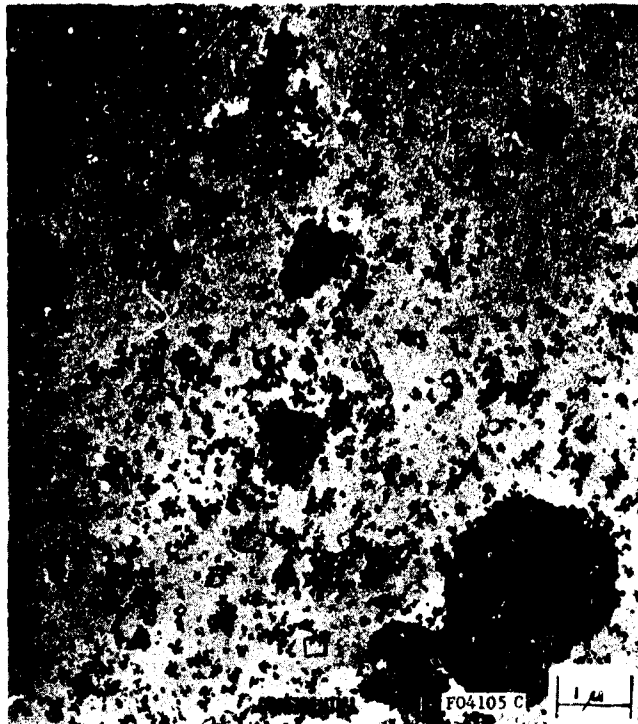


FIGURE 83. ELECTRON MICROPHOTOGRAPH OF PARTICLES ON GLASS SLIDE-MOTOR TEST T-2

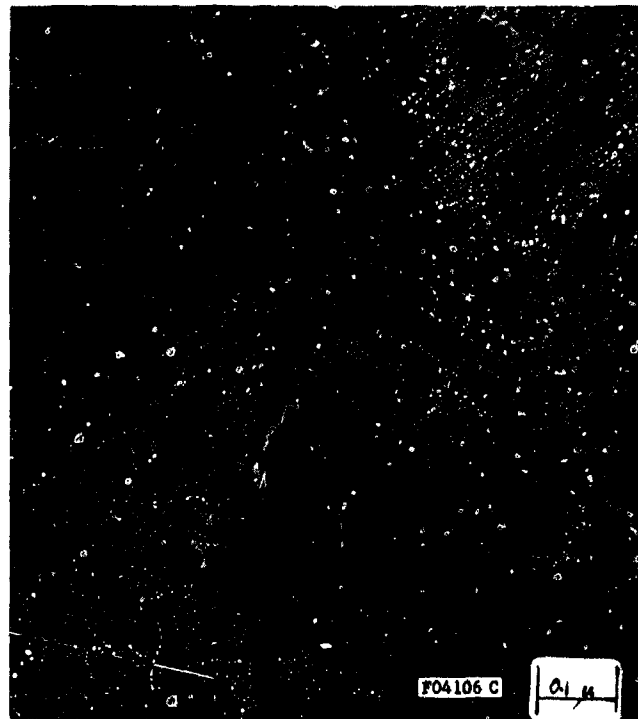


FIGURE 84. ELECTRON MICROPHOTOGRAPH OF PARTICLES ON GLASS SLIDE-MOTOR TEST T-2

CONFIDENTIAL

CONFIDENTIAL

range or distribution. Figure 81 shows the particles collected in the glass tube during Motor Test T-2. The method of removing the particles from the tube and preparing them for examination is responsible for the apparent lack of the small particles. Figure 76 shows particles collected from the glass tube during Motor Test T-3. The method of preparing the sample, in this case, did not mask a particular particle size. Figure 78 shows particles collected on the brass plate during Motor Test T-3. Those particles are similar to the others.

The serendipitous examination of one particular series of particles may have led to the finding of a different phase. Water was used to remove the nitrocellulose film from the glass slide. Normally amyl acetate is used to remove the film. Figures 83 and 84 are electron micro-photographs of the particles. The particles are typical in size and shape. However, the cubic phase which is "present" was not so obvious before. This phase has apparently been removed and what appears in the photograph is the impression of the original particle in the layer of carbon which was used to cover the slide. The use of water to remove the nitrocellulose film may have dissolved one phase. This could happen if the phase such as a chloride, was soluble in water.

Figure 84 shows an area where two particles were removed and the smaller particles which were in direct contact, at the edges and underneath, were not removed. This would tend to indicate that the particle was dissolved. The other explanation for the removal of the particle is that water has a much higher surface tension than amyl acetate, and it could more readily remove the particles. If this were the case, the particles which were in close proximity, as the particles in Figure 84 , would also be removed. This was the only time that particles of this type were found. Additional work will be done to confirm the existence of this phase.

While it would be highly desirable to discover whether or not the smallest beryllia particles are of the β structure, this has not been possible with the standard techniques in use. Also, an attempt has not been made to determine the approximate size distribution of the samples. Such an effort may eventually be undertaken, once the samples from the internal burning gram tests have been examined. Additional photographs of the particle samples have been taken and would be used for counting.

(b) (C) Aluminum Propellants

The particles collected from Motor Tests T-5, T-6 and T-7 (which utilized aluminized propellants) are shown in Figures 85 through 89 . These particles were collected with the modified particle collector which is discussed in Section IV. This particle collector used 6 glass vials in a vertical position where Vial No.1 was in the center of the plume and Vial No. 6 was 24 inches above the center of the plume. The remaining

CONFIDENTIAL

CONFIDENTIAL



FIGURE 85. PHOTOMICROGRAPH OF ALUMINA PARTICLES COLLECTED IN VIAL NO. 1
FROM MOTOR TEST T-5

CONFIDENTIAL

CONFIDENTIAL



FIGURE 86. PHOTOMICROGRAPH OF ALUMINA PARTICLES COLLECTED IN VIAL NO. 3
FROM MOTOR TEST T-5

-167-

CONFIDENTIAL

CONFIDENTIAL

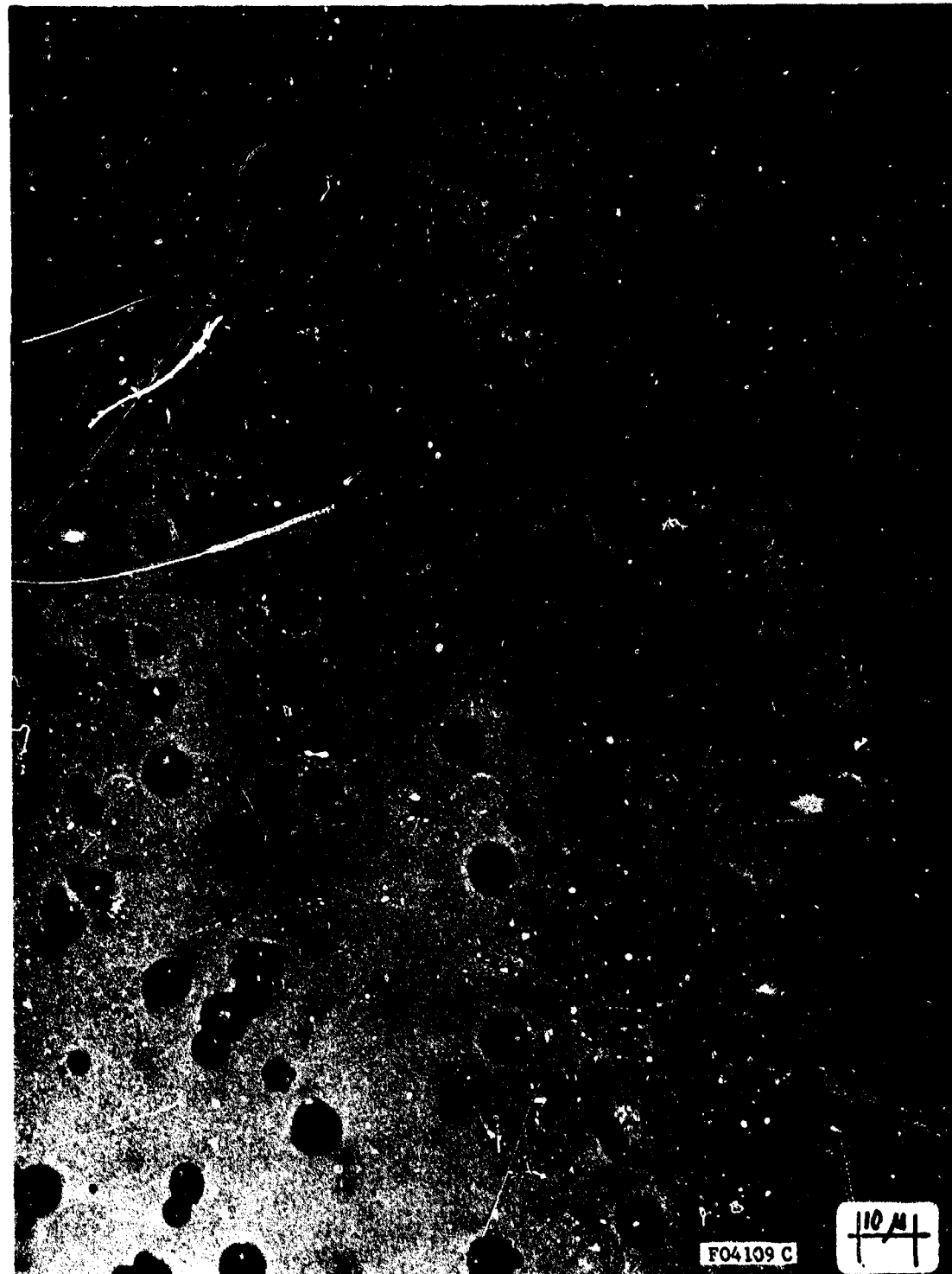


FIGURE 87. PHOTOMICROGRAPH OF ALUMINA PARTICLES COLLECTED IN VIAL NO. 5
FROM MOTOR TEST T-5

CONFIDENTIAL

CONFIDENTIAL

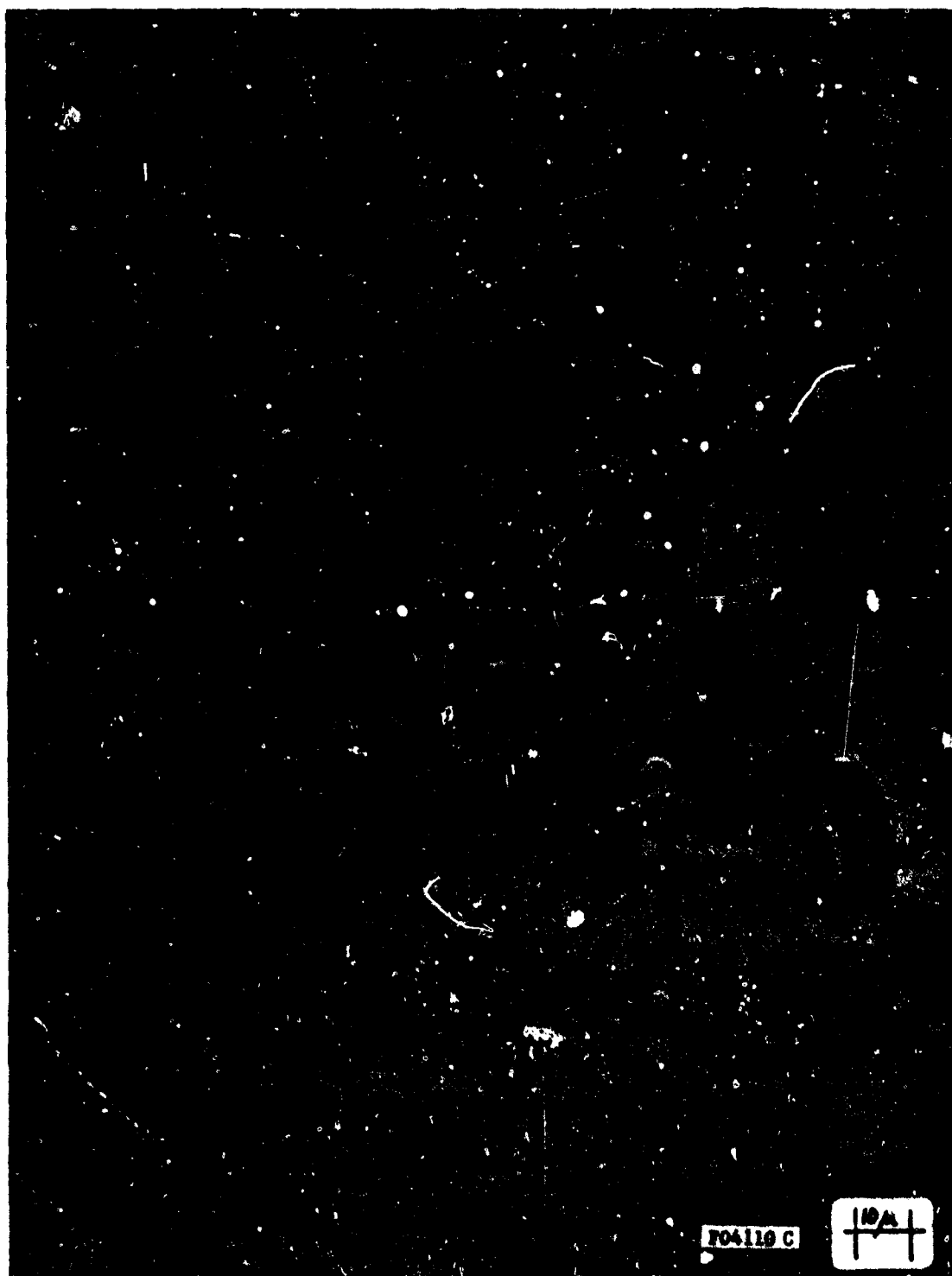


FIGURE 88. PHOTOMICROGRAPH OF ALUMINA PARTICLES COLLECTED IN VIAL NO. 3
FROM MOTOR TEST T-6

CONFIDENTIAL

CONFIDENTIAL

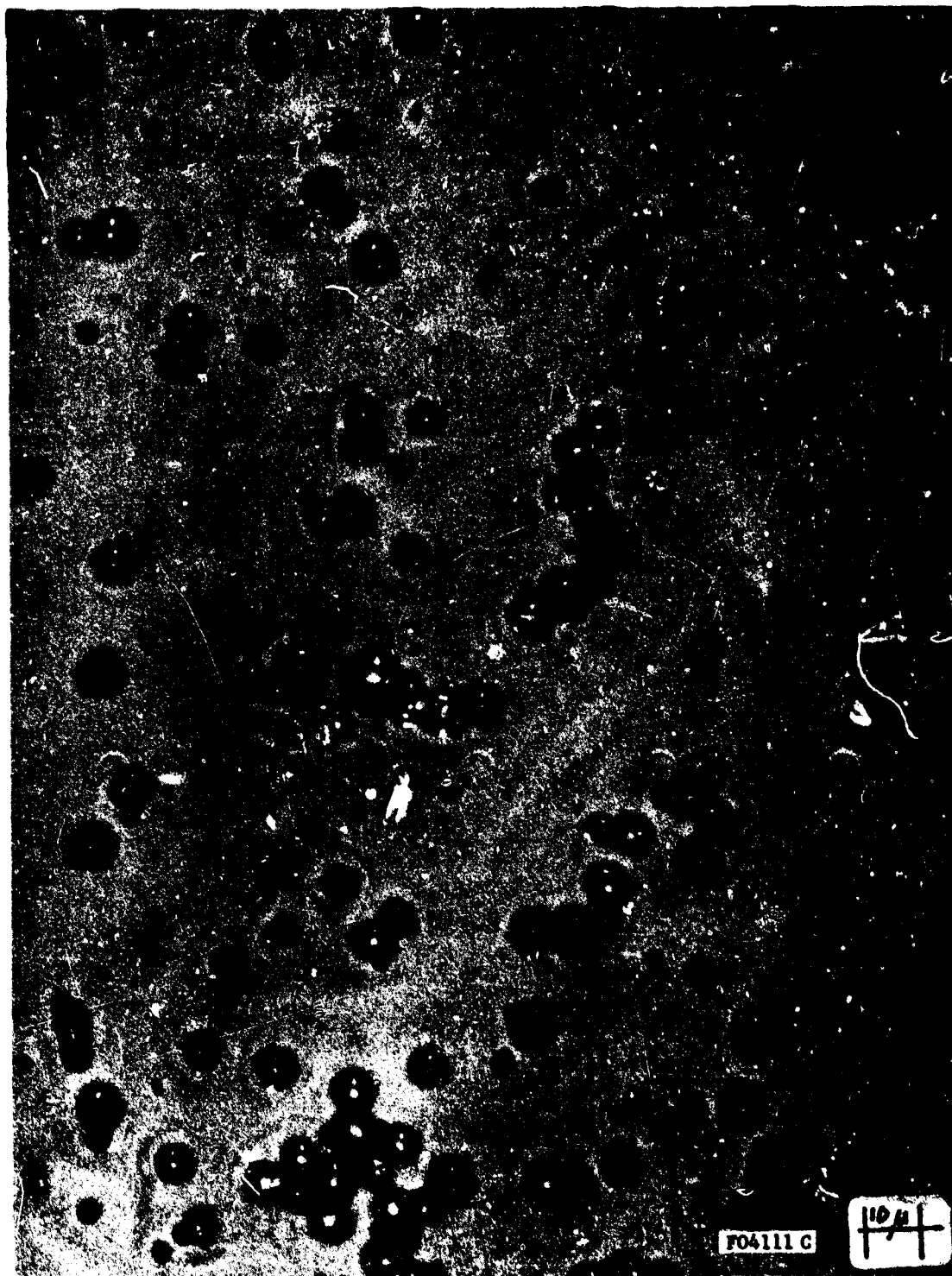


FIGURE 89. PHOTOMICROGRAPH OF ALUMINA PARTICLES COLLECTED IN VIAL NO. 3
FROM MOTOR TEST T-7

CONFIDENTIAL

CONFIDENTIAL

vials were immediately located in numerical order. The particles were removed from the vials with a slurry of 0.5 percent polyvinyl formal in ethylene dichloride and then spread on glass slides. These slides were examined by optical microscopy.

The particles were the typical spherical particles which are normally found in aluminized propellant exhausts. The particle size ranged from approximately 0.5 to 20 microns. The very small particles were not observable with the optical microscope but the number appeared to be small. There appeared to be continuous size variation with no size range having a larger number of particles. However, the mean mass particle diameter was estimated to be about 7 to 8 microns. There were very few large particles. While this observation may be related to the original aluminum metal particle size distribution, there are other plausible explanations involving the sampling and examination techniques.

The position of the vial in the exhaust plume did not result in collection of different sized or shaped particles. Figures 85 , 86 and 87 show the particles collected in Vials No's 1, 3 and 5 from Motor Test T-5. There is no obvious difference in the size, shape, or size distribution of the particles. The particles collected during Motor Test T-6 and T-7 did not give any different results. Figure 88 shows particles from Vial No.3 during Motor Test T-6 and Figure 89 shows the particles collected from Vial No. 3 during Motor Test T-7. These particles were essentially identical.

(2) (C) Samples From Other Programs

Limited work has been done on β beryllia in this quarter. Material which was prepared in the laboratory (see Reference 1, pages 117 through 120) was examined by electron microscopy. X-ray diffraction examination of this material showed it to contain 95 percent β beryllia and 5 percent graphite. Electron microphotographs of the powder are shown in Figures 90 , 91 and 92 . All of the particles appear to be crystalline and have a wide particle size range. The particle size is small, 0.01 to 0.5 micron, and in the same range as the particles collected from the motor test firings. These particles appear to have random size in the range, unlike the particles from the motor test firings which had very few particles in the 0.1 to 1.0 micron range.

(c) (U) Motor Hardware Analysis Procedure

In an effort to fully examine all hardware received and report all information, the following procedure has been established and is followed in the examination of all hardware.

- (1) All hardware is delivered in closed plastic bags in closed shipping containers.

CONFIDENTIAL

CONFIDENTIAL



FIGURE 90. ELECTRON MICROPHOTOGRAPH OF β BERYLLIA



FIGURE 91. ELECTRON MICROPHOTOGRAPH OF β BERYLLIA

CONFIDENTIAL

CONFIDENTIAL

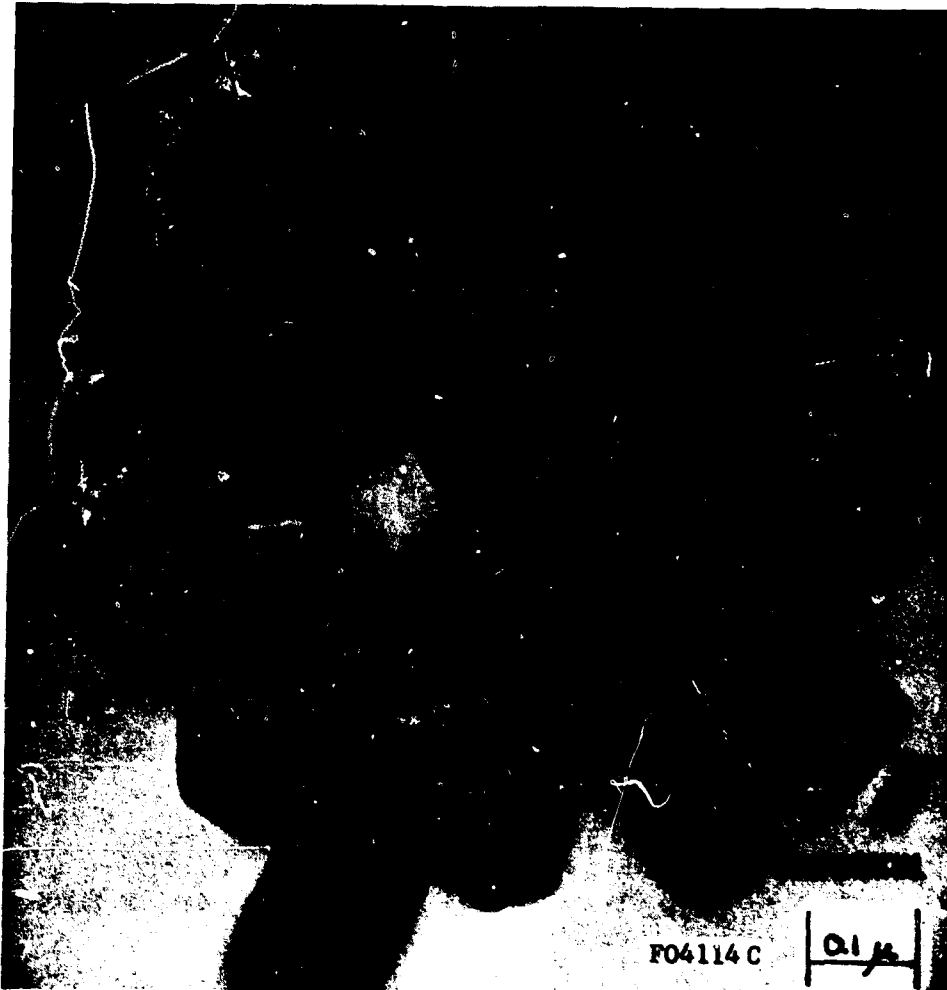


FIGURE 92. ELECTRON MICROPHOTOGRAPH OF β BERYLLIA

CONFIDENTIAL

CONFIDENTIAL

- (2) The hardware is delivered to a controlled area where it is unpacked and sprayed with clear Krylon.
- (3) All hardware is disassembled and photographed at this point. Disassembly may consist of removal of nozzle, entrance cone, and exit cone from steel housing, separation of aft closure insulator from chamber insulation, etc. Particular areas which are photographed are aft closure insulator, nozzle from the convergent side and nozzle from the divergent side. Any unusual areas are also photographed.
- (4) Samples of any deposits are taken for analysis by X-ray diffraction, X-ray spectroscopy or electron micro-photography. Normal areas where deposits are removed are aft closure insulator, entrance cap, throat area, and exit cone.
- (5) All vital dimensions will be remeasured.
- (6) Specific sections of various components will be examined and certain measurements will be taken on specific materials. These include:
 - (a) Ablating Insulators
 - Ablating insulators are cut in half and photographed.
 - The char depth is measured.
 - The char layer is examined for beryllium or aluminum compounds.
 - (b) Polycrystalline Graphite
 - All polycrystalline graphite exposed to the flame is cut in half and examined. Any erosion is determined.
 - Any areas of excessive loss of material are examined for reaction with propellant gases (Be or Al compounds) and microstructure.
 - (c) Pyrolytic graphite
 - All unusual areas are examined. Those include delamination, deformation, grooves, etc. C spacings are measured where the information might be pertinent.

CONFIDENTIAL

CONFIDENTIAL

- Deposits between individual washers are analyzed.
- Insert sections are halved, photographed, and the contour checked.

(d) Dense Tungsten

- Inserts are cut in half, photographed, and the concour checked.
- Cut surfaces are prepared for metallographic examination. Particular items or areas which are examined are grain size, grain boundries, and melted areas.
- When particularly interesting areas are found, they are subjected to examination with the electron microprobe. This equipment permits the detection of elements with atomic numbers as low as 5 (boron).

(e) Infiltrated Tungsten

- Inserts are cut in half and photographed.
- The amount of infiltrant lost is determined.
- Any areas of reinfiltration by Al compounds or by Be compounds are noted.
- Reaction between the exhaust products and the tungsten or infiltrant is noted.
- Examination is made for the loss of infiltrant from the back side, upstream or downstream ends and any reaction in those areas with the back-up material.

In all cases where it is possible to cut the nozzle in half with the upstream, downstream, and throat insert intact, this is done to allow a more complete picture for contour comparison. The procedure may be considered somewhat complicated and extensive, but it is felt that complete analysis of all hardware is useful. The procedure is also somewhat flexible and can be modified whenever interesting or unusual areas are discovered.

CONFIDENTIAL

CONFIDENTIAL

3.5 (C) CONCLUSIONS, RECOMMENDATIONS, AND FUTURE WORK

a. (C) Conclusions

Preliminary conclusions have been formulated based on the results of the laboratory studies conducted to date. These are presented below for each subtask. Caution should be exercised in generalizing or extending these conclusions out of the intended context. Conclusions which were presented in paragraph 3.5 of Reference 1 are not repeated.

(1) (C) Condensed Phase Reaction Studies

The most interesting condensed phase interaction examined is the alloying of beryllium with tungsten. The formation of WBe_{12} (melting point near 2300°F) and WBe_2 (melting point about 3000°F) is similar to the molybdenum-beryllium and tungsten-carbon systems. It is concluded that the exposure of tungsten insert surfaces to unburned beryllium metal could lead to the catastrophic failure of the insert. Oxidation of the beryllium at the tungsten surface and carbide formation, due to gaseous hydro-carbon decomposition at the tungsten surface, are probable contributing failure mechanisms.

The refractory beryllium compounds (carbide, oxide and nitride) are not directly involved in the degradation of tungsten inserts. (The role of beryllium hydroxide gas has not been experimentally examined.)

At rocket pressures, beryllia and alumina will wet graphite and tungsten as a result of the formation of the intermediate layers of carbides, oxycarbides and by tungsten dissolution, as appropriate. At sufficiently high temperatures, the intermediate layers which form on graphite are destroyed, and rapid reaction between the carbon and either oxide may occur. However, the gaseous reaction products will tend to remove the oxide deposit. Dissolution of tungsten by molten oxides could be serious over long periods of exposure time.

The mixing of silica, from insulation materials, with the metal oxides will complicate the chemistry and probably lower the melting point of the mixture (relative to the pure oxide). While such mixtures were not studied experimentally, it is believed that the sticking mechanisms and chemical reactivity of the mixtures will remain essentially unchanged.

(2) (C) Arc-Plasma Studies

While beryllia and alumina sticking on asbestos and graphite surfaces was achieved, the experimental objectives of the arc plasma study were only partially realized. At the experimental pressure, the chemical sticking mechanisms which should pertain at rocket pressures, are not faithfully

CONFIDENTIAL

CONFIDENTIAL

reproduced. Since this conclusion is most applicable to the beryllia, the observed behavioral differences of the two oxides can not be extrapolated to rocket conditions.

The observed reflection of alumina from the graphite surface, which was initially just below the alumina melting point, was anticipated. However, the temperature level at which this occurs should be significantly higher at rocket pressures. Undoubtedly, the threshold temperature for alumina reflection graphite will also be a strong function of impact velocity, impact angle, and particle size.

The initial reflection of both beryllia and alumina by asbestos phenolic is believed to be a result of the rapid thermal and mechanical degradation of the surface of the plastic during the initial pyrolysis. Soft, non-charing ablators (teflon, nylon phenolic, rubber, etc.) would be expected to reject the deposit in a similar manner.

It appears that oxide sticking on the asbestos phenolic may have commenced at the time when molten silica or silicates first appeared at the surface. Alumina (and presumably beryllia at higher pressures) was observed to stick to the graphite and to precharred asbestos phenolic. It is therefore likely that either oxide would stick on carbon or graphite cloth materials throughout the intermediate temperature range. That is, sticking will start after the initial high rate of pyrolysis is past and a reasonably strong char is formed. The sticking period will end when the char surface temperature reaches a level where the intermediate carbide and oxycarbide layers decompose to gaseous products. It is anticipated that carbon or graphite cloth insulators would accumulate less deposit than the silica-re-enforced types of insulators, both because there is no molten phase present and because the time spent in the sticking temperature range (about 3000°F to 4700°F) will be short.

At the highest material's surface temperatures, where chemical sticking can no longer occur, some of the impinged deposit may continue to flow along the surface. Rather small quantities are expected and the flow should not be continuous. Drops, beads, or streams of oxide will react with the surface forming gases which may tend to propel them along forming shallow axial grooves.

(3) (C) Hardware and Nozzle Deposits Analysis

The post-test analysis showed that the hardware tested was typical of other hardware exposed to similar conditions. There was nothing unusual or unexpected found from any of the hardware or the condensed phase deposits. Consequently, it is concluded that the equilibrium combustion objective was achieved.

CONFIDENTIAL

CONFIDENTIAL

There was no unburned beryllium metal found in any of the residue examined. Aluminum metal was found in both chamber slag and in the aft-closure insulator char. It is believed that this observation is significant and, further, that it supports the hypothesis that beryllium metal does not melt and agglomerate on the propellant surface as aluminum apparently does.

(4) (C) Exhaust Plume Sample Analysis

The condensed phase material collected from beryllium containing propellant exhausts exhibited a variety of shapes, some spherical, some irregular, but mostly crystalline. The particle size ranged from very small (<0.01 micron) to 5 to 8 microns. Differences in samples from the four propellant formulations could exist but were not noted.

All beryllium exhaust particle samples were examined by X-ray diffraction and were found to α BeO. There were no carbides, nitrides or β BeO found.

The exhaust particle samples collected from aluminum containing propellants were all spherical. The particle size ranged from 1 to 20 microns. X-ray diffraction analysis indicates that the particles are α and γ Al_2O_3 .

These results generally indicate that the desired equilibrium combustion condition was obtained in the end burning grain tests T-1 through T-7.

b. (U) Recommendations

Based on the observed existence of two beryllium-tungsten alloys with melting points which are well below the analogous carbon-tungsten compounds, it is recommended that tungsten inserts be examined for beryllium content, as well as carbon, at least when there are indications of melting or flow of exposed surfaces. Such a discovery is indicative of the tungsten insert failure (or damage) mechanism and is suggestive of poor beryllium metal combustion. Note, however, that the grain design, flow velocities, and nozzle contour must be such that deposition of unburned beryllium could have actually occurred.

It is apparent that the chemical interaction of beryllia and alumina with graphite and asbestos phenolic chars is both pressure and temperature dependent. Therefore, it is recommended that the use of low pressure arc plasma testing techniques be most carefully considered. The behavior of insulation and graphite materials in low pressure test can not be directly extrapolated to the rocket environment.

CONFIDENTIAL

The application of the cold flow modeling techniques in the present program and in Contract NAS7-408 has demonstrated its capabilities in characterizing particle impingement location, flow stagnation, recirculation flow, and flow irregularities in complex motor and gain configurations. It is recommended that the cold flow modeling technique be used in support of preliminary configuration design studies and motor insulation materials selection. It is also recommended that the technique be applied to the area of hot gas valving and ducting development studies.

The post-test analysis procedures developed for the purposes of this program could provide useful information in the analysis of nozzles failures and in the development of advanced propellant formulations. However, it is not recommended that they be applied in general both because of the associated cost and because there is no indication that "successful" firings will yield unpredictable deposit or materials behavior. The post-test evaluation of ablative materials performance and the examination of exhaust plume particles may be useful under many circumstances, at least until the ablation and propellant combustion phenomena are well understood.

c. (U) Future Work

The major task remaining in the laboratory studies is the post-test analysis of motor hardware, condensed phase deposits, and exhaust plume particle samples. The results of the analysis for all of the remaining small motor tests will be reported in the next progress report. The analysis of hardware from Tests T-9 through T-12 is in progress. Any analysis of the 500 pound development motor test hardware will be presented in the final report. It is expected that nozzles, predominantly with tungsten inserts, from several other programs will be examined during the next reporting period. The primary source of such hardware will be the Aerojet ADOBE program.

The effort to relate the results of the condensed phase reaction, plasma deposition and cold flow modeling studies will continue. Consideration of the β beryllia question will also be continued. Some effort will be devoted to the examination of the suspected chloride phase in the plume samples.

SECTION IV (C)

CORRELATION STUDIES

4.1 (U) OBJECTIVES, SCOPE AND SUMMARY

a. Objectives

The primary objectives of the correlation studies effort in this program are to obtain and correlate data (from this and other programs) in a manner which can be used to help verify and/or explain the mechanisms of beryllium propellant erosion and corrosion in rocket motors. The correlation studies effort is divided into two basic functions: correlation and instrumentation. The correlation function incorporates three basic divisions of work: data acquisition, data classification, and data correlation. The instrumentation function for this program encompasses the acquisition of data for the correlation function through thermal instrumentation, ballistic instrumentation, and exhaust plume sampling.

The objectives of the correlation function during the second reporting period of this program are outlined below.

(1) Data Acquisition

- (a) Acquire thermal and ballistic data from the motor tests of this program.
- (b) Obtain data from related programs which will aid in establishing correlations.

(2) Data Classification

- (a) Classify and record all pertinent data from the tests of this and related programs.

(3) Data Correlation

- (a) Attempt to find correlations with motor test data only. This effort will be restricted to the propellants used in this program.
- (b) Attempt correlations to support basic corrosion/erosion theories.

The objectives of the instrumentation functions for the second reporting period of this program are outlined below.

(1) Thermal Instrumentation

- (a) Continue to evaluate the instrumentation and data requirements based on performance and the program objectives.
- (b) Provide adequate and flexible instrumentation as required.
- (c) Establish a tentative list of thermal instrumentation for the remainder of the small scale motors.
- (d) Obtain or manufacture necessary special instrumentation.

(2) Exhaust Plume Sampling

- (a) Obtain exhaust plume particle samples from all tests.
- (b) Evaluate the capabilities of the exhaust plume particle sampler No. 1. Establish the need for particle sampler No. 2.
- (c) Design and fabricate a second particle sampler as required.
- (d) Evaluate the second sampler.

b. Scope

The correlation studies effort has been separated into two basic functions: instrumentation and correlation. The overall scope of the instrumentation

function is defined and limited by the requirement that sufficient instrumentation be provided on each motor to characterize the nozzle thermal history and the motor performance. In addition, the instrumentation must be provided in accordance with the test schedule. The scope of the correlation function is more difficult to define even though there are more specific requirements and limitations. The correlation effort will include the collection and organization of appropriate beryllium and aluminum propellant motor design and test data and the correlation of the results of laboratory tests, motor tests, and analytical studies. This effort will be limited to studying selected types of propellant and nozzle systems and to providing support in the general areas of the analytical efforts.

The effort expended on the correlation studies during this charter was divided almost equally between the instrumentation and correlation functions. Where it was necessary to set a priority, the instrumentation function was accomplished first. This was necessary to prevent undue delays in the design, fabrication, and test schedules.

The scope of the instrumentation function was defined and limited by the following requirements:

- (1) Adequate instrumentation will be supplied according to the fabrication and test schedule.
- (2) Exhaust volume particles will be taken from all tests.
- (3) Consideration will be given to only the small-scale motor tests.
- (4) All instrumentation will be continually reviewed for quality and quantity of data required.

The overall scope of the data correlation function has been defined and limited by the following general requirements:

- (1) State-of-the-art propellants with beryllium metal additives will be investigated.
- (2) A minimum number of aluminum propellants and test data, which are comparable to the beryllium propellants and data, will be considered.
- (3) Both composite and double base propellants will be considered and compared.

CONFIDENTIAL

During this quarter, the scope of the data correlation effort was further defined by the following requirements:

- (1) Only propellants of the type used in this program were to be examined in detail.
- (2) Correlation attempts would initially consider raw data trends. Correlation of selected data in support of specific theories will be attempted during the third reporting period.

c. Summary of Progress

The following is a brief description of the progress made in the correlation studies effort during the second reporting period:

- (1) The thermal instrumentation performance on the first seven motor tests has been evaluated.
- (2) The thermal instrumentation requirements have been tentatively established for the remainder of the small motor tests.
- (3) A radiometer was fabricated and tested on two motors.
- (4) A portion of the special thermocouples required for the small scale submerged and steep inlet nozzles have been purchased and installed. The remainder of the special thermocouples were fabricated by Aeronutronic.
- (5) The exhaust plume particle sampler No. 1 was tested and the results evaluated.
- (6) Particle sampler No. 2 was designed, fabricated, and tested. The purpose of this sampler is to obtain particle samples at various radial positions from within the plume and to minimize the loss of sample material due to handling.
- (7) Correlations of corrosion-erosion were demonstrated for selected propellants.
- (8) Correlations of the metal oxide deposition encountered during the first seven motor tests of this program were attempted.

CONFIDENTIAL

CONFIDENTIAL

4.2 (C) CORRELATION

a. (U) Data Acquisition

The motor test data obtained during the first quarter of this program were selected with the primary objective of providing a basic background of information on beryllium propellant motor design problems. This type of information was particularly useful in the initial hardware design phase of this program. The data selected for study during the second quarter of this program were chosen with the primary purpose of establishing raw data correlations. Most of the data used were from small motor tests with propellants similar to those being tested on this program. It was anticipated that, if correlation could be established with these propellants, the correlation of data from other propellants and motor configurations for which there are less data, may be simplified.

Most of the motor tests considered during this reporting period were of the type used for propellant evaluation and tailoring tests. The tests were generally short (of the order of 3 to 10 seconds). However, for most cases, the throat insert material was a polycrystalline graphite. The flame-side surface, of this type of graphite throat insert will reach temperatures, in the short firings, comparable to those attained by pyrolytic graphite insert during much longer firing. The aft closure and nozzle entrance sections of the small motors were usually polycrystalline graphite. Thus, the collection and solidification of the metal oxides on these surfaces would have much less effect on the throat deposition than is expected in larger motors. It was estimated that surface temperatures high enough to melt beryllium oxide could be attained at the nozzle throat in less than 0.5 second for some propellants. Therefore, data from these tests would be valid in evaluating the effects of various design parameters on erosion and corrosion of the graphite throat materials.

The literature survey and data acquisition required for this program are not considered complete. It is anticipated that data from other programs will be continually reviewed, evaluated, and collected for use through the duration of the program. It is expected that data from the Aerojet ADOBE program will be examined in detail during the next reporting period.

b. (C) Data Correlation

An examination of the data collected thus far indicates that the corrosion-erosion phenomenon is truly a complex function of a large number of parameters and conditions. However, an attempt was made to point out some obvious correlations with selected data. These correlations reflect the combined effects of heat transfer, mass transfer, and thermochemistry phenomena, even though the number of geometric variables was kept to a minimum. The primary objective was not to verify a given set of hypotheses, but to show that some of the beryllium motor test data will correlate on

CONFIDENTIAL

CONFIDENTIAL

some basic parameters. One of the objectives of these correlation attempts was to point out inconsistencies. It is this supposed inconsistency that has led to the conclusion that beryllium data will not correlate or behave in the "normal" manner similar to the aluminum data. An attempt has been made to illustrate a few of the reasons beryllium propellant test data appear to be inconsistent - noncorrelatable.

By examining a large number of test results from propellant tailoring motor tests, it was concluded that the primary reason correlation of data has been difficult is that the metal or metal oxide deposition on the nozzle is interfering with corrosion. In much of the data, the amount and duration of the deposition makes it impossible for gas phase corrosive attack to occur at all. However, in some cases, depending on the propellant, the test motor configuration and material, the nozzle surface was exposed to the gaseous combustion products for a significant portion of the run. Data from these tests were found to be the most useful in establishing basic correlation. For example, the results from nine 10-pound, tailoring motor tests, using Arcocel 191, 191A, and 191B propellants, were taken from Reference 15 and tabulated in Table XX for direct comparison. From the data, it can be inferred that the nozzles were exposed to the exhaust gases for the larger part of the firing time. Thus, the data from these tests should be representative of the beryllium propellants and comparable to aluminum propellant data.

One of the more common correlations attempted with aluminum propellants is that of relating erosion rate to the nozzle heat transfer. The geometry of the motors and throat inserts is nearly constant for all the tests presented in Table XX, thus eliminating some of the more important variables. The term erosion rate (δ) is generally defined as the total amount of radial throat erosion divided by the action time. This definition, however is somewhat in error when a protective deposition layer coats the nozzle for a significant portion of the run and when the erosion rate changes with time during the run. The deposition layer remains attached to the nozzle surface until the nozzle surface temperature reaches approximately the melting point of beryllia. Since alumina melts about 1000°F lower than beryllia, the presence of the deposit is not as noticeable in correlation studies. However, the standard definition of δ will be used in these correlations since: (1) the surface temperature is related to the gas side heat transfer coefficient which for a given propellant and motor configuration is related to the chamber pressure (among other things), and (2) the amount and type of material which could be deposited may also be related to the chamber pressure. Figure 93 presents a plot of erosion rate as a function of the average chamber pressure (\bar{P}_c) for the 191 propellant tests tabulated in Table XX. Note that using the uncorrected raw data, there is a correlation of the data with average chamber pressure approximately to the 0.734 power. This relationship is very close to the 0.8 power relation between the theoretical heat transfer coefficient and chamber pressure. The chamber stay-time for these tests is estimated to be about one millisecond at the low pressure and about 3 milliseconds at the highest pressure.

CONFIDENTIAL

CONFIDENTIAL

TABLE XX. MOTOR TEST DATA FOR THROAT EROSION CORRELATIONS

Propellant Weight: W_p (lbm)	Burn Time, T (sec)	Erosion Rate, δ (mils/sec)	Throat Diameter Before (D_1^*) (in.)	Throat Diameter After (D_2^*) (in.)	Burn Rate, r_b (in./sec)	Average Chamber Pressure, P_c (psia) ^c
Double base (Arcocel)						
319B	12.58	2.35	4.1	1.208	1.227	0.23
319B	9.78	2.106	0.95	1.250	1.254	0.21
319B	2.84	0.481	-61.3	1.138	1.079	0.21
191	9.95	3.51	6.13	1.067	1.110	0.3
191	9.5	3.28	3.81	1.045	1.070	0.32
191A	10.17	3.84	2.48	1.048	1.067	0.27
191A	10.26	3.45	3.91	1.000	1.027	0.30
191A	12.25	2.54	0.773	1.540	1.544	0.21
191B	10.8	4.10	3.42	1.047	1.075	0.25
191	10.83	2.36	12.7	0.820	0.880	0.44
191A	10.58	2.05	12.65	0.810	0.862	0.50
191B	10.85	3.08	8.12	0.920	0.970	0.33
Composite (Arcane)						
54	10.88	4.15	8.66	0.674	0.746	0.25
54A	10.96	4.68	6.1	0.668	0.725	0.22
						1021.5
						949.8

CONFIDENTIAL

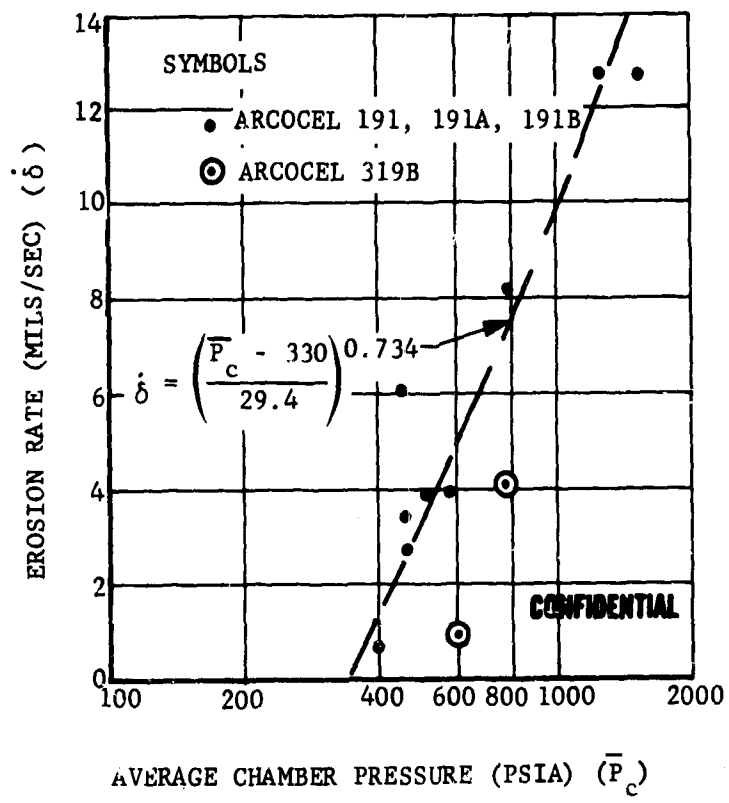
CONFIDENTIAL

TABLE XX. (Continued)

<u>Propellant</u>	<u>Burn Time,</u> τ <u>(sec.)</u>	<u>Erosion</u> δ <u>(mils/sec.)</u>	<u>Throat Diameter</u> Before (D_1^*) After (D_2^*) (in.)	<u>Burn Rate,</u> r_b <u>(in./sec.)</u>	<u>Average</u> <u>Chamber</u> P_c <u>(psia)</u>
24	10.77	5.58	-3.76	0.890	0.19
24	10.85	5.58	-3.85	0.891	0.19
53	10.97	5.07	5.525	0.877	0.200
53	10.86	5.23	6.6	0.821	0.200
53	10.95	4.73	4.76	0.828	0.220
53	10.95	4.76	6.92	0.821	0.230
53	10.65	4.65	5.27	0.821	0.229
53	10.98	4.54	4.3	0.747	0.23
53	10.96	4.56	0.983	0.821	0.23
53	10.88	4.71	3.6	0.821	0.23
53A	10.99	4.76	7.04	0.670	0.22
53B	10.77	4.62	4.12	0.671	0.22
				0.709	0.22
					980.2

CONFIDENTIAL

CONFIDENTIAL



F04115 C

FIGURE 93. NOZZLE EROSION RATE AS A FUNCTION OF CHAMBER PRESSURE FOR SELECTED DOUBLE BASE PROPELLANTS

CONFIDENTIAL

CONFIDENTIAL

The data scatter in Figure 93 may be reduced by normalizing the propellant weight, throat diameter, and average burn rate. By making several trial and error crossplots of the data from the nine 191-propellant tests, it was found that the erosion rate was proportional to chamber pressure (P_c), weight of the propellant (W_p), average throat diameter (D^*), propellant burn rate (r_b), and action time (T). Equation 9 can be used to correlate the erosion rate to within 10 percent of the actual value.

$$\delta_c = (0.00835) \left(\frac{P_c}{330} \right)^{0.734} \left(\frac{W_p}{D^*} \right)^{0.2} \left(\frac{1}{1.71 - 0.228} \right) (r_b T) \quad (9)$$

Of course, this equation applies only to the ARC 191 propellant in the ARC 10-pound tailoring motor. The equation may be used to predict erosion by iteration.

Due to the limited number of data points available for the other three beryllium propellants being considered on this program, it was not possible to develop corresponding correlations. However, to illustrate a potential correlation in what may have been considered noncorrelatable data, corrosion-erosion rate was plotted against average chamber pressure for the available ARC 319, 24, and 54 propellant data points (see Table XX and Figures 93 and 94). In addition, the more abundant Arcane 53 propellant data were plotted on Figure 94. These additional data may not necessarily be representative of the Arcane 54 composite propellant; however, they are presented to illustrate a potential trend. Note that with the Arcane 53 propellant, the erosion rate reaches a minimum at a chamber pressure of about 700 psi. At pressures either lower or higher, the data indicate that erosion rate increases. The right side of the V-shaped curve drawn on the data in Figure 94 has a slope which is only slightly greater than the one which was established for the 191 propellant data. The phenomena which cause the erosion to increase with pressures above 700 psi are probably the same for the 54 and 191 propellants (increased surface temperature causes a corresponding increased carbon reactivity). The increasing erosion with decreasing pressure, illustrated by the left side of the V-shaped curve drawn on the data in Figure 94, may be attributed to increasing available oxygen due to incomplete propellant combustion at the lower pressures. The very short time Arcane 24 tests exhibited no erosion due to deposit coating of the throat. The estimated chamber stay times range from 3.4 milliseconds at the low pressure to 5.0 milliseconds at the high pressure for the Arcane 53 propellant. The stay time corresponding to the minimum erosion is 4 milliseconds.

A study of corrosion-erosion in metallized propellants should always consider, to some extent, the problem of metal or metal oxide deposition. The material being deposited could obscure or confuse what may otherwise have been obvious conclusions. The deposition encountered in the first

CONFIDENTIAL

CONFIDENTIAL

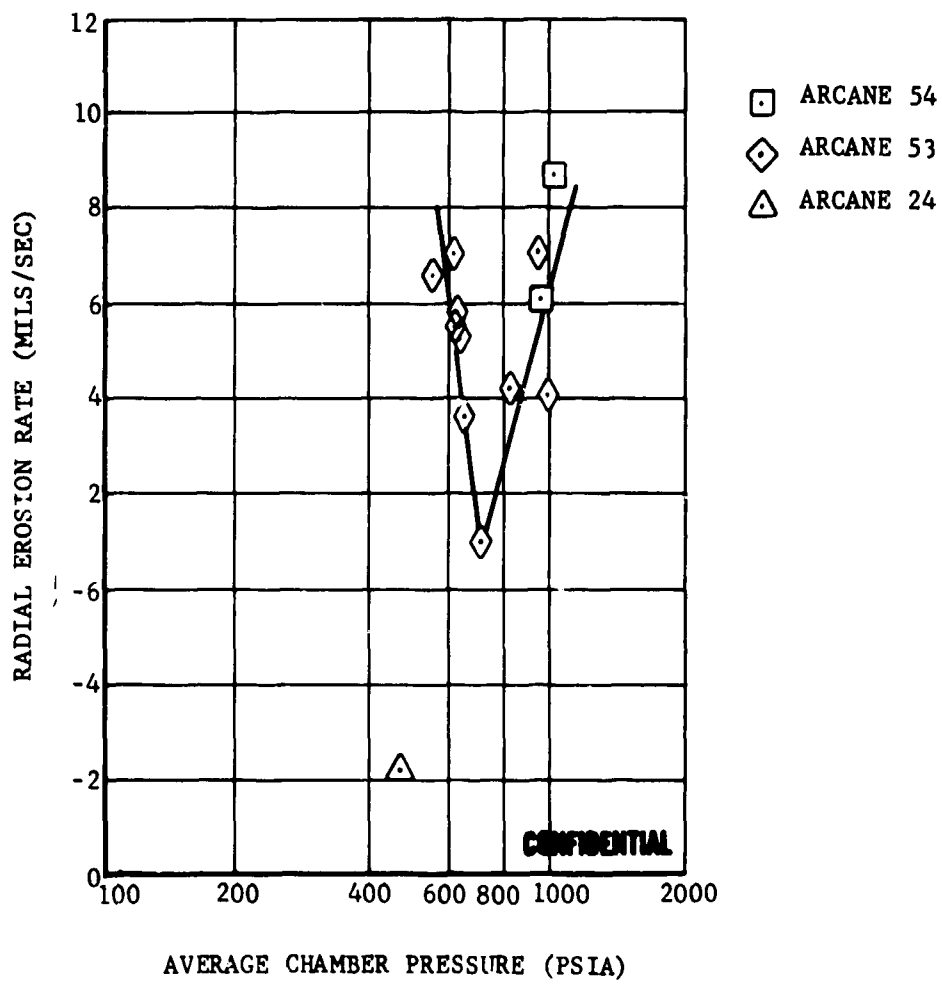


FIGURE 94. NOZZLE THROAT EROSION RATE AS A FUNCTION OF CHAMBER PRESSURE FOR SELECTED COMPOSITE PROPELANTS

F04116 C

CONFIDENTIAL

CONFIDENTIAL

seven tests of this program has proven to be a significant detriment to establishing corrosion correlations. On the other hand, the presence of such large amounts of lasting deposition points clearly to a design approach by which some beryllium propellants may be kept from seriously corroding or eroding the nozzles and other hardware.

There are certain trends displayed in the deposition data derived from the first seven motor tests that should be pointed out. Deposition data subsequently obtained during this program will be added to that already derived in order to help prove or disprove the data trends described below.

Table XXI presents a numerical compilation of the deposition and erosion data (generated in Paragraphs 2.5 and 5.2b of this report). The data in Table XXI are arranged in two basic groups: aluminum and beryllium additive propellants. Within each of these groups, the data are segregated into double base and composite propellants. Plotted on the table for each propellant are flame temperature, percent metal additive, characteristic exhaust velocity, and XSO. These are parameters commonly used in attempting correlations.

The following is a list of some of the more obvious correlations deduced from the data in Table XXI.

The deposition data available from the aluminized propellants indicate:

- (1) The total deposition-time integral is inversely proportional to the propellant flame temperature for both the double base and composite propellants.
- (2) The total deposition-time integral is proportional to the XSO for the two double base propellants (no conclusion can be made for the composite).
- (3) The maximum computed deposition thickness during the run is inversely proportional to the flame temperature for both the composite and double base propellants.
- (4) The maximum deposition is inversely proportional to the XSO for the double base propellants.

CONFIDENTIAL

CONFIDENTIAL

TABLE XXI. NOZZLE DEPOSITION AND EROSION DATA

<u>Propellant Type</u>	<u>Test</u>	$\int_{\delta dt}^{\tau}$ <u>Deposition</u>	<u>Flame Temperature</u>	<u>Percent Metal</u>	<u>C: Delivered</u>	<u>XSO</u>	<u>-δ (mils)</u>	<u>Peak Deposition</u>	<u>+δ (mils)</u>	<u>Peak Erosion</u>
191F	1	0.225	3758	13.79	5170	J.15	30	5		
319F	3	0.1235	3517	10.77	5525	0.05	23	3		
54F	4	0.533	3429	12.98	4765	0.15	35	-9		
24F	2	0.450	3400	11.95	5055	0.30	48	-1		
389	7	0.0393	3766	23.07	4800	0.15	5.5	2.5		
390*	6	0.141	3510	18.41	4910	0.05	14	1		
60	5	0.216	3417	22.14	4910	0.15	29	2.5		

* Hangfire

CONFIDENTIAL

CONFIDENTIAL

The deposition data available for the beryllized propellant tests indicate:

- (1) The total deposition-time integral and peak deposition thickness are proportional to the flame temperature and percentage of metal additive for both the double base and composite propellants.
- (2) The total deposition-time integral is inversely proportional to the delivered characteristic exhaust velocity.

In general it can be inferred from both the total deposition-time integral and the peak deposition thickness computed that the composite propellants produce more deposition than the double base propellants. This applies to both the aluminized and beryllized propellants.

CONFIDENTIAL

CONFIDENTIAL

4.3 (C) MOTOR TEST INSTRUMENTATION

a. Thermal Instrumentation

(1) (U) Conduction

The primary objective of providing conduction thermal instrumentation on the test hardware is to obtain sufficient temperature response data to experimentally characterize the performance of the nozzle and other critical motor components. In general, the measured temperature transients will be compared with the computer calculated transients. It is expected that, through multiple trials and comparisons, the various combustion and thermodynamic phenomenon may be verified and/or explained. The ultimate goal is that the complete thermal history of a given motor with a given beryllium propellant can be computed directly (or computed indirectly with minor testing to provide only key data points).

All of the first seven motors fired during this program had potential instrumentation locations, as shown in Figure 95. A tentative instrumentation list for the first 15 motors was presented in Table XVIII of Reference 1. This list was considered representative of the desired thermal instrumentation for the first 15 motor tests. However, it was anticipated that the instrumentation requirements would be modified based on the results of the first few tests. For example, type "S" thermocouples were listed for use in ports 1, 3, and 5. It was expected that type "K" could be later substituted if the recorded temperatures on the first firings were low enough. It was also anticipated that the use of ports 2, 6, 7, 13, 14, and 15 could be suspended, provided the data from these areas were not unusual. Table XXII presents a revised instrumentation list for the small scale motor tests. The instrumentation requirement listed for the first seven motor tests is representative of what was actually used on those tests.

A quick review of the quality of the thermocouple data from the first seven tests is presented in Table XXIII. The data from each thermocouple port location were judged good, fair, poor, or unusable. Classification of the data quality was based on the following requirements: (1) the soak-back temperature, or maximum temperature at that location, was clearly obtained and recorded; (2) the initial temperature rise transient was obtained; (3) the temperature decline was obtained; and (4) the curves were smooth, indicating good thermal contact and a low noise level in the recording system. Data classified as "good" had all four of the above qualities. Data classified as "fair" had qualities (1), (2), and (3), but the curves are not required to be smooth. Data classified as "poor" had qualities (1) or (2). Note in Table XXIII, that the data from some ports, such as 9, 10, and 12 were classified as "good" on most of the tests. It should be noted that very few of the thermocouples produced totally unusable data. Of the 67 thermocouples used on the first 7 tests, 48 provided data considered good, 7 fair,

CONFIDENTIAL

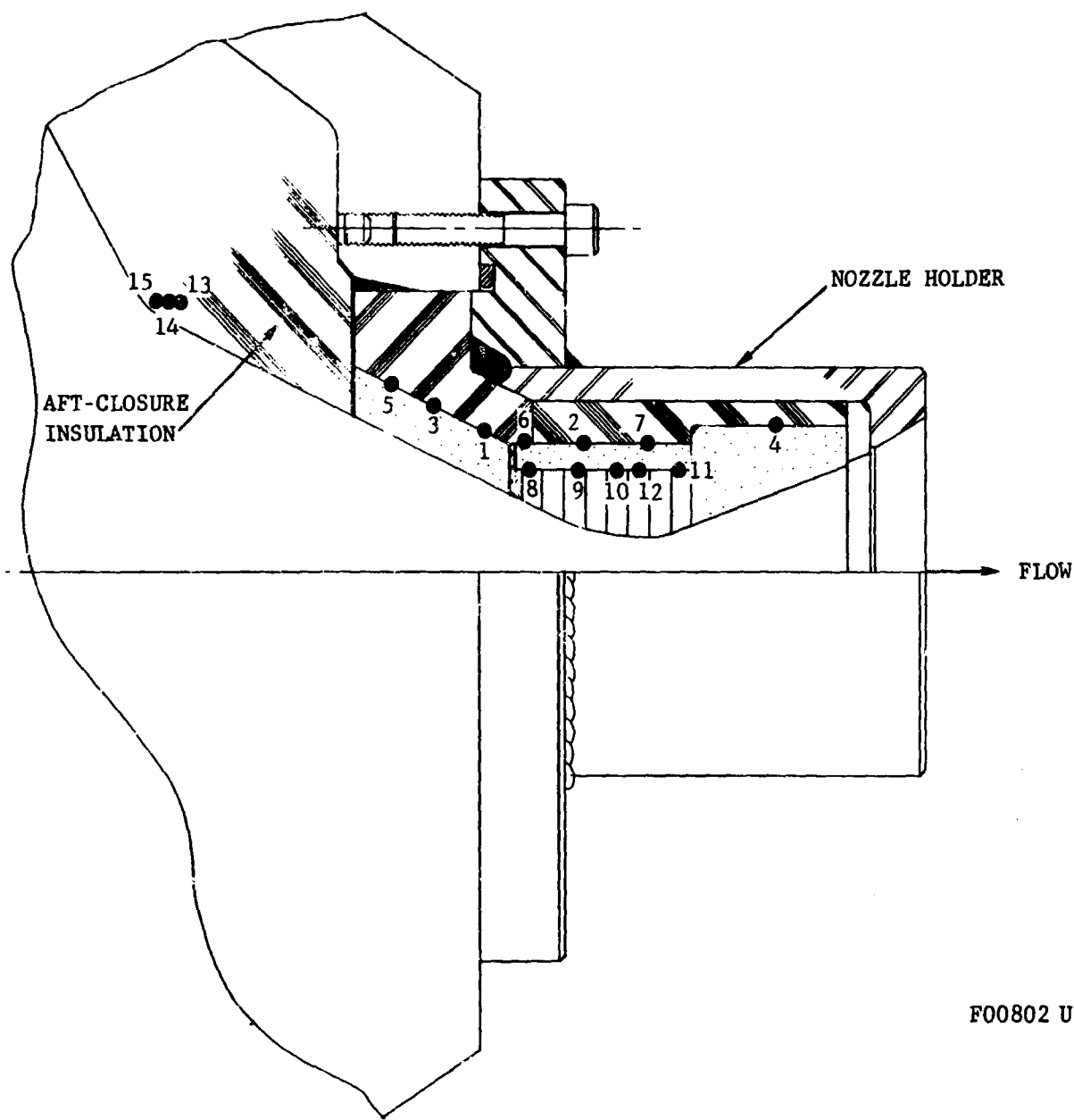


FIGURE 95. THERMOCOUPLE LOCATIONS ON NOZZLES T-1 THROUGH T-7 (A-G)

TABLE XXXII. THERMAL INSTRUMENTATION LIST (FOR SMALL SCALE MOTOR TESTS)

Test Number	1	2	3	4	5	6	7	Instrumentation Port Numbers (See Nozzle Drawings)										20	21	22	23	24	25	
								6	9	10	11	12	13	14	15	16	17	18						
T-1	K	S	K	S	K	K	S	S	S	S	S	K	K	K	K	K	K	R						
T-2	S	S	S	S	S	S	S	S	S	S	S	K	S	K	K	K	K							
T-3	S	S	K	S	K	S	K	S	S	S	K	S	K	S	K	S								
T-4	S	S	S	K	S	K	S	S	S	S	K	S	S	K	S	S								
T-5	S	S	K	K	K	K	K	S	S	S	K	S	S	K	S	S								
T-6	S	S	K	K	K	K	K	S	S	S	K	S	S	K	S	S	R							
T-7	S	K	K	K	K	K	K	S	S	S	K	S	S	K	S	S	S							
T-9																		S	K	K	K	K		
T-10	S		K			K		S	S	S	K	S	S	K	S	S	S							
T-11			K			K		S	S	S	K	S	S	K	S	S	S	K						
T-12						SI		SI	SI	SI	SI	SI	SI	SI	SI	SI	SI	SI						
T-13						SI		SI	SI	SI	SI	SI	SI	SI	SI	SI	SI	SI						
T-14						K		S	S	S	K	S	S	K	S	S	S	K						
T-15	S		K			K		S	S	S	K	S	S	K	S	S	S	K	K					
T-8	S		K			K		K	S	S	K	S	S	K	S	S	S	K	K					
T-16			K	K		K		S	S	S	K	S	S	K	S	S	S	K						
T-17	K					K		S	S	S	K	S	S	K	S	S	S	K						
T-18	KI		SI			KI		SI	SI	SI	KI	SI	SI	KI	SI	SI	SI	SI						
T-19	KI		SI			KI		SI	SI	SI	KI	SI	SI	KI	SI	SI	SI	SI						
T-20						K		K	S	S	K	S	S	K	S	S	S	SL	SL	SL	SL	SL	SL	
T-21	KI					KI		SI	SI	SI	KI	SI	SI	KI	SI	SI	SI	KI	SI	SI	SI	SI	SI	
T-22	KI					KI		SI	SI	SI	KI	SI	SI	KI	SI	SI	SI	KI	SI	SI	SI	SI	SI	

SYMBOLS:

R Radiometer, uses type K thermocouple

S Spring loaded, type S, bayonet thermocouple

K Spring loaded, type K, bayonet thermocouple

SI Special spring loaded, type S, thermocouple

KI Special spring loaded, type K, thermocouple

SL Spring loaded, type S, extra long bayonet thermocouple

6 poor, and 6 unusable. For the purpose of analysis on this program, data classified as "fair" is in most cases quite adequate. Thus, 54 of the 67 thermocouple data charts could be considered complete and adequate, 6 were partially usable, and only 6 were unusable.

TABLE XXIII. QUALITY OF THERMOCOUPLE DATA

Test Number	<u>Ports</u>														
	1	2	3	4	5	6	7	8	9	10	11	12	13	14	15
T-1	KG	SG	KF	SF	KG	KG	SP	SG	SG	SG	SG	SG	KU	KU	KU
T-2	SP		SP		SF			SG	SG	SG	KP	SF	KG	KG	KG
T-3	SP		SG	KG	SG		KF	SG	SG	SG	KG	SG			RG
T-4	SG		SG	KU	SF		KU	SU	SG		KG	SG			
T-5	SG		KG		KG		KG		SG	SG	KG	SG			
T-6	SG		KF		KF		KG		SG	SG	KP	SC	RU		
T-7	SG		KG		KG		KG		SG	SG			SG		

R	Radiometer	G	Good
S	Platinum/platinum, 10% rhodium	F	Fair
T	Type	P	Poor
K	Chromel/alumel	U	Unusable

The data from ports 13, 14 and 15 on Test T-1 were considered unusable. The primary purpose of these thermocouples was to provide data on the aft closure insulator ablation. However, the ablation rate during this run was so low that the thermocouple sensors did not experience the expected temperature rise during the run. Since the aft closure did not ablate or erode, as data from previous beryllium programs had indicated it could, the primary purpose of these thermocouples was satisfied. The secondary purpose of the aft closure thermocouples was to measure the soak-back temperature within the ablator following the motor firing. The secondary purposes could be accomplished only if the aft closure were not eroded enough to accomplish the primary objective of the thermocouples. However, following the motor firing, the leads on thermocouples 13, 14 and 15 were burned by the tail-off pyrolysis gases. Consequently, the secondary objective was not accomplished. Thus, the data were considered unusable. In contrast, the thermocouples in ports 13, 14, and 15 on run T-2 remained operative following the run because additional protective covers were placed on the thermocouple leads. Although the aft closure did not erode enough to cause the thermocouple to perform their primary function, data were obtained on the heat soak-back in the

insulator following the motor firing. These data may be used to establish the thermal diffusivity of the virgin ablative material.

The data from the radiometer in Test T-6 were considered unusable. However, the failure to obtain usable data was believed to have been caused by blockage of the light path in the radiometer tube during the 5-second ignition delay. Post-test examination of the radiometer indicated the thermocouple was still operative.

A post-test examination of the thermocouple used in ports 4, 7, and 8 of Test T-4 indicate that the thermocouples were in satisfactory condition during the run. Thus, it is believed that the unsatisfactory performance of these thermocouples was due to poor thermal contact or loose connections in the lead wire or recording systems. Poor thermal contact could have been caused by improper port cleaning or by insufficient spring loading on the thermocouple tip.

Post test examinations were performed on all of the thermocouples used on the first seven tests. Table XXIV presents the results of these examinations in coded forms. The first letter (S, K, or R) describes the type of thermocouple used ("S" is platinum/platinum-rhodium; "K" is chromel/alumel; and "R" is the radiometer, which incorporates a chromel/alumel thermocouple). The remaining letters describe the condition of the thermocouples (i.e., A means all OK; B means the sensor tip was bent; F means the ceramic portion of the sensor tip was broken; H means the damage to the thermocouple occurred during or before the firing; etc.). As can be seen in Table XXIV, most of the thermocouples were in good condition following the tests. These examinations proved helpful in determining the cause of thermocouple malfunctions and in evaluating the expected performance of thermocouples at a given location on future tests and designs. An additional post-test examination procedure has been recently adopted which includes a more extensive evaluation of the thermocouple installation. This procedure will help to establish whether the thermocouples were properly installed in cases where the data indicate poor thermal contact.

One of the primary considerations adopted for the first seven motors on this program was that the thermal instrumentation requirements would remain flexible. A large number of instrumentation ports were selected, machined, and otherwise made ready to accept instrumentation. Two types of thermocouples were selected, Types "S" and "K". Due to the lower cost, the type "K" was to be used where ever the temperature range was not great enough to require the type "S" thermocouple. Both types of thermocouples use the same installation fittings. Thus, it was possible to add or subtract thermal instrumentation and to interchange thermocouple types depending on the previous test results and the present or anticipated analytical data support requirements.

TABLE XIV. POST TEST THERMOCOUPLE EXAMINATION COMMENTS

Test <u>Number</u>	<u>Port s</u>									
	1	2	3	4	5	6	7	8	9	10
T-1	KGA	SAG	KA	SAG	KA	KA	SFMH	SFIJ	SA	SA
T-2	SFJH	SJD	SFCHG		SFCH	SFIG	SFIG	SFIG	KEJ	SAG
T-3	SA	SA	KA	SA	KA	SF	SA	SA	KA	SA
T-4	SA	SA	KA	SFIG	KA	SJF	SA			RA
T-5	SFH	KA	KB		KA		SFI	SFI	KA	SDFJ
T-6	SJE	KA	KJE		KA		SCEH	SCI	KA	SJE
T-7	SFACI	KA	KDJ		KA	SFH	SFH			SDJE

Thermocouple Type

Symbol

- R Radiometer A A11 OK H Damaged in place
- S Platinum/platinum - rhodium B Tip bent I Damaged on removal
- K Chromel/alumel C Couple broken J Tip OK
- D Shank bent M Tip melted
- E Tip stuck N Plug burnt by exhaust
- F Ceramic broken P Depressed properly
- G Gas leaks Q Not depressed far enough

A pretest list of the anticipated thermocouple requirements for the first 15 motor tests was presented in Table XVIII of Reference 1. By comparing this table with Table XXII of this report it can be noted that: (1) nozzle C (or T-1) was fired first; consequently, the exploratory instrumentation of nozzle A (or T-2) was transferred; (2) thermal instrumentation of port No. 7 was not suspended; (3) the use of type "S" thermocouples was continued in port No. 1 on the aluminum analog motors; (4) the radiometer was added to test F (or T-6); and (5) three thermocouples were not installed due to manufacturing errors.

A revised list of the thermal instrumentation requirements for the remainder of the small scale motor tests is also presented in Table XXII. This list was generated based on the results of the previous motor firings, the anticipated analytical support data requirements, and the motor design limitations.

Figures 96 through 101 are drawings of the different types of nozzles to be used on the remainder of the small scale tests. These drawings illustrate the location of the thermocouples and the numbering system used to identify each thermocouple (or thermocouple port) location. The nozzles shown in Figures 96 and 100 can use the standard spring-loaded bayonet type thermocouples; whereas, the nozzles shown in Figures 97, 98, 99, and 101 require custom built thermocouples.

The thermocouples used in ports 19 and 20 on the steep inlet nozzles (as shown in Figures 98 and 99) are extra long, spring-loaded, bayonet types. Three standard bayonet thermocouples were remanufactured, incorporating a 3-inch extension of the bayonet. Two of the three thermocouples use platinum/platinum-rhodium sensors (Type "S") and the third is equipped with chromel/alumel (Type "K"). The third one is to be used only if one of the others is broken during installation or handling.

The thermocouples used in the throat section of nozzles T-12 and T-13 (shown in Figures 97 and 98) were specially manufactured by Hi-Cal Engineering. Figure 102 illustrates the Hi-Cal thermocouple. All of these thermocouples incorporate spring-loaded platinum/platinum-rhodium sensor tips. A continuity check of these thermocouples following installation indicated that 3 of the 10 were inoperative. This high mortality rate coupled with the 8-week demonstrated delivery time, prompted the decision to build the special thermocouples for future nozzles at Aeronutronic. Figure 103 illustrates the special submerged type thermocouples manufactured by Aeronutronic for use on nozzles T-18, T-19, T-21, and T-22. Both platinum/platinum-rhodium and chromel/alumel thermocouple sensors were used in the fabrication. All of the special thermocouples required for the remainder of the small scale motor tests (16 Type "S" and 6 Type "K") have been manufactured. Since the special submerged type thermocouples are installed within the nozzle insulation, none of them are considered salvageable.

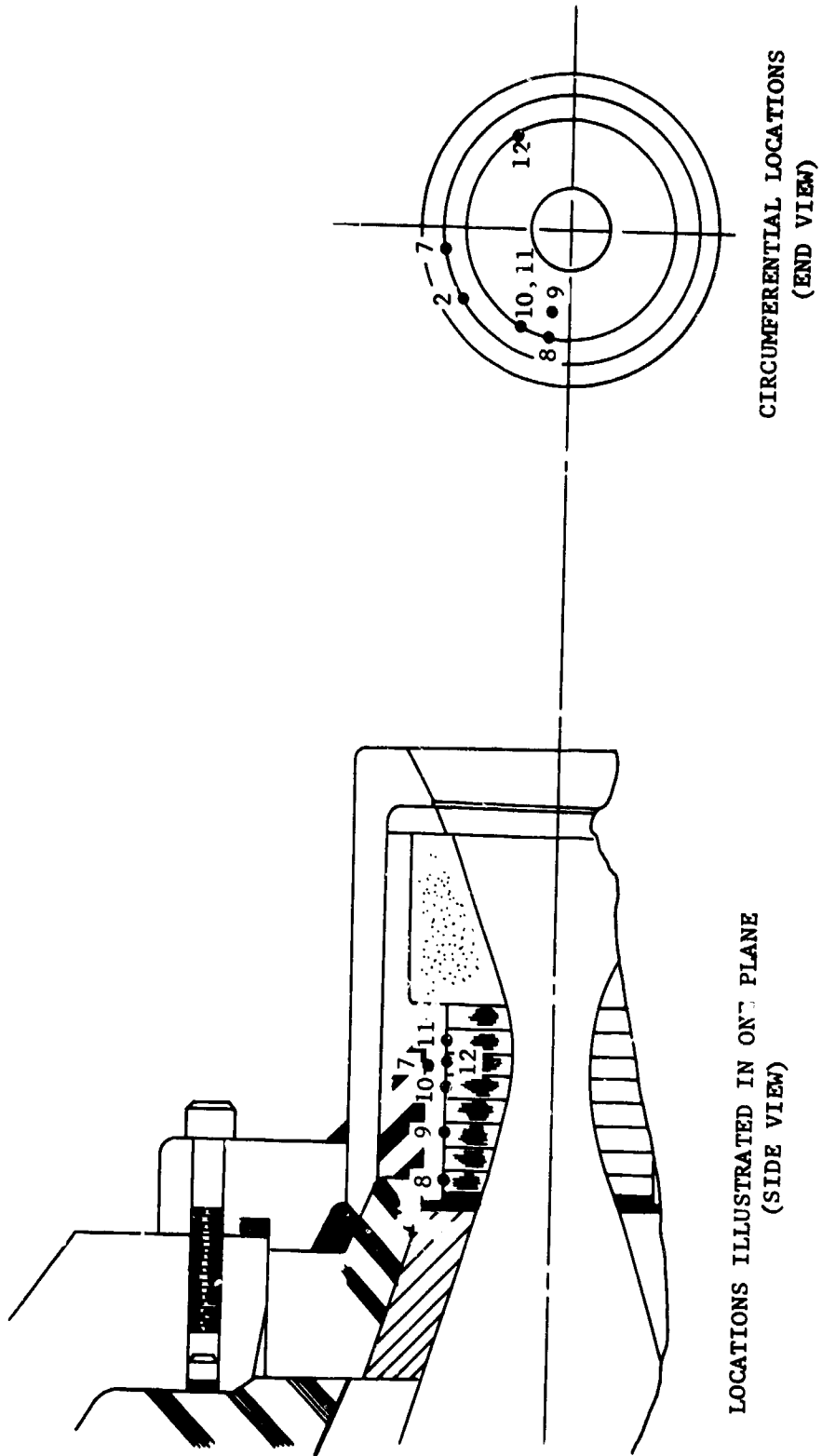


FIGURE 96. THERMOCOUPLE LOCATIONS FOR NOZZLE T-20

FO4117 U

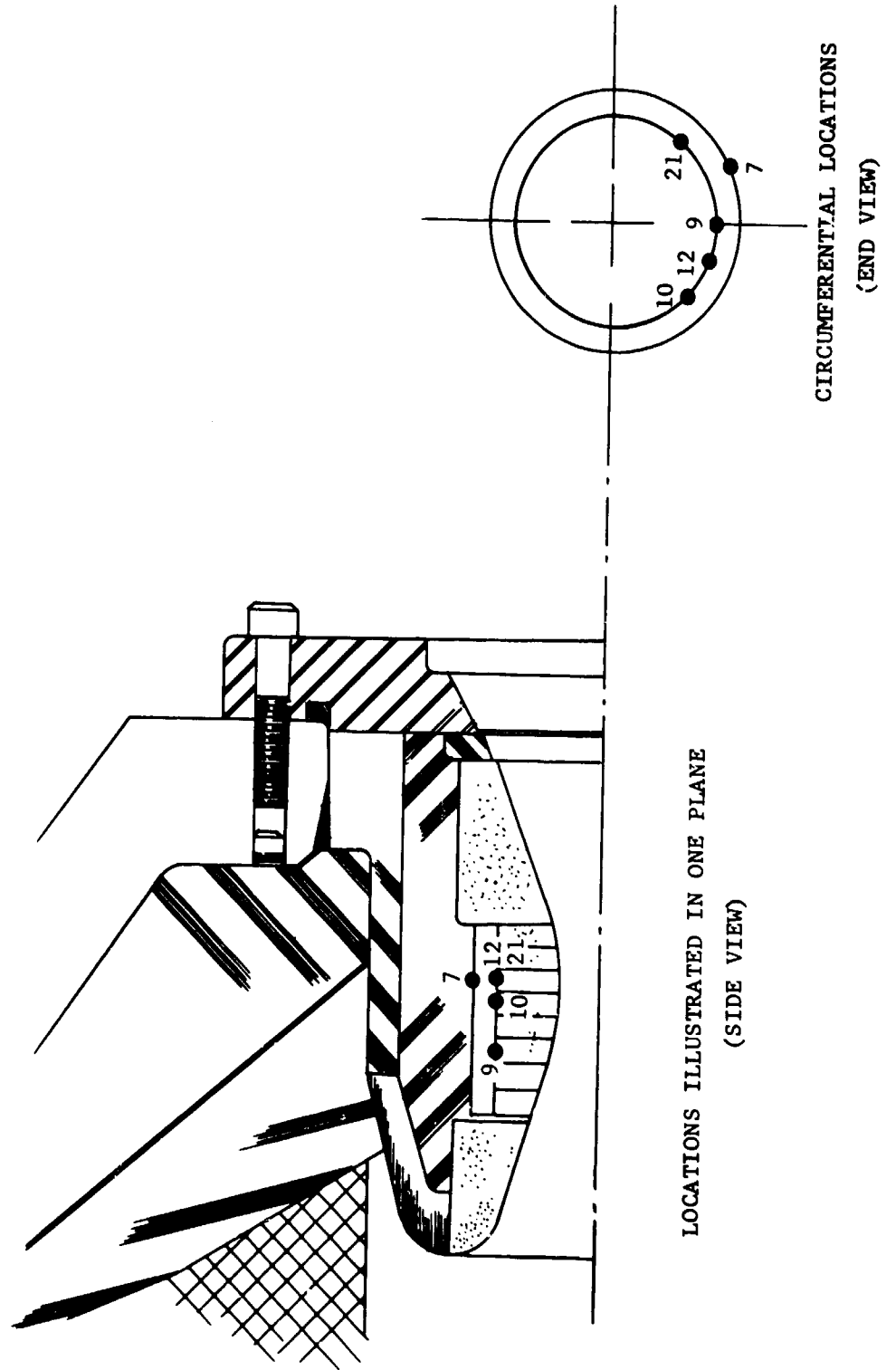


FIGURE 97. THERMOCOUPLE LOCATIONS FOR NOZZLE T-12

FO4118 U

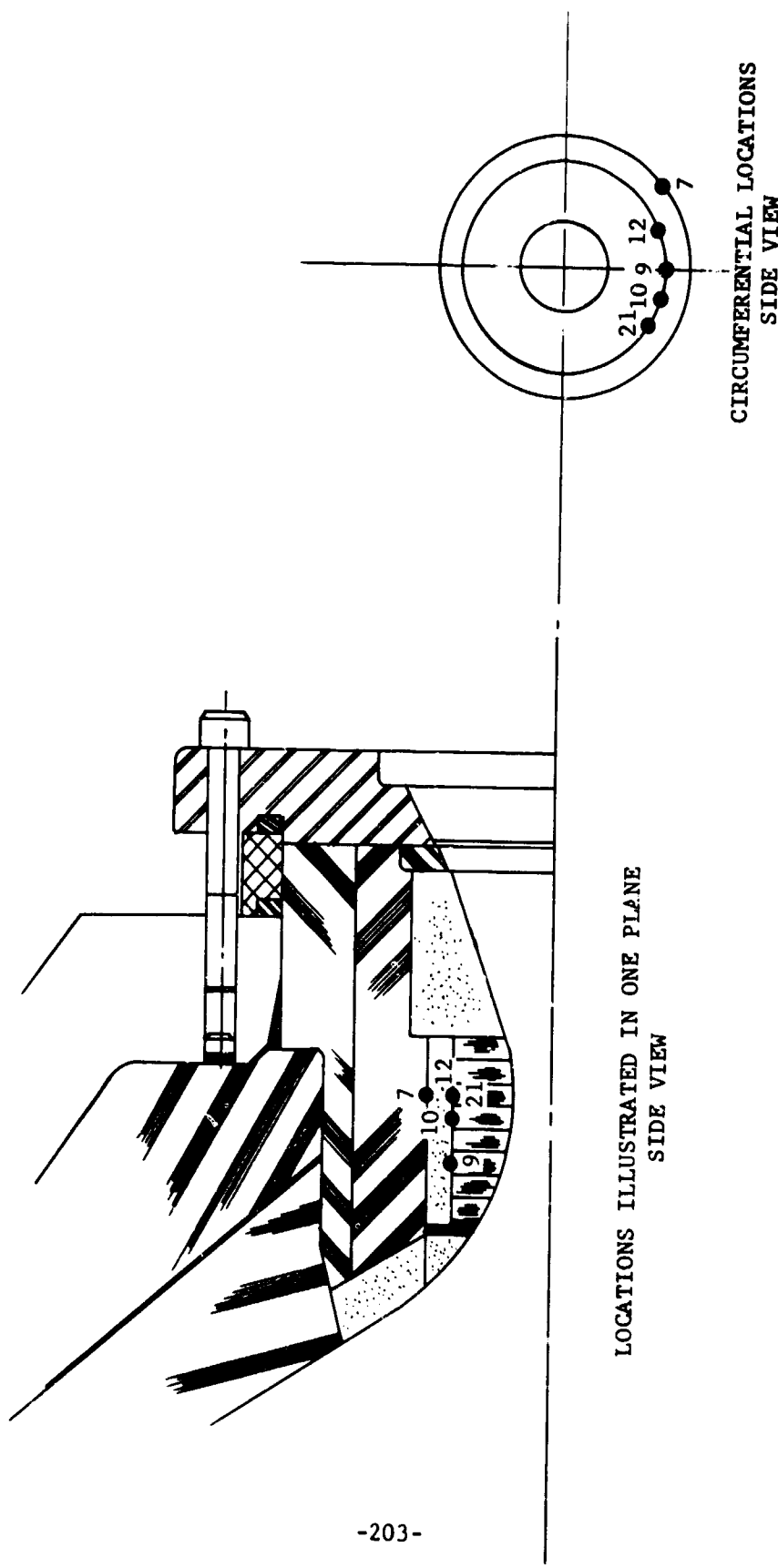
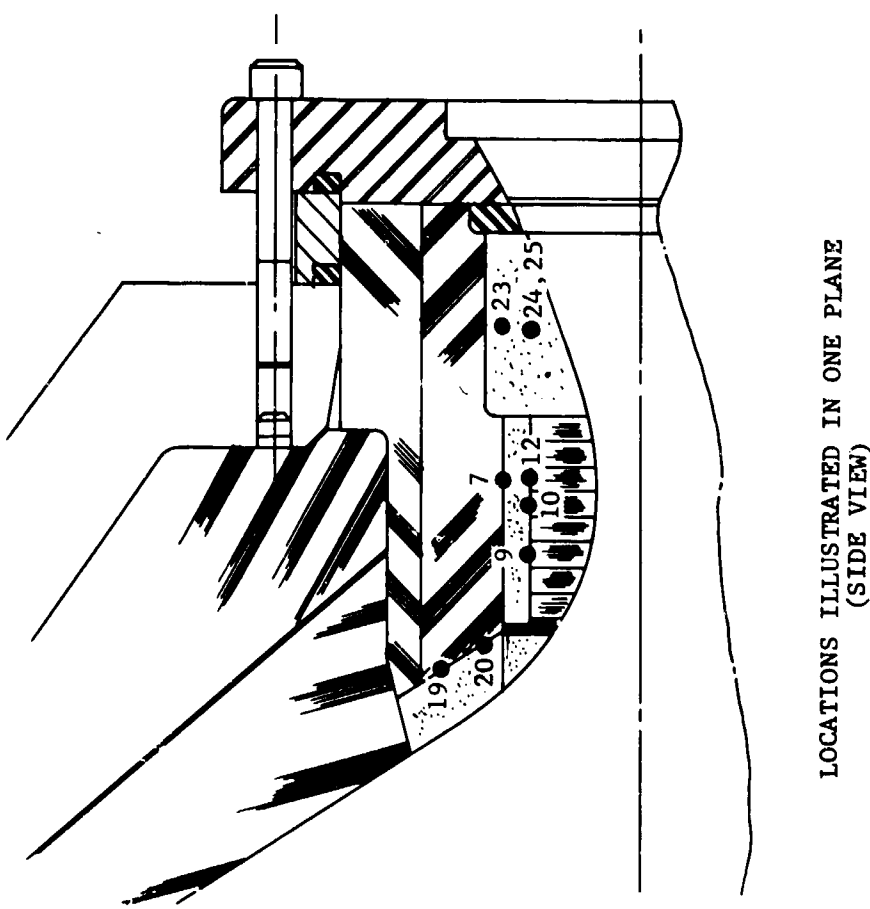


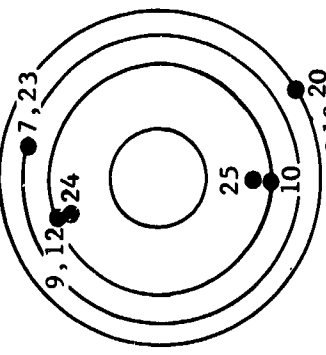
FIGURE 98. THERMOCOUPLE LOCATIONS FOR NOZZLE T-13

F04119 U



LOCATIONS ILLUSTRATED IN ONE PLANE
(SIDE VIEW)

-204-



CIRCUMFERENTIAL LOCATIONS
(END VIEW)

F04120 U

FIGURE 99. THERMOCOUPLE LOCATIONS FOR NOZZLES T-21 AND T-22

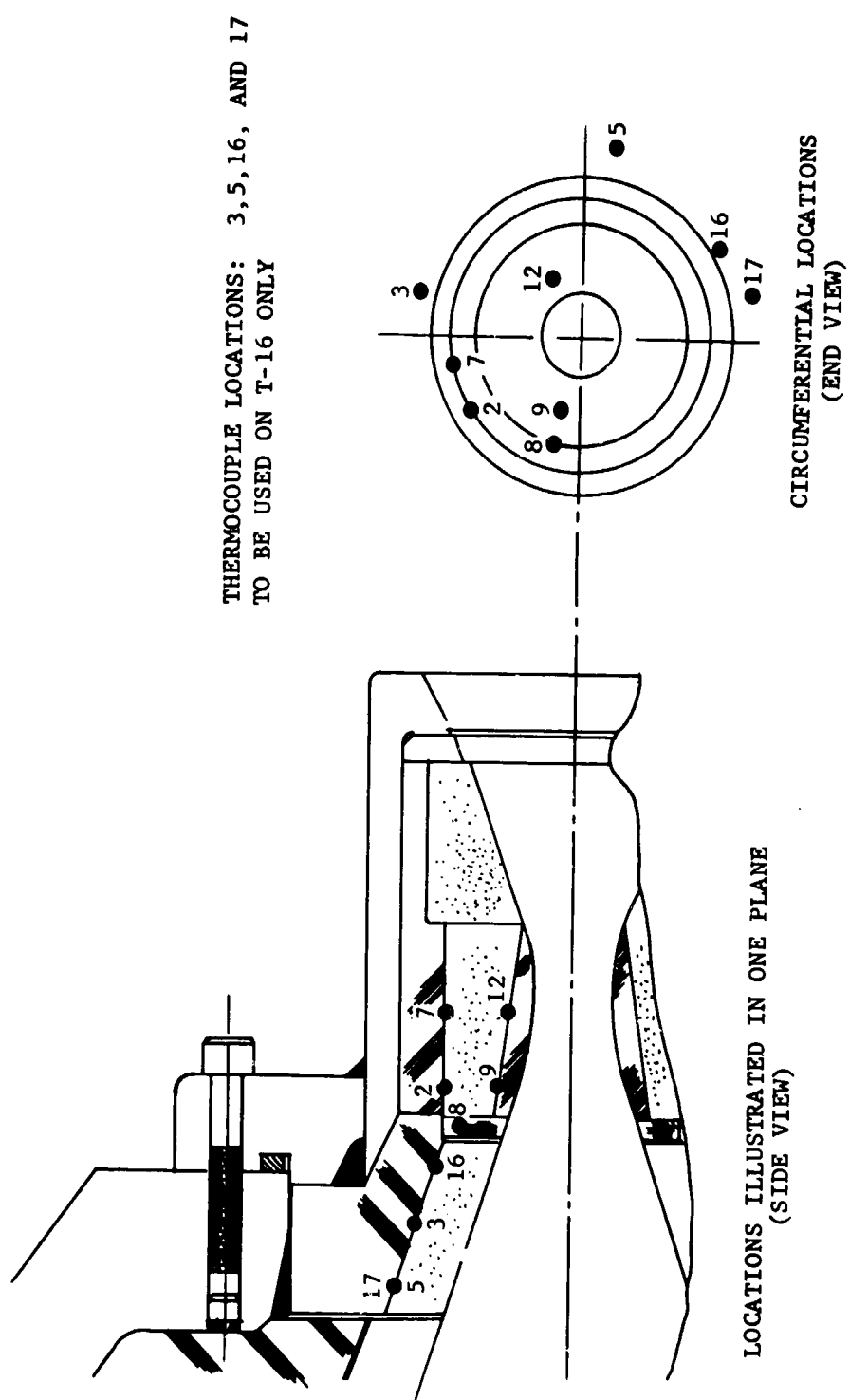


FIGURE 100. THERMOCOUPLE LOCATIONS FOR NOZZLE T-16

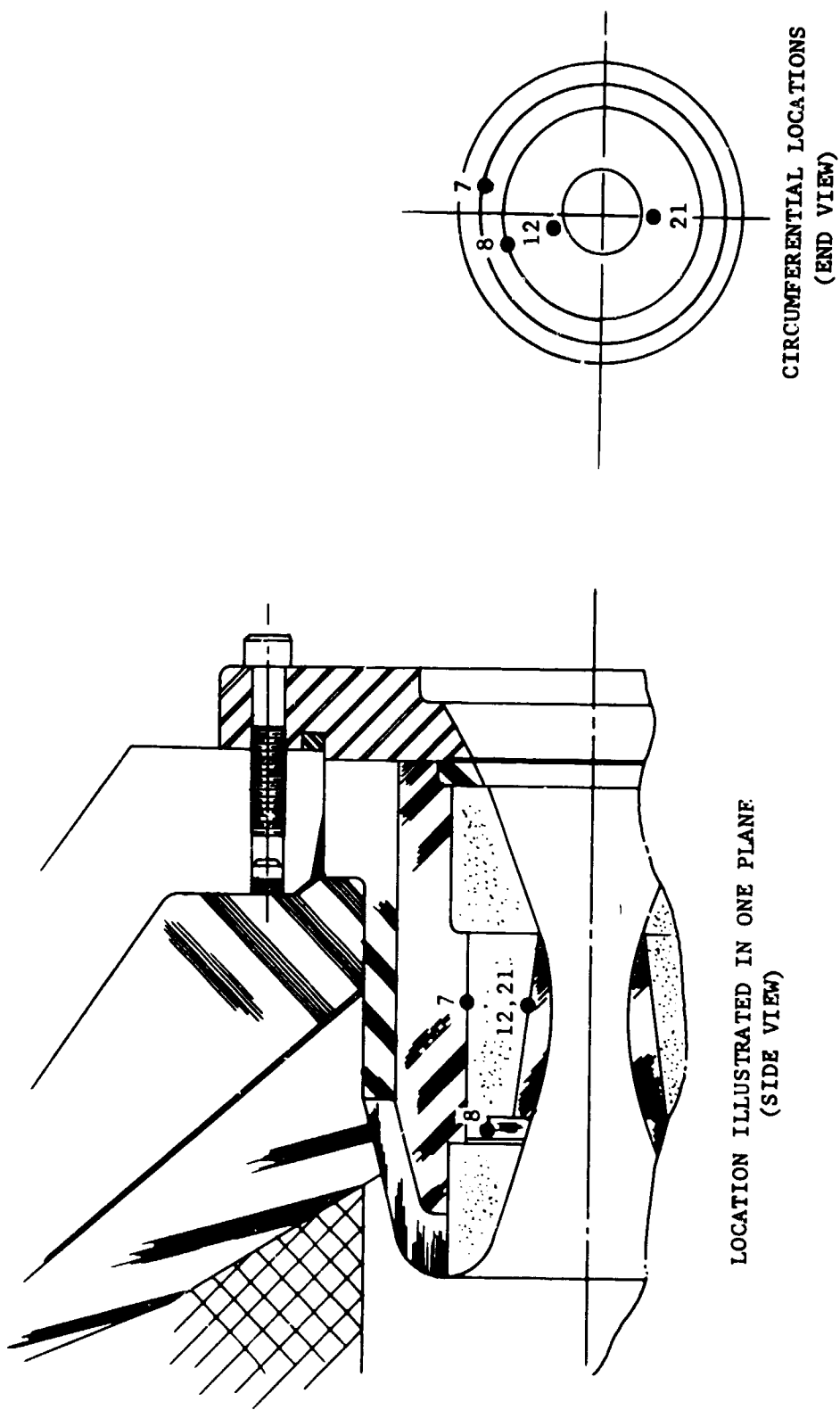
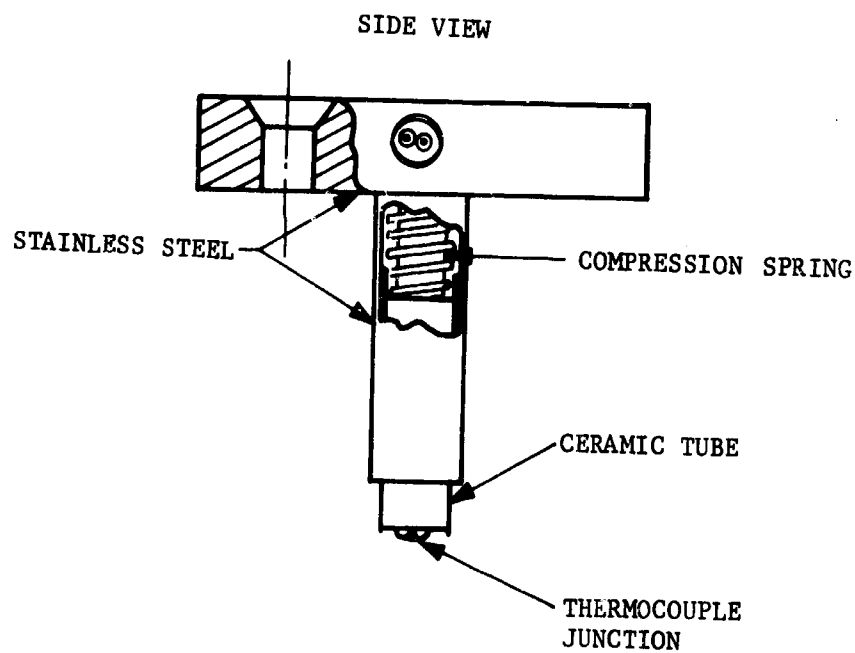
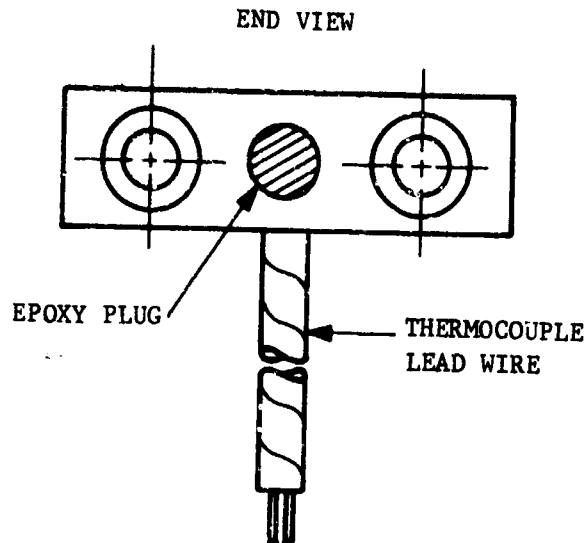


FIGURE 101. THERMOCOUPLE LOCATIONS FOR NOZZLES T-18 AND T-19



F04121 U

FIGURE 102. HY-CAL ENGINEERING SPECIAL SUBMERGED THERMOCOUPLE

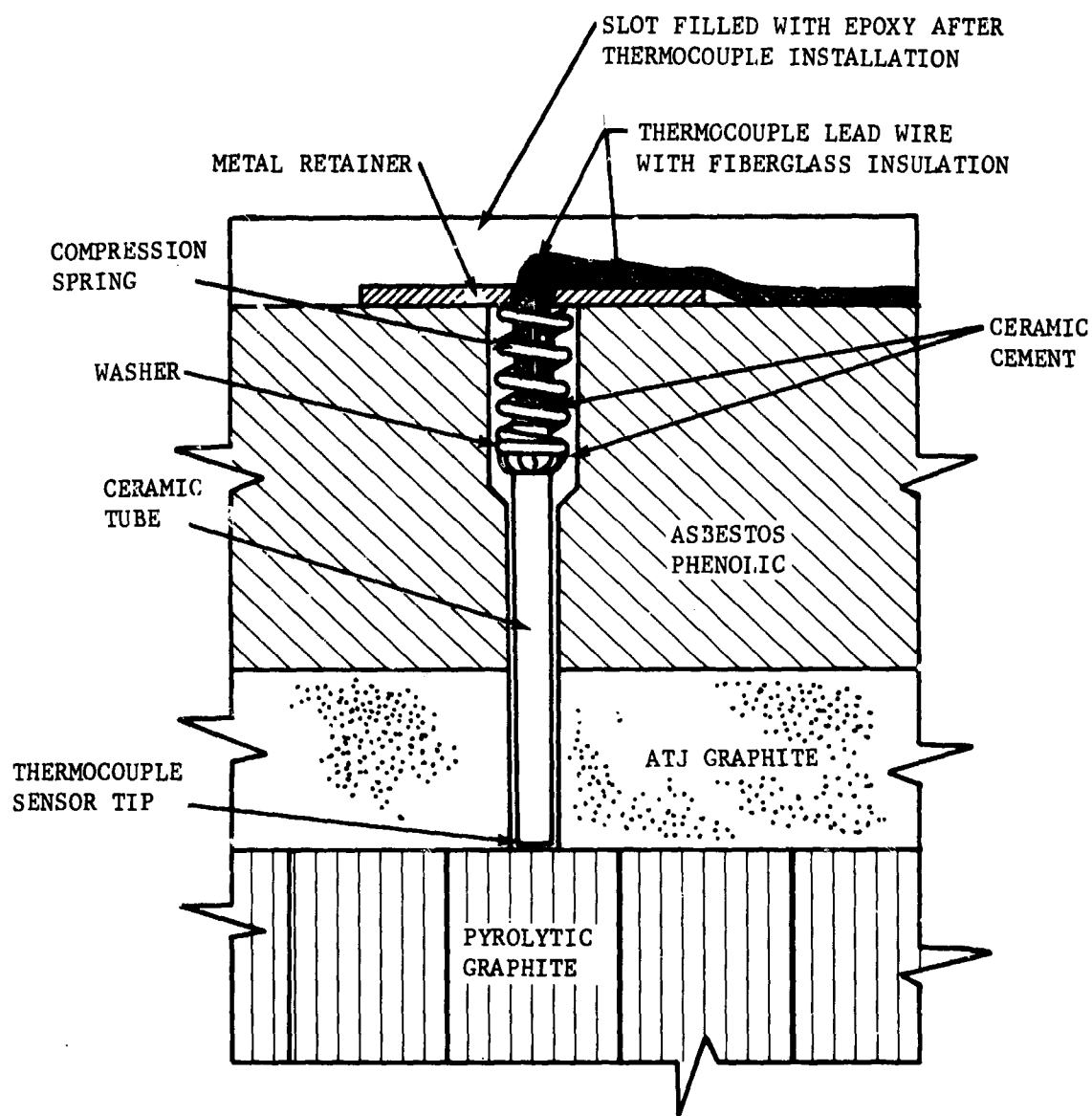


FIGURE 103. AERONUTRONIC SPECIAL SUBMERGED THERMOCOUPLE DESIGN (TYPICAL INSTALLATION)

CONFIDENTIAL

(2) (C) Radiation

A radiometer for measuring combustion chamber radiation has been fabricated and tested. The primary objective of this instrument was to obtain thermal data which could be used to: (1) evaluate the combustion chamber particle cloud radiation and (2) to compute the theoretical ablation of the aft closure and chamber liner material.

A verbal and pictorial description of the radiometer was presented in Section IV, Reference 1. Basically, the radiometer consisted of a molybdenum disilicide slug calorimeter which was insulated from and mounted in a 3/16-inch OD stainless steel tube. Molybdenum disilicide was selected because it had a good combination of absorptivity and conductivity.

Since it was not practical to gas purge the light path portion of the stainless steel tube, it was anticipated that the light path would be blocked by slag from the combustion chamber or by the stainless steel tube itself, when melting occurs. To help prevent slag from running along the aft closure and into the radiometer port, the stainless steel tubular body of the radiometer was scarfed parallel to the aft closure surface and extended about 0.2 inch past the aft closure insulator surface into the combustion chamber. In this position, it was estimated that the light path would be obstructed by the melting stainless steel tube within about one second. Thus, the total useful life expectancy of the radiometer was estimated to be one second at the most, and it was considered possible that slag or debris from the ignitor or the combustion products could render the radiometer inoperative in even less time.

The output of the radiometer used on motor Test T-3 is presented in Figure 104. In addition to the temperature of the molybdenum disilicide slug, the chamber pressure is plotted as a function of time. Note that the slope of the slug temperature-time curve is relatively constant at about 400°F/sec during the startup transient. This is an indication that the particle cloud is dense and that the temperature of the particles is not a strong function of chamber pressure.

From Figure 104 it is apparent that the light path in the radiometer was blocked at about 0.7 second but was cleared again at about 0.9 second. After about 1.15 seconds, the light path was again blocked and remained closed for the run duration. Post-test examination of the radiometer revealed that the radiometer was improperly installed and did not extend 0.2 inch into the combustion chamber. The scarfed end of the radiometer was submerged in and protected by the aft closure insulation. The blockage of the light path during this run was attributed to slag flow along the insulator surface. The stainless steel tip was not melted during the firing.

CONFIDENTIAL

CONFIDENTIAL

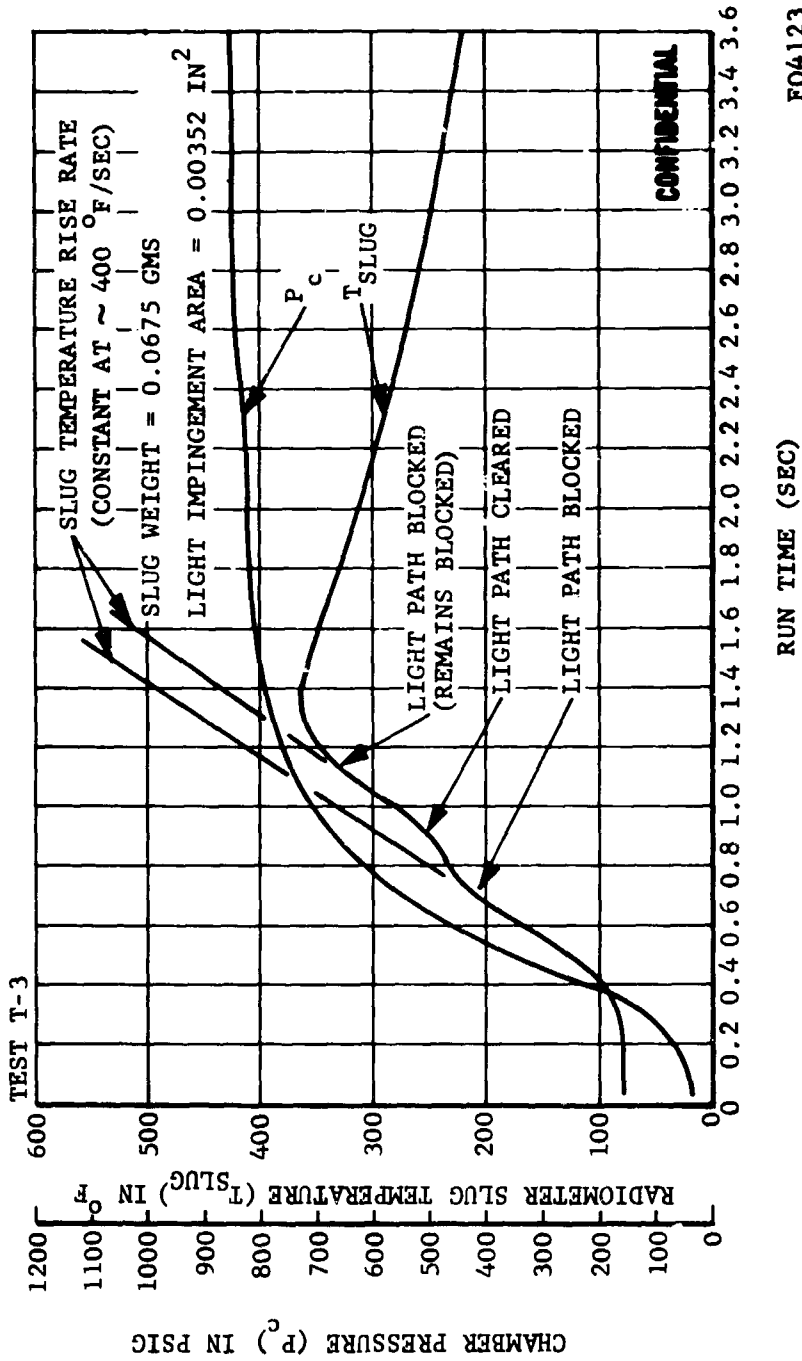


FIGURE 104. RADIOMETER PERFORMANCE

CONFIDENTIAL

CONFIDENTIAL

A more detailed discussion of the data from the radiometer can be found in Paragraph 2.5b. This paragraph provides an analysis of the resulting experimental gas particle cloud radiation parameters.

The radiometer was refurbished and used again on motor T-6. However, no data were obtained during this firing. A post-test examination of the radiometer indicated that it was properly installed and that the scarfed end was melted. Figure 121 presents a plot of the thrust and chamber pressure during motor firing T-6. Note that there was a 5 second ignition delay on this test. It was concluded that the radiometer light path tube was either plugged or melted during the ignition delay.

Motor numbers T-8 through T-20 will use internal burning grains. Consequently, it is not possible to incorporate the radiometer again until motors T-21 and T-22. Because the chamber radiation has not proved to be a significant problem on these early tests, it is anticipated that the radiometer will not be used again on this program.

b. (U) Ballistic Instrumentation

An evaluation of the propellant and motor performance requires that the following ballistic data be taken during each test run: (1) axial thrust, (2) chamber pressure, and (3) ambient pressure.

It was anticipated that the motors used in the small scale motor tests would normally produce about 1000 to 1500 pounds thrust at chamber pressures between 600 to 1000 psi. However, to ensure that data would be obtained, even if the motor performance were abnormal, two strain gage, dual bridge axial thrust mounts with a 0 to 2000 pound range and two pressure transducers with ranges of 0 to 1000 psig and 0 to 2000 psig were used. The data taken during each test run were recorded on a digital recording system at 17 to 18 millisecond intervals. An oscilloscope was also used to record chamber pressure and thrust; this system was used only for redundancy.

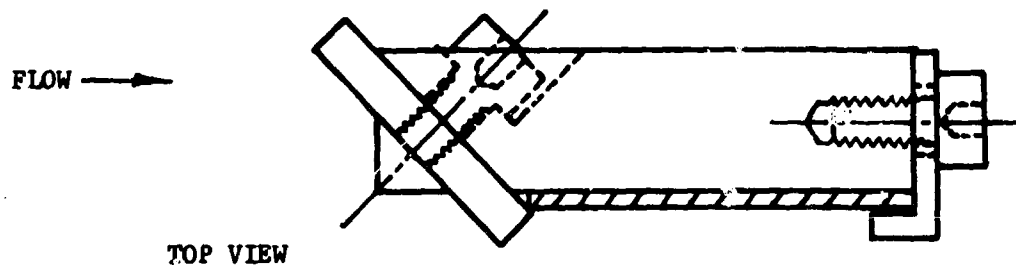
Nozzle throat and exit cone measurements were taken before and after each firing. It should be noted that in some cases the throat and exit cone deposition was inadvertently chipped off by the measuring instruments. The differences between the measured final throat diameters and the computed actual throat diameters are illustrated in Figures 132 through 138.

c. (U) Exhaust Plume Sampling

Exhaust plume particle samples were taken from within the plumes of the first seven motor tests. It is anticipated that these samples will help to explain the degree of combustion, etc., that occurred during the firings. The particle samplers used on the first five motor firings incorporated seven different methods of collecting particles (see Figure 105). This sampler was used to help gain information necessary to fabricate

CONFIDENTIAL

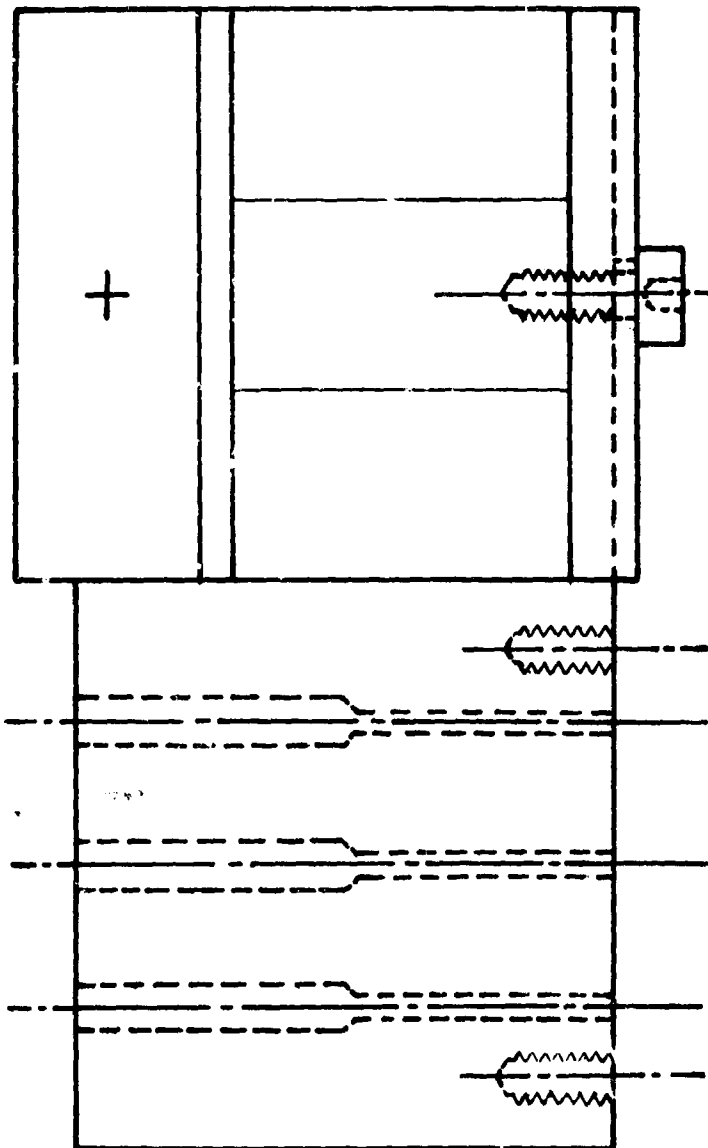
CONFIDENTIAL



TOP VIEW

EXHAUST PLUME
CENTER LINE

FLOW →



SIDE VIEW

F00807 U

FIGURE 105. EXHAUST PLUME PARTICLE SAMPLED NO. 1

-212-

CONFIDENTIAL

THIS PAGE IS UNCLASSIFIED

CONFIDENTIAL

a more elaborate sampler. However, it was decided that a more elaborate sampler was not necessary at this time.

Much of the particulate sample taken from the tests was being lost in handling. Consequently, it was decided that a second sampler should be fabricated to minimize the loss. One of the more effective methods for collecting particle samples, as demonstrated by the first sampler, was a glass tube which was closed on one end and open to the gas flow on the other. Particle Sampler No. 2 incorporated this concept (see Figure 106). This sampler incorporates small glass bottles to catch the particles. The open end of each bottle faces the gas stream and holds the particles when they are forced in by their own momentum. After the test, the bottles are removed from the sampler and capped. Thus, the loss of particulate matter can be kept to a minimum.

Particle Sampler No. 2 employs 6 sampling bottles. The bottles are spaced on the sampler at radial positions perpendicular to the nozzle centerline. This was done to detect any possible stratification in the particle type or size distribution. An examination of the bottles following tests T-6 and T-7 indicated that the sampler can collect sufficient material for analysis. At present it is anticipated that Particle Sampler No. 2 will be employed on all subsequent tests. There are no plans for a more elaborate sampler.

4.4 (C) CONCLUSIONS, RECOMMENDATIONS, AND FUTURE WORK

a. (C) Conclusions

It was found that correlations of beryllium metal based propellant nozzle erosion data may have been obscured or confused by extensive metal oxide deposits. By selecting data for which the deposition remains on the nozzle for a small fraction of the run-time, it was found that corrosion-erosion can be related to chamber pressure, etc. The data derived from the first seven motor tests of this program indicate that the amount of deposition attainable for double base propellants is less than that for composites.

b. (U) Recommendations

No recommendations are made at this time.

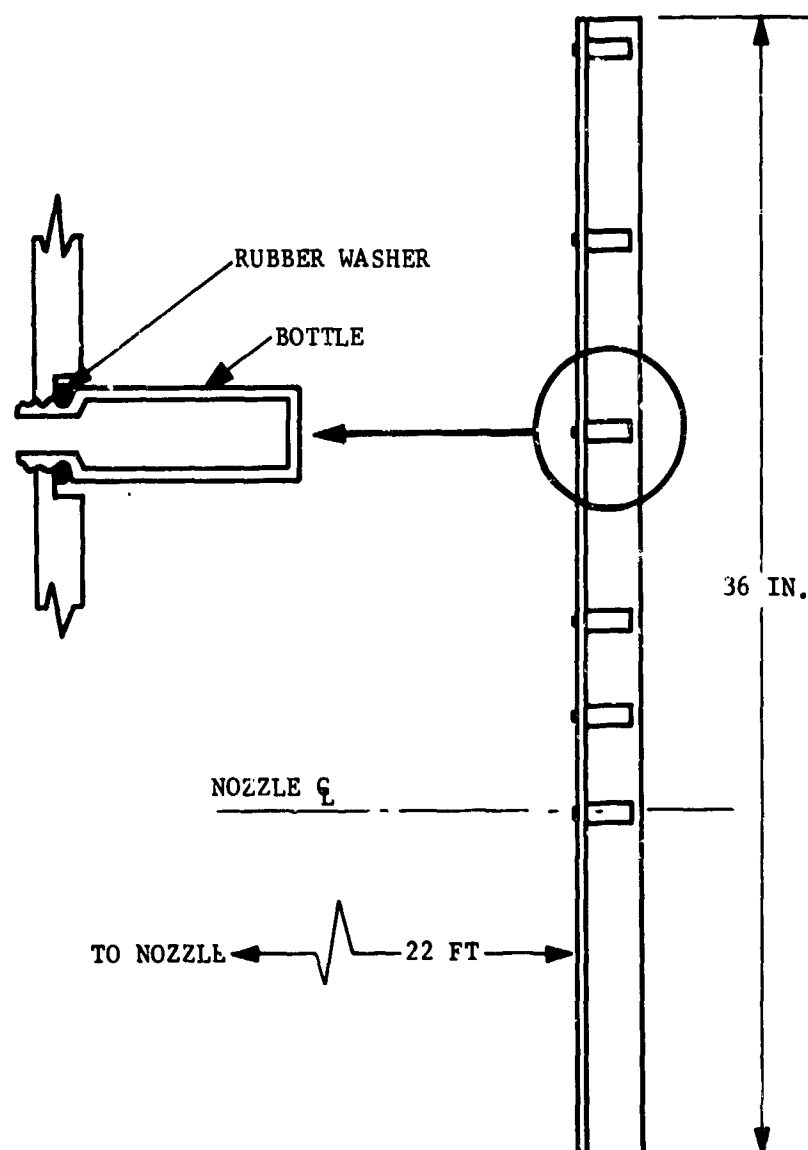
c. (U) Future Work

The following is a brief list of the correlation studies planned for the third reporting period of this program:

- (1) The thermal instrumentation will be continually evaluated. Alterations in the number, type, and location of thermocouples on future tests will

CONFIDENTIAL

CONFIDENTIAL



F04124 U

FIGURE 106. EXHAUST PLUME PARTICLE SAMPLER NO. 2

CONFIDENTIAL

be made in accordance with the anticipated support data requirements and the capability of the instruments.

- (2) The thermal instrumentation requirements for the remainder of the motors in this program will be tentatively established.
- (3) The data acquisition from other programs will continue during the third quarter. Emphasis will be placed on establishing correlation with general and specific theoretical hypotheses.
- (4) Emphasis will be placed on attempting correlations of data from the laboratory tests and motor tests of this program.

SECTION V (C)

MOTOR DESIGN, FABRICATION AND TEST

5.1 (U) OBJECTIVES, SCOPE AND SUMMARY

a. Program Objectives

The overall objectives of the motor design, fabrication, and test task of the program were present in Paragraph 5.1 of Reference 1 and have not changed. The specific objectives for the second reporting period were:

- (1) Select two beryllium propellant formulations based on the results of Motor Tests T-1 through T-4, for use in Motor Tests T-9 through T-21.
- (2) Fabricate and deliver seven internal burning grains; four of the Type I design, two Type II, and one Type III.
- (3) Complete modifications of the ADOBE hardware to accommodate the internal burning grain designs.
- (4) Fabricate and deliver ten nozzles, 11 aft closure insulators, and three chamber liners.
- (5) Design nozzles for Motor Tests T-16 through T-21.
- (6) Conduct the first 14 small motor tests.

b. Scope

In general, the scope of this program task is the same as previously described in Paragraph 5.1 of Reference 1. However, extensive delays in motor testing, because of bad weather at AFRPL and damage to the motor cases during the initial firings, have made it necessary to freeze the designs sooner than was initially planned. In this process, a rather large number of detailed changes, relative to the initial plan, have occurred.

The propellant formulation, grain design, nozzle contour, and nozzle materials for each of the 27 motor tests are given in Table XXI. The small motor tests are numbered T-1 through T-22 and the development motor tests are numbered T-51 through T-55. The most important changes in the detailed test plan are enumerated below.

- (1) Test T-8 was originally to be an end-burning grain using the aluminum analog of the Arcane 24 F propellant. It is now specified as an internal burning, slotted (Type II) grain using the aluminum analog of the Arcocel 191F propellant. Except for the propellant formulation, this test will be identical to Test T-10.
- (2) The five grain design tests (T-9, T-10, T-11, T-14, and T-15) originally featured only the two beryllium double base propellants, Arcocel 191F and 319BRF. The Arcane 54F composite has been substituted for the Arcocel 191F in Test T-11.
- (3) The materials tests, T-16 through T-21, were to have used the Arcocel 191F propellant. Test T-19 now uses the Arcocel 319 BRF propellant with a submerged tungsten nozzle.
- (4) Test T-21 was originally designated as a materials test and T-22 as a utility test. Test T-21 would have featured a significantly thicker pyrolytic graphite heat sink than previously employed. Motor Tests T-21 and T-22 have been changed to a new series which will examine non-equilibrium combustion effects. The Arcocel 191F and Arcane 54F propellants will each be used in an end-burner configuration. The grain will be positioned so that it is within about one-eighth of an inch of the aft closure insulation at the grain outer diameter. The steep inlet nozzle, as in Test T-13, will be used in these tests.

Table XXV. SMALL MOTOR DESIGN SUMMARY

<u>Test Number</u>	<u>Propellant</u>	<u>Grain Design</u>	<u>Nozzle Contour</u>	<u>Insulator</u>	<u>Flame Side Materials</u>	<u>Throat</u>	<u>Type of Test</u>
T-1	Arcocel 191F	Remote End Burner	Conventional, 20° Inlet	Asbestos Phenolic	ATJ Graphite	Pyrolytic Graphite Washers	Beryllium Propellant Formulation Tests
T-2	Arcane 24F	Remote End Burner	Conventional, 20° Inlet	Asbestos Phenolic	ATJ Graphite	Pyrolytic Graphite Washers	
T-3	Arcocel 319BRF	Remote End Burner	Conventional, 20° Inlet	Asbestos Phenolic	ATJ Graphite	Pyrolytic Graphite Washers	
T-4	Arcane 54F	Remote End Burner	Conventional, 20° Inlet	Asbestos Phenolic	ATJ Graphite	Pyrolytic Graphite Washers	
T-5	Arcane 60	Remote End Burner	Conventional, 20° Inlet	Asbestos Phenolic	ATJ Graphite	Pyrolytic Graphite Washers	
T-6	Arcocel 390	Remote End Burner	Conventional, 20° Inlet	Asbestos Phenolic	ATJ Graphite	Pyrolytic Graphite Washers	Aluminum Analog Propellant Tests
T-7	Arcocel 389	Remote End Burner	Conventional, 20° Inlet	Asbestos Phenolic	ATJ Graphite	Pyrolytic Graphite Washers	
T-8	Arcocel 389	Internal Burner Type II	Conventional, 18° Inlet	Asbestos Phenolic	ATJ Graphite	Pyrolytic Graphite Washers	
T-9	Arcocel 191F	Type I	Conventional, 18° Inlet	Asbestos Phenolic	ATJ Graphite	Pyrolytic Graphite Washers	
T-10	Arcocel 191F	Type II	Conventional, 18° Inlet	Asbestos Phenolic	ATJ Graphite	Pyrolytic Graphite Washers	Grain Design Tests
T-11	Arcane 54F	Type I	Conventional, 18° Inlet	Asbestos Phenolic	ATJ Graphite	Pyrolytic Graphite Washers	

TABLE XXV. SMALL MOTOR DESIGN SUMMARY (Continued)

<u>Test Number</u>	<u>Propellant</u>	<u>Grain Design</u>	<u>Nozzle Contour</u>	<u>Insulator</u>	<u>Flame Side Materials</u>	<u>Throat</u>	<u>Type of Test</u>
T-12	Arcocel 191F	Type II	Submerged	Carbon Cloth	ATJ Graphite	Pyrolytic Graphite Washers	Nozzle Contour Tests
T-13	Arcocel 191F	Type II	Steep Inlet	Asbestos Phenolic	ATJ Graphite	Pyrolytic Graphite Washers	Pyrolytic Graphite Washers
T-14	Arcocel 319BRF	Type I	Conventional, 18° Inlet	Asbestos Phenolic	ATJ Graphite	Pyrolytic Graphite Washers	Pyrolytic Graphite Washers
T-15	Arcocel 319BRF	Type III	Conventional, 18° Inlet	Asbestos Phenolic	ATJ Graphite	Pyrolytic Graphite Washers	Grain Design Tests
T-16	Arcocel 191F	Type I	Conventional, 18° Inlet	Asbestos Phenolic	ATJ Graphite	Tungsten	Tungsten
T-17	Arcocel 191F	Type I	Conventional, 18° Inlet	Asbestos Phenolic	Carbon Cloth	Tungsten	Insulation and Throat Materials Tests
T-18	Arcocel 191F	Type I	Submerged	Carbon Cloth	ATJ Graphite	Tungsten	Tungsten
T-19	Arcocel 319BRF	Type I	Submerged	Carbon Cloth	ATJ Graphite	Tungsten	Tungsten
T-20	Arcocel 191F	Type I	Conventional, 18° Inlet	Asbestos Phenolic	Carbon Cloth	Pyrolytic Graphite	Non-equilibrium Combustion Effects
T-21	Arcocel 191F	Close End Burner	Steep Inlet	Asbestos Phenolic	ATJ Graphite	Pyrolytic Graphite	Pyrolytic Graphite
T-22	Arcane 54F	Close End Burner	Steep Inlet	Asbestos Phenolic	ATJ Graphite	Pyrolytic Graphite	Pyrolytic Graphite

- (5) The development motor tests originally were to feature two grain designs, one propellant, and three nozzle throat materials. The present plan is to use one grain design, two nozzle contours of differing submergence, the two double base propellants, and only tungsten and pyrolytic graphite throat materials.

All of the changes described above were made as a result of an evaluation of the relative potential data return from a wide variety of design candidates. All available motor test data were used in the decision process. It should not be inferred that any of the changes represent preferences or opinions concerning the ultimate utility of any of the propellants, designs, or nozzles materials.

The scope of work during the reporting period was also revised to include the repair of the ADOBE motor cases which were damaged during Tests T-1 and T-2. Significant revisions in the sealing scheme used at the forward end of the grain were necessary. The nature of the damage and the corrective action are described in Paragraph 5.2.

c. Summary of Progress

During this reporting period, the following progress was made toward the achievement of the task objectives:

- (1) Selection of the propellant formulations and grain designs for each of the small motor tests was completed.
- (2) Propellant grains for Motor Tests T-8 through T-15 were delivered to AFRPL.
- (3) Nozzles and motor insulation sections for motor tests through T-15 and T-14, respectively, were fabricated and delivered to AFRPL.
- (4) Required modifications to the ADOBE chambers, as a result of damage during testing and to accommodate the internal burning grain designs, have been completed.
- (5) Small Motor Tests T-1 through T-7 and T-9 through T-11 have been completed.

- (6) Two propellant formulations, one grain design, two submerged nozzle contour designs, and two nozzle throat materials have been selected for use in the development motor tests.
- (7) Fabrication of nozzles for Motor Tests T-16 through T-20 and motor insulation sections for Tests T-16 through T-22 was about 60 percent complete at the close of the period. Propellant grains for Motor Tests T-16, T-17, T-21 and T-22 were also nearly finished. The procurement of grain casting hardware and raw materials for the development motor grains was initiated during the final month of the reporting period.

5.2 (C) SMALL MOTOR TESTS

a. (U) Small Motor Design

(1) (U) Propellant Grain Design

All grain designs for the small motor tests were completed during the first reporting period of this program. Figures 47, 48, 49 and 50 in Reference 1 illustrate the single end-burning and three internal-burning grain designs that are being used in this test phase. The internal-burning grains are cast, overwrapped, and then bonded into the micarta insulation sleeves.

(2) (U) Motor Case Design

Small Motor Tests T-1 and T-2 (end-burning grains) indicated that the method used to seal the head end of the ADOBE motor case, as described in Paragraph 5.2b of Reference 1, was inadequate. Each test resulted in a partial burnthrough of the ADOBE motor case just forward of the steel bearing plates. It has been concluded that the burning of the cases occurred during the last second or two of firing in both instances. As the grain burning surface reached the head end epoxy inhibitor, the periphery of the inhibitor was exposed first due to a slight dishing of the propellant surface. This dishing, however slight, is a result of temperature gradients through the propellant cross section (i.e., higher temperature and higher burn rate near the insulated outer diameter of the grain).

The epoxy grain inhibitor and RTV sealant on the steel bearing plate were too weak to resist the pressure differential between the working and wood filled sections of the chamber. A blowthrough occurred at the exposed point (or points in the case of the second chamber). The flow of the hot gas through a limited area into the void spaces forward of the bearing plate caused a partial consumption of the chamber wall. The extent of the

damage was a furrow in the steel wall, roughly one-half inch deep, and extending one to three inches axially forward from the point of breakthrough. The damage was confined to a circumferentially narrow area which was sharply defined. According to the hypothetical beryllium combustion model, the gases flowing into the forward section of the motor should have been highly oxidizing. The major oxygen bearing constituent, water, reacts exothermically with the metal. Thus, the metal was burned away rather than simply melted.

When properly isolated, the filled portion of the chamber need not act as a pressure vessel. The restoration of both ADOBE motor cases was therefore reduced to supplying a more positive seal between the working and wood filled sections of each chamber. Both chambers were machined on the ID from the aft flange to the plane of the original bearing plate surface. This operation removed 0.070 inch from the ID and provided a 32 finish to the surface. A new aluminum bearing plate was machined for each of the ADOBE chambers. These plates were fitted into the chambers with an O-ring seal on the outer diameter. In one case, this plate was inserted on top of the existing wood filler blocks and unsealed steel bearing plate. No rework of the chamber wall, other than that required to provide a suitable surface for an O-ring seal, was effected. On the second chamber, the existing wood filler blocks and steel bearing plate were removed. A new set of blocks was machined with a stack up length equal to the original length of both the blocks and the plate.

For the remaining end-burner tests, the existing chamber liners were shortened by an amount equal to the thickness of the aluminum plate and slotted an additional 0.75 inch at the grain end. The longer slot was necessary to accommodate an asbestos phenolic disk, with a diameter equal to that of the propellant grain, inserted into the liner forward of the grain. Each asbestos phenolic disk was fitted with an O-ring seal. Thus, the disk provided a redundant pressure seal as well as increased insulation capability. Figure 107 illustrates the reworked ADOBE chamber configuration as used in Tests T-3 through T-7. For convenience of comparison with Figure 51 of Reference 1, the chamber illustrated is the one in which the existing wood filler blocks and bearing plate were retained.

The motor case designs used in conjunction with the internal-burning grains are illustrated in Figures 108, 109 and 110 for the Types I, II and III internal-burning grain designs, respectively. The conversion from the end-burning grain series requires only minor modifications. Additional thicknesses of filler blocks allow the grains of varying lengths to be butted against the aft closure insulator. Since these internal burning grains have no chamber liners other than the micarta tubing into which they were bonded, the asbestos phenolic disk seals directly against the chamber wall. The length tolerance buildup of the various components within the chamber are accounted for by a series of aluminum pancake shims which can be inserted between the aluminum bearing plate and the asbestos phenolic disk. This ensures the required close fit between the aft end of the grain and the aft closure

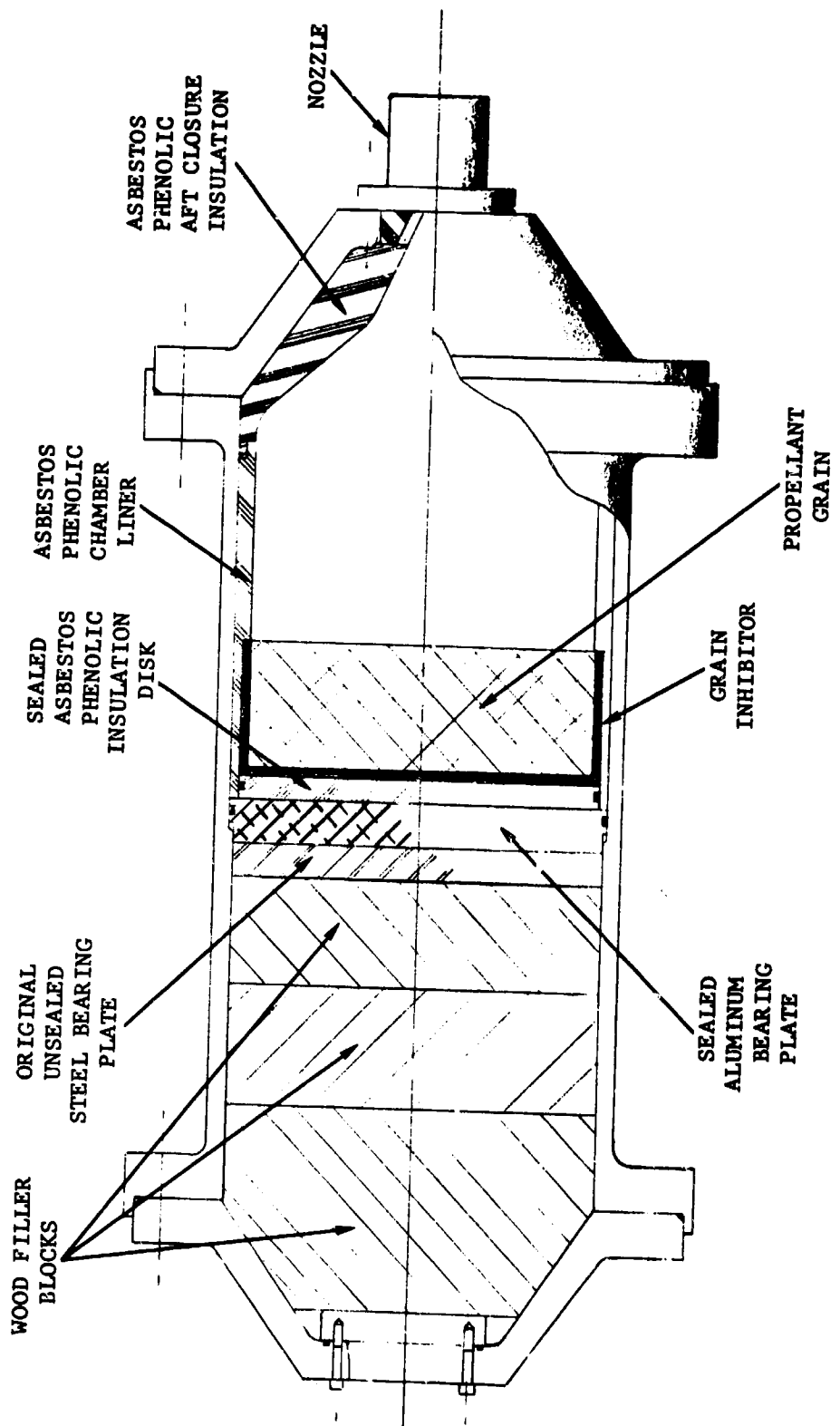


FIGURE 107. MODIFIED MOTOR CASE DESIGN - END BURNING GRAINS

F04125 U

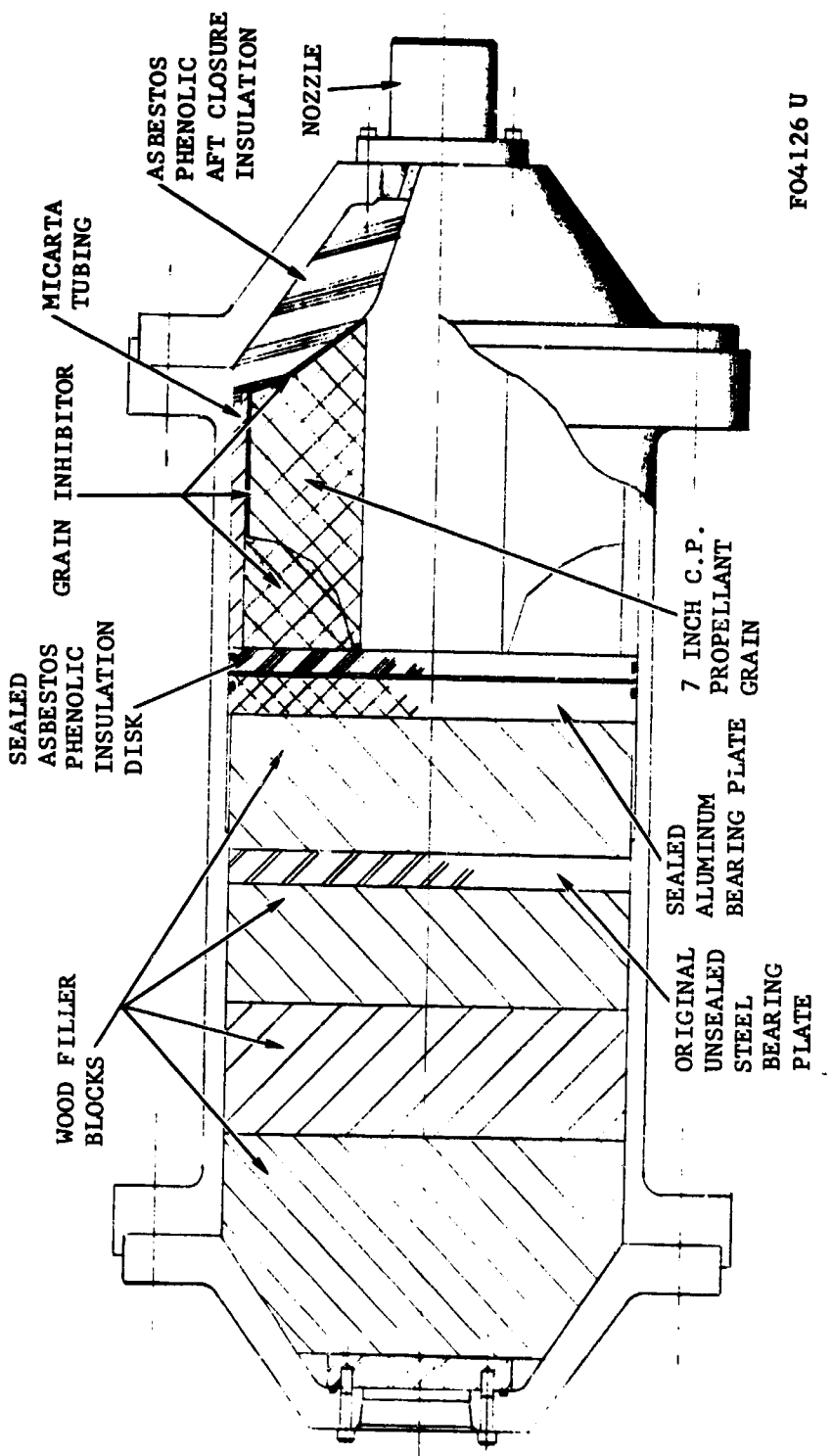
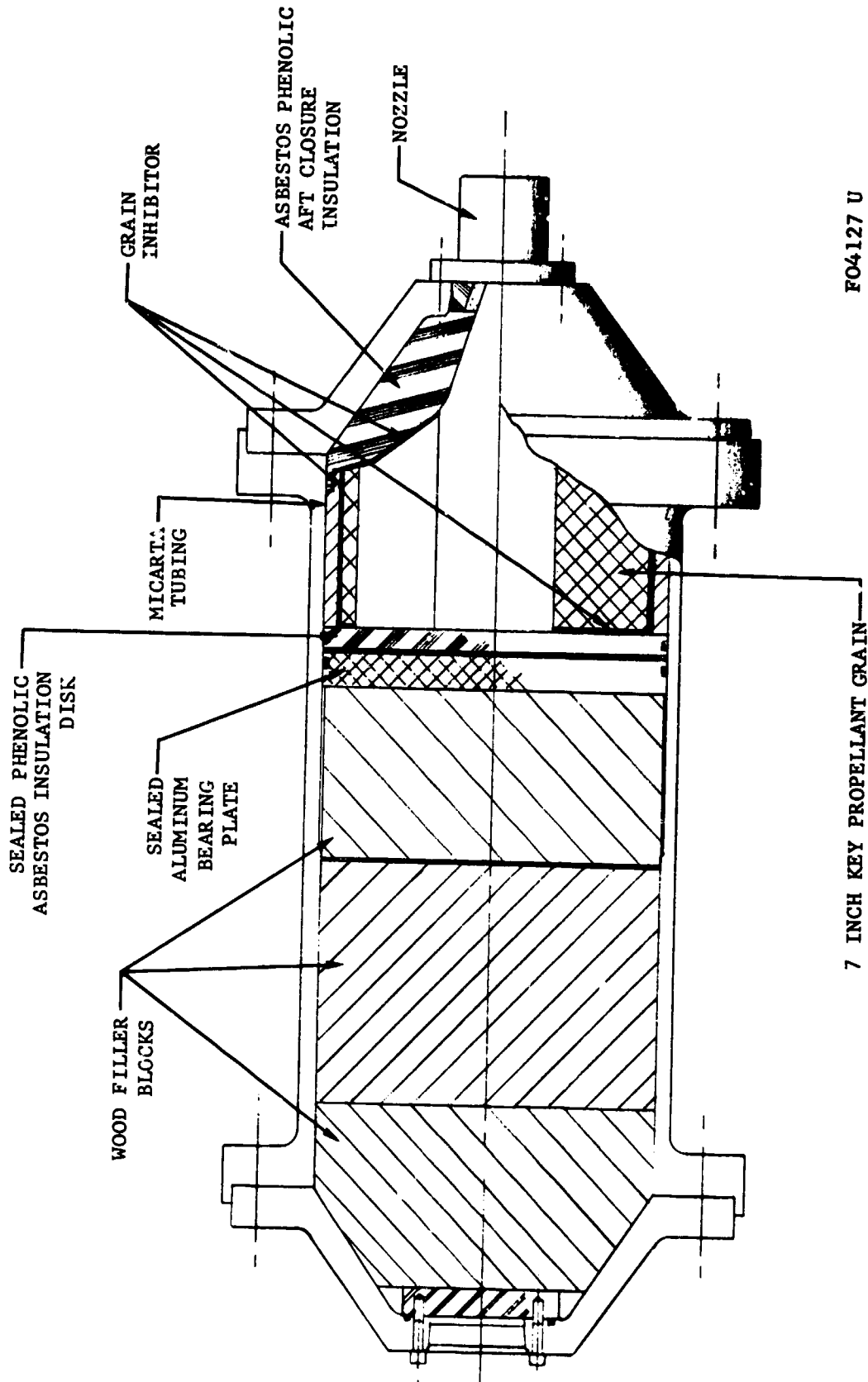


FIGURE 108 . MOTOR CASE DESIGN - INTERNAL BURNING GRAINS TYPE I



FO4127 U

7 INCH PROPELLANT GRAIN

FIGURE 109. MOTOR CASE DESIGN - INTERNAL BURNING GRAINS TYPE II

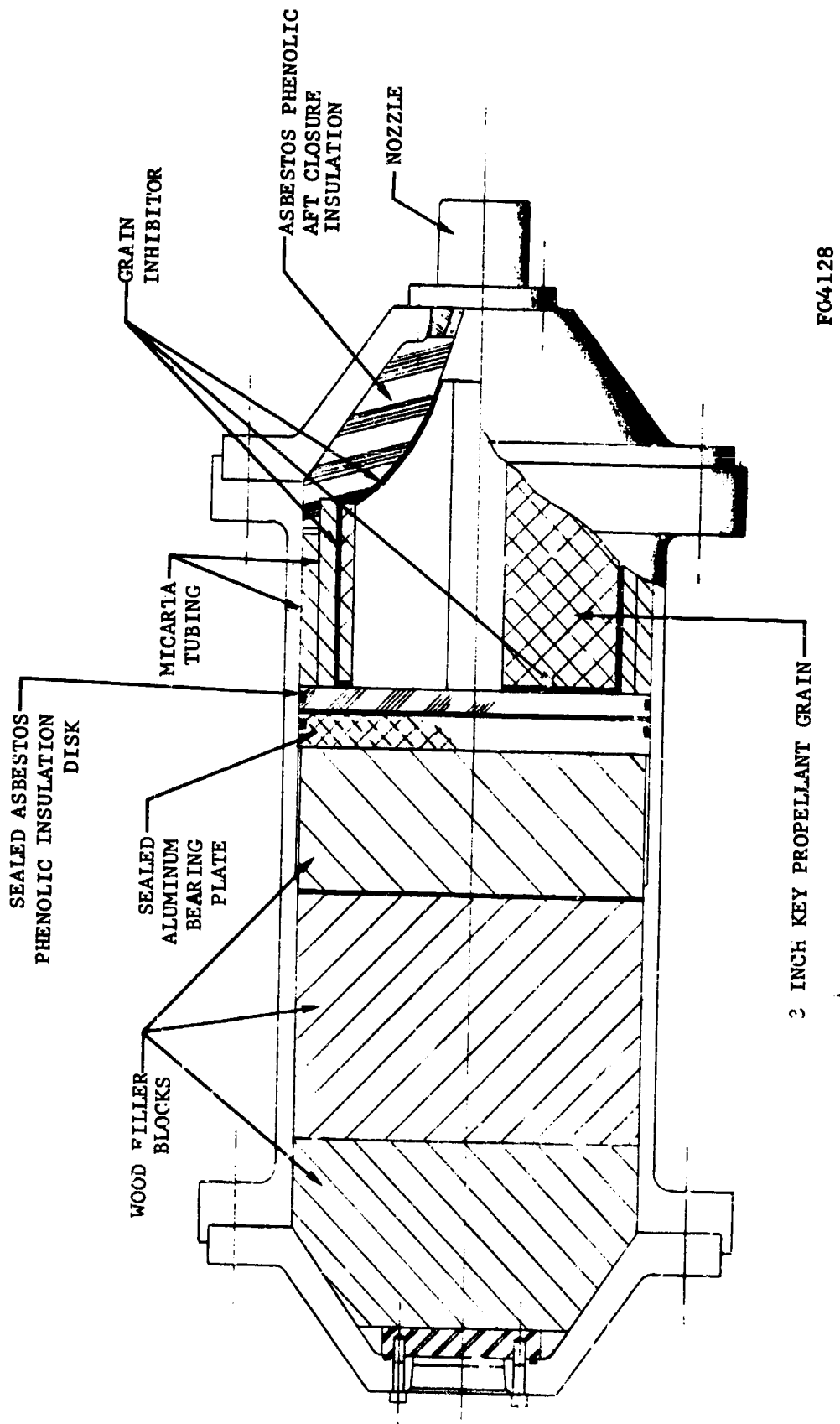


FIGURE 110. MOTOR CASE DESIGN - INTERNAL BURNING GRAIN TYPE III

FC4128

2 INCH KEY PROPELLANT GRAIN

closure insulation. Sealing of the grain to closure insulation is accomplished with a Cab-O-Sil filled Genepoxy-Versamid resin cured at room temperature. The head end of the grain is bonded to the asbestos phenolic disk with RTV-60. The gap between the grain OD and the oversized chamber ID is virtually eliminated by insertion of two aluminum clam shell shims.

(3) (U) Nozzle Design

During this reporting period, the remainder of the small scale nozzles were designed (nozzles for Tests T-8 and T-16 through T-22). The individual geometries of these eight nozzles are essentially the same as those pictured in Figures 53, 54 and 55 of Reference 1. The important differences in materials and configuration details are described below.

The nozzle for Test T-8 was originally designed to be fired with the aluminum analog of Arcane 24F in an end-burner configuration. This nozzle has been redesigned to the same configuration as that of T-10 which is illustrated in Figure 53 of Reference 1. Test T-8 will utilize Arcocel 389, the aluminum analog of the Arcocel 191F used in Test T-10, and the Type II grain configuration as in Test T-10.

The nozzle designed for Test T-16 is illustrated in Figure 111. It differs from the nozzle shown in Figure 53 of Reference 1 in that the pyrolytic graphite throat has been replaced by a tapered tungsten insert with a single pyrolytic graphite washer upstream of the insert. Except for the throat insert, all configuration details are the same as those used in the other conventionally contoured nozzle internal-burning grain tests. Test T-16 was designed specifically to compare the performance of tungsten with pyrolytic graphite under identical conditions of propellant type, configuration, throat size, and firing conditions (i.e., a comparison with Test T-9).

The nozzle design for Test T-17 is shown in Figure 112. This nozzle is identical to that of T-16 except for the substitution of a carbon cloth phenolic entrance for the graphite entrance of T-16. This test will provide relative performance characteristics of these entrance materials and their influence on the throat insert performance under similar test conditions.

Test T-18 will utilize the nozzle design shown in Figure 113. The basic configuration of this nozzle is identical to the submerged nozzle shown in Figure 55 of Reference 1, with the tungsten insert substitution as in Test T-16. Thus, T-18 is a materials comparison test with T-12, its pyrolytic graphite counterpart.

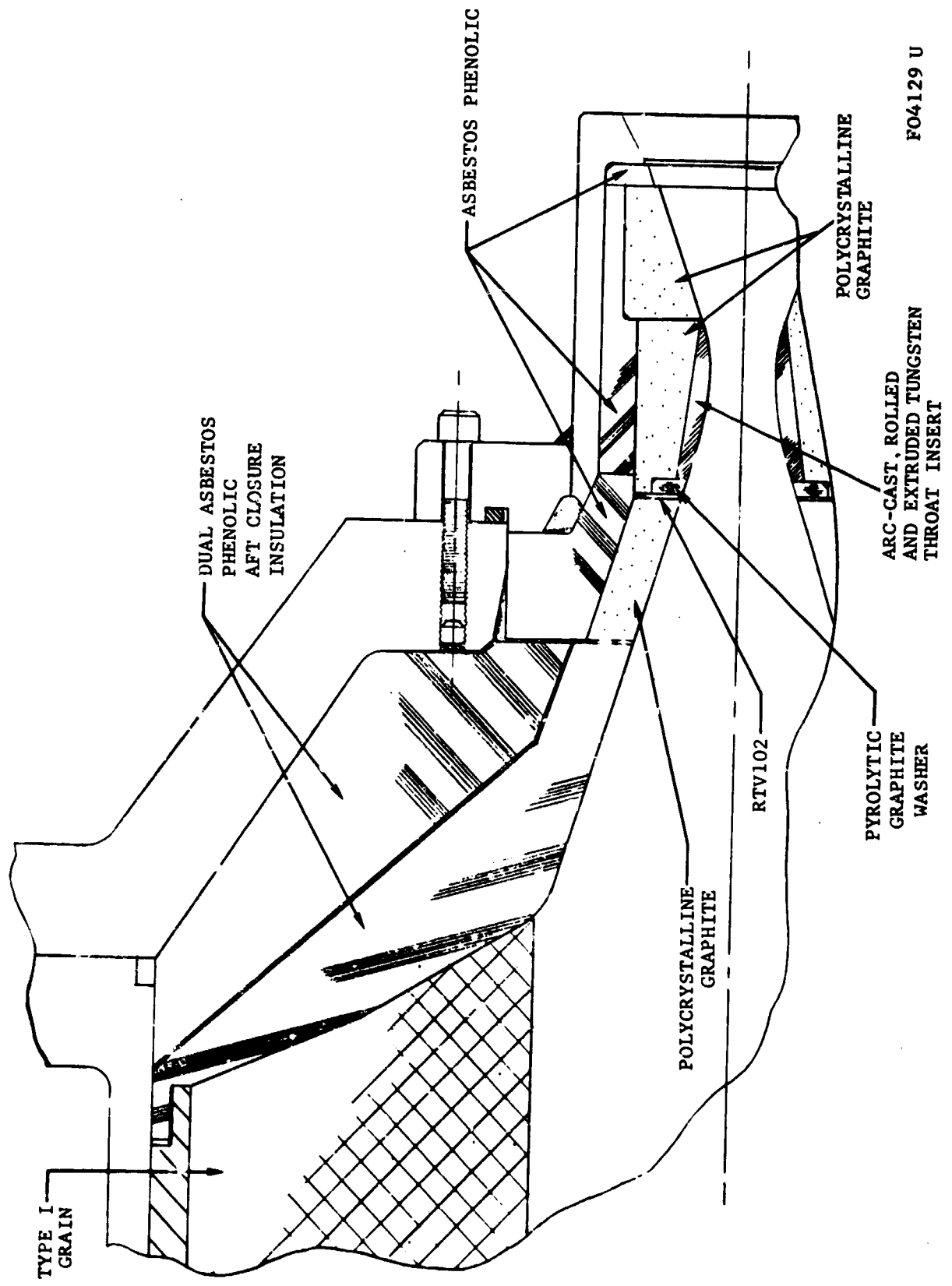


FIGURE 111. NOZZLE DESIGN FOR TEST T-16

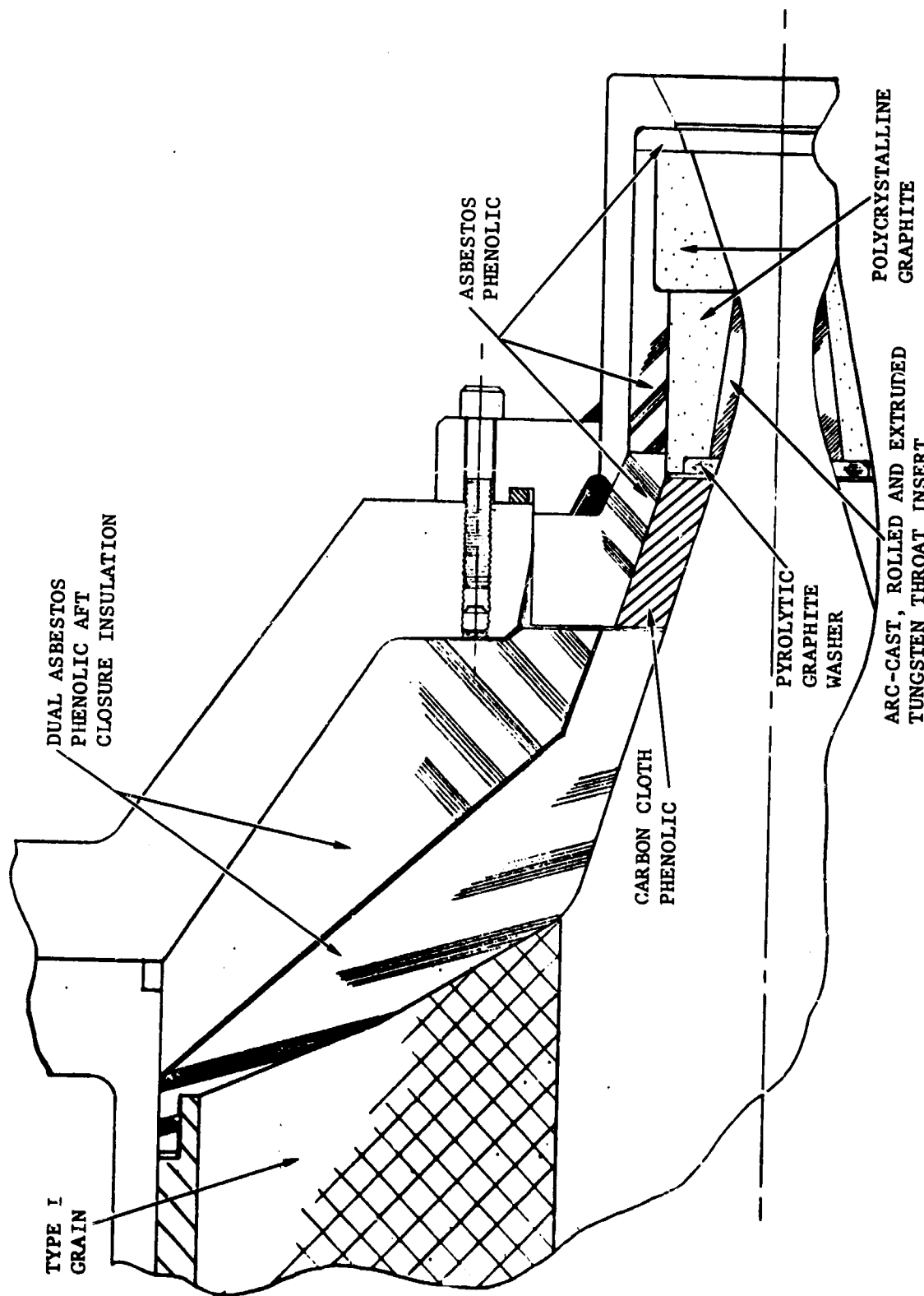


FIGURE 112. NOZZLE DESIGN FOR TEST X-17

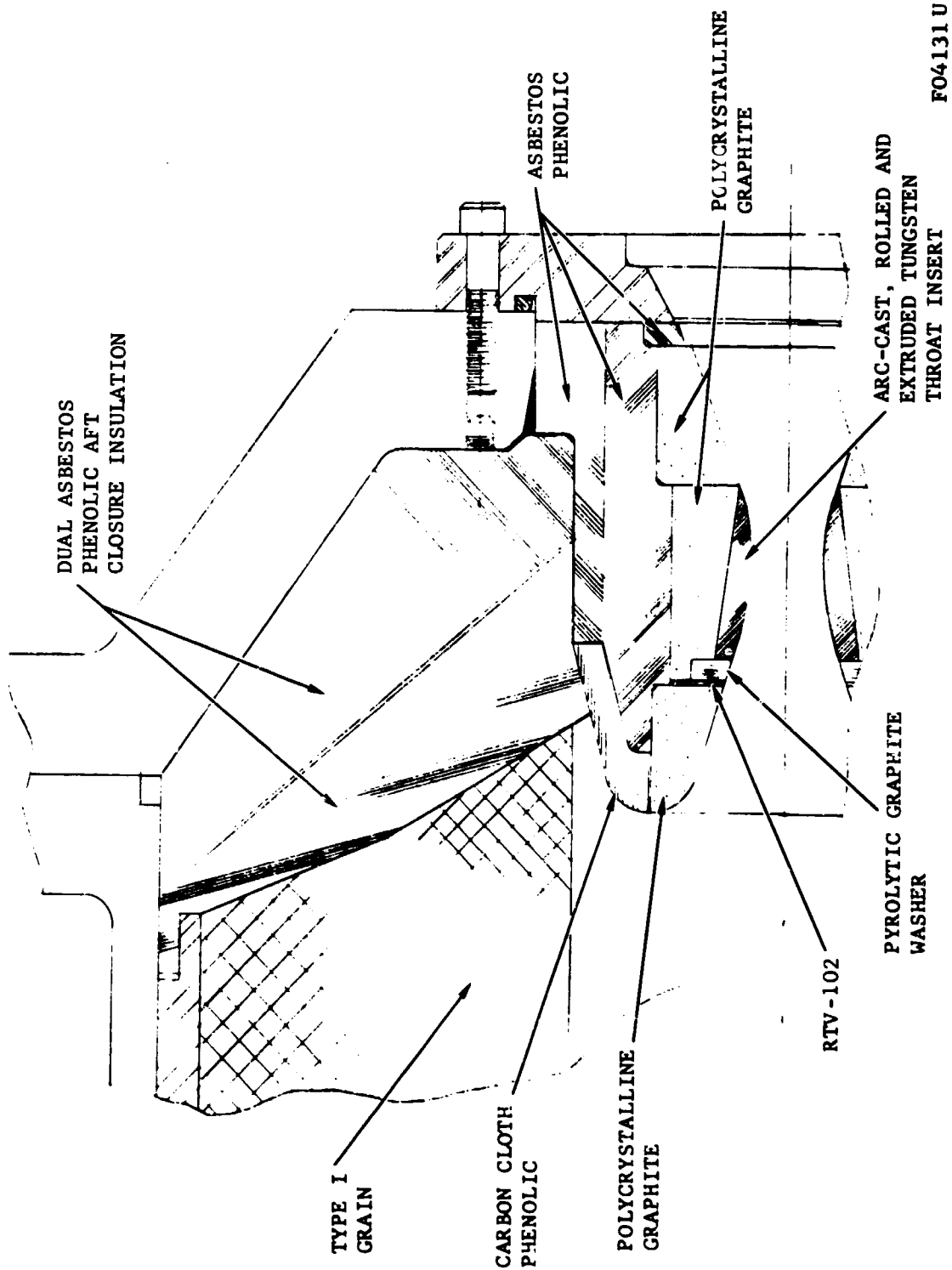


FIGURE 113. NOZZLE DESIGN FOR TESTS T-18 AND T-19

CONFIDENTIAL

The nozzle designed for Test T-19 is identical in all respects to T-18, shown in Figure 113. Test T-19 will, however, utilize Arcocel 319BRF in a Type I grain configuration whereas T-16, T-17 and T-18 are to be tested with Arcocel 191F in the Type I grain configuration. Test T-19 will therefore serve to compare the effect of double base propellant formulation differences on identical nozzle designs.

Test T-20 will employ the nozzle design shown in Figure 114. It is identical to the design pictured in Figure 53 of Reference 1, with a substitution of carbon cloth phenolic for the graphite entrance. It is identical to Test T-9 in terms of propellant type and configuration. Test T-20 therefore provides a comparison with T-9 that parallels the entrance materials comparison of tungsten nozzles T-17 and T-16.

The design of nozzles T-21 and T-22 are identical to each other and to the nozzle design for T-13 shown in Figure 54 of Reference 1. The nozzles for T-21 and T-22 are illustrated in Figure 115. Tests T-21 and T-22 will utilize the Arcocel 191F and Arcane 54F propellant, respectively. The propellant will be cast in an end burning configuration similar to that of Tests T-1 through T-7, but will be positioned as close as possible to the aft closure insulation. Figure 115 shows the relationship of the propellant grains to the aft closure insulation and nozzle. These tests will be used to study the effects of non-equilibrium combustion on the nozzle and closure insulation performance.

A two-piece aft closure insulation section will be used in Test T-15 through T-22. The section adjacent to the steel closure is to be reused. Two such sections were machined from the aft closure insulations from the aluminum end-burner tests T-5 and T-6. These reusable sections differ slightly, as indicated in Figures 112 and 113, to accommodate the two basic nozzle types. Individual flame side sections will be made for each test using the two-piece closure insulation. The two sections will be bonded together with RTV-50.

b. (C) Test Results

Ten small motor tests were conducted during this reporting period. The results of the first seven (end burning grains) designated T-1 through T-7 are presented here. The data and associated empirical analyses of these tests have been classified into three categories. The first category contains ballistic data which include determinations of characteristic exhaust velocities, specific impulses, and the generation of the various chamber pressure and thrust versus time curves. The second category is nozzle performance. This area encompasses general throat dimension changes as determined from before and after test measurements, as well as including a special treatment of nozzle throat radius change as a function of firing time. The ultimate values of throat radii changes as functions of time are derived from three basic approaches, each of which is discussed in the

CONFIDENTIAL

CONFIDENTIAL

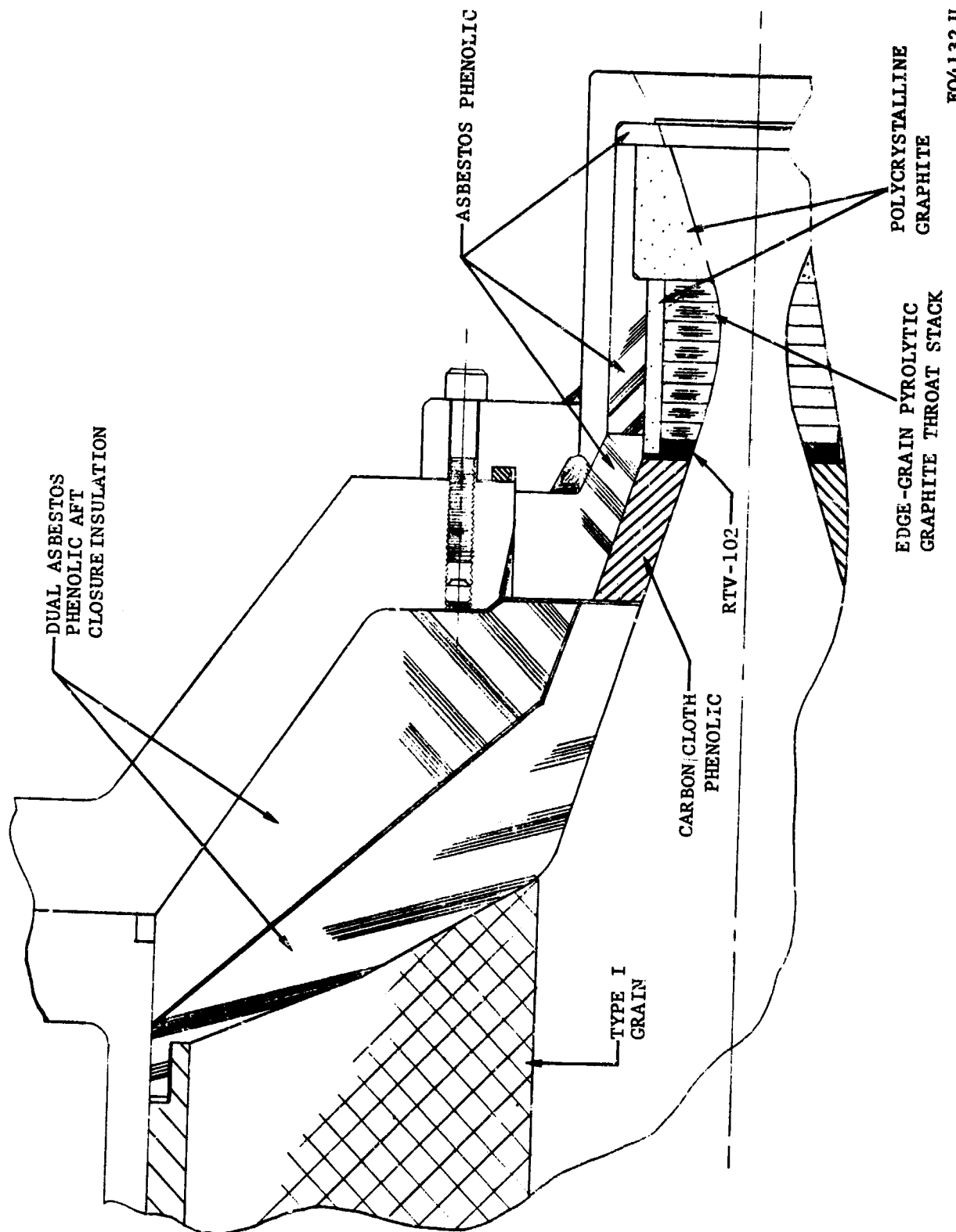


FIGURE 114. NOZZLE DESIGN FOR TEST T-20

FO4 132 U

CONFIDENTIAL

CONFIDENTIAL

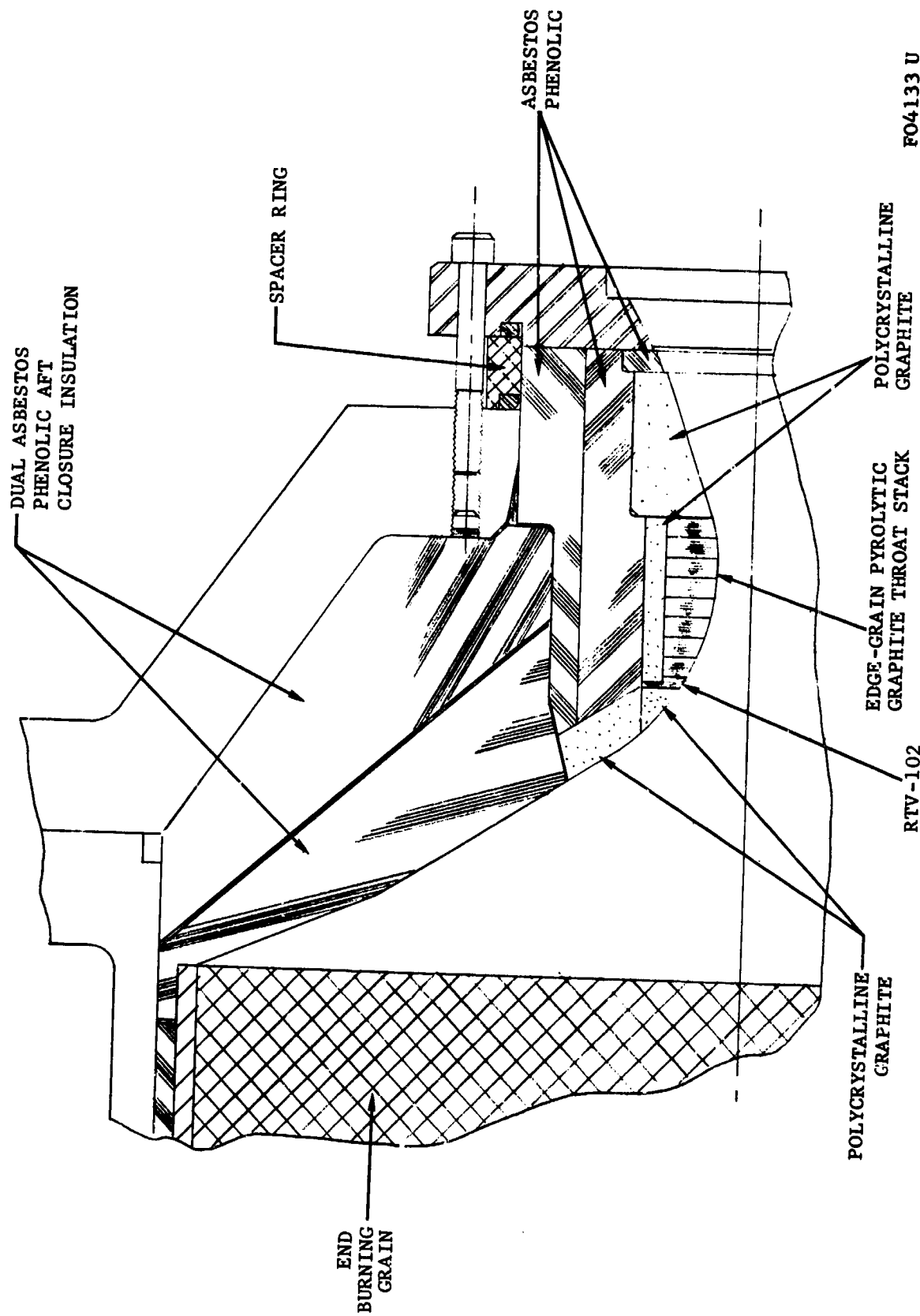


FIGURE 115. NOZZLE DESIGN FOR TESTS T-21 AND T-22

CONFIDENTIAL

CONFIDENTIAL

the following paragraphs. The third category of test results is thermal corrosion and post-test analysis data. A discussion of the thermal data is presented in Paragraph 2.5. The interpretation of corrosion-erosion measurements is given in Paragraph 2.3 and the post-test analysis results are given in Paragraph 3.4. The other two categories are treated below.

(1) (C) Ballistic Data

The ballistic performance was computed for the first seven motor tests in order that (1) the overall motor and propellant performance could be compared with similar configurations tested previously under other contracts, and (2) the degree of propellant combustion could be examined more closely.

The integral average throat area (including the effects of throat deposition and/or erosion) together with the nozzle exit diameter, exit half angle, and average specific heat ratio, were compiled at Aeronutronic and delivered to Telecomputing Services, Inc. (servicing AFRPL) for use in performance calculations. The following is a list of the parameters computed from the raw test data: (1) action time, (2) apparent action time (pressure), (3) ignition delay time, (4) maximum chamber pressure, (5) pressure-burn time integral, (6) average chamber pressure for burn time, (7) total pressure-time integral, (8) maximum thrust, (9) thrust-action time integral, (10) average thrust from action time, (11) exit pressure, (12) measured impulse, (13) specific impulse corrected to 1000 psia and optimum expansion, (14) specific impulse corrected to zero degree half angle, (15) characteristic exhaust velocity, (16) mass discharge, (17) discharge coefficient, and (18) thrust coefficient.

The action time, as computed by the TSI computer program, is based on the maximum thrust attained during the run. The starting time point corresponds to the time during the startup transient when the chamber pressure is 10 percent of the maximum chamber pressure that occurs during the run. Similarly, the burnout time is designated as the time when the chamber pressure is 10 percent of the maximum attained pressure (see Figure 116). Normally, in specific impulse calculations, the action time is based on the intersection of the start (or tailoff) transient slope and the more horizontal burn pressure slope (see Figure 117). Again, in the more conventional method for establishing action time, the time which corresponds to the pressure which is 10 percent of the pressure designated or illustrated in Figure 117 is chosen as the start or end point (as appropriate) defining the period of propellant burning. In either method, the designated action time is somewhat arbitrary. However, the resulting value of specific impulse can be significantly altered depending on which method was used. Table XXVI presents both the TSI and Aeronutronic (ADP) computed specific impulse values.

The characteristic exhaust velocity, (C^*) in most cases, is computed using the average of the initial and final nozzle throat diameters. However,

CONFIDENTIAL

CONFIDENTIAL

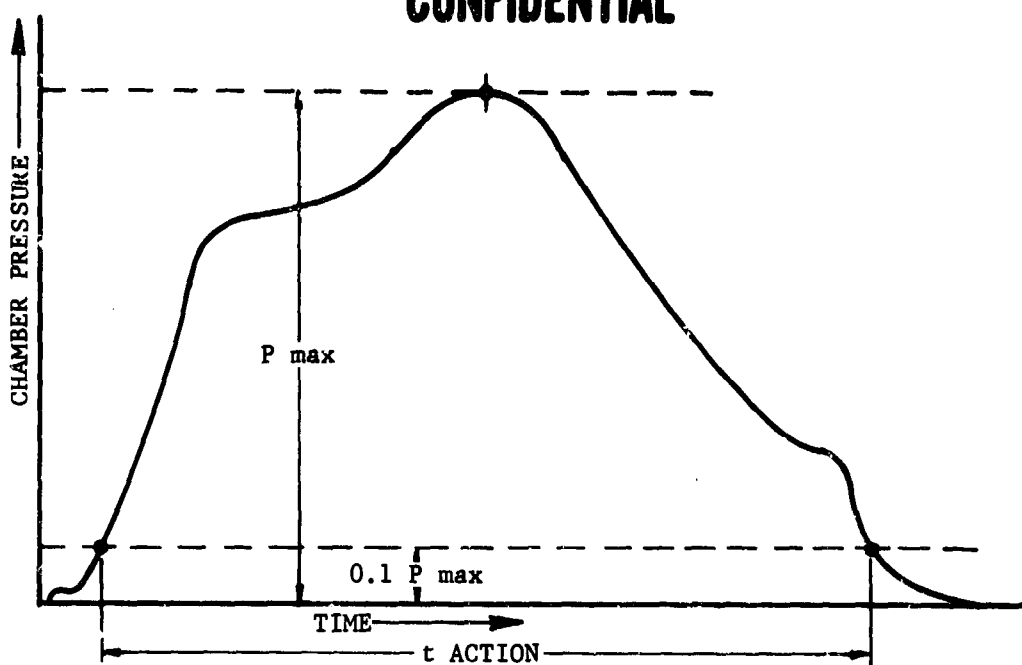
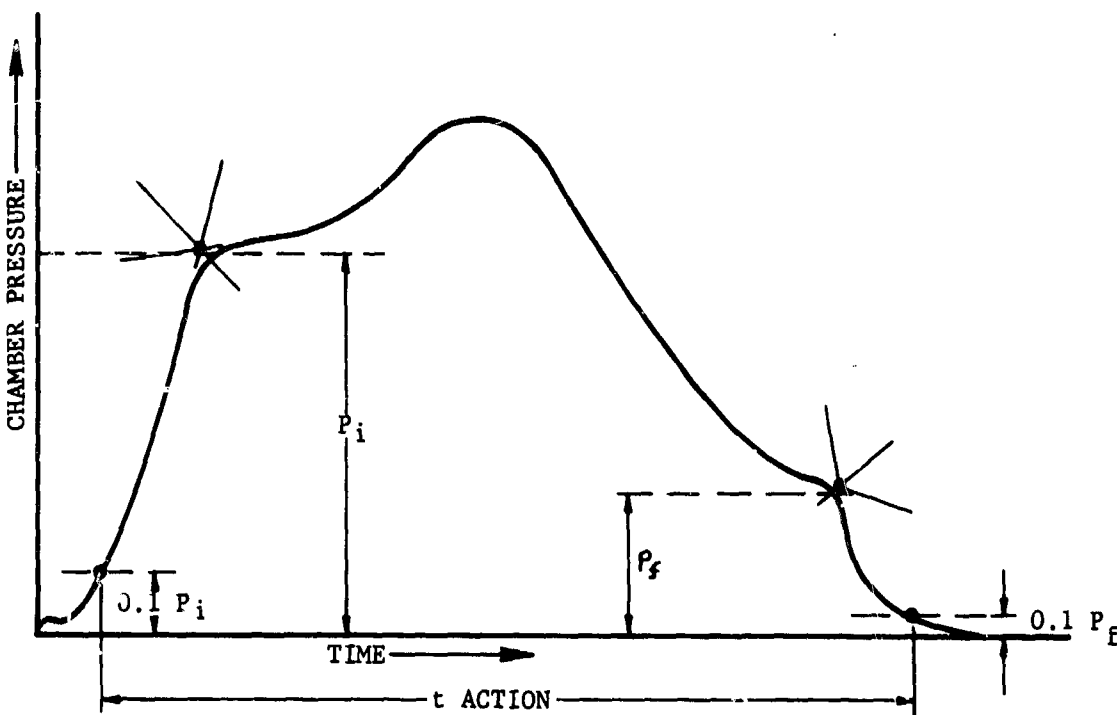


FIGURE 116. ACTION TIME DEFINITION - TSI METHOD



F04134 C

FIGURE 117. ACTION TIME DEFINITION - ADP METHOD

CONFIDENTIAL

CONFIDENTIAL

TABLE XXVI. BALLISTIC DATA, TESTS T-1 THROUGH T-7

Test Number	Propellant	Action Time, t_a (seconds)	Propellant Weight (lb)	$\frac{P_c}{P_{max}}$	$\frac{F_c}{F_{max}}$	Chamber Pressure (psig)	Thrust (1b) \bar{F}	C^* (fps)		$\frac{ISP}{ISP_{ADP}}$	$\frac{ISP}{ISP_{TSI}}$
								C^*_{EQ} (800 psia)	C^*_{TSI}		
T-1	Arocel 191F	19.4	101.28	.1180	.818	1820	1230	5448	5386	5170	232 to 236
T-2	Arcane 24F	28.8	105.734	.965	.723	1165	867	3420	5453	5055	229 to 236
T-3	Arocel 319BRF	17.5	98.11	.1105	.737	1655	1372	5510	5704	5525	246 to 5755
T-4	Arcane 54F	26.2	105.567	.880	.799	1020	929	5297	5338	4890	233 to 5414
T-5	Arcane 60	24.96	112.43	.925	.830	1120	1019	5123	5062	4910	225 to 5108
T-6	Arocel 390	27.54	107.55	.720	.536	1180	868	5279	5023	4910	220 to 5041
T-7	Arocel 389	17.24	110.59	.1010	.935	1550	1430	5197	4893	4800	226 to 4904

-236-

CONFIDENTIAL

CONFIDENTIAL

this value can be somewhat erroneous, especially when the nozzle involved experiences both liquid or solid metal oxide deposition (which decreases the throat area) and chemical corrosion or mechanical erosion. To illustrate the potential error in computing the values of C^* by the more conventional method, which uses the average between the initial and final throat diameters, C^* computations were made for the first seven motor firings using the instantaneous throat radius history derived from Figures 139 through 145. The following equation for C^* was used for these calculations:

$$C^* = \left[t_a r^2 - 2r \int_{t_a}^{t_a} \delta dt + \int_{t_a}^{t_a} \delta^2 dt \right] \left[\frac{\pi}{t_a} \right] \left[\frac{g}{\omega} \right] \left[\int_{t_a}^{t_a} P_c dt + P_\infty t_a \right]$$

where

t_a = action time (sec)

r = throat radius (inches)

δ = change in throat radius (inches)

ω = weight of propellant (lbm)

P_c = chamber pressure (psig)

P = ambient pressure (psia)

g = gravitational constant (ft lbm/lbf sec²)

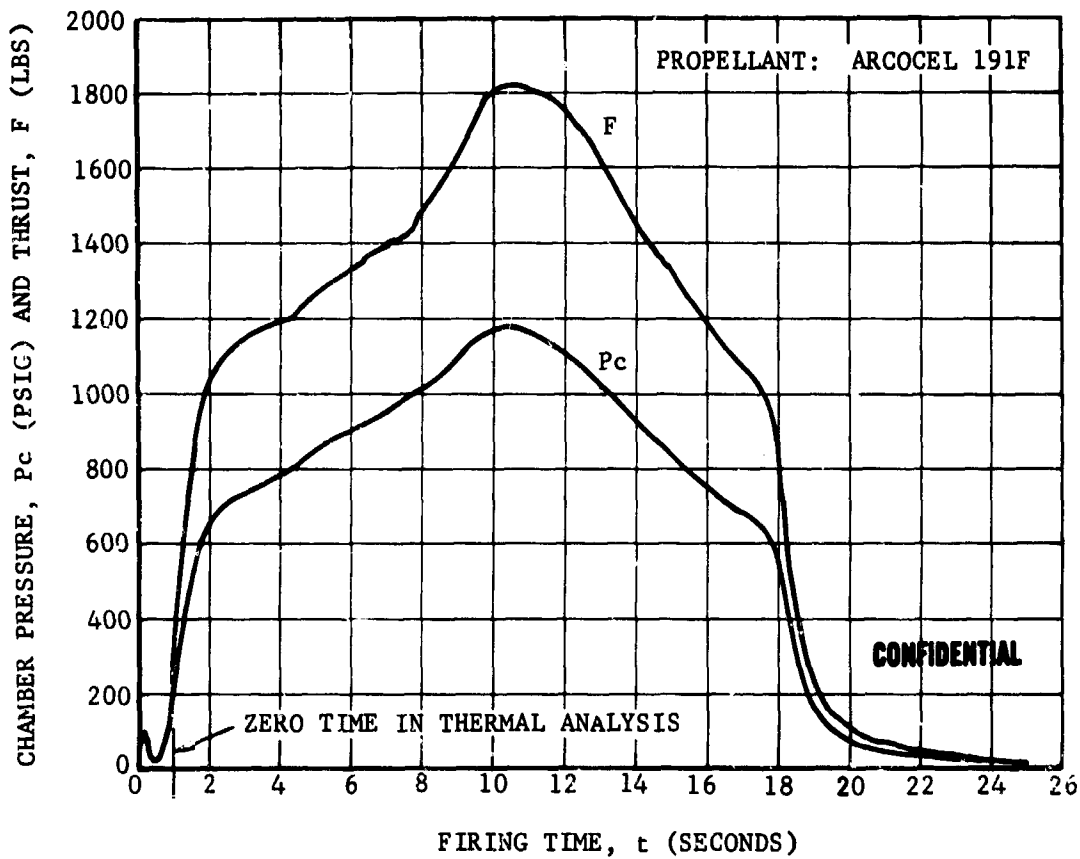
Note that the second order change in throat radius term has been neglected. The resulting values of C^* are tabulated in Table XXVI along with the TSI values (which were computed with the average of the initial and final throat diameters).

It is anticipated that later in this program, the relation between the theoretical C^* and pressure will be computed for each of the propellants used. At that time, a theoretical C^* will be computed for each firing. The theoretical value will be a pressure dependent time averaged value which can be compared directly with both the present ADP and TSI computed values. However, for cursory comparison, the theoretical equilibrium C^* for the nominal 800 psia chamber pressure is presented. A comparison with this theoretical value of C^* is not necessarily meaningful.

Maximum and average values of chamber pressure and thrust for Tests T-1 through T-7 are listed in Table XXVI with the aforementioned calculated values of C^* and specific impulse. Figures 118 through 124 illustrate the chamber pressure versus time histories of these first seven tests. For

CONFIDENTIAL

CONFIDENTIAL



FO4135 C

FIGURE 118. CHAMBER PRESSURE AND THRUST VERSUS FIRING TIME TEST T-1

CONFIDENTIAL

CONFIDENTIAL

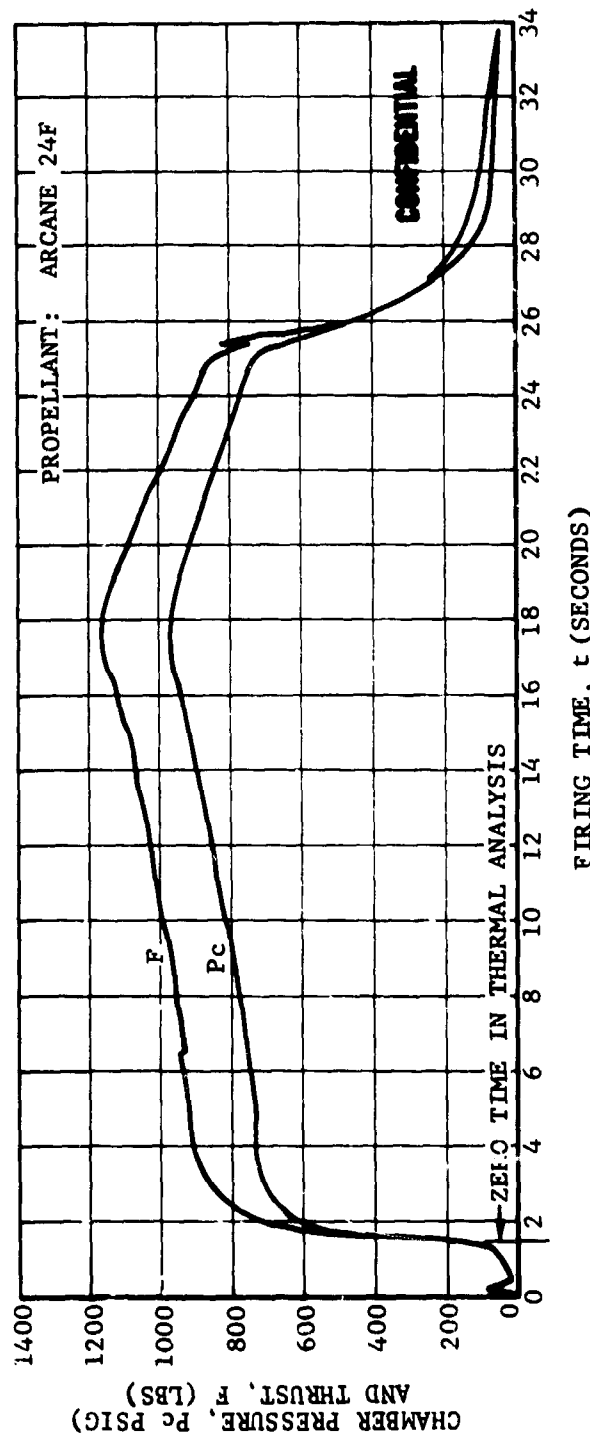
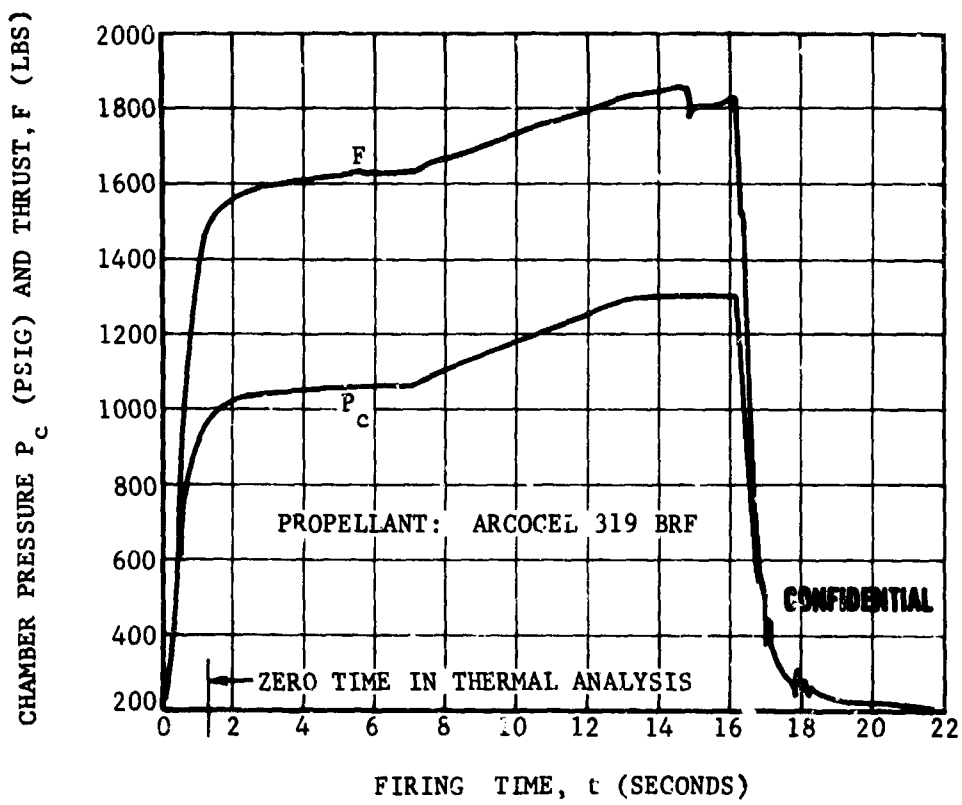


FIGURE 113. CHAMBER PRESSURE AND THRUST VERSUS FIRING TIME TEST T-2

CONFIDENTIAL

CONFIDENTIAL



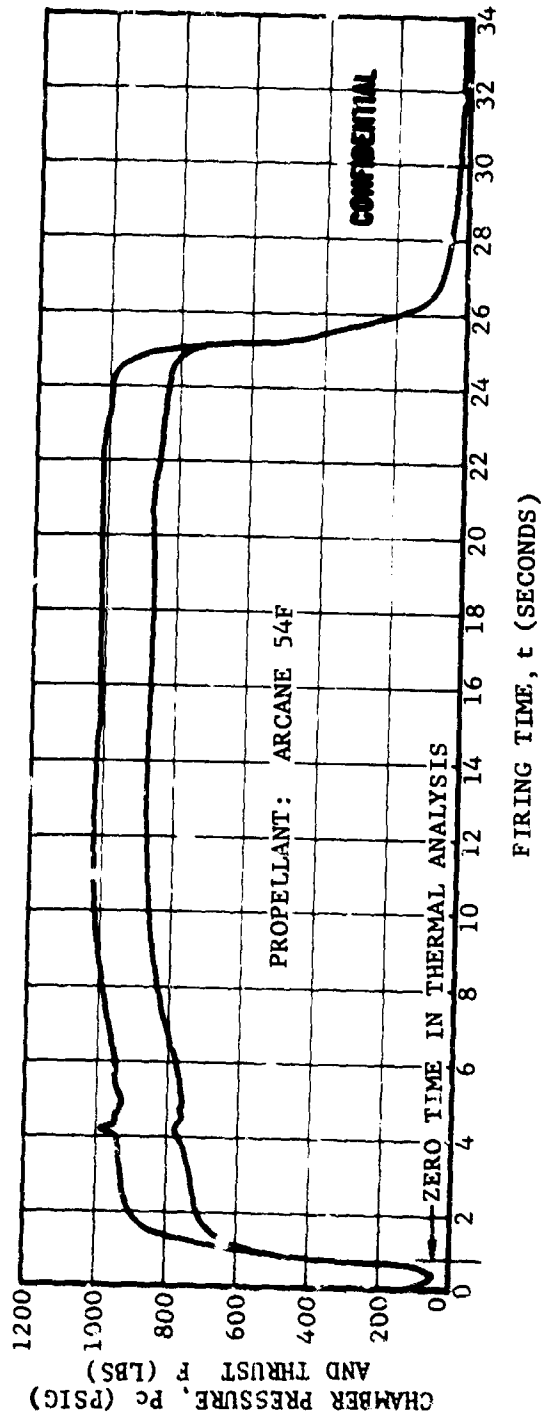
F04137 C

FIGURE 120. CHAMBER PRESSURE AND THRUST VERSUS FIRING TIME TEST T-3

-240-

CONFIDENTIAL

CONFIDENTIAL



FO4138 C

FIGURE 121. CHAMBER PRESSURE AND THRUST VERSUS FIRING TIME TEST T-4

CONFIDENTIAL

CONFIDENTIAL

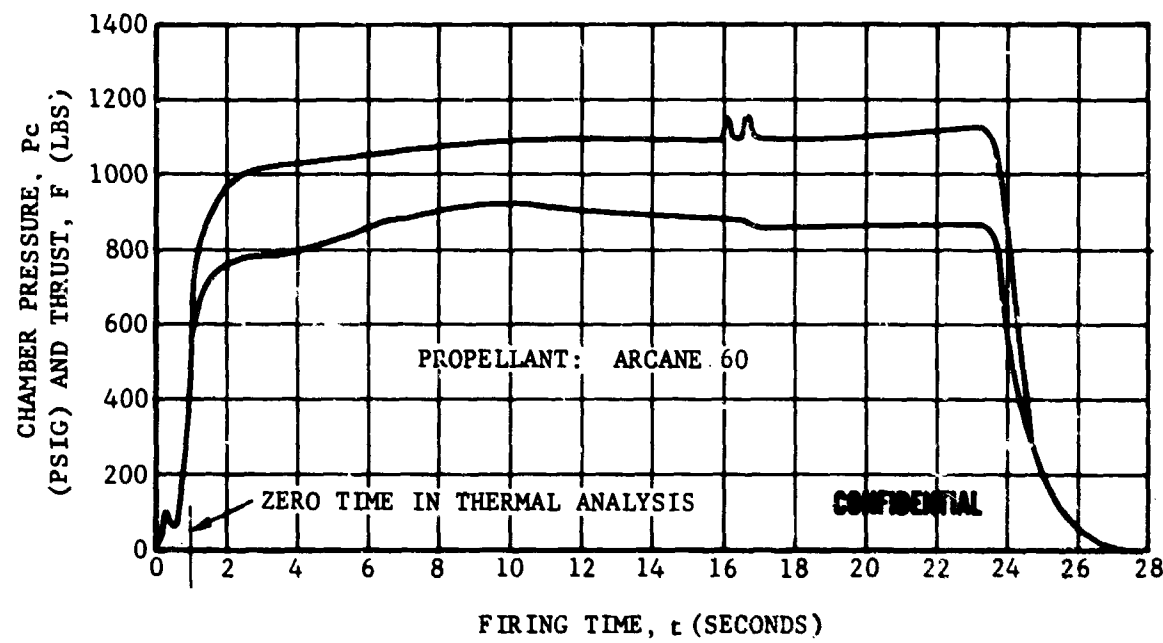


FIGURE 122. CHAMBER PRESSURE AND THRUST VERSUS FIRING TIME TEST T-5

CONFIDENTIAL

CONFIDENTIAL

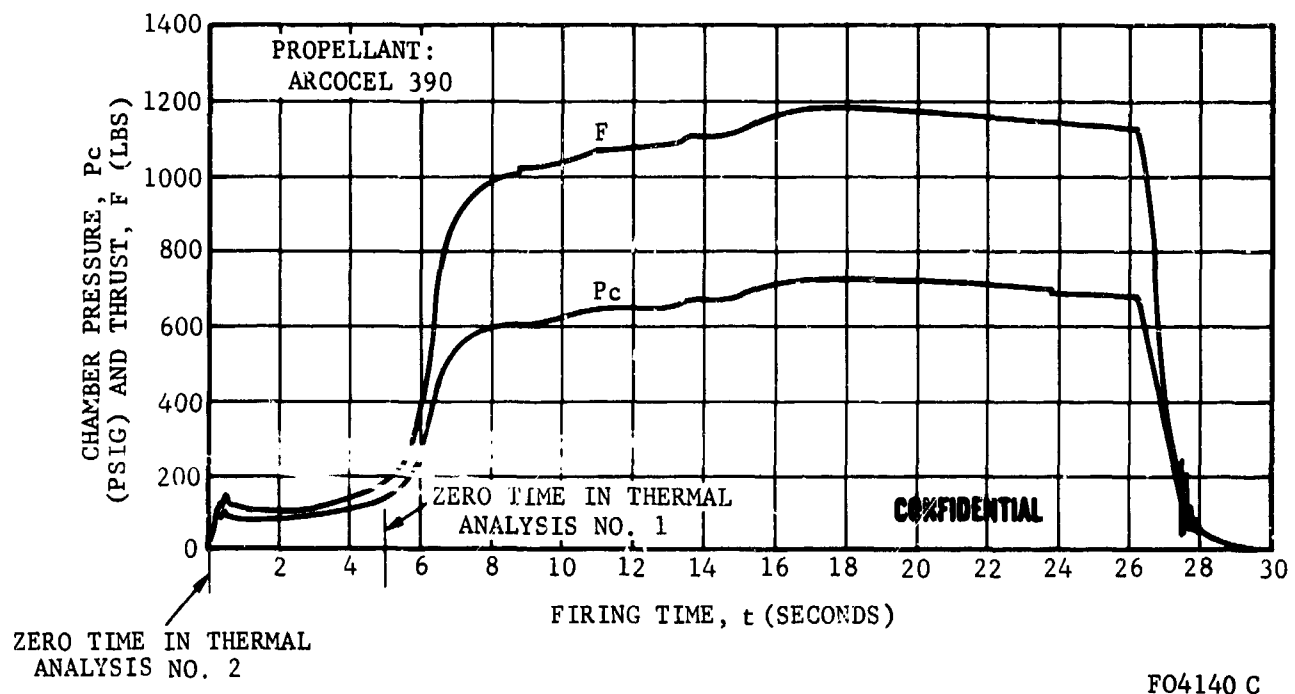
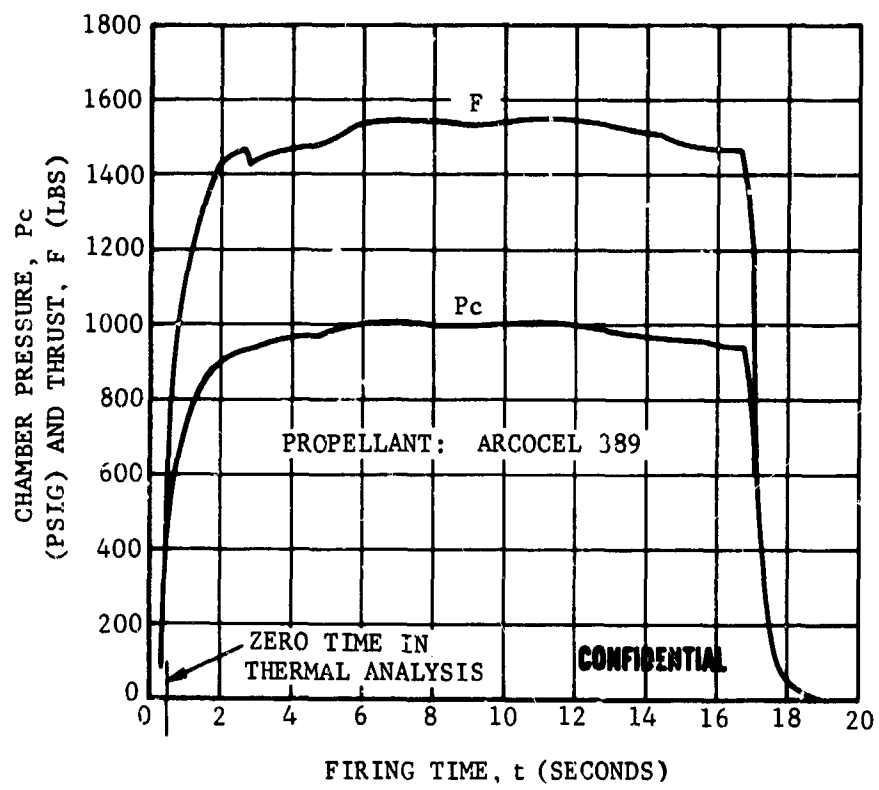


FIGURE 123. CHAMBER PRESSURE AND THRUST VERSUS FIRING TIME TEST T-6

CONFIDENTIAL

CONFIDENTIAL



FO4141 C

FIGURE 124. CHAMBER PRESSURE AND THRUST VERSUS FIRING TIME TEST T-7

CONFIDENTIAL

CONFIDENTIAL

convenience, thrust versus time for each of these motor tests is also plotted with pressure in Figures 118 through 124. The zero time selected for use in the thermal analyses, described in Paragraph 2.5, is indicated on the time scale in each figure.

(2) (C) Nozzle Performance

(a) (U) General Data and Analysis Requirements

Measurements of nozzle throat diameters before and after firing were made for Tests T-1 through T-7. These values are listed in Table XXVII with generalized values of erosion rates. The generalization of nozzle performance as tabulated in Table XXVII by no means presents a complete picture of nozzle behavior during a given firing cycle, nor does it permit a true evaluation of motor performance.

A deposit on the nozzle throat affects nozzle material performance significantly. There are three primary ways in which the metal oxide deposit acts upon a nozzle throat. Each of these actions is protective in nature. The deposit provides a physical barrier against erosive attack from abrasive particles in the propellant gas stream. It also provides protection against the corrosive reaction of the gas stream with the nozzle flame front materials. The third protective mechanism is the significant reduction in heat transferred to the nozzle wall due to the relatively low thermal conductivity of the metal oxide deposit. Since the susceptibility of the nozzle to the corrosion/erosion mechanisms is a strong function of temperature, the reduction of nozzle thermal response is inherently protective.

The effect on motor performance due to nozzle dimension changes that occur during firing is demonstrated by the variation in values of C^* computed by TSI as compared to those computed by Aeronutronic (Table XXVI). The characteristic exhaust velocities determined by Aeronutronic take into account instantaneous throat diameter changes that occur due to either an erosion/corrosion mechanism and/or to the coating of the nozzle throat with a metal oxide deposit.

A sequential development of analyses for estimating throat radius change, as a function of firing time, for Test T-1 through T-7 is presented in the following paragraphs. The first technique described is the method of calculating deposition as evolved for Aeronutronic simulator tests (simulator deposition data will eventually be compared with the solid propellant test data). The development of the K_n method is then presented and its limitations are discussed. A method which utilizes thrust to pressure ratios for calculating instantaneous throat radius changes is also derived and discussed. Finally, curves of throat radii changes as functions of firing times which are derived from a complementary usage of the K_n and F/P methods are presented in Figures 139 through 145.

CONFIDENTIAL

CONFIDENTIAL

TABLE XXVII. GENERAL NOZZLE THROAT PERFORMANCE

Test Number	Propellant	Action Time t_a (seconds)	Throat Diameter \bar{D}_t		Change in Throat Radius, $\frac{\pm \delta}{\delta}$ (inches)		Throat Erosion or Shrinkage Rate $d\delta/dt$ (mils/sec)
			Before	After	+ = Erosion	- = Shrinkage	
1	Arcocel 191F	19.4	1.166	1.176	+5.0		+0.258
2	Arcane 24F	28.8	1.030	1.029	-0.5		-0.017
3	Arcocel 319BRF	17.5	1.190	1.196	+3.0		+0.172
4	Arcane 54F	26.2	1.030	1.011	-9.5		-0.363
5	Arcane 60	25.0	1.044	1.049	+2.5		+0.100
f	Arcocel 390	27.5	1.200	1.202	+1.0		+0.036
7	Arcocel	17.2	1.146	1.151	+2.5		+0.143

CONFIDENTIAL

(b) (U) The C^* Method for Calculating Throat Radius Changes

In prior programs conducted by Aeronutronic in which the solid propellant simulator has been utilized, the ballistic equation which relates C^* to chamber pressure, propellant flow rate and nozzle throat area has been employed to predict nozzle throat geometry changes that occur during a motor firing. This has been possible because the simulator maintains a constant weight flow rate of propellant, \dot{w} , throughout any given firing. This constant \dot{w} , coupled with a C^* value, which is essentially constant for any specific simulator propellant mixture ratio, permits a simplification of the general ballistic equation as shown below

$$C^* = \frac{P_c A_t g_o}{\dot{w}} \quad (10)$$

where

P_c = motor chamber pressure, psia

C^* = characteristic propellant velocity, fps

A_t = nozzle throat area, in.²

g_o = acceleration due to gravity (constant)

\dot{w} = propellant weight flow rate, lb/sec

Equation (10) is satisfied at any and all instances throughout a given firing and therefore:

$$C^* = \frac{(P_{c_0}) A^* g_o}{\dot{w}} = \frac{P'_c A'_t g_o}{\dot{w}} \quad (11)$$

where:

(P_{c_0}) = initial chamber pressure, psia

P'_c = chamber pressure at any time during firing, psia

A^* = original throat area, in.²

A'_t = throat area at any time during firing, in.²

but since C^* and \dot{W} are constants, Equation (11) can be reduced to

$$(P_c)_o A^* = \dot{P}_c' A'_t \quad (12)$$

or

$$A'_t = \left[\frac{(P_c)_o}{\dot{P}_c'} \right] A^* \quad (13)$$

and

$$(P_c)_o = \left[\frac{(A_t)_f}{A^*} \right] (P_c)_f \quad (14)$$

where the subscript, f, refers to final values.

In Equation (14), $(A_t)_f$ and A^* are measured values, and $(P_c)_f$ is determined from the pressure-time trace of the motor firing. The value of $(P_c)_o$ is determined in this manner since some difficulty can be encountered in making a judgment of where $(P_c)_o$ occurs, especially if it is masked by early deposition or erosion, or if the startup transient is prolonged. Equation (13) can be converted for direct calculations of deposition (and/or erosion) by utilizing it in the form of Equation (15) below.

$$-\delta = r_o - \sqrt{\left[\frac{(P_c)_o}{\dot{P}_c'} \right] \frac{A^*}{\pi}} \quad (\text{for deposition}) \quad (15)$$

where

$-\delta$ = decrease in throat radius, in.

r_o = original throat radius, in.

or

$$+\delta = \sqrt{\left[\frac{(P_c)_o}{\dot{P}_c'} \right] \frac{A^*}{\pi}} - r_o \quad (\text{for erosion}) \quad (16)$$

where

$+\delta$ = increase in throat radius, in.

CONFIDENTIAL

Initially, this approach was attempted in conjunction with the solid propellant and burning grains fired during the present contract by assuming a constant $\dot{\omega}$. Calculated changes in throat dimensions were found to be unrealistically high and indicated the fallacy of assuming $\dot{\omega}$ to be a constant or average value. The very fact that deposition does occur, and therefore nozzle geometry changes are effected, precludes the use of the aforementioned equation for calculating deposition. In this case, we have a solid propellant grain which, in the case of each propellant formulation, is pressure sensitive to varying degrees in terms of burn rate and mass or weight flow rate. Thus, as deposition results in throat restriction and an accompanying chamber pressure rise, variations in burn rate and flow rate are encountered. This is not a problem in the case of the Aer-nutronic solid propellant simulator where flow rate metering compensates for chamber pressure variations. Eventually, it is intended to compare the alumina deposition data calculated in this manner, from Contract AF 04(611)-9904, with that obtained from Tests T-5 through T-7.

(c) (C) The K_n Method for Calculating Nozzle Throat Radius Changes

Noting the restrictions of the C^* method, the problem then becomes one of utilizing a relationship between throat geometry changes and chamber pressure (or a parameter related to chamber pressure in which flow and burn rate changes are compensated for). The K_n method is ideally suited to this purpose since the simple and burning grain would have an essentially neutral pressure-time history, except for nozzle throat area change effect. The calculation of nozzle throat radius change as a function of firing time utilizing the K_n method is accomplished in the following manner.

The first step is to establish burn rate curves as a function of chamber pressure for each of the propellants used. This is done by utilizing strand burner data and is shown for each of the seven propellants used in this program in Figures 125 through 131. A preliminary K_n curve for each propellant can then be determined using the point slope method. The value of K_n for the seven propellants at 800 psia is taken from data supplied by Atlantic Research Corporation, the manufacturer of the propellant grains. This point, coupled with the slope which is the complement of the established burn rate slope, defines the preliminary K_n curve. These curves are plotted as a function of chamber pressure in Figures 125 through 131. For convenience they are shown on the same plots as the associated burn rate curves. An interpretation of operating chamber pressure (without deposition and/or erosion) is made from the chamber pressure versus time curves of the actual motor firing. Utilizing this chamber pressure, K_n is recalculated from Equation (17)

$$K_n = \frac{S_b}{A^*} = \frac{\text{measured constant}}{A^*} \quad (17)$$

CONFIDENTIAL

CONFIDENTIAL

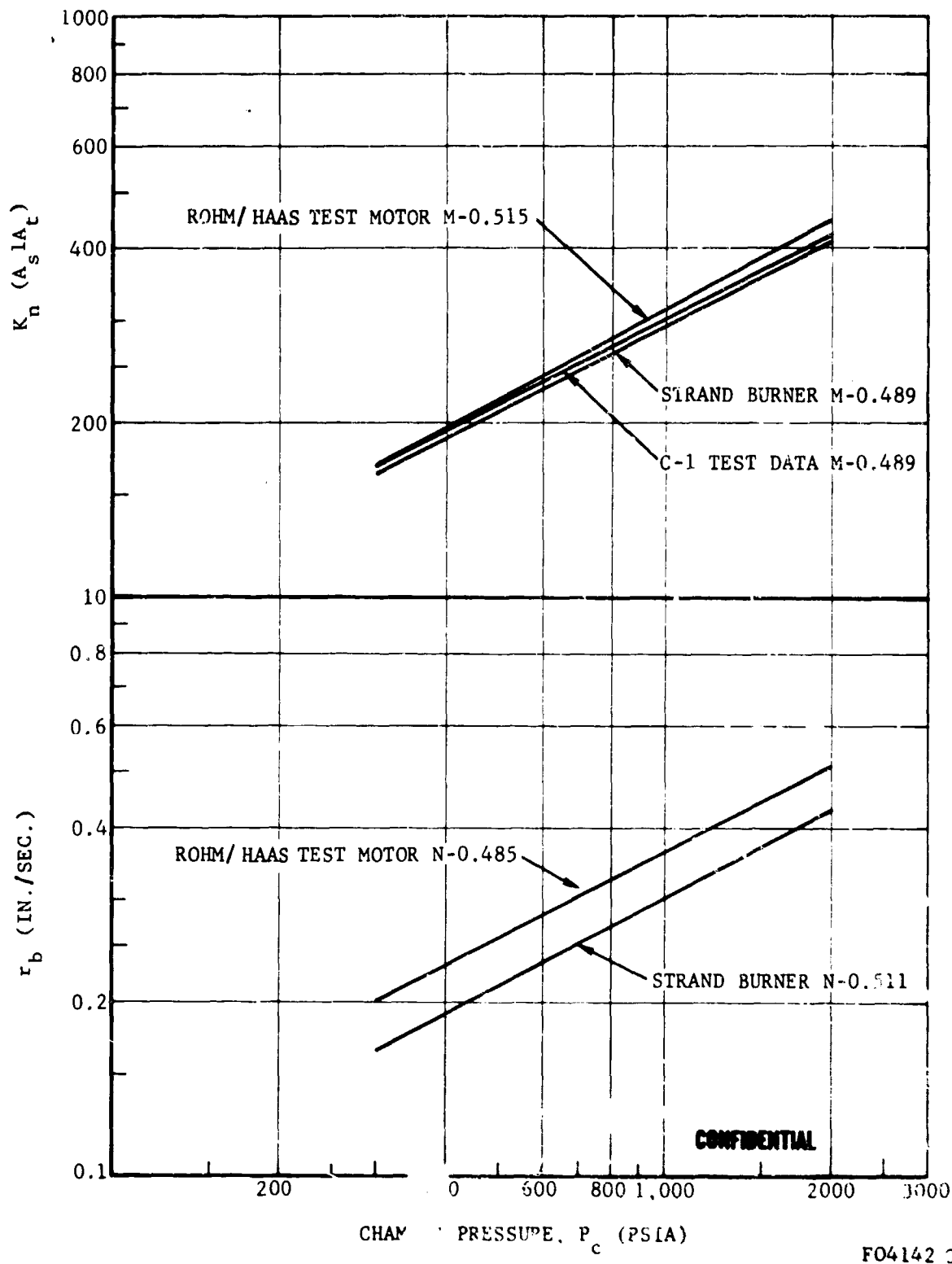
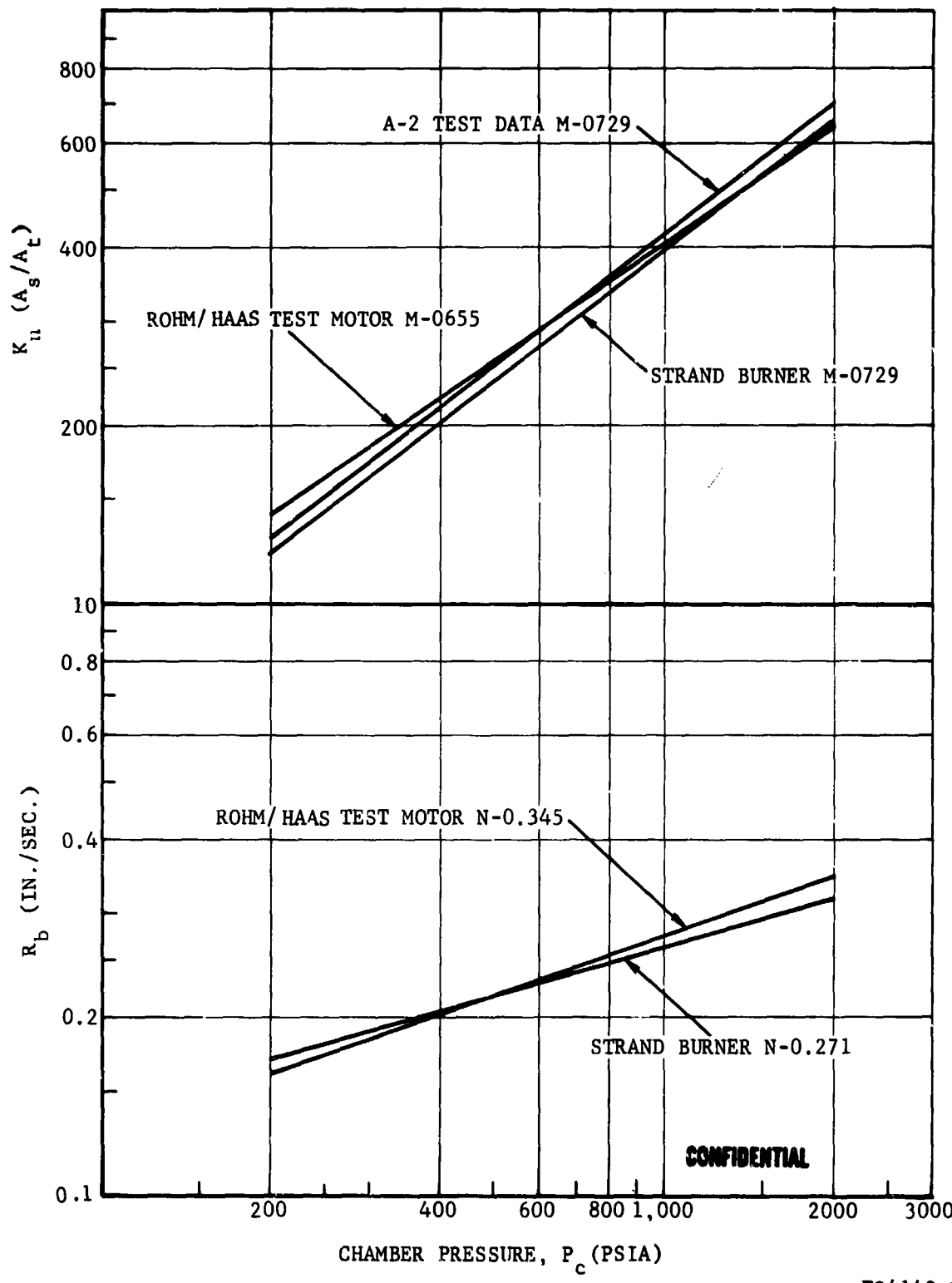


FIGURE 145. r_b AND K_n V. VS CHAMBER PRESSURE FOR MODEL 191F

CONFIDENTIAL

CONFIDENTIAL



F04143 C

FIGURE 126. R_b AND K_n VERSUS CHAMBER PRESSURE FOR ARCAE 24F

CONFIDENTIAL

CONFIDENTIAL

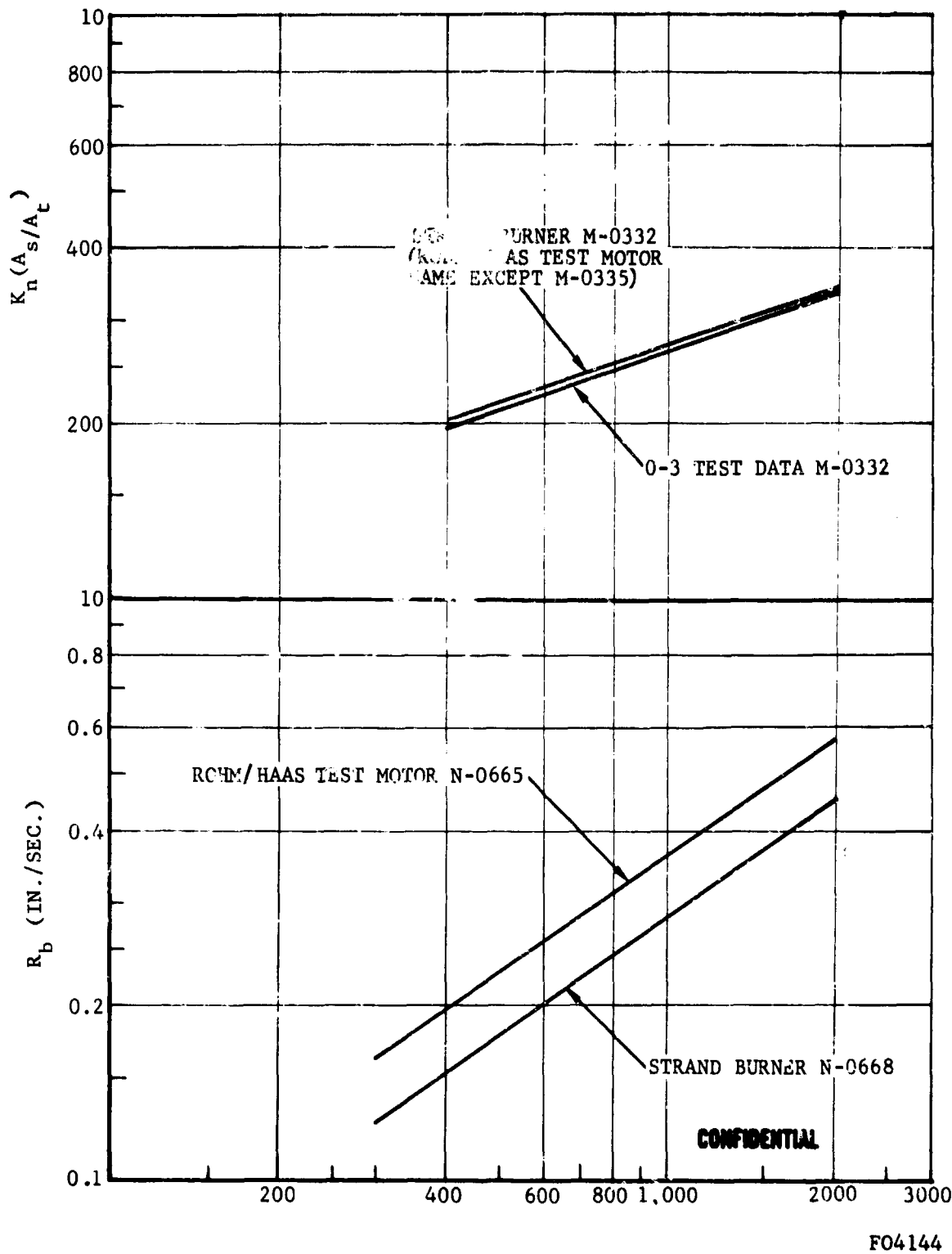
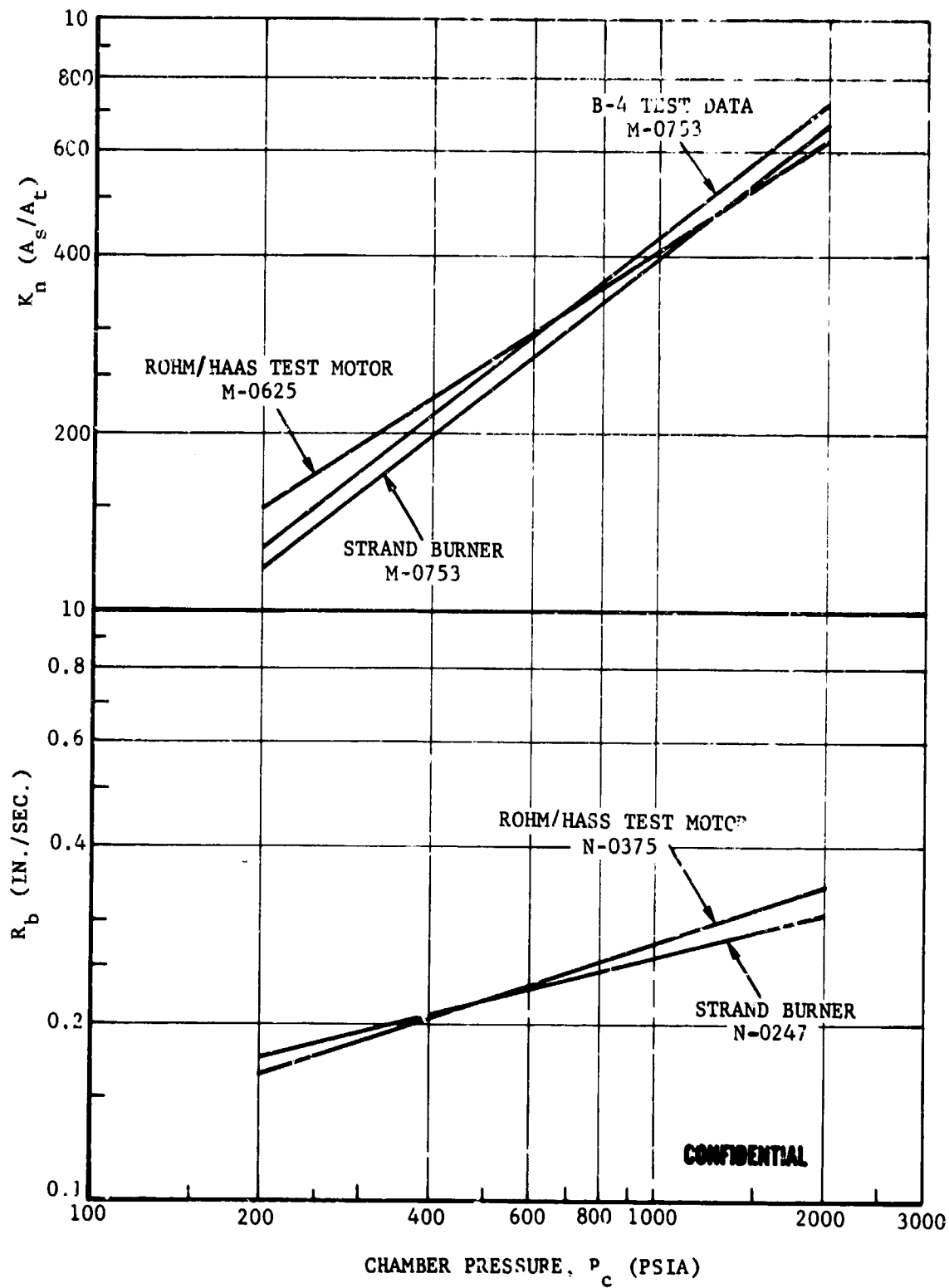


FIGURE 127. R_b AND K_n VERSUS CHAMBER PRESSURE FOR ARCOCEL 319BRF

CONFIDENTIAL

CONFIDENTIAL



FOL 45 C

FIGURE 128. R_b AND K_n VERSUS CHAMBER PRESSURE FOR ARCANE 54F

-253-

CONFIDENTIAL

CONFIDENTIAL

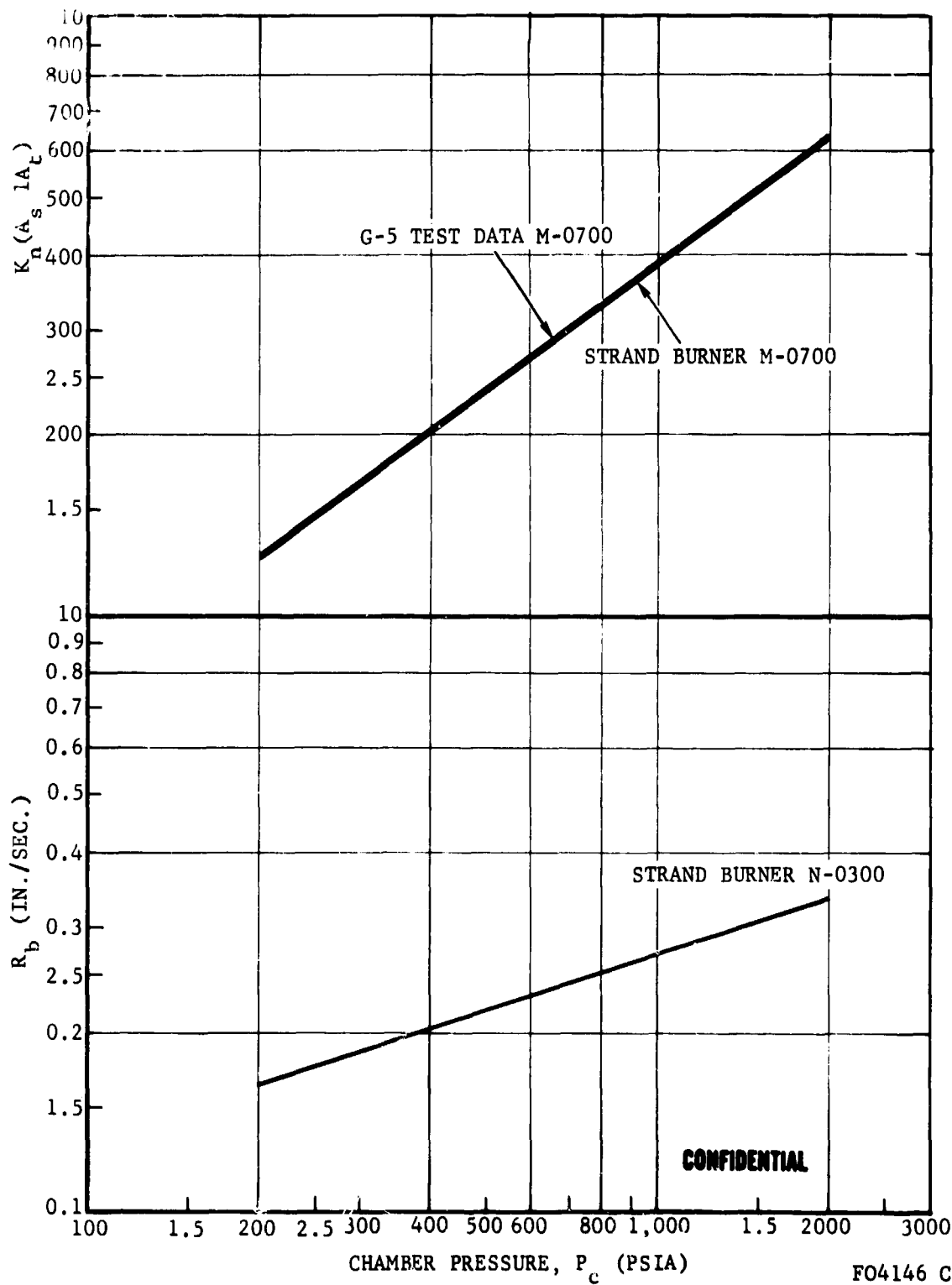


FIGURE 129. R_b AND K_n VERSUS CHAMBER PRESSURE
FOR ARCANE 60

CONFIDENTIAL

CONFIDENTIAL

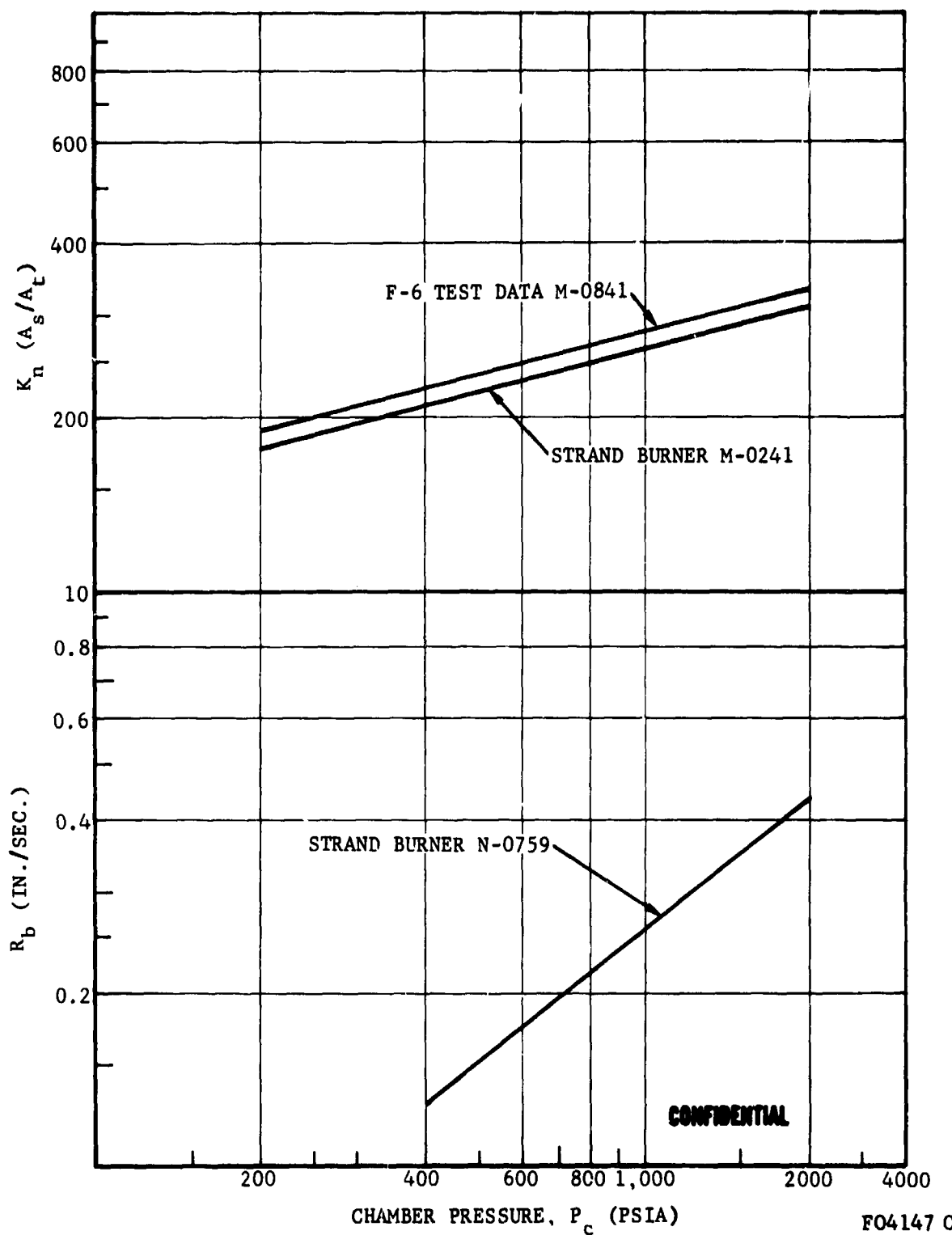


FIGURE 130. R_b AND K_n VERSUS CHAMBER PRESSURE FOR ARCOCEL 390

CONFIDENTIAL

CONFIDENTIAL

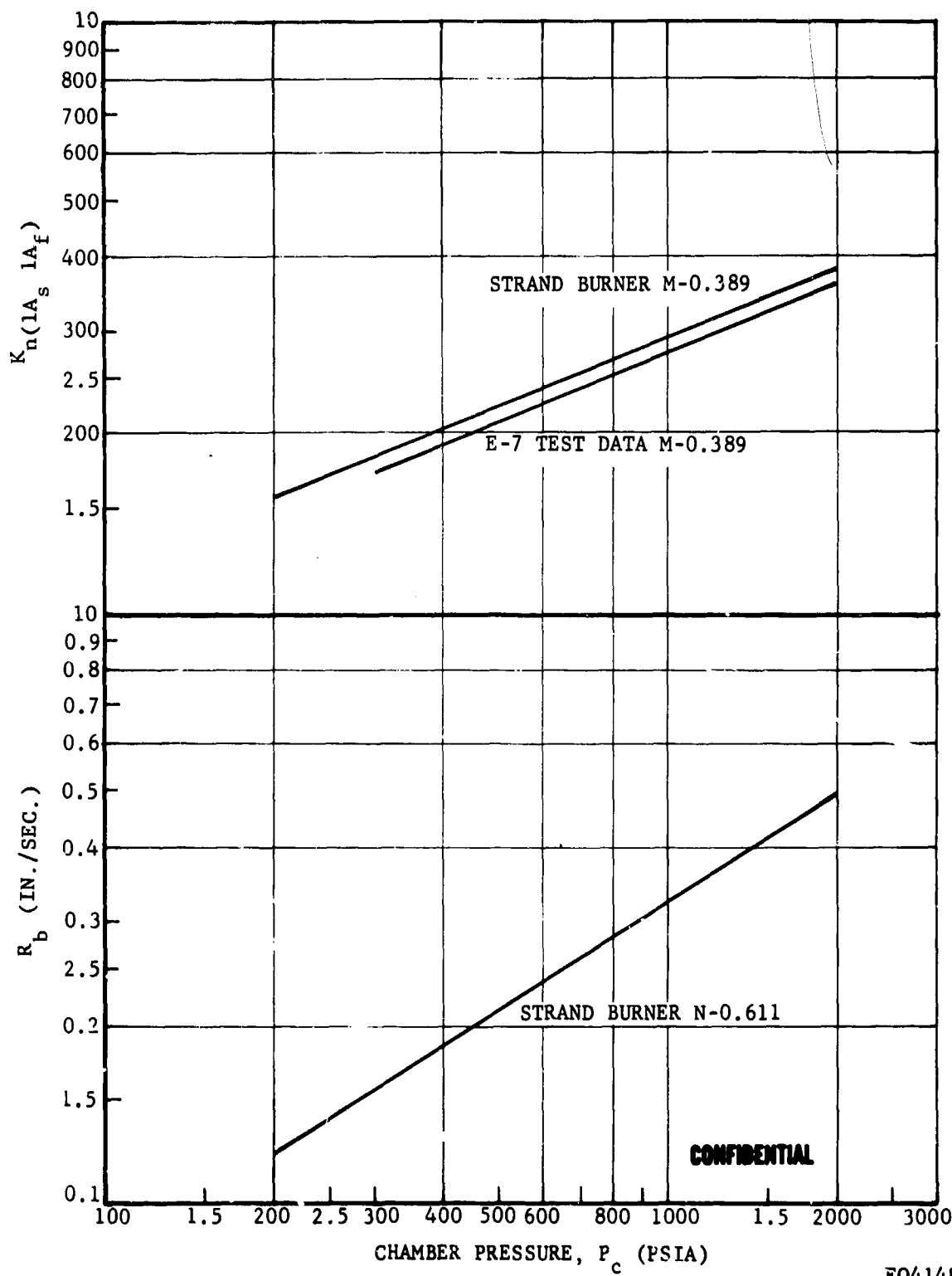


FIGURE 131. R_b AND K_n VERSUS CHAMBER PRESSURE FOR ARCOCEL 389

F04148 C

CONFIDENTIAL

CONFIDENTIAL

where

S_b = propellant burn surface (assumed constant for end burning grains).

This K_n' value for each individual test is then used to establish an adjusted curve having the same slope as the experimental curve. These curves are also shown in Figures 125 through 131. The assumption that propellant surface area is constant throughout any given firing, even for an end burning grain, is not entirely valid. The high diameter to web ratios of the grain configuration used, coupled with the insulating properties of the surrounding grain inhibitor, tend to produce some coning of the propellant grain. This, in turn, will distort the K_n curve to some extent. It is felt, however, that the magnitude of this effect is sufficiently small to permit its neglect in these calculations.

The final process in the determination of nozzle throat radius change as a function of firing time follows essentially the same line of reasoning as that used in the pressure ratio method (Equations (15) and (16)). In this case, however, specific propellant burn rate and flow rate variations are accounted for by using K_n' as a measure of pressure changes rather than the ratio of pressure change alone. The mechanics of this process are shown in Equation (18).

$$A_t' = \frac{S_b}{K_n'} \quad \text{from Equation (17)} \quad (18)$$

where

S_b = a measured constant propellant surface area, in.²

K_n' = is determined from the adjusted K_n curve at various values of P_c throughout the firing

or

$$\delta = r_o - \sqrt{\frac{S_b}{\pi K_n'}} \quad \text{(for deposition)} \quad (19)$$

or

$$+\delta = \sqrt{\frac{S_b}{\pi K_n'}} - r_o \quad \text{(for erosion)} \quad (20)$$

CONFIDENTIAL

CONFIDENTIAL

Figures 132 through 138 show the results of the calculations of δ as a function of firing time for each of the seven propellant formulations tested. The deposition curves, calculated by the method described above (K_n Method), are plotted on the same scale as those derived by the F/P method which is described in the following paragraph. The F/P method of deposition calculation complements the K_n method. The nozzle geometry and propellant grain configurations used in these tests are shown in Figures 52 and 47, respectively, of Reference 1.

(d) (C) The F/P Method for Calculating Nozzle Throat Radius Change

The definition of the instantaneous nozzle throat radius during a test run is necessary to properly evaluate the thermal and ballistic performance of the motor. If the instantaneous propellant burning surface area is constant, or otherwise known, and if sufficient burn rate data are available to compute the propellant burn rate pressure exponent, then the K_n method can be easily used to determine any changes in nozzle throat radius which may have occurred during the test run. However, where either or both the instantaneous burn surface or the burn rate pressure exponent are not known, it is necessary to use the relationship between the delivered thrust and chamber pressure to estimate changes in this nozzle throat.

The F/P method, described here, uses the basic relationship between the thrust, chamber pressure, and throat area described in Equation (21).

$$A^* = \frac{F}{P_c C_F} \quad (21)$$

The thrust coefficient, C_F , in this equation is a variable and is assumed to be dependent only on chamber pressure. The F/P method is based on the assumption that the pressure dependency of the delivered thrust coefficient will tend to be related to the pressure dependency of the ideal thrust coefficient by a constant of multiplication (K), as defined in the following equation.

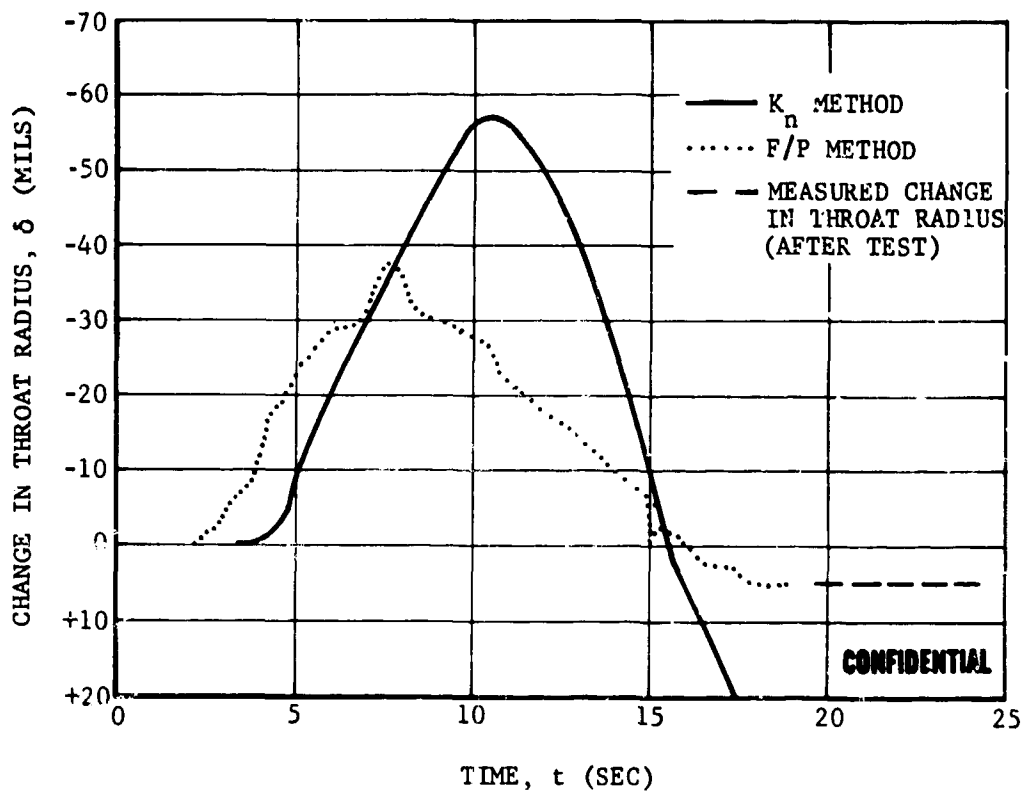
$$A^* = \frac{F}{P_c K C_F} \quad (22)$$

Thus once the constant is established for the individual run, then the throat area can be computed using Equation (23) and the measured thrust to pressure ratio.

$$(C_F)_T = \left\{ \left(\frac{2\gamma^2}{\gamma-1} \right) \left(\frac{2}{\gamma+1} \right)^{\frac{\gamma+1}{\gamma-1}} \left[1 - \left(\frac{P_e}{P_c} \right)^{\frac{\gamma-1}{\gamma}} \right] \right\}^{1/2} + \left(\frac{P_e - P_\infty}{P_c} \right) \left(\frac{A_e}{A^*} \right) \quad (23)$$

CONFIDENTIAL

CONFIDENTIAL

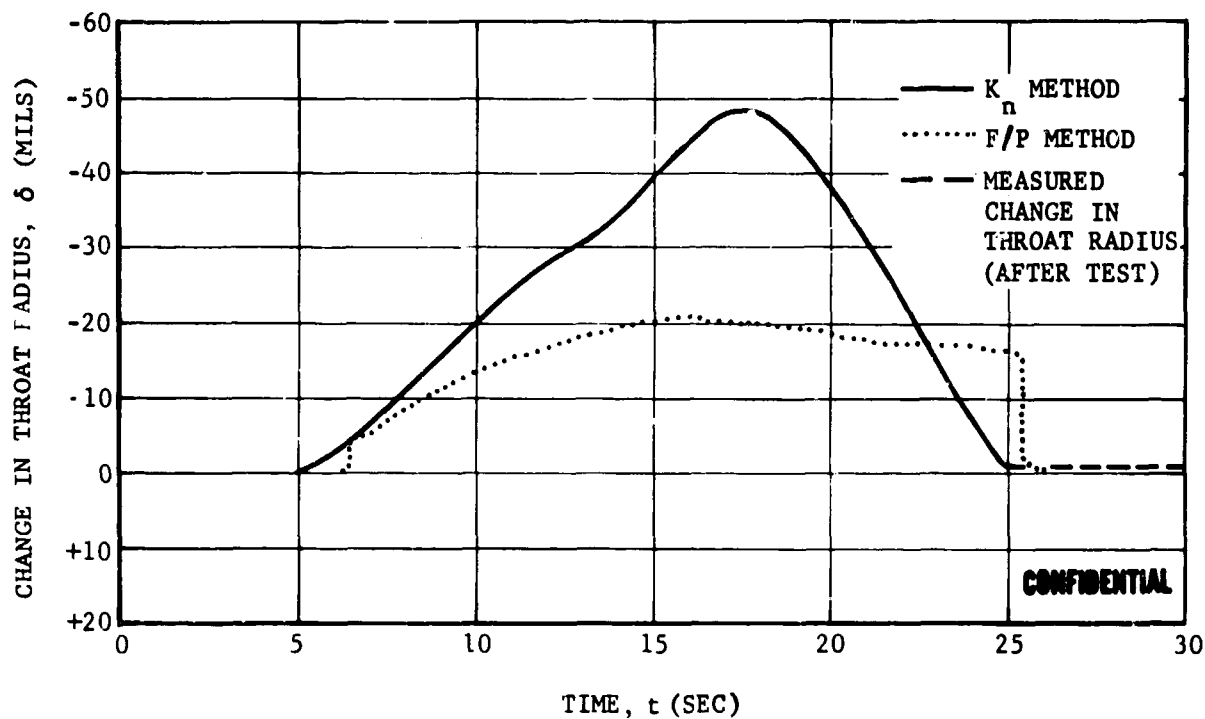


F04149 C

FIGURE 132. CHANGE IN NOZZLE THROAT RADIUS VERSUS FIRING TIME TEST T-1

CONFIDENTIAL

CONFIDENTIAL

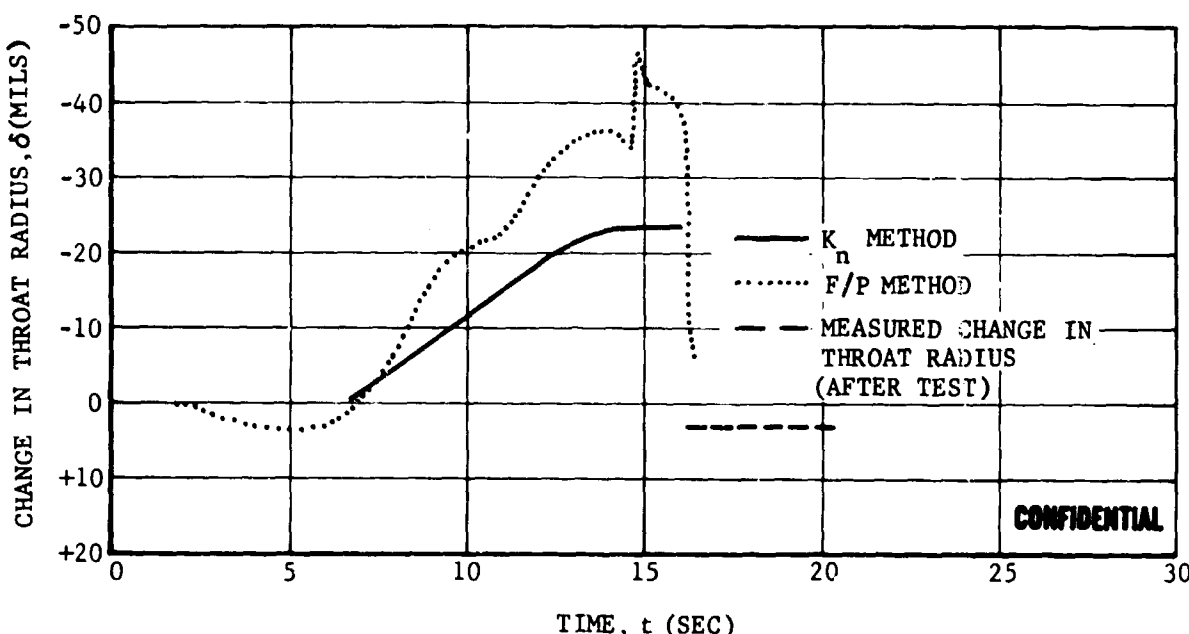


F04150 C

FIGURE 133. CHANGE IN NOZZLE THROAT RADIUS VERSUS FIRING TIME TEST T-2

CONFIDENTIAL

CONFIDENTIAL

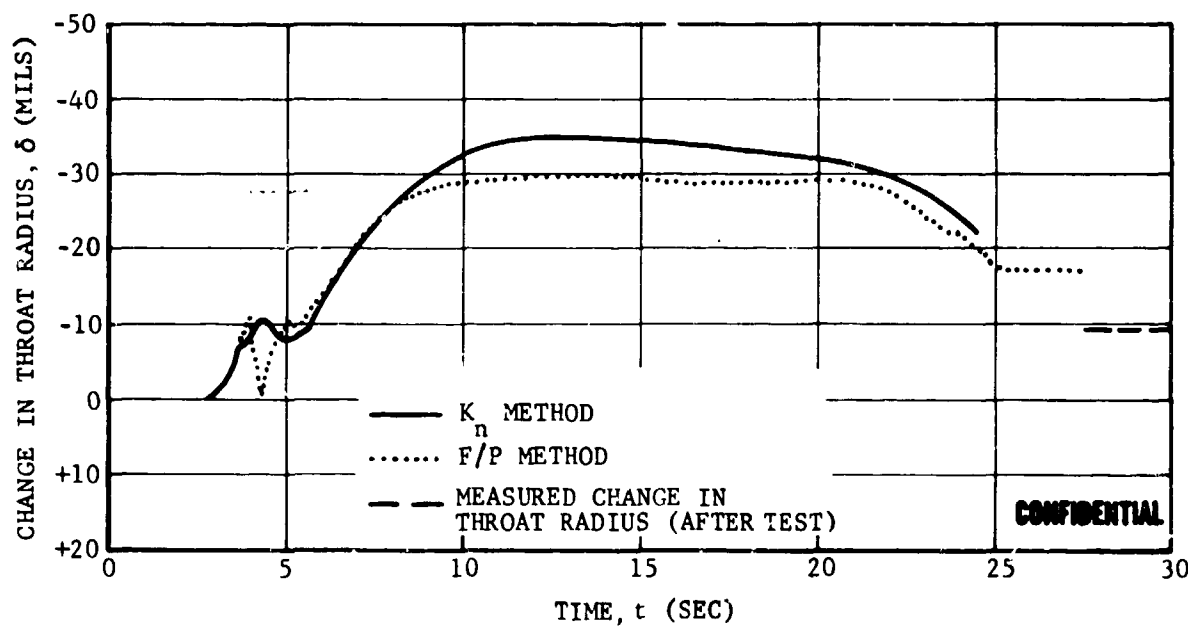


F04151 C

FIGURE 134. CHANGE IN NOZZLE THROAT RADIUS VERSUS FIRING TIME TEST T-3

CONFIDENTIAL

CONFIDENTIAL



FO4152 C

FIGURE 135. CHANGE IN NOZZLE THROAT RADIUS VERSUS FIRING TIME TEST T-1.

CONFIDENTIAL

CONFIDENTIAL

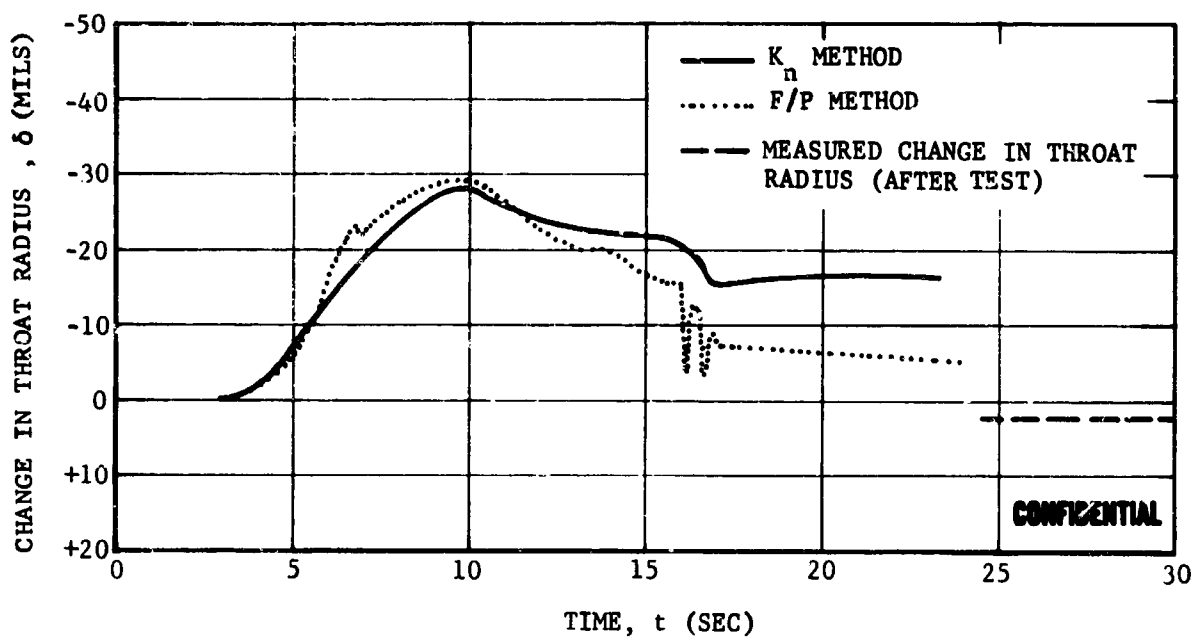
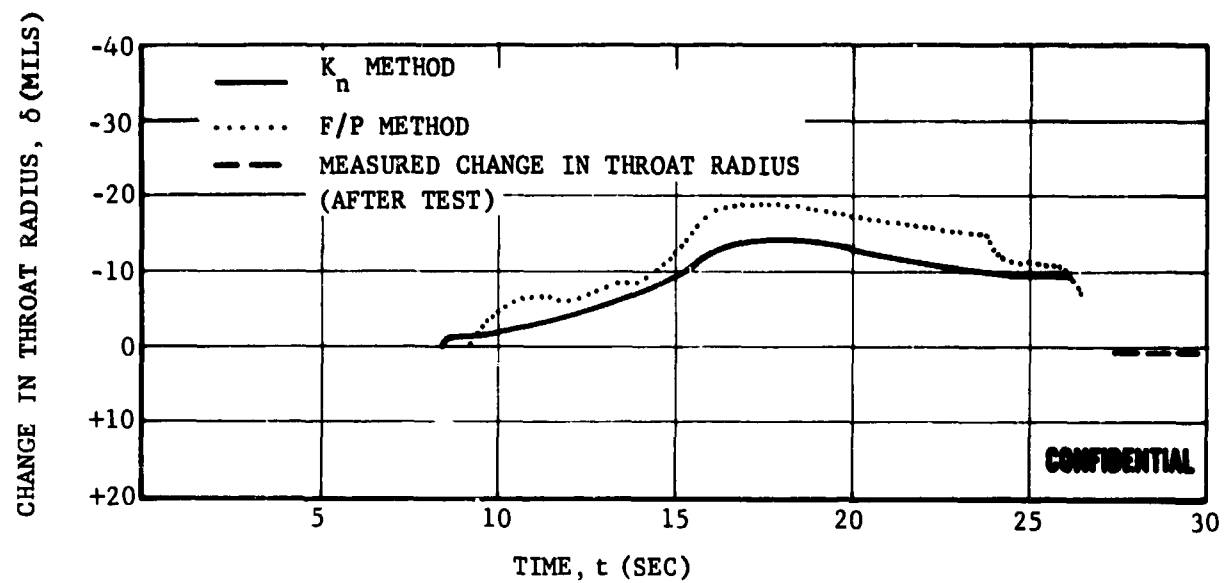


FIGURE 136. CHANGE IN NOZZLE THROAT RADIUS VERSUS FIRING TIME TEST T-5

F04153 C

CONFIDENTIAL

CONFIDENTIAL



F04154 C

FIGURE 137. CHANGE IN NOZZLE THROAT RADIUS VERSUS FIRING TIME TEST T-6

CONFIDENTIAL

CONFIDENTIAL

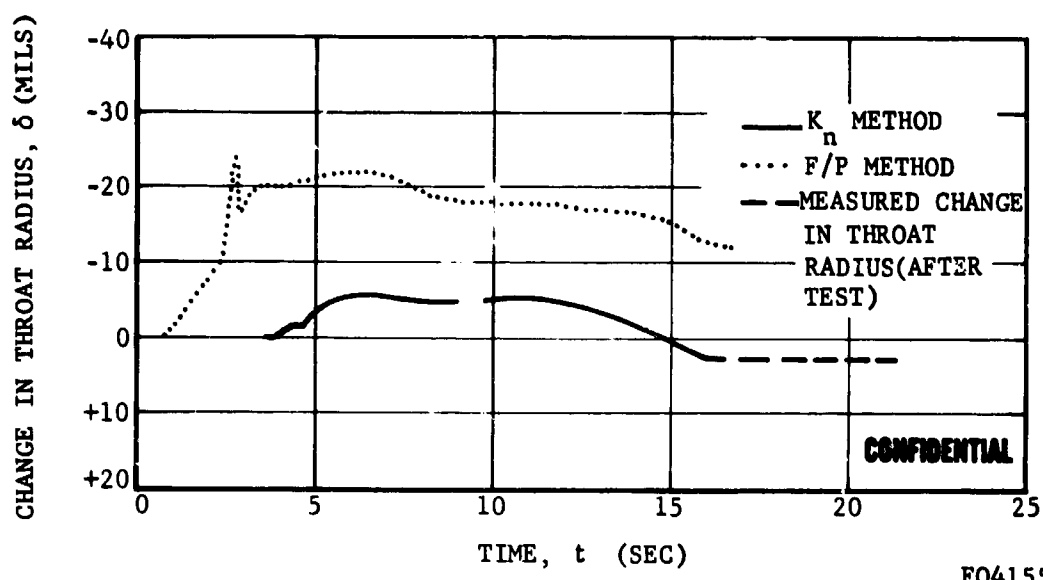


FIGURE 138. CHANGE IN NOZZLE THROAT RADIUS VERSUS FIRING TIME TEST T-7

CONFIDENTIAL

CONFIDENTIAL.

To further simplify the analysis, it was assumed that the nozzle area ratio does not change during the run (i.e., throat deposition or erosion does not significantly alter the area ratio). In addition, it was assumed that the specific heat ratio does not change significantly at chamber pressures above 500 psia. The following is a brief discussion of the application of this basis method.

The first step is to establish a plot of the ideal thrust coefficient as a function of chamber pressure. The ambient pressure and the nozzle expansion ratio are known parameters, leaving the selection of the effective specific heat ratio (γ) as the only difficult parameter to establish. The equilibrium combustion properties were examined for each propellant considered in this program. It was found that the calculated equilibrium specific heat ratio did not vary more than 5 percent between the throat and this exit plane on any individual propellant or more than 7 percent between propellants. Consequently, only one ideal thrust coefficient curve was drawn for the analysis of the first seven motor tests of this program. The value of the average effective specific heat ratio used in establishing this plot was = 1.10.

The second step is to determine the constant of multiplication (K) that relates the actual thrust coefficient to the ideal. This step is predicated on the requirement that there is some point during the run where the throat area is known. Provided the instrumentation data recording lag is negligible, the start transient and the first second or so of the run should provide the best place to establish the constant (K). This is done by simply plotting KC_F (see Equation (22)) using delivered thrust and pressure and the initial throat area (A^*). If several points are plotted using measured values during the startup transient and the first few seconds of the run, it will be noted that the KC_F (delivered) curve tends to parallel the ideal C_F curve. However, at some point the curves will begin to diverge, indicating metal oxide deposition or erosion depending on the direction of the deviation. The constant of multiplication K which relates the two C_F curves can be established with the data which are in the time period where the two curves tend to be parallel.

The third and final step is to establish the nozzle throat area or throat radius as a function of run time. This is done by solving for A^* , using Equation (22), K, the pressure dependent ideal thrust coefficient curve, and the time dependent measured throat to pressure ratio.

The F/P method provides a fair estimate of the instantaneous throat area change even though there are several critical assumptions required. Probably the most significant error in this method is introduced by metal oxide deposition on the exit cone. The relationship between thrust and pressure can be significantly altered when sufficient material is deposited on the exit cone to change the effective nozzle expansion ratio or to cause

CONFIDENTIAL

CONFIDENTIAL

flow separation. Errors caused by exit cone deposition can be identified during a given run when it is observed that abrupt changes in the thrust are not accompanied by similar changes in the chamber pressure. If any such phenomena occur at any time during a run, then it is possible that the instantaneous throat areas computed by this method are inaccurate at other times during the run. Motor Test T-7 provides a good example of this phenomenon. Note in Figure 124 that the thrust and chamber pressure appear to be rising normally during the first few seconds of the firing. At about 4 seconds into the run, the thrust suddenly drops. There is no corresponding drop in chamber pressure. It is possible at this point that an accumulation of exit cone deposits were dislodged. If the constant K were computed during the start transient as was done in Figure 138, then a significant error may be induced in the estimated throat area (or throat radius change, δ , as shown in Figure 138. Consequently, it is recommended that this method be used in cases where confidence in the K_n method is sufficiently low to warrant this extra effort required and only in cases where exit cone deposition does not obviously compromise the results.

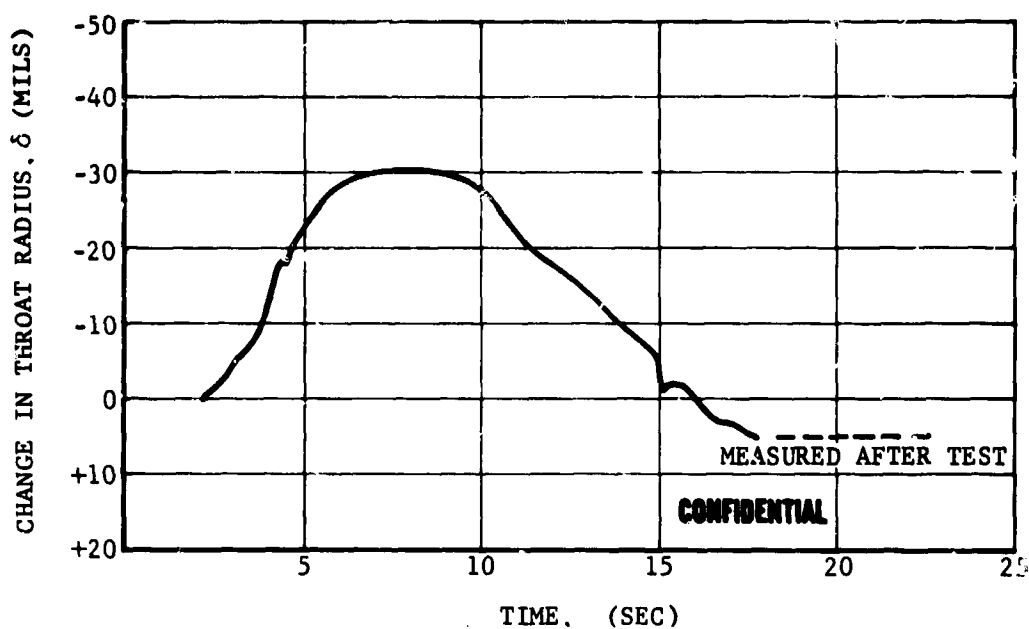
(e) (C) Combined K_n and F/P Method for Motor Tests
T-1 through T-7

Estimated changes in nozzle throat radii vs firing times for Tests T-1 through T-7 were made using a composite of the methods of deposition calculation described in the preceding paragraphs. These throat changes, due to deposition and/or erosion, are presented in Figures 139 through 145. The manner in which the K_n -F/P curves were composited is described below.

For Test T-1 (Figure 134), the F/P method in its entirety was chosen as being more representative of the nozzle throat behavior during firing. Indicators were that there was a significant amount of burn rate variation throughout the firing due to irregular grain burning and/or erosive burning which invalidated the K_n method of calculating the throat changes that occurred. This is borne out by the excessive theoretical nozzle erosion which the K_n method predicts (Figure 132). The deposition spike on the F/P method curve which occurs at 7-1/2 seconds into the firing, as shown in Figure 132, was judged to be the result of deposit being blown off the exit cone, and not representative of throat deposition. For Tests T-2, T-3, T-4, (Figures 140, 141 and 142), the K_n method was considered satisfactory for use in calculating the nozzle throat changes, except for the initial erosion of T-3. The K_n method cannot account for predeposition erosion which is accompanied by a chamber pressure rise. Therefore, the F/P method was utilized for the initial 7 seconds of firing in the case of T-3. The F/P method was utilized for the calculation of throat radius changes during the firing of Test T-5 (Figure 143). The irregular throat response at 15 seconds was deemed to be deposit sloughing off the exit cone. Tests T-6 and T-7 (Figures 144 and 145), again used the K_n method for deposition calculations except for the initial erosion of T-6 which was taken from the F/P method.

CONFIDENTIAL

CONFIDENTIAL

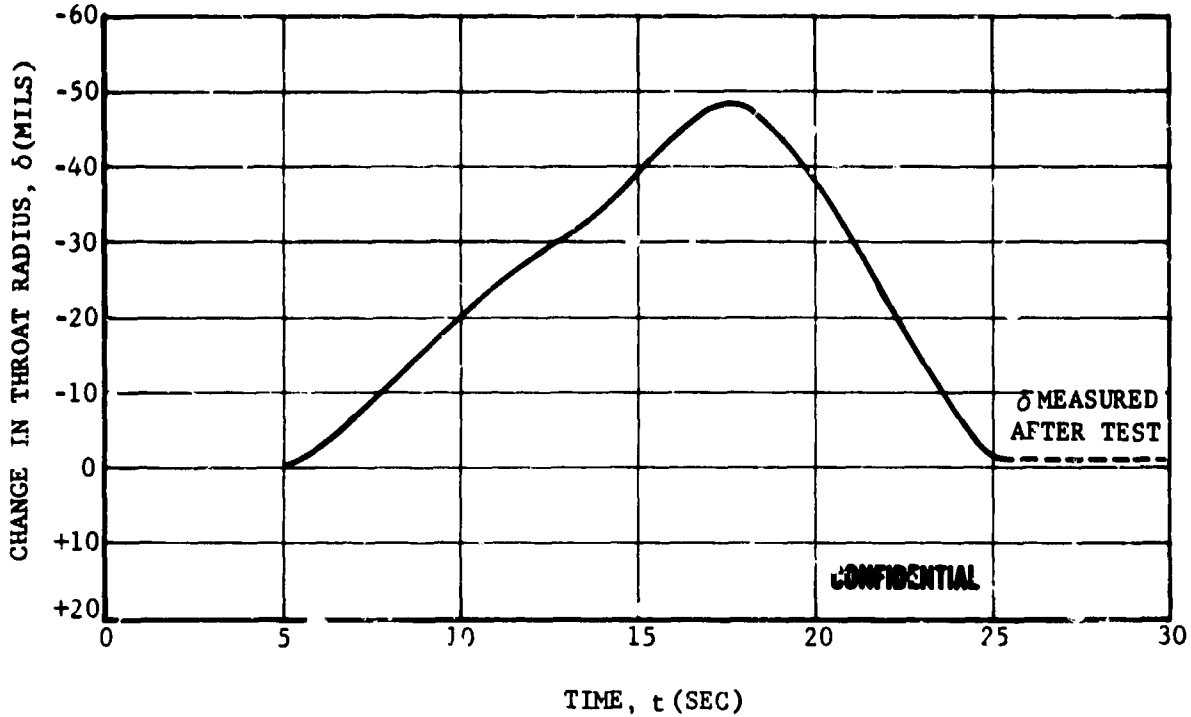


F04156 C

FIGURE 139. ESTIMATED CHANGE IN NOZZLE THROAT RADIUS VERSUS FIRING TIME USING A COMPOSITE OF THE K_n AND F/P METHODS TEST T-1

CONFIDENTIAL

CONFIDENTIAL



F04157 C

FIGURE 140. ESTIMATED CHANGE IN NOZZLE THROAT RADIUS VERSUS
FIRING TIME USING A COMPOSITE OF THE
 K_n AND F/P METHODS TEST T-2

CONFIDENTIAL

CONFIDENTIAL

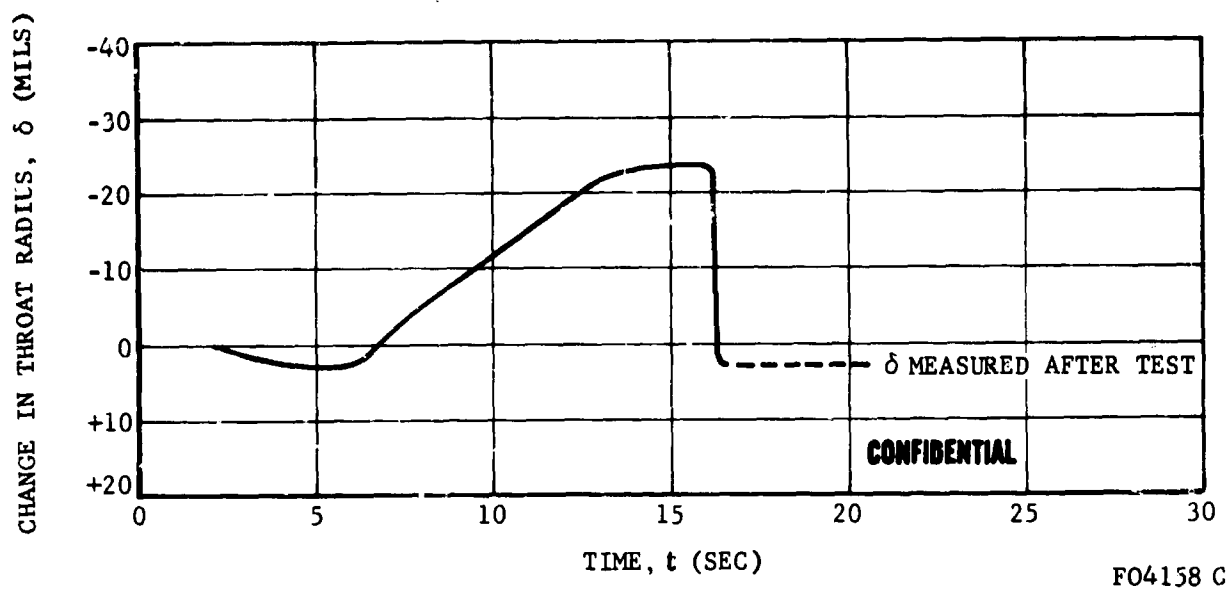


FIGURE 141. ESTIMATED CHANGE IN NOZZLE THROAT RADIUS VERSUS FIRING TIME
USING A COMPOSITE OF THE K_n AND F/P METHODS TEST T-3

CONFIDENTIAL

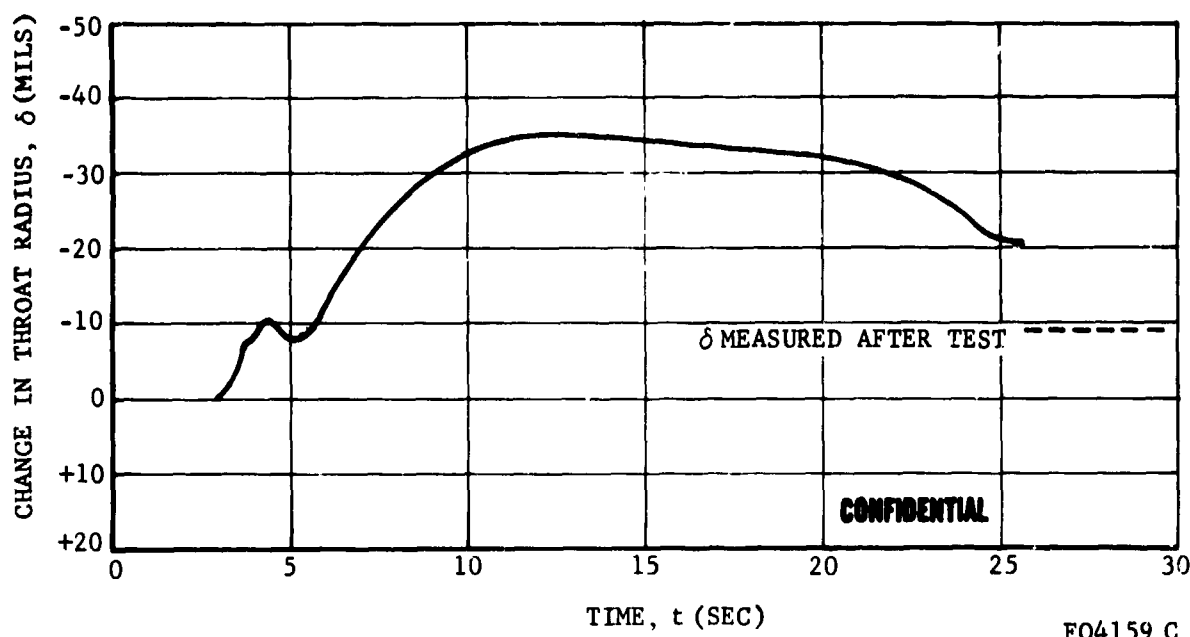


FIGURE 142. ESTIMATED CHANGE IN NOZZLE THROAT RADIUS VERSUS
FIRING TIME USING A COMPOSITE OF THE
 K_n AND F/P METHODS TEST T-4

F04159 C

CONFIDENTIAL

CONFIDENTIAL

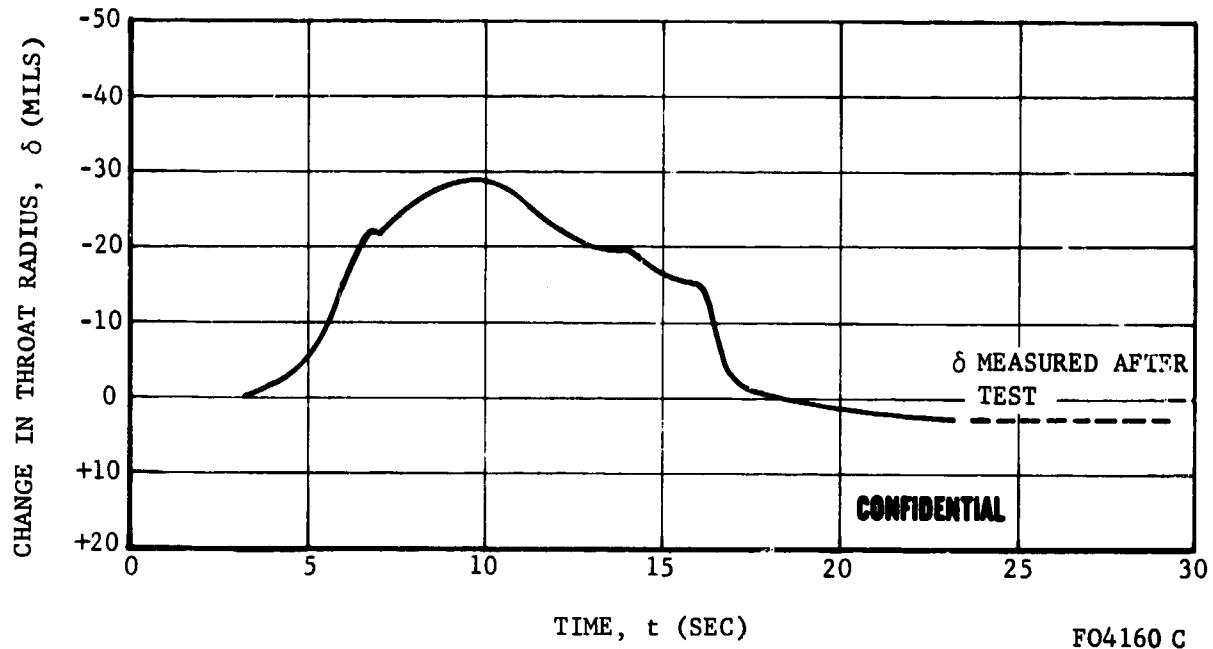
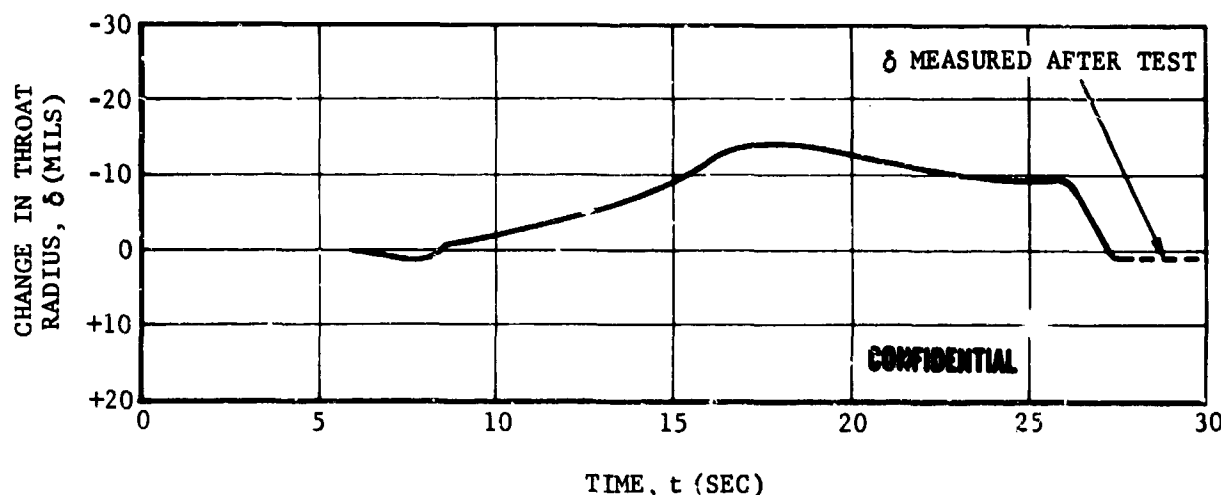


FIGURE 143. ESTIMATED CHANGE IN NOZZLE THROAT RADIUS VERSUS FIRING TIME USING A COMPOSITE OF THE K_n AND F/P METHODS TEST T-5

CONFIDENTIAL

CONFIDENTIAL

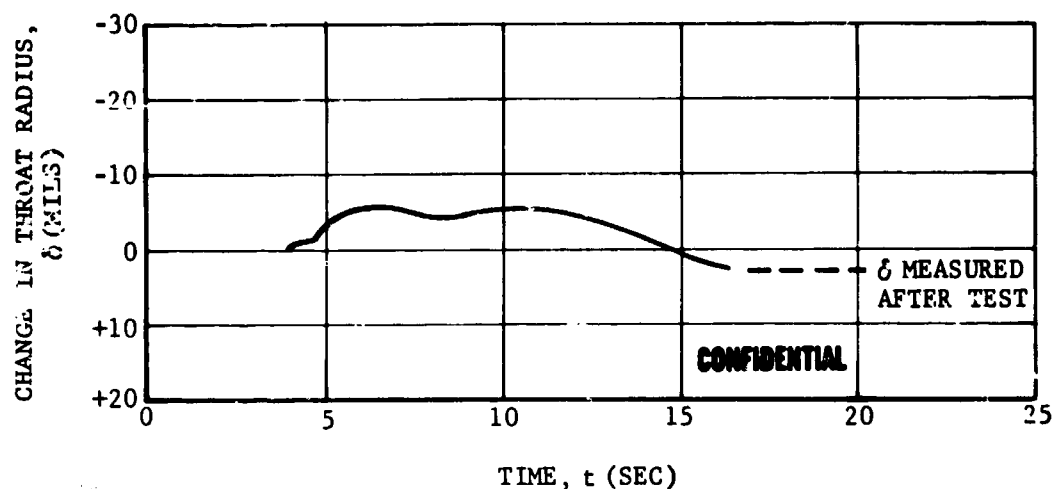


FO4161 C

FIGURE 144. ESTIMATED CHANGE IN NOZZLE THROAT RADIUS VERSUS FIRING TIME USING A COMPOSITE OF THE K_n AND F/P METHODS TEST T-6

CONFIDENTIAL

CONFIDENTIAL



FO4162 C

FIGURE 145. ESTIMATED CHANGE IN NOZZLE THROAT RADIUS VERSUS FIRING TIME
USING A COMPOSITE OF THE K_n AND F/P METHODS TEST T-7

CONFIDENTIAL

CONFIDENTIAL

(3) (C) Discussion of Test Results

The pressure and thrust histories for Tests T-1 through T-7 are given in Figures 118 through 124, respectively. It should be recalled that the motor configurations are essentially identical in these tests and that the design strongly favors complete combustion of the propellant. The end-burning grain design should produce essentially neutral burning, except for the coupling of the propellant burn rate and the nozzle throat area variations. It must be observed that there are similar trends and numerous detailed dissimilarities in the ballistic data from these tests.

Clearly, the two double base beryllium propellants, Tests T-1 and T-3, reflect more radical pressure excursions than the composites, Tests T-2 and T-4. This is due to the inherent differences in the dependence of burn rate on pressure. However, the calculated deposition and erosion histories show the composites as having thicker throat deposits. Thus, each type of propellant (and to a lesser degree, each individual propellant) appears to exhibit a relatively independent character which is a function of its burning properties and the condensed phase deposition. The deposition is, in turn, a function of the motor contour, grain design, the thermal response of the wall materials and, finally, certain propellant properties (completing a dependence loop). The propellant properties of interest include metal loading, metal particle size distribution, and (probably) the metal particle combustion kinetics which pertain to the formulation in question. The thermal response of the wall materials is also coupled to the propellant via the convection and radiation heat transfer properties.

There is no obvious evidence that the lack of pressure neutrality in the beryllium tests was detrimental in terms of materials performance. Any unanticipated pressure effects would necessarily be obscured by the deposit that causes the pressure excursion. The major complication introduced by the non-neutrality is that the heat transfer and corrosion post-test analyses become more complicated. Unfortunately, the results of such analyses also become less accurate and less general.

It is interesting to consider cases where there is little deposition on the nozzle surfaces or where the deposit residence time is short relative to the action time. The propellant tailoring tests described in Paragraph 4.2 are representative of such cases. The expectation is that significant corrosion-erosion of the nozzle throat (ATJ graphite) will, through the propellant burn rate coupling, produce significant variations in the pressure excursion for each type of propellant. Because pressure is directly related to the magnitude of the basic heat transfer, corrosion, and erosion phenomena, the double base propellants will appear to be less corrosive, compared to composites of nominally equivalent corrosivity. On an equilibrium combustion basis, individual members of each propellant class will be more corrosive than others when they have either greater potential corrosivity or a greater burn rate dependence on pressure.

CONFIDENTIAL

CONFIDENTIAL

When both deposition and corrosion-erosion occur over significant portions of the firing, the comparison of propellant test data becomes even more complex. Here, all the propellant and motor design characteristics enter the picture in determining the deposition history and the extent of thermochemical insulation derived from deposition. The individualistic nature of beryllium propellants will most probably be exaggerated further. Thus, flame temperature has an important influence on the deposition history, with the highest flame temperature producing the greater maximum deposit thicknesses at the throat, but over a shorter period of time (see Figures 139 and 141). Since the double base propellants tend to have the higher flame temperatures, they may exhibit higher total surface regression than the composites for equivalent firing times. This is a reversal of the expectation when deposit effects are not important. It is apparent, then, that a great deal of consistency or correlation should not be expected from the results of beryllium propellant tests when deposition effects are important. Furthermore, burn rate pressure dependence can be an important correlation parameter.

Clearly, there is no inherent reason why aluminum propellants should not exhibit the same general characteristics. However, the significantly low melting point of alumina suggests that the maximum amount of mass storage, on the surfaces upstream of the throat, must be less than in the case of beryllia. While comparable maximum deposit thicknesses may conceivably be observed, the period over which the nozzle throat is covered should be shorter for alumina than beryllia. This is illustrated by Figures 142 and 143. When Figure 145 is compared with Figure 139, the same observation can be made. Note that the very high flame temperature of the Arcocel 389 propellant (relative to the alumina melting point) is probably causing more melting and higher liquid flow velocity.

Unfortunately, the total amount of deposition of either beryllia or alumina cannot be directly inferred from the throat deposit histories. It is probable that the alumina and beryllia particle sizes are different so that the potential amounts of the oxides hitting the contour are different. Of course, the amount of oxide which sticks to the wall, and subsequently flows over the throat, should also vary considerably. Aeronutronic simulator and vertical mud motor firings normally produce minimal throat deposition effects for aluminum propellants. This is clearly not the case in this program as can be seen from Figures 143 through 145.

It is believed that the great majority of aluminum propellant firing data has not been affected by deposition. Extensive deposition has been observed for the two special cases of very small nozzle throat area and for restart operation. In general, alumina deposition is neglected, especially in heat transfer and corrosion analyses. When such an assumption is valid for aluminum propellants, it is probably not for beryllium propellants and poor correlation of results should be expected. In this case, aluminum propellants should prove to be most corrosive, especially

CONFIDENTIAL

CONFIDENTIAL

for the relatively low temperature composites. When the non-deposition assumption is valid for both metal additives, the beryllium propellants are, theoretically, slightly more corrosive. Otherwise, the effects of comparable burn rate dependency on pressure should pertain to either type of propellant. It follows, then, that nozzle corrosion-erosion data for aluminum propellants should reflect dependencies on motor design and flame side materials selection in the same manner as is expected for the beryllium propellants. However, the quantitative performance of nozzle and insulation materials, which is a function of deposit insulation, should be quite different.

To this point, the hypothesis concerning the existence of major differences in the metal combustion kinetics has been ignored. If complete combustion of the beryllium metal particles is admitted as an additional propellant variable, then transient variations in propellant corrosivity, heat transfer properties, and condensed phase deposition are to be expected. Any superficial comparison of test results when combustion kinetics has been involved would almost certainly lead to confusion. This is adequately illustrated by the Arcocel 191 and Arcane 53 data given in Paragraph 4.2.

At the present time, the weight of evidence suggests that each metallized solid propellant will exhibit a certain amount of individuality. Motor geometry, materials, operation, and thermal design effects will tend to accentuate this situation. It appears logical to assume that each motor test must be evaluated in terms of the basic thermal, structural, mass transfer, and chemical phenomena. In general, this would require the evaluation of the heat transfer, deposition, and corrosion-erosion at every instant throughout the firing period. The more prevalent practice of characterizing motor firing data in terms of overall average properties (average chamber pressure, average erosion rate, average thrust coefficient, etc.) will not lead to great improvements in the understanding of the behavior of beryllium propellant exhaust interaction with motor materials. The one apparent exception is that tests, featuring a common propellant, similar motor component geometries, identical flame side materials and similar thermal protection capacity, should be directly comparable. The influence of each of the design variables, exclusive of the propellant formulation, can be evaluated by making one parameter change at a time. Many of the scheduled small motor tests follow these rules. As long as the motor and materials performance is evaluated properly, it should be possible to compare the test results directly.

With regard to Tests T-1 through T-7, a distinction must be made between motor performance and propellant performance. A discussion of the propellant combustion, C^* , and impulse efficiencies is given in Paragraph 2.3. Motor performance efficiencies have not been calculated from the data given in Table XXVI. Average, rather than instantaneous, values would tend to be somewhat low and should not be compared directly with other motor test results. It is estimated that as much as 5 percent of the propellant mass,

CONFIDENTIAL

CONFIDENTIAL

in the form of beryllia, is retained in the motor or flows through the nozzle without contributing to thrust. Furthermore, the large exit cone heat sink tends to cold-trap deposit. Exit cone deposits are likely to produce flow detachment and induce side thrust losses. It appears that gravity promotes the formation of thicker deposits on the bottom half of the exit cone than on the top. In general, more conventional motor designs would be expected to give higher motor efficiencies simply because the deposition induced losses should be less serious.

5.3 (U) DEVELOPMENT MOTOR TESTS

During the reporting period, the preliminary grain design, propellant selection, and nozzle designs were established for the five development motor tests. These tests have been designated T-51 through T-55.

A single grain design has been selected for use in all tests. The design is similar to the Type II and III designs used in the small motor tests. The cylindrical grain port diameter will be approximately four inches and the grain outside diameter will be approximately nineteen inches. The single axial slot, one inch wide, extends over the entire grain length. The aft end of the grain will be contoured to fit the aft closure insulation surface which is parallel to the ADOBE aft closure. It will also be relieved to accept submerged nozzles. The forward end of the grain will be contoured to achieve nominally neutral burning. The overall grain length will be approximately 40 inches. The propellant weight will be about 500 pounds and the burning time will be 25 seconds, nominal. Tests T-51, T-52, and T-54 will use the Arcocel 191F propellant formulation. Tests T-53 and T-55 will use the Arcocel 319 BRF propellant formulation.

Two submerged nozzle configurations will be used. The first design will be used for Tests T-51, T-52 and T-53. The second, which will be submerged approximately three inches deeper and approach the initial grain-burning surface (about one-half inch separation), will be used for Tests T-54 and T-55. The throat inserts for Tests T-51, T-53, and T-54 will be edge grain oriented pyrolytic graphite washers. The inserts for Tests T-52 and T-55 will use tungsten with a polycrystalline graphite backup. The nose caps for these nozzles will use carbon cloth phenolic. A polycrystalline graphite section will precede the throat insert. RVD graphite has tentatively been selected for the entrance section while ATJ graphite will be used in the nozzle exit cone section.

The original plan, to use two grain designs in this series of tests, proved to be impractical as other relatively simple, neutral designs significantly exceeded the ADOBE motor case length. However, certain aspects of the propellant exhaust flow field and the grain's proximity to nozzle surfaces will be varied simply by changing the degree of nozzle submergence. These changes are actually preferred relative to those which could be accomplished by grain design. The original plan to include a polycrystalline graphite

CONFIDENTIAL

CONFIDENTIAL

throat insert in one test was changed to permit the use of a second propellant formulation. While a third propellant choice, Arcocel 54F, was also contemplated, practical difficulties arose with respect to procuring the appropriate beryllium powder for a composite grain.

Procurement of the grain casting hardware, propellant ingredients, and motor insulation materials has been initiated. It is currently expected that these motor tests will be conducted in July and August, 1966. The results of the tests will be published in the final report.

5.4 (C) CONCLUSIONS, RECOMMENDATIONS, AND FUTURE WORK

a. (C) Conclusions

From a relatively macroscopic point of view, the objectives of the first seven motor tests were achieved. There were no indications that the nozzle and motor insulation surfaces were exposed to other than equilibrium combustion products. The combustion chamber flow velocities were approximately 6 ft/sec so that the chamber stay time varied from approximately 300 to 400 milliseconds over the firing period. Since these times are much greater than those which are thought to be required for metal particle ignition and combustion, the equilibrium combustion (with respect to the hardware) conclusion is accepted.

The general appearance of the asbestos phenolic chamber liner and aft closure insulation confirm the analytical and laboratory study predictions that (1) the alumina and beryllia will stick to the insulation char surface, and (2) the resulting deposit is protective. These conclusions would probably not pertain to the insulation materials which yield significantly weaker or lower temperature chars. That is, thermally induced char erosion would tend to oppose the retention of the oxide deposits. It is apparent that insulation thickness requirements could be reduced when beryllia deposits can be reliably retained on the char surface. These conclusions should not be immediately extended to the carbon or graphite cloth phenolic materials. This is because the role of the asbestos or silica in maintaining low char temperatures (relative to the oxide melting point) and in particle sticking is undoubtedly important.

For the uniform axial flow condition (end burner), deposition apparently occurs along the aft closure insulation surface with subsequent flow of the molten oxide over the nozzle throat surface. Both the time required for the deposit to reach the throat and the throat deposit thickness history are strongly dependent on the oxide melting point and the flame temperature. It is also apparent that gravity effects have a significant influence on the behavior of the deposit as it flows over the nozzle contour.

CONFIDENTIAL

CONFIDENTIAL

From the post firing condition of the graphite nozzle surfaces, it is concluded that the alumina and beryllia deposits are protective. That is, significant thermal and chemical insulation are observed. At graphite surface temperatures above the melting point of the oxide and/or above the temperatures where the metal carbides (or oxy-carbides) are not thermally stable, the chemical and thermal insulation effects will be extensively lost. However, it is predicted that corrosive attack by the liquid beryllia phase at these high surface temperatures will be less severe than the hydrogen and oxygen attack from which the graphite surface would be shielded.

It is concluded that there were two distinct time periods in which corrosion occurred. The first is the period from ignition to the time when the deposit first coats the throat surface. Since surface temperatures are low, the oxygen and water reactions with graphite dominate. During this period, kinetic reaction limitations are most likely. However, this is also the period when the insulation pyrolysis gases may be most effective in neutralizing the oxidation potential of the propellant combustion products. This effect is contingent upon the retention of the ablation gases near the nozzle surface (boundary layer). The influence of the oxide deposits on the location and distribution of the pyrolysis gases has not been determined.

The second corrosion period occurs after the oxide deposits have melted and flowed away. The major portion of the nozzle throat surface is presumed to be exposed primarily to the propellant exhaust gases, the insulation pyrolysis gases, or mixtures of these. During this period, the hydrogen-carbon reactions should become increasingly important and may ultimately dominate. The Arcocel 191F and its analog, Arcocel 389, were hot enough that the deposits were shed, and the high temperature corrosion regime was entered for the final few seconds of firing. The others were coated with deposit until the end of firing and therefore only the low temperature corrosion occurred. Because of the gravity effect, the throat regression experienced in the high temperature regime was circumferentially nonuniform. In addition, the measured surface regression may include material shrinkage effects. Therefore, the measurements must be carefully interpreted. The throat corrosion measured on those nozzles which experienced only the first corrosion regime appear to be symmetrical. In this case, the small amount of corrosion measured tends to support the equilibrium combustion argument.

The Arcocel 390 (Arcocel 319BRF analog) firing was abnormal. However, it has been concluded that the results of the test are useful. The pressurization of the forward portion of the ADOBE chamber that occurred in the Arcocel 191F and Arcane 24F firings (T-1 and T-2) apparently modified the initial portion of the pressure decay. It does not appear that the results were otherwise influenced. The damage to the steel chamber which accompanied the leak is thought to have been caused by localized burning rather than simple melting of the steel. In accordance with the beryllium

CONFIDENTIAL

CONFIDENTIAL

propellant combustion model, this could most easily have occurred if the leaking gas had not burned with beryllium prior to reaching the chamber wall. The potential reactions of water vapor with the steel are significantly exothermic.

It is quite clear that the behavior of aluminum and beryllium exhausts is extensively similar with respect to their influence on the insulation and nozzle materials behavior. This is particularly true in terms of the occurrence and effects of oxide deposits. Under equilibrium combustion conditions, it is theoretically predicted that beryllium propellants should be only slightly more corrosive than their aluminum analogs once the oxide deposit effects disappear. However, the higher melting point of the beryllia with respect to alumina may lead to higher total corrosion by the aluminum analog. It should be noted that the thermodynamic stability of the aluminum and beryllium carbides plays an important role in determining the graphite surface temperature at which the deposit protection is lost. This temperature is a relatively strong function of the nozzle pressure. The time at which the deposit is lost will obviously be a function of the nozzle thermal designs as well as of the deposit conductance.

It is concluded that numerous motor and nozzle design similarity conditions must be satisfied before corrosion-erosion measurements can be correlated with propellant formulation. The reduced importance of deposition effects in most aluminum propellant firings leads to an overall impression that the data correlate. The characterization of aluminum firings by "averages," while very imprecise, has been reasonably successful. The same approach for beryllium propellants should and has been observed to be much less successful. Similarly, comparison of beryllium with aluminum propellant test data should be confusing when the averaging approach is taken. However, it is expected that the basic heat transfer, mass transfer, and chemistry phenomena act on motor materials in a consistent (universal) manner. If these phenomena are examined at every instant throughout the firing, the understanding of both beryllium and aluminum propellant behavior, with respect to materials performance, can be understood and correlated. Other conclusions regarding heat transfer, deposition effects, and motor performance are presented in the preceding sections of this report.

b. (U) Recommendations

A recommendation has been made to AFRPL that the scope of the motor tests be changed. Basically the change would add three small motor tests designated T-23, T-24, and T-25. At the same time, the Development Motor Test T-55 would be eliminated. Test T-23 would be identical to Tests T-21 and T-22 except that the Arcocel 319BRF propellant would be used. Test T-24 would be identical to Test T-21 except that the submerged nozzle design of Test T-12 would be used. Test T-25 would be identical to Test T-9 except that the radial thickness of the pyrolytic graphite washers would be

CONFIDENTIAL

CONFIDENTIAL

increased significantly. This recommendation was based on relative judgments concerning the value of the data to be obtained. It should not be implied that any judgment of the designs or nozzle materials capabilities has been made.

c. (U) Future Work

During the next reporting period, the following tasks will be completed:

- (1) All of the small motor grains, nozzles and insulation components will be manufactured and delivered to AFRPL for testing.
- (2) All of the small motor tests will be conducted and the post-test analysis of data and hardware will be completed.
- (3) All designs for the development motor tests will be completed.
- (4) The manufacture of all motor components for the development motor tests will be completed. The propellant grains and motor hardware will be delivered to AFRPL for test.

SECTION VI (U)

INDUSTRIAL HYGIENE AND SAFETY

The Industrial Hygiene program progress during this period has been limited due to delays in the motor testing phase, and consequently a reduced handling of beryllium material within the laboratory. Post-test analysis of the condensed phase reaction studies were continued and completed in January. Additionally, post-test analysis of exhaust particles, nozzle deposits and chamber deposits has been completed for the beryllium and aluminum end burner tests.

Statistical evaluation of the quantitative sampling results are continuing. The major effort during this reporting period, in accordance with the program plan, has been in monitoring the laboratory operations. Baseline, background and statistically acceptable variables have been defined within the laboratory environment. No beryllium incidents have occurred.

Repair work on contaminated ADOBE motor cases was completed without incident. This work was conducted under stringent personnel and environmental control procedures. Enclosure of the experimental saw was completed and extensive acceptance tests have been conducted using non-beryllium parts.

A major effort was devoted to the acceptable decontamination of the arc plasma facility (Control Area #2). Absolute filter dry methods and triple application of wet methods were used combined with necessary Industrial Hygiene and Safety Program requirements for personnel protection. The post-experiment medical program for personnel engaged in this portion of the experiment has been completed. No significant medical findings were evident.

Out-plant air sampling is continuing with the sampling program being expanded due to an increase in the number of point source emission locations. This is the result of the addition of new beryllium programs. Selection of the new sampling locations was predicated on extensive meteorological studies.

Cumulative program sample results are given in Table XXVIII.

TABLE XXVIII. CUMULATIVE BERYLLIUM SAMPLING RESULTS

No. <u>Samples Taken</u>	Type Location	Hours Sampled	Avg. mcg/m ³ Concentration	Max. mcg/m ³ Concentration
18	Personnel - MM Controlled Area #1	75.0	less than .096	.51
5	Personnel - MSA Controlled Area #1	9.1	less than .450	.71
3	Personnel - MSA Controlled Area #2	4.5	.34	.38
6	High Volume Cut-Plant Stations	14.3	.0009	.003
11	High Volume Controlled Area #1	29.3	less than .022	.1600
9	High Volume	6	.059	.24

16	Wipe Samples	NA	1.94	5.3
2	Sewerage effluent	NA	less than .001 mg/l	.001 mg/l

As a major beryllium propellant producer, Atlantic Research Corporation routinely follows Government approved industrial hygiene procedures. The subcontractor has reported that the results of their industrial hygiene sampling program have shown no toxic beryllium concentrations above the allowable limits. In addition, no accidents or incidents involving beryllium have been reported during the second reporting period.

CONFIDENTIAL

SECTION VII (C)

PROGRAM INTEGRATION AND DEMONSTRATION

7.1 (C) PROGRAM INTEGRATION

The physical aspects of nozzle performance are of primary interest in the present program. Functionally, it is required that the inner geometric contour of the nozzle be maintained within acceptable limits during the motor firing period. This contour is the surface of the refractory nozzle materials and, as such, is exposed to the thermal, physical and chemical actions of the rocket exhaust environment. As a direct consequence of such actions, the material which forms the contour may be removed at significant rates. The object of nozzle design technology is to either (1) employ materials such that their inherent thermal, chemical resistance and structural capacities are not exceeded or (2) moderate the degree to which the environment acts on, or the degree to which the material must react to, the environmental actions. Experience with beryllium propellants indicates that the physical response of the preferred graphite, tungsten and ablative insulation materials, presumably employed in accordance with (1) above, is not characteristic of their behavior in other propellant systems. Both extreme and erratic behavior has been recorded. Investigation of cooled nozzle performance, as in (2) above, has not been seriously undertaken for the obvious reasons.

The present program has been predicated on four major assumptions regarding the dominant causal factors which lead to poor and erratic nozzle materials performance with beryllium propellants. These are:

- (1) Chemical actions peculiar to beryllium propellants may be operative but the fundamental capacity limitations of the material of interest is independent of the propellant system.
- (2) There should be a reasonably small increase in beryllium propellant convective heat transfer and corrosion rates compared to analog aluminum propellants. This observation follows from
 - (a) beryllium propellants have higher theoretical performance, implying higher stagnation energy levels and lower molecular weights, both of which tend to increase heat transfer and corrosion; and
 - (b) ideal, thermodynamic equilibrium heat transfer and corrosion theory predicts such an increase.

CONFIDENTIAL

CONFIDENTIAL

- (3) Beryllium oxide deposits melt at a substantially higher temperature than the metal oxides of other propellants and may, therefore, shield the nozzle contour from corrosion and provide thermal insulation to a relatively greater degree. When the extent of oxide protection changes with grain or motor contour design, or when propellants are changed with small scale nozzles, then the nozzle and ballistic performance parameters should not correlate well.
- (4) Ideal, theoretical characterization of the composition and energy state of the combustion products may be particularly misleading for beryllium propellants. It is apparent that the mechanisms of metal particle combustion and the particle burning times are significantly different for beryllium as compared with aluminum. To complete the cycle, incomplete combustion of beryllium propellants would potentially introduce new and/or unexpected chemical actions on nozzle materials.

Basically, the program results during the second reporting period tend to support the validity of these assumptions. Furthermore, the present results provide only one apparent contradiction of the program integration discussion presented in the first progress report, Section VII of Reference 1.

The reported motor test results were intended to provide a direct comparison of the extent to which the propellant exhaust acts on the nozzle contour as the propellant composition is systematically varied. All other design parameters were essentially fixed; the end burning grains were installed approximately 24 inches from the nozzle throat (12 inches from the aft closure insulation at its outside diameter); the chamber velocities were about 10 ft/sec so that residence times (with respect to the throat) were of the order of 200 to 250 milliseconds during the firing; the exhaust flow was uniform in the axial direction. The objects in conducting the tests in this manner were to achieve a very high degree of combustion and to minimize exhaust flow nonuniformities which would prevent stable nozzle boundary layer growth. Then, with the thermochemical state of the exhaust known, the actions of the exhaust on the nozzle contour were to be interpreted in terms of the original formula of the four beryllium and three aluminum analog propellants.

In general, the test results do not reflect the very high degree of uniformity which might be predicted through the use of the standard, but superficial, correlating criteria (such as oxidation ratio, flame temperature, etc.). However, they do appear to be highly systematic when the effects of deposition are considered in detail. Thus, in each test, a significant amount of time (t_1) passes before either alumina or beryllia arrives at the throat

CONFIDENTIAL

CONFIDENTIAL

surface. The deposit continues to cover the throat to time t_r , which in several instances exceeded the grain burnout time, t_b . The degree to which the throat area was reduced by deposition varied for each test. Furthermore, each propellant has a different burn rate pressure dependence. It follows that each motor should exhibit individualistic tendencies which are a reflection of the coupling between the grain burning characteristics and throat deposition.

It is particularly important to note that composite propellants are least responsive to throat deposition. If (1) the throat surface temperatures reach levels where the oxide sticking mechanism is lost (t_r less than t_b) or if (2), during tailoff, sticking is lost at lower temperatures, there will be little or no visual evidence that throat deposition has occurred. On the other hand, double base propellants will exhibit serious chamber pressure excursions for small nozzles, providing a positive indication of deposition even though deposits are not present after the firing. It should be noted that when the grain burning characteristics and/or burning surface history are not well known, it will be very difficult to construct the throat deposit thickness history from the motor ballistic data. It is also apparent that the propellant performance characteristics (efficiency) cannot be accurately interpreted unless the deposit thickness history is known.

The general behavior of the transient throat deposition phenomenon can be viewed in the following sequential manner.

- (1) Condensed phase impaction occurs where the exhaust is turned by the aft closure or nozzle inlet. The impact "source" is located some distance & upstream of the throat.
- (2) Ablative surfaces reject the deposit for some small but finite time because of the high initial ablation rate and/or the lack of a liquid surface layer.
- (3) When sticking begins, the deposit will be solidified at the contour interface due to the low prevailing heat transfer rate and the low thermal conductivity of the oxide deposit.
- (4) The oxide surface may always be molten or will melt after a short time. The gas surface shear will tend to move the liquid downstream to cover new surfaces. The liquid will react with carbon or graphite surface material until a stable carbide interlayer is formed. If the surface (such as ATJ graphite) is initially too hot, the

CONFIDENTIAL

CONFIDENTIAL

deposit should provide insulation, permitting the surface temperature to fall and a chemical bond to be established (at about 5200°F for alumina and 4800°F for beryllia).

- (5) The deposit "overflow" process will continue until time t_1 when it reaches the throat. Since the deposit alters the smoothness of the contour, new material may be deposited just ahead of the flow as it propagates toward the throat. Since the throat is a heat sink, the deposit may fuse to a great extent, slowing the propagation rate in spite of the increasing gas shear forces.
- (6) The motor-nozzle contour acts as a capacitor in that a large amount of oxide material may be stored. Eventually the oxide will not be cooled sufficiently by the contour material and the oxide will melt at an increasing rate. The liquid film velocities will increase. Large amounts of material may move past the throat. This material may be cold trapped by the cooler exit cone surfaces or it may pass completely through the nozzle.
- (7) When the supply of liquid is diminished at any point, the deposit thickness will decrease and contour temperatures will rise. More of the oxide will melt and flow downstream until the stored material is eliminated and a balance is achieved between the impaction-sticking rate and the liquid film flow rate.
- (8) At any point along the contour, the surface temperatures may eventually rise to levels where the oxide will not stick. Liquid may still be flowing over these surfaces from the cooler regions upstream. In this case, droplet or bead flow is expected and some corrosion (axial grooving) should occur. Such action could continue to the end of firing unless all condensed phase impaction ceases or all particles which impact are rejected.
- (9) Because of gravity and surface tension effects, the liquid oxide should not uniformly cover the nozzle throat during the later stages of the firing.

CONFIDENTIAL

CONFIDENTIAL

This type of qualitative model can be used to identify the design parameters which affect the transient throat deposition. The following list includes most of the recognized parameters.

- (1) Materials, including aft closure insulator, nozzle entrance, throat, exit cone and the order of appearance.
- (2) Contour geometry, especially the contour length (l) and surface area upstream of the throat (contraction ratio).
- (3) Grain design, including those parameters which determine the oxide particle velocity vector, erosive burning and incomplete metal particle burning.
- (4) Propellant, including the burning characteristics, metal loading, metal type (Be or Al) and metal particle size distribution.
- (5) Thermal design, particularly the heat sink capacity of the nonablating contour materials.

At the present time it is apparent that an analytical model cannot be conveniently constructed to predict the origin, propagation and thickness of condensed phase deposits. Considering (1) the lack of high temperature oxide property data, (2) the potential effect of silica and carbon impurities, (3) the requirement for accurate ballistic data, and (4) the large number of design parameters involved, it is unlikely that empirical data correlation efforts would be successful. However, for any particular motor application it should be possible to deduce the relative effectiveness of competitive combinations of free design parameters by means of the heat transfer and corrosion measurement techniques being used in this program.

Aside from its influence on motor ballistics, the deposit provides thermal insulation and complete chemical protection of the graphite and carbonaceous char materials along the contour, as long as it remains. As the throat diameter is increased the ballistic performance effects and errors diminish to insignificance. This is because the deposit thickness is limited by its melting point and thermal conductivity. The melting point of beryllia is nearly 1000°F above that of alumina while the thermal conductivity of beryllia is about three times that of alumina. At least in the throat region, the thermal insulation effect of the reported tests can be evaluated simply by multiplying the area of the alumina deposit thickness history curve by three and comparing the result with the area of the beryllia deposit history curve. The alumina was about half as effective

CONFIDENTIAL

CONFIDENTIAL

as the beryllia for the highest temperature analog pair (Tests T-1 and T-7). The alumina was about 20 percent more effective than the beryllia for the low temperature composite analog pair (Tests T-4 and T-5). However, in a slightly longer firing the advantage of the alumina might have disappeared since the deposit in Test T-4 was not removed at burnout.

Considering the corrosion protection afforded by the deposit, alumina should have the advantage since the carbide interlayer is stable at higher temperatures than beryllia (apparently by 400°F at about 500 psia throat pressure). On the other hand, except for short tests with low temperature propellants, the beryllia will retard the temperature rise to a greater extent, counteracting the alumina's advantage. In the reported tests, the deposit arrived over the throat surface before the temperature reached the melting point of the appropriate oxide. If this had not been the case (as with an ATI throat insert), the corrosion protection should still pertain but much of the thermal insulation effect would be lost, reducing the overall oxide residence time. With both the thermal and corrosion factors considered in detail, it should not be expected that nozzle erosion data could be correlated when throat deposition has occurred. With appropriately chosen sets of test parameters, beryllium propellants could actually be shown to be either more or less corrosive than aluminum propellants.

It should be noted that, in Section 7.1 of Reference 2, it was suggested that the high temperature corrosion (above 4500°F) would probably not be affected by chemical kinetic reaction restraints (hydrogen-carbon reactions). The comparison of the results of Tests T-1 and T-7 with an approximate analytical prediction suggests that this may not be true. Close examination of the surface of the pyrolytic graphite showed that there were a large number of pits, approximately 0.05 inch long, 0.01 inch wide and 0.05 inch deep. The pits resemble surface delaminations which may have opened on cooldown. However, these could also be preferred reaction sites. Much larger pits and circumferential grooves have been observed in pyrolytic graphite which has been at 5000°F or above for longer periods of time. There was no nodule erosion of the pyrolytic graphite and the pits were concentrated on the upper half of the throat surface which probably lost the deposit protection earliest. The exit cones suffered minor surface pitting on these two tests. Exit cone temperatures were not recorded. The pits could have started to develop early in the test, before deposition, and they were not well developed in the axial direction. Similar pitting was not observed with the cooler propellants. Once the deposit protection is lost, such erosion pits would be expected to develop rapidly, with or without the benefit of corrosion.

There is an alternate to the kinetic reaction limitation explanation for the low surface regression rate. The high temperature hydrogen reactions produce acetylene which is convected downstream in the boundary layer. The simple corrosion rate theory presumes that the boundary layer is well

CONFIDENTIAL

CONFIDENTIAL

developed and mass transport effectively occurs by diffusion to and from the wall. When the nozzle inlet, and probably part of the pyrolytic graphite throat insert section, is coated with oxide, the boundary layer is not developed with respect to the acetylene distribution. The highest surface temperatures are known to occur upstream of the throat where corrosion could not be accurately measured. It is possible, then, that the concentrations of the acetylene at the throat surface (and downstream of the throat) are higher than the theory could predict. This would effectively reduce the throat corrosion rate. It is also likely that the hydrocarbons which reach the turbulent outer portion of the boundary layer will react with water vapor, neutralizing its effect on corrosion. The consumption of the hydrocarbon by this means would not significantly accelerate the diffusion of the acetylene away from the wall, since the primary concentration gradients should be confined to the sublayer portion of the boundary layer.

It is unfortunate that the analysis of the ballistic and particle sampling test data has not provided a clearer picture of the propellant combustion. A similar problem appears to exist for the data from other small motor test programs. Evidently, improved experimental techniques, which includes thermal instrumentation, are required. For the present it is presumed that the nonequilibrium chemistry deviations were significantly less important than they would be for much shorter chamber residence times. Subsequent tests with smaller residence times may help to clarify this situation. The efforts being devoted to the evaluation of the exhaust gas side convective heat transfer coefficient will be continued and the comparison of the results with the advanced boundary layer theory predictions could also be enlightening.

The laboratory studies have confirmed the existence of two low melting tungsten-beryllium alloys. These apparently will form only through direct contact of the two metals. It is predicted that the combination of beryllium alloying at low temperatures and the formation of tungsten carbides at higher temperatures is the primary cause of tungsten insert failures. Incomplete combustion of (at least) the larger beryllium metal particles, high grain port velocities and particle impact on tungsten are probably all required to provide a source of beryllium for tungsten alloying. Therefore, this phenomenon must occur early in the firing. It is not obvious that there will be any residual beryllium in the tungsten after continued heating and/or carbon attack. A number of tungsten inserts, from this and other programs, will be examined during the next reporting period in an effort to gain more evidence.

During the remainder of the program, the primary task will be to evaluate the program test results. These tests introduce the additional complications of (1) grain design, (2) nozzle contour variations, (3) nozzle inlet material changes, (4) nozzle throat material changes, (5) chamber residence time variation and (6) scale changes. All test results will be interpreted

CONFIDENTIAL

CONFIDENTIAL

in terms of the ballistic, heat transfer and corrosion phenomena. All results will be compared with the theoretical results to establish the validity and/or utility of the analytical and experimental design tools.

In conclusion, the two most important results of the program are reiterated. First, the actions of beryllium and analog aluminum propellants are (or can be) extensively similar with respect to graphitic materials. This may not be true for dense tungsten. Secondly, pyrolytic graphite heat sink nozzles can be designed to give satisfactory performance with beryllium propellants. By exploiting the advantages of beryllia deposit protection, the nozzles can probably be designed to give better performance in beryllium systems than in aluminum.

7.2 (U) PROGRAM DEMONSTRATION

The analytical prediction techniques developed in this program will be demonstrated through correlation with available beryllium motor test firing data. This demonstration will be performed after the completion of the program motor firings. It is planned to select a motor design for which test results are or will soon be available from some other beryllium propellant program. It is not expected that such results would have been previously included in the data correlation work. Furthermore, the propellant and grain design are not expected to be ones specifically used in the present program.

CONFIDENTIAL

REFERENCES

1. *Smallwood, W. L., et al, Beryllium Erosion Corrosion Investigation for Solid Rocket Nozzles (U), First Quarterly Progress Report, Confidential, Contract AF 04(611)-10753, AFRPL-TR-65-205, November 1965.
2. *Simmons, B. A. and Dockham, R. L., Development of a Small, Solid-Rocket Missile Propulsion System (U), Confidential, Contract AF 04(694)-739, BSD-TR-65-200, 15 December 1965.
3. Kuehl, D. K., "Ignition and Combustion of Aluminum and Beryllium," AIAA Journal 3, December 1965, pp 2239-2247.
4. Macek, A., Friedman, R. and Sempie, J. M., Techniques for the Study of Combustion of Beryllium and Aluminum Particles, Project SQUID, Technical Report ARC-8-P, University of Virginia, Charlottesville, Virginia, February 1964. (See also succeeding semiannual reports.)
5. Elliott, D. G., Bartz, D. R. and Silver, S., Calculation of Turbulent Boundary-Layer Growth and Heat Transfer in Axisymmetric Nozzles, Jet Propulsion Laboratory, Technical Report No. 32-387, California Institute of Technology, Pasadena, California, 15 February 1963.
6. Price, F. C., et al, Internal Environment of Solid Rocket Motors, Final Technical Report, Contract AF 04(611)-9072, AFRPL-TDR-64-140, 30 July 1964.
7. Carlson, D. J., Alumina Absorption and Emittance, Final Technical Report, ARPA Contract NOnr 3606(00), Aeronutronic Publication No. U-2627, 31 May 1964.
8. Fontenot, J. E., "Thermal Radiation From Solid Rocket Plumes at High Altitude," AIAA Journal 3, Technical Note, May 1965, pp 970-972.
9. Eckert, E. R. G. and Drake, R. M., Heat and Mass Transfer, McGraw-Hill Book Co., New York, 1959.

REFERENCES (Continued)

10. Wilhelm, J. R., Ablation of Refrasil-Phenolic Nozzle Inserts in Solid Propellant Exhaust Environments, AIAA Preprint No. 64-223, Presented at The 1st AIAA Annual Meeting, Washington, D.C., June 29 - July 2, 1964.
11. Armour, W. H., et al, An Investigation and Feasibility Demonstration of Nozzles for Restartable Solid Rocket Motors (U), Final Report, Confidential, Contract AF 04(611)-9904, AFRPL-TR-66-53, 31 March 1966.
12. Bird, R. B., Stewart, W. E. and Lightfoot, E. N., Transport Phenomena, John Wiley & Sons, New York, 1962.
13. Hansen, M., Constitution of Binary Alloys, McGraw-Hill Book Co., New York, 1958.
14. Pearson, W. B., A Handbook of Lattice Spacings and Structures of Metals and Alloys, Pergamon Press, New York, 1958.
15. *Shaver, R. G., et al, Development of High-Energy Solid Propellant Formulations (U), Final Report, Confidential, Contract AF 04(611)-8180, AFRPL-RTD-TDR-63-1064, July 19